Thèse de Doctorat

Etude des manganites Ruddlesden-Popper $RE_xA_{2-x}MnO_4$ (RE : La, Nd et A : Sr, Ca) en vue de leur application en tant que matériaux d´électrode de pile à combustible à oxide solide (SOFC)

Présentée à

l´Universidad Industrial de Santander
et
l´Université de Lille 1

pour obtenir le grade de
Docteur en Chimie
(Spécialité: Molécules et Matière Condensée)

par

Mónica Viviana SANDOVAL RINCÓN

Soutenue le 13 Octobre 2017 devant la commission d'examen composée de :

Rapporteurs : Dr. Maria Teresa CALDES, Institut des Matériaux Jean ROUXEL
Dr. Liliana MOGNI, Centro Atómico Bariloche - CNEA
Examinateurs : Dr. Martha Eugenia NIÑO, Universidad Industrial de Santander
Dr. Fabian Alirio RÍOS, Universidad Industrial de Santander

Directeurs de Thèse : Dr. Gilles GAUTHIER
Dr. Pascal ROUSSEL
Co-encadrante : Dr. Caroline PIROVANO

Doctoral Thesis

Study of Ruddlesden-Popper manganites $RE_xA_{2-x}MnO_4$ (RE: La, Nd and A: Sr, Ca) with potential application as electrode materials in Solid Oxide Fuel Cells (SOFC)

A dissertation submitted to the

Universidad Industrial de Santander
and
Université de Lille 1

To obtain the degree of Doctor in Chemistry
(Specialty: Molécules et Matière Condensée)

by

Mónica Viviana SANDOVAL RINCÓN

Defended on October 13, 2017

Reviewers: Dr. Maria Teresa CALDES, Institut des Matériaux Jean ROUXEL
Dr. Liliana MOGNI, Centro Atómico Bariloche - CNEA
Examiners: Dr. Martha Eugenia NIÑO, Universidad Industrial de Santander
Dr. Fabian Alirio RÍOS, Universidad Industrial de Santander

Thesis directors: Dr. Gilles GAUTHIER
Dr. Pascal ROUSSEL
Co-director: Dr. Caroline PIROVANO

ACKNOWLEDGEMENTS

I wish to express my deep gratitude to my advisor *Profe* Gilles Gauthier for giving me the opportunity to realize this thesis by his side. Certainly, his knowledge, support, kindness and fine sense of humor made me grow professionally and allowed me to love even more the chemistry. I also deeply thank Caroline Pirovano and Pascal Roussel for their contributions and to make their laboratory available to me, as well as for their patience with my spoken French.

I also thank those who provided invaluable technical assistance: Florence Porcher, Nora Djelal, Laurence Burylo, Edouard Capoen, Romain Jooris and Olivier Gardoll. I also need to mention "my little students" Maria Alejandra Murcia, Andrea Prada, Silvia Durán, Silvia Flórez, Carolina Cardenas, Giovanny Rodriguez, Jose David García and Santiago Palencia who helped me enormously in experimental development.

I appreciate the collaboration of the Grupo de Investigación en Tecnologías de Valorización de Residuos y Fuentes Agrícolas e Industriales para la Sustentabilidad Energética (INTERFASE), Unité de Catalyse et Chimie du Solide (UCCS), Laboratoire Léon Brillouin (LLB-CEA) and Laboratorio de Difracción de Rayos X (Parque Tecnológico Guatiguará-UIS) which was fundamental for the experimental development of this thesis.

I thank COLCIENCIAS for my Ph.D. scholarship and French Government for the “Eiffel excellence scholarship". I also thank the financial support of the Vicerrectoría de Investigación y Extensión of the Universidad Industrial de Santander (Projects 1333 and 1854), of COLCIENCIAS (Project 110265842833 - contract 038-2015) and of Chevreul institute (FR 2638), Ministère de l’Enseignement Supérieur et de la Recherche, Région Hauts de France and FEDER.

Also, I want to thank my friends July, Marito, Jose Luis, Lina, Oscar, Silvia, Mimi, Zulma, Sebastian, Carolina, Margarita, Nicolas and Lila who shared with me so many nice moments during these years, and especially to Coki who enjoyed with me the stay in France (also cooked).

I heartfelt thanks goes to my mami, my papi, Kelly and David, and especially thanks to my beloved husband Camilo, for his love and support.

Finally, I would like to thank all who contributed to the realization of this thesis.

Moni

RESUME

TITRE : Etude des manganites Ruddlesden-Popper $RE_xA_{2-x}MnO_{4\pm\delta}$ (RE : La, Nd et A : Sr, Ca) en vue de leur application en tant que matériaux d´électrode de pile à combustible à oxide solide (SOFC)

AUTEUR : Mónica Viviana SANDOVAL RINCÓN

MOTS-CLEFS : SOFC symétrique, Ruddlesden-Popper, Manganite, Diffraction de Rayons X sur poudre, Diffraction de Neutrons sur poudre, Conductivité électrique, Réactivité, Spectroscopie d'Impédance Electrochimique.

DESCRIPTION :

Les manganites de type Ruddlesden Popper $RE_xA_{2-x}MnO_4$ (RE : La, Nd et A : Sr, Ca) ont été étudiées en tant que possibles matériaux d'électrode pour piles à combustibles à oxyde solide symétriques. Trois séries de composés $La_xSr_{2-x}MnO_{4\pm\delta}$ (x=0.25, 0.4, 0.5 et 0.6), $Nd_xSr_{2-x}MnO_{4\pm\delta}$ (x=0.4 et 0.5) et $Nd_xCa_{2-x}MnO_{4\pm\delta}$ (x=0.25, 0.4 et 0.5) ont été synthétisées pures avec succès. Les matériaux $RE_xSr_{2-x}MnO_{4\pm\delta}$ avec RE : La, Nd sont stables sous atmosphère réductrice et présentent des Coefficients d'Expansion Thermique (TEC) compatibles avec ceux des électrolytes. L'étude *In situ* par Diffraction de Neutrons sur poudre à haute température du composé $La_{0.5}Sr_{1.5}MnO_{4\pm\delta}$ (L5S15M), sous flux d'hydrogène, révèle la formation de lacunes d'oxygène sur les sites équatoriaux de la couche pérovskite. Des valeurs élevées de conductivité électrique ont été obtenues (35.6 S cm^{-1} sous air et 1.9 S cm^{-1} sous H_2/Ar). Les propriétés électrochimiques de l'électrode L5S15M ont été examinées par Spectroscopie d'Impédance Electrochimique (EIS). L'influence sur les performances électrochimiques à la fois de la température de frittage et de la composition de l'électrode (L5S15M pur ou composite L5S15M:GDC) a été étudiée dans les deux atmosphères, cathodiques et anodiques. Du côté de la réduction de l'oxygène, le transfert d'électrons entre l'électrode et l'oxygène, et l'incorporation des

ions oxygène dans l'électrode sont les principales étapes limitantes pour des électrodes frittées à 1150 et 1200 °C. L'augmentation de la température de frittage à 1250 °C conduit à l'accumulation de Sr à l'interface GDC/YSZ et la dégradation consécutive de la cellule. L'électrode composite n'apporte aucune amélioration. Pour l'oxydation de l'hydrogène, trois étapes limitantes ont été identifiées : le transfert de charge à l'interface électrode/électrolyte, l'adsorption dissociative de l'hydrogène et la diffusion de surface. Pour chacune des électrodes, le processus de diffusion de surface représente la contribution majoritaire à la résistance de polarisation totale. Le meilleur compromis entre température de frittage et composition est obtenu pour une électrode de L5S15M pur frittée à 1150 °C. Finalement, les résultats extraits des mesures par EIS ont permis de comprendre la nature des processus mis en place au sein de l'électrode, révélant que le comportement électrochimique de $La_{0.5}Sr_{1.5}MnO_{4\pm\delta}$ pouvait être amélioré par la modification de la surface de l'électrode.

ABSTRACT

TITLE: Study of Ruddlesden-Popper manganites $RE_xA_{2-x}MnO_{4\pm\delta}$ (RE: La, Nd and A: Sr, Ca) with potential application as electrode materials in Solid Oxide Fuel Cells (SOFC).

AUTHOR: MÓNICA VIVIANA SANDOVAL RINCÓN

KEYWORDS: Symmetrical SOFC, Ruddlesden-Popper, Manganite, Powder X-ray diffraction, Neutron powder diffraction, Electrical conductivity, Reactivity, Electrochemical Impedance Spectroscopy.

DESCRIPTION:

The Ruddlesden Popper manganites $RE_xA_{2-x}MnO_4$ (RE: La, Nd and A: Sr, Ca) have been studied as possible electrode materials for symmetrical Solid Oxide Fuel Cells. Three series of compounds $La_xSr_{2-x}MnO_{4\pm\delta}$ (x=0.25, 0.4, 0.5 and 0.6), $Nd_xSr_{2-x}MnO_{4\pm\delta}$ (x=0.4 and 0.5) and $Nd_xCa_{2-x}MnO_{4\pm\delta}$ (x=0.25, 0.4 and 0.5) were successfully synthesized as single phases. The $RE_xSr_{2-x}MnO_{4\pm\delta}$ materials with RE: La, Nd are stable under reducing atmosphere with electrolyte-compatible Thermal Expansion Coefficients (TECs). *In situ* high temperature neutron powder diffraction study of $La_{0.5}Sr_{1.5}MnO_{4\pm\delta}$ (L5S15M), under flowing hydrogen, reveals formation of oxide-ion vacancies on the equatorial sites of the perovskite layer. High electrical conductivities were obtained (35.6 S cm^{-1} in air and 1.9 S cm^{-1} in H_2/Ar). Electrochemical properties of L5S15M electrode were investigated by Electrochemical Impedance Spectroscopy (EIS). The influence of both sintering temperature and electrode composition (pure L5S15M or L5S15M:GDC composites) on the electrochemical performance was studied in both cathode and anode atmosphere. For oxygen reduction, the electron transfer between the electrode and oxygen, and the incorporation of oxygen ions into the electrode are the main rate-limiting steps for electrodes sintered at 1150 and 1200°C. Increasing the sintering

temperature to 1250°C leads to Sr accumulation at the GDC/YSZ interface and subsequent cell degradation. The composite electrode does not show any improvement. For hydrogen oxidation, three limiting steps are identified: charge transfer at the electrode/electrolyte interface, dissociative adsorption of hydrogen and surface diffusion. For all electrodes, the surface diffusion process represents the highest contribution to the total polarization resistance. The best compromise between sintering temperature and composition is reached for pure L5S15M electrode sintered at 1150 °C. Finally, the results extracted from EIS measurements allowed understanding the nature of processes taking place within the electrode, proposing that the electrochemical behavior of $La_{0.5}Sr_{1.5}MnO_{4\pm\delta}$ could be improved with modification of the electrode's surface.

RESUMEN

TÍTULO: Estudio de las manganitas Ruddlesden-Popper $RE_xA_{2-x}MnO_{4\pm\delta}$ (RE: La, Nd y A: Sr, Ca) con potencial aplicación como materiales de electrodo en Celdas de Combustible de Óxido Sólido (SOFC).

AUTOR: MÓNICA VIVIANA SANDOVAL RINCÓN

PALABRAS CLAVE: SOFC simétrica, Ruddlesden-Popper, Manganita, Difracción de Rayos-X de polvo, Difracción de Neutrones, Conductividad Eléctrica, Reactividad, Espectroscopía de Impedancia Electroquímica.

DESCRIPCIÓN:

Las manganitas Ruddlesden Popper $RE_xA_{2-x}MnO_4$ (RE: La, Nd y A: Sr, Ca) han sido estudiadas como posibles materiales de electrodo para Celdas de Combustible de Óxido Sólido simétricas. Tres series de compuestos $La_xSr_{2-x}MnO_{4\pm\delta}$ (x=0.25, 0.4, 0.5 y 0.6), $Nd_xSr_{2-x}MnO_{4\pm\delta}$ (x=0.4 y 0.5) y $Nd_xCa_{2-x}MnO_{4\pm\delta}$ (x=0.25, 0.4 and 0.5) fueron sintetizadas satisfactoriamente como fases puras. Los materiales $La_xSr_{2-x}MnO_{4\pm\delta}$ con RE: La, Nd son estables en atmósfera reductora, presentando Coeficientes de Expansión Térmica (TECs) compatibles con los electrolitos. El estudio en atmósfera reductora por Difracción de Neutrones *in-situ* a alta temperatura del material $La_{0.5}Sr_{1.5}MnO_{4\pm\delta}$ (L5S15M), reveló la formación de vacancias de iones óxido en los sitios ecuatoriales de la capa perovskita. Para este material se obtuvo también una alta conductividad eléctrica (35.6 S cm^{-1} en aire y 1.9 S cm^{-1} en H_2/Ar). Las propiedades electroquímicas del electrodo L5S15M fueron investigadas por Espectroscopía de Impedancia Electroquímica (EIS). La influencia tanto de la temperatura de sinterización como de la composición del electrodo (L5S15M puro o L5S15M:GDC composites) sobre el rendimiento electroquímico fue estudiada en atmósfera oxidante y reductora. Para la reducción de oxígeno, la

transferencia de electrones entre el electrodo y el oxígeno, y la incorporación de iones oxígeno dentro del electrodo, son los principales pasos limitantes de la velocidad para los electrodos sinterizados a 1150 y 1200 °C. El incremento de la temperatura de sinterizado hasta 1250 °C, condujo a la acumulación de Sr en la interfase GDC/YSZ y subsecuente degradación de la celda. El electrodo composite no presenta ninguna mejora del rendimiento. Para la oxidación de hidrógeno, se identificaron tres pasos limitantes: transferencia de carga a la interfase electrodo/electrolito, adsorción disociativa de hidrógeno y difusión superficial. Para todos los electrodos, la difusión superficial representa la mayor contribución a la resistencia de polarización total. La mejor relación entre la temperatura de sinterizado y la composición fue lograda para el electrodo puro L5S15M sinterizado a 1150 °C. Finalmente, los resultados extraídos desde las medidas de EIS, permitieron entender la naturaleza de los procesos que tienen lugar dentro del electrodo, proponiendo que el comportamiento electroquímico de $La_{0.5}Sr_{1.5}MnO_{4\pm\delta}$ podría ser mejorado con la modificación de la superficie del electrodo.

TABLE OF CONTENTS

LIST OF FIGURES

CHAPTER 1

CHAPTER 2

CHAPTER 3

LIST OF TABLES

CHAPTER 3

LIST OF ANNEXES

INTRODUCTION

The exhaustion of traditional energy sources (fossil fuels), climate change, increased oil dependence and rising energy costs create the need to find alternative energy solutions especially for developing countries which are now more vulnerable than ever to the energy deficit. Because of this, it is essential to start contributing to the development and application of alternative renewable sources or to use them in a more efficient way, in order to address the energy crisis and participate to a cleaner environment. The generation of energy through Solid Oxide Fuel Cells (SOFC), an electrochemical device that operates at high temperature, is a possible option since this highly efficient technology is based on the direct conversion of fuels into electricity. In those systems, efficiency values are theoretically higher than those of thermal machines (such as motors, turbines, etc.) and have the huge advantage of being able to use a diversity of fuels such as hydrocarbons, alcohols, synthesis gas, among others, which cannot be used directly in low temperature fuel cells [1][2]. However, one of the main critical issues to solve for viable SOFCs is their high prices mainly related to the difficulty in finding and producing efficient, reliable, durable and cheap cell materials for the three main components of the device, *i.e.* the anode, the electrolyte and the cathode.

The currently used SOFC materials present numerous drawbacks and several issues still needs to be addressed. For instance, Ni/YSZ cermet at the anode exhibit numerous drawbacks that are even more pronounced when used in cells operating with hydrocarbon fuels. At the cathode, lanthanum strontium manganite ($La_{1-x}Sr_xMnO_3$) is the state-of-the-art material but such electrocatalyst requires a high activation energy, *i.e.* high operating temperatures are needed, which is not in favor of sustainable process and result in cell materials degradation. Hence, one research

[1] S. Mekhilef, *et al.*, *Renew. Sustain. Energy Rev.*, vol. 16, no. 1, pp. 981-989, 2012.
[2] N. Mahato, *et al*., *Prog. Mater. Sci*., vol. 72, pp. 141-337, 2015.

axis consists in finding materials able to operate at lower temperatures. One advantage of decreasing the operating temperature is the opportunity to use low-cost metallic interconnecting materials between the cells and to limit the electrode degradation, caused by the chemical and/or thermomechanical incompatibility between the components. However, decreasing SOFC operating temperature results in slower kinetics of the oxygen reduction reaction and large polarization losses [3]. On the other hand, the complications for anode's production are mainly due to (i) the deposition of carbon due to the catalytic cracking reaction [4][5], (ii) the low tolerance to sulfur which is present in real fuels as H_2S molecules for example [6] and (iii) the mechanical instability of Ni/YSZ caused by delamination after several redox cycling [7].

In recent years, researchers have focused on finding better electrocatalysts for electrode reactions by studying new structural arrangements exhibiting some anisotropy (two-dimensional structure) in order to find mixed ionic and electronic conducting materials (MIEC). The mixed conductivity can potentially extend the triple phase boundary (TPB) active region over the entire electrode, thus greatly reducing the electrode polarization at low operating temperature. In this context, the present investigation focuses on the study of mixed conducting materials of K_2NiF_4-type structure (Ruddlesden-Popper phases) for potential application as electrodes in symmetrical cells. In this innovative configuration, the same material is used for both electrodes (air and hydrogen), which potentially simplifies the assembly process by allowing co-sintering of the electrodes and minimizes the problems related to the mechanical stress due to the differences in thermal expansion coefficients. The Ruddlesden-Popper phases, particularly the lanthanum nickelates $La_2NiO_{4+\delta}$ possess structural and transport properties that have made them promising

[3] R. Pelosato, *et al.*, *J. Power Sources*, vol. 298, pp. 46-67, 2015.
[4] M. Kogler, *et al., Mater. Chem. Phys*., vol. 173, pp. 508-515, 2016.
[5] Y. Zhang, *et al.*, *J. Power Sources*, vol. 279, pp. 759-765, 2015.
[6] H. Chen, *et al.*, *Appl. Energy*, vol. 179, no. 5, pp. 765-777, 2016.
[7] Y. Zhang, *et al., Solid State Ionics*, vol. 180, pp. 1580-1586, 2009.

candidates for Intermediate Temperature SOFC cathode materials [8][9]. Unfortunately, these nickel materials are not suitable for the anodic side because they are unstable in reducing atmosphere. In contrast, RP manganites could be proposed as symmetrical electrode, since the presence of manganese in the structure seems to be a key element for such dual function, what is the case for example for $La_{0.75}Sr_{0.25}Cr_{0.5}Mn_{0.5}O_{3-\delta}$ (LSCM) perovskite that exhibits a good stability in both reducing and oxidizing environments and an anodic behavior comparable to Ni/YSZ cermet [10][11].

This thesis presents the study of the $RE_xA_{2-x}MnO_4$ oxides with RE: La, Nd and A: Sr, Ca as possible electrode materials in symmetrical Solid Oxide Fuel Cells, including the determination of the range of compositions that can be prepared in air, the stability study in oxidizing and reducing atmospheres, the evaluation of chemical and thermo-mechanical compatibility with the common electrolytes, the determination of the electrical characteristics as a function of temperature and atmosphere, and finally the evaluation of the electrochemical properties of symmetrical cells operated in air and hydrogen.

The first chapter describes the scientific context of the research, the operation of solid oxide fuel cells and the essential requirements for the three main components of the cell, namely the electrolyte, cathode and anode. In addition, a comprehensive literature review of the electrode materials used in the past years, including a description of the properties (or issues) of both the well-known perovskite and Ruddlesden-Popper materials is given. This chapter also presents the advantages of a symmetric cell configuration, and the electrode materials reported so far, satisfying the corresponding specific requirements.

---

[8] R. J. Woolley and S. J. Skinner, *Solid State Ionics*, vol. 255, pp. 1-5, 2014.
[9] R. K. Sharma, *et al., J. Power Sources*, vol. 316, pp. 17-28, 2016
[10] D. M. Bastidas, *et al.*, *J. Mater. Chem.*, vol. 16, no. 17, pp. 1603-1605, 2006.
[11] S. Tao and J. T. S. Irvine, *J. Electrochem. Soc*, vol. 151, no. 2, pp. A252-259, 2004.

Chapter 2 presents the study of preparation conditions to obtain single phases within the $RE_xA_{2-x}MnO_4$ families with RE: La, Nd and A: Sr, Ca, the structural characterization performed using X-ray Powder Diffraction data (XRPD) and the evaluation of the thermal stability of the same materials under reducing conditions. This preliminary part of the work allows to make a first selection of potential electrode materials for symmetrical SOFC. The structural behavior during redox cycling of selected compositions, using *in situ* high temperature XRD and TGA measurements is then presented, that is completed with a deep study by *in situ* neutron powder diffraction (NPD) of one of the most promising and representative compositions, in order to get a further insight into the process of oxygen vacancies formation during reduction. Finally, the last selection is based on the analysis of the thermal stability and chemical compatibility of the remaining compositions with common electrolytes (LSGM, GDC and YSZ), completed by the determination of their electrical properties in air and hydrogen using the four-probe method.

The Chapter 3 concerns the determination of the optimized fabrication conditions for symmetric cells using the selected material of Chapter 2; the influence of electrode sintering temperature and electrode composition (composite) is described and thoroughly analyzed, based on the determination by Electrochemical Impedance Spectroscopy (EIS) of the electrochemical behavior in the oxygen reduction reaction (cathode) and the hydrogen oxidation reaction (anode). The results are discussed in order to correlate the different contributions that constitute the cathode and anode polarization resistances with the nature of the limiting steps of the corresponding electrode reactions and the characteristic parameters of the electrode elaboration process.

CHAPTER I

STATE OF THE ART

1.1 INTRODUCTION

1.1.1 ENERGETIC AND ENVIROMENTAL CONTEXT

Nowadays, environmental issues such as global climate change, natural resources depletion and air pollution, have strongly attracted world's attention. Currently, most countries are highly dependent on fossil fuels, since the latter are widely used to handle energy demand in industry, communication, transportation, food production, as well as domestic purposes [1][2][3]. According to the statistics of the International Energy Agency (IEA), total global energy consumption reached 21962 TWh in 2014, which was mainly supplied by 36%, 4%, 22%, 20% and 1.5% from coal, oil, natural gas, hydro sources and biofuels/waste, respectively. For its part, Colombia produces 74% of its energy from hydro sources, 9% from coal, 15% from natural gas and 1.4% from biofuels/waste (see Figure 1) [4]. Given the imminent consumption of fossil fuels, the emissions of CO_2, SO_x and NO_x have been growing during the last decades. As some reports indicate, these emissions have increased of about 16 million tons in the last 20 years, which would generate a global warming of 2 °C by the middle of the 21st century [5][6].

Figure 1. Electricity generation by fuel (a) in the world and (b) in Colombia.

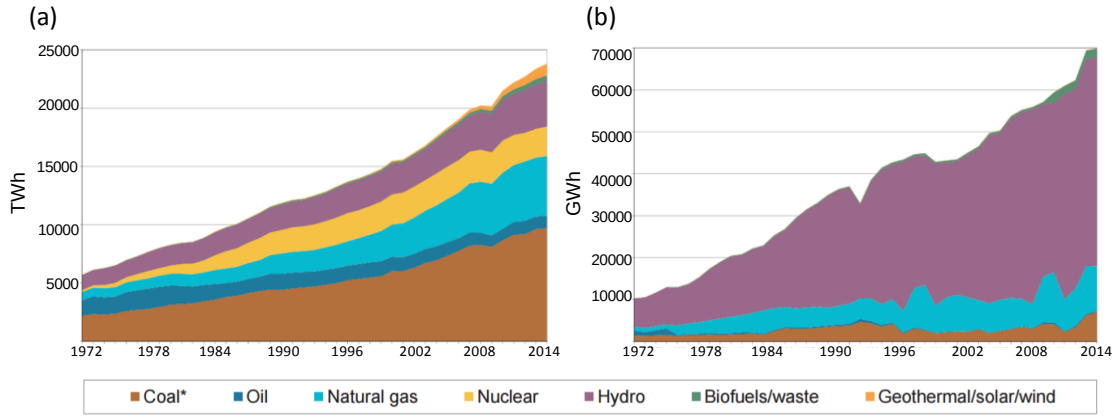

Taken from web: http://www.iea.org/statistics

In response to the need to decrease the fossil fuels depletion and the pollution, some potential solutions have evolved, including energy conservation through improved energy efficiency and an increase in environmental-friendly energy technologies, such as renewable sources and fuel cells [7][8][9][10]. In this context, hydrogen, a clean energy carrier that can be produced from any primary energy source, and fuel cells which are very efficient energy conversion devices, with the largest energy content of any fuel. In brief, the hydrogen and fuel cells open the way to integrated clean energy devices with high efficiency, durability and availability [11][12].

1.1.2 FUEL CELLS AND THE HYDROGEN ECONOMY

The economy based on hydrogen energy can be considered as a long-term transition process, which will allow to change the current energy system to one which attempts to combine the cleanliness of hydrogen as an energy carrier with the efficiency of fuel cells, as devices to transform energy into electricity and heat [13][14]. Hydrogen can be produced from water, both by conventional electrolysis and advanced high temperature processes; from nuclear or solar energy, biomass, coal, as well as fossil fuels using steam reforming process [15]. Currently, the annual production of H_2 is about 0.1 Gton, from which 90-95% is consumed by the petrochemical industries and 5-10% by people in everyday life. In addition, the overall global demand for hydrogen is expected to increase by around 5-6% annually up to the year 2020, as a result of demand from petroleum refinery operations, and for the production of ammonia and methanol. However, it should be also pointed out that the foremost factor that will determine the specific role of hydrogen technologies will likely be energy demand [16][17][18].

In the development of new hydrogen technologies, the fuel cells are considered as promising devices for use as source of heat and electricity. Indeed, these systems allow the electrochemical recombination of hydrogen and oxygen to produce electricity, with characteristics such as high efficiency (up to more than 60%) and

reliability; modular structure makes them suitable for a variety of applications, excellent performance and limited or no atmospheric or acoustic emissions [19][20].

Fuel cells may be classified based on their operating temperature regime: (i) at low temperature (23-150 °C) such as AFC (alkaline fuel cell), PEMFC (proton exchange membrane fuel cell) and DMFC (direct methanol fuel cell), (ii) at medium temperature (150-220 °C) such as PAFC (phosphoric acid fuel cell) and at high temperature (600-1000 °C) such as MCFC (molten carbonate fuel cell), DCFC (direct carbon fuel cell) and SOFC (solid oxide fuel cell). Likewise, these can also be divided according to the type of electrolyte (liquid, ceramic or polymer) and the electrodes used, or depending on the nature of the ion exchanged between the electrodes (OH^-, CO_3^{2-}, H^+, O^{2-}). Among all this variety, the most promising technologies are the PEMFC (Proton Exchange Membrane Fuel Cell) and the SOFC (Solid Oxide Fuel Cell) [21][22][23].

1.2 SOLID OXIDE FUEL CELL (SOFC)

A solid oxide fuel cell (SOFC) is a ceramic-based electrochemical device that converts the chemical energy of a fuel gas and an oxidant gas directly to electrical energy and heat without combustion as an intermediate step, giving much higher conversion efficiencies than conventional thermomechanical methods. A SOFC system usually utilizes a solid ceramic as the electrolyte and operates at extremely high temperatures (600-1000 °C). The operating temperature allows internal reforming, promotes rapid electrocatalysis with non-precious metals, and produces high quality by-product heat for co-generation. SOFCs are favored for high-power applications since they can reach an electrical efficiency between 35 and 43% and a combined heat and power (CHP) efficiency up to 90% [22][24][25].

A SOFC is built of five key types of components: electrolyte, anode, cathode, interconnects and seals. Figure 2 shows a SOFC scheme.

Figure 2. Scheme of a Solid Oxide Fuel Cell (SOFC). Taken from [26][27].

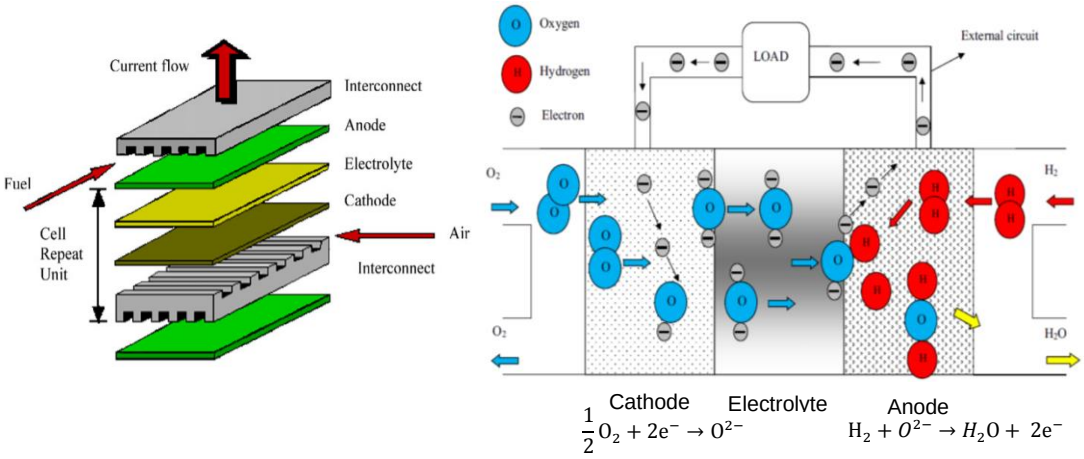

The electrolyte at the heart of each cell is a solid ceramic oxide that facilitates the generation of oxygen vacancies and carries the charge between the half reactions at the cathode and anode. The cathode (or the air electrode) and the anode (or the fuel electrode) are the sites of each half reaction: oxygen reduction and fuel oxidation, respectively. The roles of interconnects are the electrical connection between cells and the gas distribution within the cell stack. The seals, used in some planar designs, bond components together and provide gas-tightness [27][28][29].

1.2.1 THERMODYNAMIC PRINCIPLES

The operation of a SOFC involves the reduction of the oxidant at the cathode and the oxidation of the fuel at the anode. At present, the most common fuel and oxidant for use in SOFCs are hydrogen and oxygen (electrochemically active). Oxygen molecules consume electrons at the cathode and get reduced to oxide ions, which diffuse through the electrolyte and results in the generation of ionic current. At the cathode, the reaction can be represented as:

$$\frac{1}{2}O_2 + 2e^- \rightarrow O^{2-} \qquad (1\text{-}1)$$

Eq. 1-1 can be presented in Kröger–Vink notation as:

$$\frac{1}{2}O_2 + 2e^- + V_{\ddot{O}} \rightarrow O_O^x \qquad (1\text{-}2)$$

where $V_{\ddot{O}}$ is a vacant oxygen site while O_O^x is an oxide ion sitting at its allocated oxygen site in the oxide sublattice cathode. As apparent from the above equations, the oxygen reduction process in utilizing oxide ion has three basic requirements: (i) presence of oxygen, (ii) presence of electrons, and (iii) diffusion of oxide ions (from reaction site (cathode) to the electrolyte). As a result, the electrode material must possess high electronic conductivity and be porous to facilitate gas permeation to and from the reaction sites. Oxide ions move through the electrolyte and at the same time, oxygen vacancies migrate from the anode side to the cathode side via an ion conducting electrolyte. After migrating through the electrolyte, the oxide ions emerge at the anode and react with fuel (for example H_2 or CO) as follows:

$$2O^{2-} + 2H_2 \rightarrow 2H_2O + 4e^- \qquad (1\text{-}3)$$

$$2O^{2-} + 2CO \rightarrow 2CO_2 + 4e^- \qquad (1\text{-}4)$$

The electrons produced during the reactions are carried by the current collector in the anode to an external load via externally connected electrical circuit [30][31].

The SOFC is therefore considered to be an oxygen concentration cell, and the electromotive force (*emf*) or reversible (thermodynamic) voltage, E_r, is given by the Nernst equation:

$$E_r = \frac{RT}{4F} ln \frac{P_{O_{2(cathode)}}}{P_{O_{2(anode)}}} \qquad (1\text{-}5)$$

where *R* is the gas constant, *T* the temperature (K), *F* the Faraday constant, and P_{O_2} the oxygen partial pressure at the electrode. Since, air is fed as an oxidant through the cathode side of the SOFC, the P_{O_2} at the cathode is 0.21 atm. In laboratory experiments related to SOFCs, the commonly used hydrogen gas is generally fed at the anode, and the overall cell reaction can be expressed as [32]:

$$H_{2(g)} + \frac{1}{2}O_{2(g)} \rightarrow H_2O_{(g)} \qquad (1\text{-}6)$$

Under open circuit conditions, with electrochemical potential of oxide ions equilibrated across the oxide-ion conducting electrolyte, a voltage difference, *E*, the

Nernst potential, appears between the anode and the cathode. It is related to the net free energy change, ΔG, of the reaction via the following relation:

$$\Delta G = -nFE = -2FE \qquad (1\text{-}7)$$

where n denotes the number of electrons participating in the reaction. The Nernst potential, *E*, is the open circuit voltage, OCV, and is given in terms of the various partial pressures by:

$$E = E^0 + \frac{RT}{4F} ln\left(\frac{p_{O_2}^c p_{H_2}^a}{p_{H_2O}^a}\right)^2 \qquad (1\text{-}8)$$

Where $p_{O_2}^c$ is the partial pressure of oxygen in the cathode gas, $p_{H_2}^a$ and $p_{H_2O}^a$ are respectively the partial pressures of H_2 and H_2O in the anode gas, R is the gas constant, F the Faraday constant, and T the absolute temperature.

As seen in Figure 3, the fuel cell voltage is significantly deviated from the theoretical potential (also called reversible standard potential, 1.23 V). The dependence of *E* on current density can be estimated assuming the respective cathodic and anodic chambers as being continuously stirred tank reactors.

Figure 3. Typical polarization curve describing the relationship between cell voltage and current density.

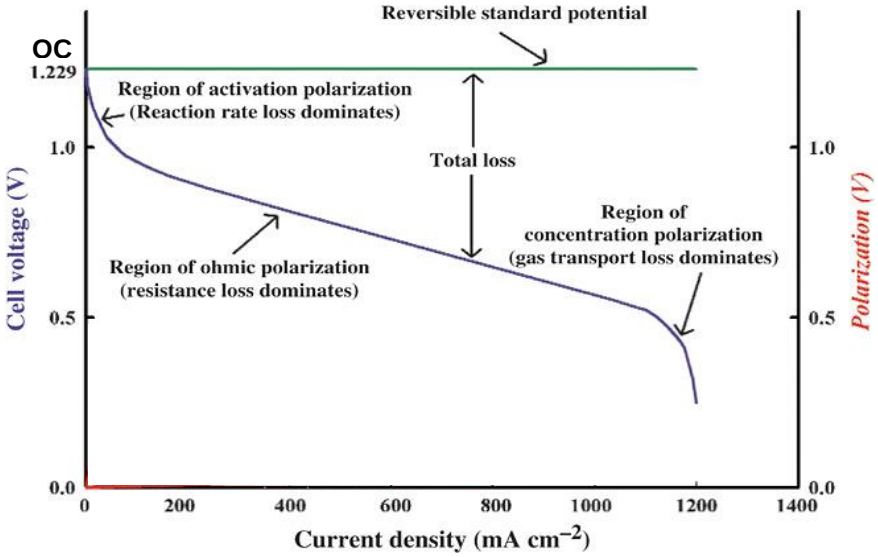

Taken from [33]

In an operating SOFC, the cell voltage is always less than the theoretical Nernst value because of some electrochemical or polarization losses. The cell polarization or overpotential 'η' is the difference between the theoretical and the operating voltages, and it includes: (i) resistance (ohmic), (ii) diffusion (concentration) polarization and (iii) charge transfer (activation) polarization [31].

1.2.1.1 Ohmic polarization

Ohmic loss arises due to resistance offered to the flow of ions in ionic conductors or electrons in electronic conductors. Transport of oxide ions through the electrolyte is thus governed by the ionic resistivity of the electrolyte. Similarly, transport of electrons (or electron holes) through the electrodes (the cathode and the anode) is governed by their respective electronic resistivities (corrected for porosity and the possible existence of secondary, insulating phases). Because of these ohmic resistances, at a given current density, there is a voltage loss, η_{ohm}, given by:

$$\eta_{ohm} = (\rho_e I_e + \rho_c I_c + \rho_a I_a + R_{contact})i \qquad (1\text{-}9)$$

where ρ_e, ρ_c, and ρ_a, are respectively electrolyte, cathode, and anode resistivities, and I_e, I_c, and I_a, are respectively electrolyte, cathode, and anode thicknesses, and $R_{contact}$ is any possible contact resistance. In a SOFC, the main contribution to η_{ohm} is due to the electrolyte material [45], since its (e.g. yttria-stabilized zirconia, YSZ) ionic resistivity is much greater than electronic resistivities of the cathode (e.g. Sr-doped LaMn03, LSM), and the anode (e.g. Ni + YSZ cermet). For example, the ionic resistivity of YSZ at 800°C is ~50 Ω cm. By contrast, electronic resistivity of LSM is 10^{-2} Ω cm and that of the Ni/YSZ cermet is on the order of 10^{-4} Ω cm. Thus, the electrolyte contribution to ohmic polarization can be large, especially in thick electrolyte supported cells.

1.2.1.2 Concentration polarization

Concentration polarization occurs when the reacting molecules are consumed at a faster rate, or when products are not removed quickly enough from the reaction sites. This lowers the concentration of reactant species, *i.e.*, low oxygen partial pressures (pO_2) at the cathode or low partial pressure of fuel (pH_2) at the anode compared with that of bulk supply. However, such a behavior leads to a reduction in the voltage output, and creates a significant disadvantage when high current is drawn from the SOFC. In extreme cases, the concentrations of reacting molecules (gases) reduces to zero at the reaction site, current drops to a limiting unsustainable value, and the fuel cell ceases to run. This polarization loss η_{conc} is a function of several parameters, given as:

$$\eta_{conc} = f(Diffusivity\ (H_2 - H_2O, O_2), Microstructure, Partial\ Pressures, Current\ Density$$

1.2.1.3 Activation polarization

Activation polarization arises whenever reacting chemical species are participating. Thus, for a reaction to proceed, the activation energy barrier of the rate determining step of the reaction taking place in multiple steps must be overcome. This requires an extra potential energy and is governed via Butler–Volmer relation:

$$i = i_0 \left\{ exp\left(\frac{\propto nF\eta_{act}}{RT}\right) - exp\left(\frac{-(1-\propto)nF\eta_{act}}{RT}\right)\right\} \qquad (1\text{-}10)$$

where 'i_0' is the exchange current density, '*α*' is the transfer coefficient, '*n*' is the number of electrons participating in the reaction at electrode, and 'η_{act}' is the activation overpotential. This equation relates to the rate of charge transfer of the reaction occurring at the electrocatalyst (electrode)/electrolyte interface, i.e., 'i ' or current density to the activation overpotential ''η_{act}' The activation polarization arises during transfer of charges between the electronic and ionic conductors, and therefore, it is also termed as charge transfer polarization. Nevertheless, when current densities are considerably low, Eq. (10) reduces to:

$$\eta_{act} \approx \left(\frac{RT}{nFi_0}\right) i = R_{ct} i \qquad (1\text{-}11)$$

Where, $\left(\frac{RT}{nFi_0}\right)$ or R_{ct} is intrinsic charge transfer resistance limited to specific electrode/electrolyte interface area. Activation polarization is typically an issue occurring in cathodes. This is attributed to the slow oxygen reduction reaction kinetics, which involves the breaking of high strength bonds present in oxygen molecules [34]. Thus, the reaction rate using oxygen gas as an oxidizer (at cathode) becomes slower by several orders of magnitude compared with fuel oxidation reactions at the anode. In a single phase MIEC electrode, the charge transfer reaction occurs over the entire electrode/gas phase interface, and the exchange current density is given by [30][31]:

$$i_0(cathode) = f(partial\ pressure\ of\ oxygen, oxygen\ vacancy\ concentration\ in\ the\ MIEC, oxygen\ vacancy\ mobility\ in\ the\ MIEC, electronic\ defect\ concentration\ in\ the\ MIEC, and\ temperature)$$

1.3 SOFC COMPONENTS

1.3.1 ELECTROLYTE

In order to work efficiently, the electrolyte must meet certain characteristics. It should behave as an electronic insulator with high ionic conductivity (~0.1 S cm^{-1} at operating temperature), in order to allow easy migration of the oxygen anions. It must be thermally and chemically stable over a wide range of temperatures (from room temperature to 1000 °C, at least) and oxygen partial pressures (from ~0.2 atm for the cathode to ~10^{-20} atm for the anode). In addition, it must possess reliable mechanical properties (such as fracture strength >400 MPa) and have Thermal Expansion Coefficient (TEC) values compatible with adjoining cell components [35]. The candidate electrolytes for an SOFC are mainly materials with fluorite structure such as YSZ ($(ZrO_2)_{1-x}(Y_2O_3)_x$ with (x~0.08-0.1)) or GDC ($Ce_xGd_{1-x}O_{2-x/2}$) or with

perovskite structure such as lanthanum gallate LSGM, $La_{1-x}Sr_xGa_{1-y}Mg_yO_3$ (x, y =0.1, 0.2) [36][37][38].

The most commonly used electrolyte material is yttria-stabilized zirconia $(ZrO_2)_{0.92}(Y_2O_3)_{0.08}$ (8YSZ). The yttrium doping has been added to improve the ionic conductivity of ZrO_2 and to stabilize the cubic fluorite phase. 8YSZ reports the highest ionic conductivity of 0.14 S cm^{-1} at 1000 °C and a TEC of $10.9x10^{-6}$ K^{-1} (from room temperature to 1000 °C) [39]. Electrolytes based on ceria such as $Ce_{0.9}Gd_{0.1}O_{1.95}$ (GDC) are reported to have a higher conductivity, particularly at low temperatures, and a lower polarization resistance, compared to YSZ electrolyte. Average TEC value of GDC is 12.2 $x10^{-6}$ K^{-1} in the temperature range of 30-850 °C. However, GDC electrolyte cannot be efficiently used under reducing conditions due to the partial reduction of Ce^{4+} to Ce^{3+} (> 600 °C). This becomes an issue during the operation, since induces an electronic conductivity (and deleterious lattice expansion) that generates an internal short circuit, resulting in a performance degradation [40][41][42]. Nevertheless, GDC is sometimes used with YSZ acting as barrier layer to protect the electrode from unfavorable reactions [43][41]. On the other hand, $La_{0.8}Sr_{0.2}Ga_{0.8}Mg_{0.2}O_{3-\delta}$ (LSGM) is also an interesting electrolyte, since it has high conductivity at lower temperature (0.14 S cm^{-1} at 800 °C) and a TEC of $11.5x10^{-6}$ K^{-1}. However, the single phase LSGM is hardly obtained and does not possess good mechanical strength [44].

1.3.2 CATHODE

1.3.2.1 Requirements

The main function of the SOFC cathode is to convert the oxygen to oxide ions (Eq. 1). To be performed correctly, the cathode must present the following characteristics: (i) stability under oxidizing atmosphere during fabrication and operation, (ii) high

electronic conductivity (preferably more than 100 S/cm in oxidizing atmosphere), (iii) sufficient electrocatalytic activity, thus low polarization for the electrochemical reduction of oxygen, (iv) high oxide ion conductivity, (v) adequate porosity to allow fast diffusion of O_2 gas through the cathode to the cathode/electrolyte interface, (vi) matching thermal expansion coefficient with the other cell components to avoid cracking and delamination during fabrication and operation, including thermal cycling, (vii) good chemical compatibility with the electrolyte and interconnect materials and (viii) low cost [45][46].

Nowadays, extensive researches have been dedicated to decrease the operating temperature of the SOFC from 1000 °C (currently used) to 600-800 °C. The decreasing operating temperature would imply several advantages such as: improvement of the mechanical properties leading to a good long-term stability, possibility of using low-cost interconnectors such as stainless steel, besides facilitating the start-up and shut-down procedures. However, lowering temperature generally leads a decrease of the electrodes activity generating large polarization resistances, especially at the cathode [47][48].

It is generally accepted that when a pure electronic conductor is used as cathode, the oxygen reduction takes place only at, or near, the triple phase boundaries (TPBs) between the electrode, the electrolyte and oxygen gas. Nevertheless, this reaction zone should not be dimensionally limited by a planar solid interface; instead, it should be distributed in whole cathode surface (Figure 4). A viable solution is to provide a single-phase electrode with mixed conductivity permitting both oxide ion and electron mobility within the cathode material. Such materials are named Mixed Ionic and Electronic Conductors (MIEC). Generally, using MIEC cathodes will enhance the SOFC performance, because these materials are supposed to provide three simultaneous pathways for incorporation of the oxygen through the whole cathode: the electrode surface pathway, electrode bulk pathway and electrolyte surface pathway [49][50][51][52].

Figure 4. Diagram showing the TPB improvement, due to the mobility of both the oxide ions and the charge carriers. (a) Electronic conductor and (b) mixed conductor. Taken from [53]

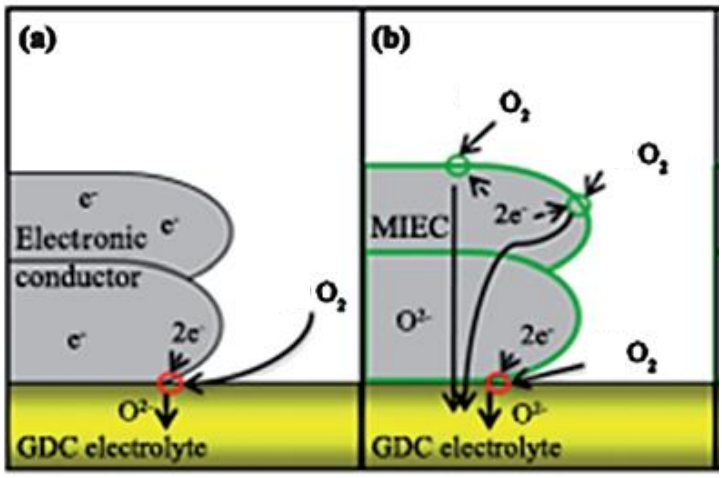

Different mechanisms have been proposed to describe the cathodic reaction (Eq. 1-1 and 1-2). Concerning the oxygen reduction at the MIEC surface and in the bulk, De Souza [54] and Adler [55][56] suggest that the mechanism consists in: (i) dissociative oxygen adsorption, (ii) ionization of the oxygen atom, (iii) incorporation of adsorbed oxygen in the cathode bulk, (iv) bulk diffusion and (v) oxygen incorporation from the cathode bulk into the electrolyte [51][57][58], which will be described in detail in Annex 8.

1.3.2.2 Cathode Materials

Perovskite Structures

Most of the materials that have been developed for cathode in the last 15 years correspond to the perovskite structure, usually expressed as ABO_3, where A and B are cations with different sizes. Figure 5 shows the typical structure of the cubic perovskite ABO_3.The larger A cations are coordinated to 12 oxygen anions and

correspond to the center of the cell, while the B cations are coordinated to 6 oxygen anions in octahedral position [58]. The formation of a perovskite structure can be roughly estimated according to the Goldschmidt's tolerance factor (t), as follows:

$$t = (r_A + r_O)/\sqrt{2}(r_B + r_O) \quad (1\text{-}12)$$

where r_A, r_B and r_o represent the ionic radii of the A, B site cation and oxygen ion, respectively. The perovskite structure is generally considered stable if the t value ranges from 0.85 to 1.0 [59]. In these structures, it is possible to make full or partial substitutions of A or B cations, which modifies the overall valence of the metals (if accepted) and can introduce vacancies at the oxygen lattice. The formation of these lattice defects would become very important for some special properties, such as oxygen ion and electron conductivities [60].

Figure 5. ABO_3 perovskite structure

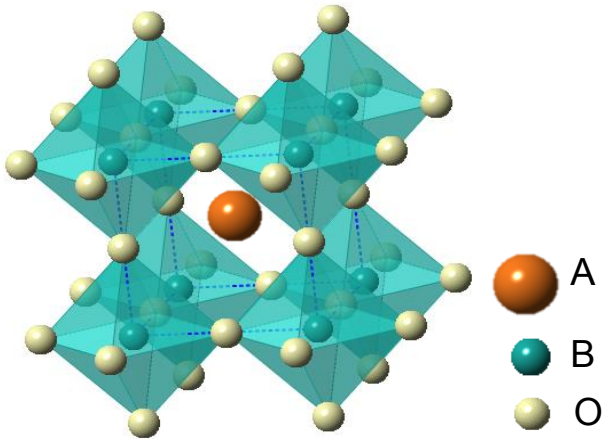

$La_{1-x}Sr_xMnO_3$ (LSM) perovskite, almost a pure electronic conductor, is the state-of-the-art cathode material for high-temperature SOFC that typically operates at temperature higher than 800 °C. It is demonstrated that the substitution of La^{3+} by Sr^{2+} in $La_{1-x}Sr_xMnO_{3\pm\delta}$ ($x \leq 0.5$) does not increase the oxygen vacancy concentration, but instead causes the oxidation of manganese cations, which effectively increases

the electron-hole concentration and improves the electrical conductivity [61]. The defect reaction can be given as:

$$La_{La}^{x} + Mn_{Mn}^{x} + SrO + +0.5O_2 \longleftrightarrow Sr_{La}^{'} + Mn_{Mn}^{\cdot} + 0.5La_2O_3 + 0.5O_O^{x} \quad (1\text{-}13)$$

The temperature dependence of electrical conductivity of $La_{1-x}Sr_xMnO_{3\pm\delta}$ is shown in Figure 6 [62]. The electronic conductivity of the series increases with increasing Sr concentration, with a maximum of ~ 400 S cm^{-1} for x=0.5 at 1000 °C. However, at 1200 °C (temperature of the cathode fabrication) the $La_{1-x}Sr_xMnO_{3\pm\delta}$ perovskites reacts with YSZ electrolyte to form $La_2Zr_2O_7$ and $SrZrO_3$ for x ≥ 0.3 [63][64]. Therefore, LSM compositions used in cathode application have Sr concentration of 10-20 mol%, for example, $La_{0.8}Sr_{0.2}MnO_3$ (hereinafter called LSM), which is one of the most important cathodes in the state-of-the-art SOFCs [65].

Figure 6. Temperature dependence of the electrical conductivity σ of $La_{1-x}Sr_xMnO_{3+\delta}$ in Arrhenius coordinates. Taken from [62].

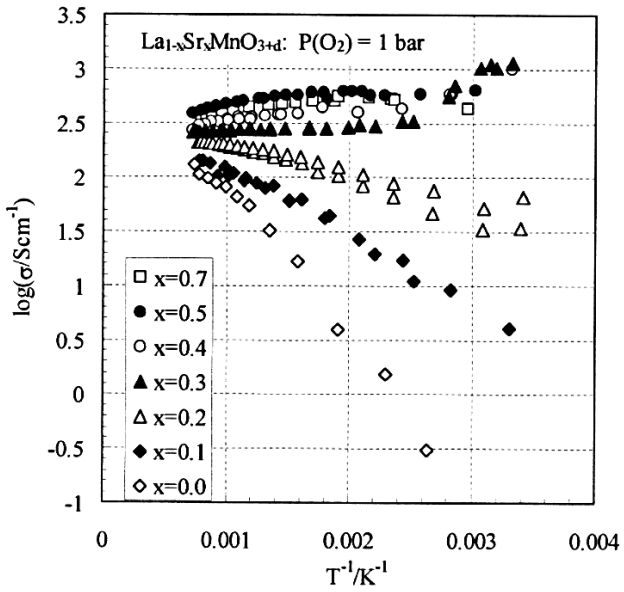

Although LSM is a good electronic conductor, with an appropriate TEC (11.8 x 10^{-6} K^{-1} [66]), high thermal stability and electrochemical activity for the oxygen reduction reaction, its oxygen ion conductivity is very low (5.93 x 10^{-7} S cm^{-1} at 900 °C [67]).

The latter feature is particularly important at low temperature. When the temperature is reduced to intermediate/low temperature range (600-700 °C), a significant increase of the polarization resistance is observed. For example, in open circuit potential (OCP) conditions the overall electrode resistance in air increased from ~0.38 Ω cm^2 at 900 °C to ~51 Ω cm^2 at 700 °C, as seen in Figure *7* [68].

Figure 7. Impedance curves of the O_2 reduction reaction on LSM electrode as a function of dc bias at different temperatures in air. Adapted from [68].

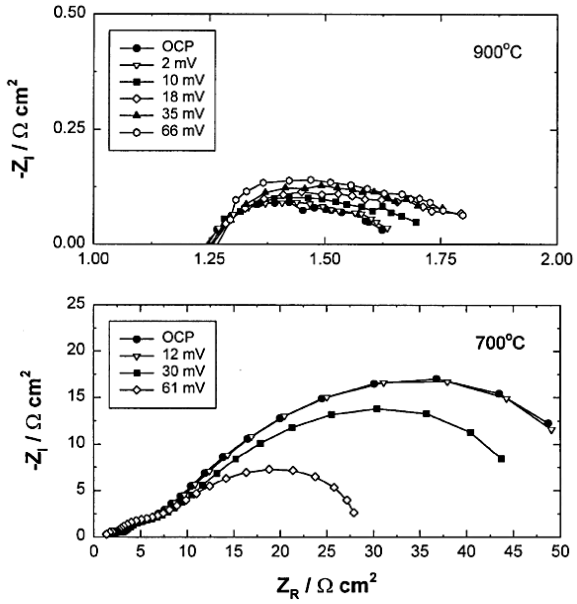

A strategy to improve the transport properties was to use a porous composite consisting of an electronic conducting cathode material and an appropriate amount of good ionic conducting electrolyte material such GDC or YSZ. For example, the replacement of pure LSM electrode with a LSM-YSZ composite electrode enhanced the performance of SOFCs due to the presence of active triple phase boundary (TPB) points between LSM, YSZ and gas phase in the bulk points between LSM, YSZ and gas phase in the bulk of the electrode. Kenjo and Nishiya [69] found that the polarization resistance (Rp) at 900 °C decreases with increasing YSZ-LSM weight ratio, with the minimum occurring at a weight ratio of YSZ-LSM=1.0. Ostergard *et al*. [70] reported that the addition of up to 40 wt.% YSZ to the cathode

improves its performance as a result of better adhesion to the base electrolyte and the increased area of the TPB. Wang *et al*. [71] reported that the dissociative adsorption and transfer of oxygen are comparable rate-determining steps on pure LSM, the addition of YSZ accelerate both steps due to enlargement of the TPB area [72].

Another approach is to use mixed ionic and electronic conducting (MIEC) perovskites, which supplies a significantly extended active region for oxygen reduction reaction. During the last 10-15 years, researchers have proposed a large number of alternative cathode compositions, some of which will be discussed below [73][74][75].

$La_{0.6}Sr_{0.4}Co_{0.2}Fe_{0.8}O_{3-\delta}$ (LSCF) is a MIEC that has attracted great interest for low-temperature SOFCs, due to its high activity for oxygen reduction. This material reports an improved performance with respect to LSM, that has been attributed to extension of the catalytically active area (TPB) to the entire surface of the cathode, transforming it into an internal diffusion electrode (IDE) [76][77][78][79]. LSCF has an electrical conductivity of 350-400 S cm^{-1} at 600 °C, and high ionic conductivity of $1x10^{-2}$ S cm^{-1} at 800 °C [80][81], which is well superior to that reported for LSM cathode. However, the TEC value reported for LSF (15-17.5 x 10^{-6} K^{-1} between 30 and 1000 °C) is much higher than that of common electrolytes [82][83]. In addition, LSCF is not chemically compatible with YSZ electrolyte, forming $La_2Zr_2O_7$ and $SrZrO_3$ during sintering [84]. To solve this issue, as LSCF does not react with GDC [61], a GDC layer has been deposited on YSZ surface, which acts as a diffusion barrier, since it has been demonstrated that Sr is the element that diffuses to the surface of the electrolyte and creates parasitic phase layer with zirconium (Figure 8) [85][86]. On the other hand, the electrochemical properties of LSCF (using GDC interlayer) have been measured using different composites (LSCF-GDC) and preparation methods for the cathode. For example, when LSCF was deposited by spray pyrolysis (250-300 nm) on a GDC/YSZ electrolyte, the polarization resistance

(R_p) at 750 °C was found as low as 0.015 Ω cm^2 [43][87], while when using a 50-50 LSCF-GDC composite, R_p value was 0.06 Ω cm^2 at the same temperature, using slurry spray (2-3 µm) [88].

Figure 8. EDX diffusion profiles on (a, b) LSCF/YSZ and (c, d) LSCF/GDC showing the Sr segregation. Taken from [89].

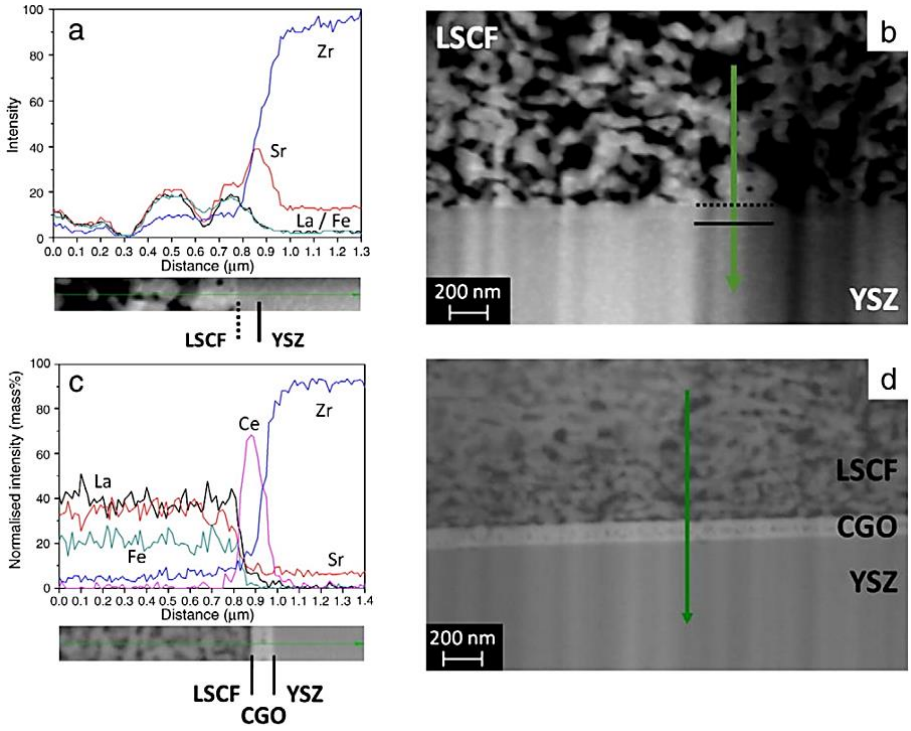

Another interesting perovskite-type cobalto-ferrite with $Ba_{0.5}Sr_{0.5}Co_{0.8}Fe_{0.2}O_{3-\delta}$ (BSCF) composition has also been widely recognized as an alternative cathode material for IT-SOFCs, due to its high oxygen permeability, showing an oxygen self-diffusion coefficient (D^*) of 3.3×10^{-7} cm^2 s^{-1} at 700°C, which is higher by several orders than LSM (5.2×10^{-18} cm^2 s^{-1}) [90][91]. For example, using SDC ($Sm_{0.2}Ce_{0.8}O_2$) as electrolyte in an anode-supported cell (NiO-SDC), BSCF showed good electrochemical properties at low temperature (0.055 - 0.071 Ω cm^2 at 600 °C) [48][92]. However, the difficulty of using this material relies in its high TEC value, with a value of 20 × 10^{-6} K^{-1} (50 – 1000 °C). It has been demonstrated that this

mismatch of TECs between BSCF and the electrolytes (*i.e.* YSZ), could causes problems of delamination, crack or a poor contact cathode-electrolyte, resulting in a larger resistance polarization (5-6 Ω cm^2 at 800 °C) [93][94].

Ruddlesden-Popper Structures

The Ruddlesden-Popper (RP) phases are formulated as $A_{n+1}B_nO3_{n+1}$ or $(AO)(ABO_3)_n$ with n = 1, 2, 3, 4…The crystal structure of the series consists of n perovskite blocks ABO_3 separated by a rock-salt (AO) layer, the value of n determining the number of perovskite layers (Figure 9). The *A*-cations are rare earths elements (RE) located in the perovskite and rock-salt slabs and the *B*-cations are transition metal elements occupying the anionic octahedral coordination of the perovskite block. The RP structures exhibit high two-dimensional (2D) character, compared to the 3D perovskite, with reported enhanced transport properties. In general, depending on the chemical nature of the cations in the different layers, these structures have the ability to accommodate a significant amount of non-stoichiometric oxygen atoms, which enable the modification of the physicochemical properties [95][96][97][98].

Figure 9. Ruddlesden-Popper unit cells for (a) n = 1 (RPn1), (b) n = 2 (RPn2), and (c) n = ∞ (perovskite) structures.

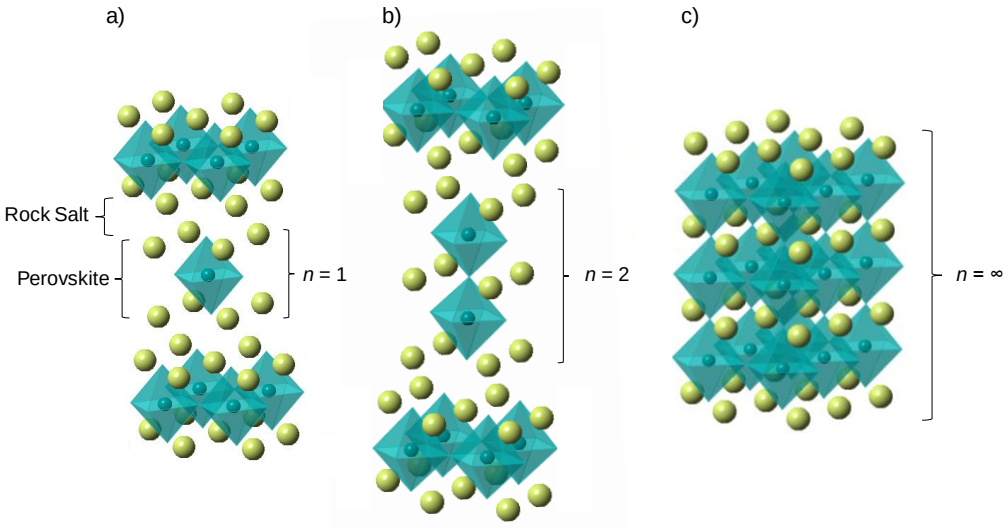

The first member of the RP series (n=1), of K_2NiF_4-type has the general formula A_2MO_4 described as a succession of one single perovskite layer ABO_3 alternating with one rock salt AO layer along the *c*-direction. $La_2NiO_{4+\delta}$ is a MIEC material with oxygen hyper-stoichiometry (δ = 0.24 [99]), which has attracted growing attention as cathode for intermediate temperature SOFCs. The oxygen excess is associated to the incorporation of interstitial oxygen in the rock-salt layer, which would increase both the capacity for oxygen reduction and the oxygen diffusion (*D**) [100][101][102]. In addition, $La_2NiO_{4+\delta}$ provides an electrical conductivity of 70-80 S cm^{-1} at 800 °C as well as a high oxygen diffusion coefficient of 3.38 x 10^{-8} cm^2 s^{-1} at 703 °C [103][104][99]. This material has a TEC of 13 x 10^{-6} K^{-1} (27-1000 °C), which is compatible with the usual electrolytes [105]. Despite these features, the use the $La_2NiO_{4+\delta}$ as electrode will also depend on its compatibility with the YSZ and GDC electrolytes. In this way, Montenegro Hernández *et al.* performed the reactivity test at 900 °C for 2 h (powder test) and for 72 h (pellet test), finding that, in both cases, there is high reactivity with formation of secondary phases such as $La_3Ni_2O_7$, La_2NiO_4, $La_2Zr_2O_7$, $LaNiO_3$, La_2O_3 and NiO [106], limiting its use as cathode for SOFC.

On the other hand, the substitution of the A site with Sr ($La_{2-x}Sr_xNiO_{4+\delta}$) was proposed, in order to explore the influence of the alkaline earth on the transport properties. In 2015, Inprasit *et al.* found that Sr substitution decrease the amount the oxygen interstitial, *i.e.* the oxygen content was δ= 0.14(3), 0.15(1), 0.17(1) and 0.20(2) for x= 0.2, 0.4, 0.6 and 0.8, respectively [107][99][108]. The electrical conductivity was higher for x= 0.8, with values of 160 S cm^{-1} (500 °C), however the oxygen diffusion coefficient (*D**) was 2.26 x10^{-9} cm^2 s^{-1} (800 °C) [109][107].

By this way, combining the good properties but limitations of LSM described above and the layered structure of the RP phases, manganites with general formula $La_xSr_{2-x}MnO_4$ have been proposed as promising candidates for which a higher thermochemical stability has been reported compared to the classical perovskite

structure, especially at low oxygen partial pressure ($pO_2 < 10^{-10}$ Pa) [110]. Munning *et al.* studied the $La_xSr_{2-x}MnO_{4\pm\delta}$ solid solutions ($0 \leq x \leq 1.4$) as cathode materials, reporting good stability until 800 °C in air, TECs values between 14 and 16.5 10^{-6} K^{-1} compatible with YSZ and GDC electrolytes and a moderate electrical conductivity with a maximum of ~ 6 $S.cm^{-1}$ for x=0.2 at 900 °C in air [111]. Subsequently, the research carried out by Liping *et al.* presented advances on the reactivity of $La_xSr_{2-x}MnO_{4\pm\delta}$ (x= 0.4, 0.5, 0.6) series with GDC electrolyte, giving a good thermomechanical compatibility between them until 1000 °C. The electrical conductivity for this series was about 5.7 S cm^{-1} at 800°C in air, with an activation energy between 0.24 and 0.29 eV (100-800 °C) [112]. In addition, the electrochemical properties in air were investigated for $La_xSr_{1.5}MnO_4$ (x= 0.35, 0.4, 0.45), demonstrating that the lowest polarization resistance value at 750 °C was obtained with x= 0.35 (R_p=0.25 Ω cm^2) [113].

In summary, over the years, several cathode materials have been developed, always with the aim of decreasing the operating temperature, the reactivity with the electrolyte and improving the ionic and electronic conductivity and the cell efficiency. Materials with Ruddlesden-Popper are promising but were not so much studied in the case of $(La,Sr)_2MnO_{4\pm\delta}$ manganites, although recent literature gives insight of the interest of the series.

1.3.3 ANODE

The main role of the SOFC anode is to provide reaction sites for the electrochemical oxidation of the fuel. The anode material must satisfy a number of requirements simultaneously, among them: (i) (electro)catalytic activity for fuel oxidation (including catalytic reforming and/or partial oxidation) including fuel flexibility without carbon deposition and sulfur poisoning, (ii) redox stability as, during the cell working life, the anode will possibly experience changes of partial pressure (pO_2) and even could be

exposed to air, so will need to withstand the oxidation, (iii) chemical compatibility with the other components, involving interdiffusion of constituting elements and or reaction with secondary phases formation (iv) physical compatibility, that is a minimal TEC mismatch with other adjacent cell components to avoid cracking and delamination during fabrication, operation and thermal cycling, (v) high electronic conductivity, which is essential for easy transfer of electrons on the anode and (vi) ionic conductivity, that could be achieved with the use of a composite or a MIEC material [114][115][116][30][31].

However, the identification of a material that meets all these characteristics is very challenging and a great number of materials have been proposed, including Ni or Cu based cermets and several mixed oxides in particular of perovskite structure. The most widely used anode materials are described below.

Ni/YSZ cermet anode material

Ni/YSZ cermet is the most commonly used anode material in SOFCs, mainly because it satisfies many of the requirements describe above. On one hand, YSZ provides both ionic conductivity to allow the O^{2-} diffusion and structural support for the anode that prevents Ni sintering, as provided by Ni electronic conductivity and catalytic activity for fuel oxidation [117]. The composition of the cermet is typically 40 vol.% Ni and 60 vol.% YSZ, with a porosity of ~40 %. The TEC of nickel (16.9×10^{-6} K^{-1}) is much larger than that of YSZ (11.0×10^{-6} K^{-1}), however, when the cermet is formed, the TEC is ~11.8×10^{-6} K^{-1} (50-1000 °C), which is close to those of other SOFC components [118][119]. In addition, the electrical conductivity of this Ni/YSZ cermet is in the range of 10^2 to 10^4 S cm^{-1} at 1000 °C, depending on the microstructure or the preparation technique [120][121].

However, despite its many advantages, Ni/YSZ faces several issues such as redox instability, carbon deposition when using hydrocarbon fuels and low tolerance to sulfur [122][123].

The degradation during redox cycles refers to the chemi-mechanical instability of the cermet under oxygen partial pressure variation of more than 20 orders of magnitude, *i.e.* during reduction and oxidation, which causes dimensional change, structural stresses and, eventually, mechanical failure. Initially, this phenomenon was studied by Klemensø *et al.*, who proposed a model illustrating the redox mechanism in Ni/YSZ cermet that explains the severe cracking and electrode delamination that can be observed (Figure 10) [124]. It has been demonstrated that the reduction process that converts NiO to Ni generates a shrinkage of nickel oxide particles of around 40 vol.%, leading to an increase in porosity without drastic changes in the bulk dimensions of the cermet. However, in some situations when the fuel supply gets interrupted or the pO_2 increases in the vicinity of compressive seals, small air leakage to the anode are generated, and oxidize Ni to NiO. This oxidation results in a severe dimensional modification with a volumetric expansion of ~ 69% that creates fractures and loss of integrity of the cell. In addition, even if the ideal anode conditions are restored, *i.e.* NiO back to Ni, the original microstructural state of the anode is not generally recovered, which worsen the stability problems [125][126][127][128].

On the other hand, Ni/YSZ cermet is also susceptible to carbon deposition or coking, when more complex fuels than hydrogen are used, such as ethanol, methanol or natural gas, due to the fact that nickel is a good catalyst for cracking, forming coke especially when the fuel is used without sufficient steam provision. For methane, it is generally accepted that the formation of carbon proceeds either via methane dissociation (Eq. 9) or according to the Boudouard reaction (Eq.10) [129]:

$$CH_4 \rightleftarrows C + 2H_2 \qquad (1\text{-}14)$$

$$2CO \rightleftarrows C + CO_2 \qquad (1\text{-}15)$$

Figure 10. Model illustrating the redox mechanism in Ni/YSZ cermets (a) the sintered state, (b) the short-term reduced state, (c) the long-term reduced state, and (d) the reoxidized state. Taken from [124].

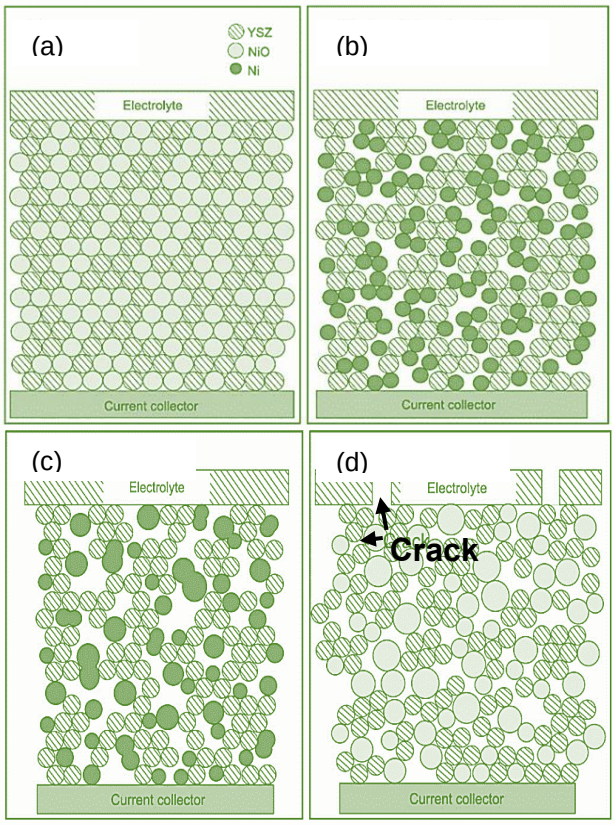

Fracture of fuel cells by deposition and diffusion of high levels of carbon into the bulk of the Ni has long been recognized as a key problem of direct methane fuel cells with Ni-based anodes. Examination of the scanning electron microscopy (SEM) image and EDX mapping of the Ni/YSZ anode revealed that the majority of deposited carbon is located on the Ni surface (Figure 11) [130]. In addition, studies on types of carbon produced on anodes during exposure to hydrocarbon fuels at temperature range of 625 - 900 °C showed that carbon was deposited in graphitic and disordered form. Graphitic carbon has been suggested to be responsible for anode degradation by dissolution into the bulk of the Ni/YSZ cermet resulting in volume expansion and breakage of the Ni-Ni network [131][132][133] .

Figure 11. The Ni/YSZ anode fuel cell image and scanning electron microscopy (SEM) micrograph/ EDX mapping of the (a) Ni/YSZ surface; (b) coke that is deposited on the Ni/YSZ surface; and (c) coked spot on the Ni/YSZ surface after stability test in CH_4. Taken from [130]

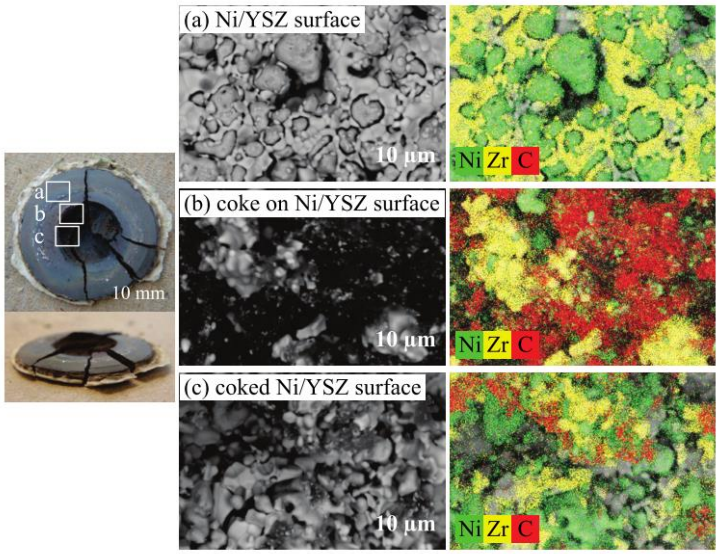

In general, the carbon formation on metal particles can lead to deactivation by several mechanisms: (i) strong chemisorption as a monolayer or physical adsorption in multilayers, (ii) encapsulation of metal particles, (iii) growth of carbon filaments (whisker carbon) or (iv) dissolution of carbon atoms into the metal. Indeed, in all cases, the carbon deposition covers or blocks the active sites of the anode, causing stress, fracture or volume expansion that lead to cell performance degradation [134][135][136][137].

One of the main advantages of SOFC cells is the ability to operate using different hydrocarbon fuels, including hydrogen-rich synthesis fuels derived from coal or natural gas. Unfortunately, all fossil fuels contain some amounts of contaminants with H_2S dominating among them. Sulfur compounds might as bare used as additives in many commercially available fuel sources, for example, the natural gas (Colombia) contains 6 ppmv of H_2S. These Sulfur compounds are known to interact with Ni in Ni/YSZ cermet and passivate the active sites, hence resulting in a

performance loss and degradation of the anode [138][139]. Sulfur tolerance capability of SOFC anode has become a critical standard for the advance of SOFC towards commercialization. Several studied demonstrated that the sulfidation reaction on the Ni/YSZ cermet occurs even with small amount of H_2S in ppm level, causes a sharp drop in cell performance within the first few minutes of exposure, followed by a gradual, but persistent, deterioration in performance for several days [140]. In addition, in the operation temperature, the critical H_2S concentration for Ni/YSZ degradation decreases suggesting that sulfur poisoning of SOFC systems operating at intermediate temperatures (IT) (typically 700-850 °C), which are known as IT-SOFC systems, can be irreversible, whereas the performance degradation in high temperature (HT)-SOFC (> 900 °C) can be reversible [141][118].

1.3.3.1 Other anode materials

Due to the aforementioned issues related to Ni-based cermets, many studies have been carried out to find new materials that will present improved performances. Among the most promising options are the perovskite oxides, most of them being Mixed Ionic and Electronic Conductors (MIEC), including Mn-substituted $La_{1-x}Sr_xCrO_3$ (LSCM), La-substituted $SrTiO_3$ (LST) and $Sr_2MgMoO_{6-\delta}$ materials, which will be described below [142].

By combining the electronic conduction and stability properties in reducing conditions of $La_{1-x}Sr_xCrO_3$ phases with the electrocatalytic properties associated to higher redox and coordination flexibility of manganese with respect to chromium, one of the first mixed oxide proposed for anode in replacement of Ni cermets was $La_{1-x}Sr_xCr_{1-y}Mn_yO_{3-\delta}$ (LSCM); it is known that the Mn substitution into the B-site increases the electrochemical activity for the H_2 oxidation as compared to Sr-doped $LaCrO_3$. At low partial pressure of oxygen, the manganese decreases its oxidation state, enhancing oxide-ion migration [143][144]. In specific works concerning $(La_{0.75}Sr_{0.25})Cr_{0.5}Mn_{0.5}O_3$ (LSCM) perovskite, such composition was shown very

promising as anode material for SOFCs due to its electrical and electrocatalytic properties, both in hydrogen and methane. TGA and XRD analyses carried out in air and 5% H_2 demonstrated that LSCM is stable upon redox cycling. The total conductivities of LSCM at 900 °C were 38.6 S cm^{-1} in air and 1.49 S cm^{-1} in 5% H_2, with activation energies of 0.18(1) eV (20-300 °C) and 0.56(1) eV (320-900 °C) in air and 5% H_2, respectively. Moreover, using YSZ as electrolyte, polarization resistance values of 0.51 Ω cm^2 and 0.87 Ω cm^2 have been obtained in wet 5% H_2 and wet CH_4, respectively, at 900 °C, which is comparable with the electrochemical performance of a Ni/YSZ cermet in similar conditions. Likewise, due to its stability in both oxidizing and reducing conditions, LSCM has already been used as electrode in symmetrical fuel cells, which will be discussed later [145][146][147][148].

Among alternative solution, La-doped $SrTiO_3$ perovskites (LST) have been evaluated as potential anode materials for SOFCs. The partial substitution of Sr^{2+} by a trivalent ion such as La^{3+} facilitates the reduction of Ti^{4+} to Ti^{3+} under reducing conditions, thus enhancing the electrical conductivity, which increases up to two orders of magnitude with a maximum of 247 S cm^{-1} at 700 °C for x=0.2 in the $La_xSr_{1-x}TiO_{3+\delta}$ series [149][150]. In the same way, the $La_{0.33}Sr_{0.67}TiO_{3+\delta}$ phase was proposed as anode material, reporting an electrical conductivity of ~30 S cm^{-1} at 800 °C in wet 5% H_2/Ar, and an anodic R_p = 1.17 Ω cm^2 at 900 °C in wet 3% H_2/Ar when a LST-YSZ composite was used. Despite its apparent tolerance to sulfur poisoning (20-1000 ppm), LST presents very limited activity for oxidation of fuels such as CH_4 [151][152][153][154].

$Sr_2MgMoO_{6-\delta}$ (SMMO), double perovskite has also been investigated as potential SOFC anode. In this phase, the transport properties are strongly influenced by the valence states of the elements, since it has been shown that the oxidation state (+2) of Mg ions does not change, whereas the oxidation state of Mo ions changes from +6 to +5, generating oxygen vacancies in the double perovskite structure. Thus, the electrical conductivity varies from 2 x 10^{-2} S cm^{-1} with pO_2= 0.21 atm to 8 x 10^{-1} S

cm^{-1} with pO_2= 10^{-17} atm at 800 °C. In addition, EIS measurements of SMMO/GDC/SMMO symmetric cell indicate ASR (Area Specific Resistance) values of 0.07 Ω cm^2 at 800 °C, measured in wet 20% H_2/Ar [155][156][157]. The ASR is calculated multiplying the polarization resistance (R_p) by the surface of the electrode, and all divided by 2 since the cell is symmetrical.

The main state-of-the-art SOFC cathode and anode materials with some of their properties are summarized in Table 1.

Table 1. State-of-the-art SOFC cathode and anode materials.

	Composition	TEC (x 10^{-6} K^{-1})	σ (S cm^{-1})	Ref.
Cathode	$La_{0.8}Sr_{0.2}MnO_{3-\delta}$	11.8 (27-1000 °C)	150-180 (700 °C)	[66][158]
	$La_{0.6}Sr_{0.4}Co_{0.2}Fe_{0.8}O_{3-\delta}$	17.5 (30-1000 °C)	300-330 (800 °C)	[82]
	$Ba_{0.5}Sr_{0.5}Co_{0.8}Fe_{0.2}O_{3-\delta}$	20.0 (50-1000 °C)	15 (700 °C)	[93][159]
	$La_2NiO_{4+\delta}$	13.0 (24-1000 °C)	70-80 (800 °C)	[103][105]
	$Nd_2NiO_{4+\delta}$	12.7 (27-1000 °C)	30-40 (700 °C)	[104]
	$La_{1.6}Sr_{0.4}NiO_{4+\delta}$	13.2 (30-1000 °C)	40 (800 °C)	[109][83]
	$LaBaCo_2O_{5+\delta}$	16.9 (25-800 °C)	45-50 (800 °C)	[160][161]
	$PrBaCo_2O_{5+\delta}$	21.5 (25-1000 °C)	700 (800 °C)	[162]
Anode	Ni/YSZ cermet	11.8 (50-1000 °C)	10^2-10^4 (1000 °C)	[163][119]
	$(La_{0.75}Sr_{0.25})Cr_{0.5}Mn_{0.5}O_3$	11.4 (30-900 °C)	38.6 (air, 900 °C)	[145][148]
			1.49 (5% H_2, 900 °C)	
	$La_{0.33}Sr_{0.67}TiO_{3+\delta}$	11.5 (50-1000 °C)	30 (5% H_2, 800 °C)	[154]
	$La_4Sr_8Ti_{11}Mn_{0.5}Ga_{0.5}O_{37.5}$	-	0.5 (10^{-15} atm, 900 °C)	[164]
	$Sr_2MgMoO_{6-\delta}$	13.8 (300-500 °C)	8x10^{-1} (10^{-17} atm,	[156][155]
		18.8(500-800 °C)	800 °C)	
	$Ce_{0.25}Sr_{0.75}Cr_{0.5}Mn_{0.5}O_3$	~12.8 (277-677 °C)	32.8 (argon, 900 °C)	[165][166]
		~15.8(677-1100 °C)	1.0 (wet 2% H_2, 900 °C)	
	$Sr_2Fe_{1.5}Mo_{0.5}O_{6-\delta}$	13 (200-700 °C)	2.8 (5% H_2, 800 °C)	[167][168]

1.4 SYMMETRICAL CELLS

Symmetrical Solid Oxide Fuel Cells (sSOFC) is a new approach, in which the same electrode material can be used simultaneously as cathode and anode. This configuration leads to more simplified assembly since it would require a single thermal treatment for electrode elaboration, reducing problems of chemical incompatibility between components and difference of thermal coefficients (a single interface to optimize). In addition, using this configuration it would be possible to minimize sulphur poisoning and carbon deposition by simply reversing the gas flows. However, the electrodes for symmetrical cells must meet the requirements for both anode and cathode materials, *i.e.* must possess catalytic activity towards oxygen reduction and fuel oxidation, stability and acceptable electrical conductivity (ideally MIEC) both in oxidizing and reducing environment and a minimum change in the TEC during the redox cycle in order to avoid cracking problems during operation [169][170].

$La_{0.75}Sr_{0.25}Cr_{0.5}Mn_{0.5}O_{3-\delta}$ (LSCM) was proposed by Ruiz-Morales *et al.* [171] and Irvine *et al.* [147] as a suitable electrode material in symmetrical cells due to its good performance as both anode and cathode material at high temperatures. Initially, it was verified that LSCM is stable upon redox cycling. During heating in 5% H_2/ 3% H_2O at 900 °C for 120 h, the rhombohedral cell was transformed to an orthorhombic cell, even so, the perovskite structure is retained with an increase in unit cell volume of only 1%. The ASR obtained in a symmetric configuration with a LSCM-YSZ composite as electrode were 1.62, 1.85, 2.18 and 2.05 Ω cm^2 at 950 °C in air, H_2/ 3% H_2O, 100% H_2 and 100% CH_4, respectively. Additionally, the cell showed good performances with maximum power densities of 546 and 347 mW cm^{-2} using 100% H_2 and CH_4 at 950 °C, respectively.

As mentioned earlier, lanthanum-doped strontium titanate oxides (LST) have been suggested as promising anode materials, due to their high electrical conductivity and

ability to operate with sulphur-containing fuels [172][173][174]. Some titanates such as $La_4Sr_8Ti_{12-x}Fe_xO_{38-\delta}$ ($1.8 \leq x \leq 7.2$) [175], $La_{0.4}Sr_{0.6}Ti_{1-y}Co_yO_{3+\delta}$ ($0 \leq y \leq 0.5$) [176] and $La_{0.5}Sr_{0.5}Co_{0.5}Ti_{0.5}O_{3-\delta}$ [177] have been proposed as electrodes in sSOFC. For the $La_4Sr_8Ti_{12-x}Fe_xO_{38-\delta}$ (LSTF) $1.8 \leq x \leq 7.2$ series, Canales-Vásquez *et al.* showed that all compositions were stable in oxidizing and reducing conditions, and the electrical conductivity in both atmospheres increased with the substitution of Fe for Ti. The best results were obtained for x=7.2 (LSTF60), for which the power density was 100 mW cm^{-2} at 950 °C using wet H_2 as the fuel, using LSTF60:YSZ:CeO_2 as electrode and YSZ as electrolyte [175]. On the other hand, the study of $La_{0.5}Sr_{0.5}Co_{0.5}Ti_{0.5}O_{3-\delta}$ (LSCT) reveled that, in reducing conditions (5% H_2/N_2), this phase undergoes a transition from the orthorhombic *Pbnm* to the oxygen-deficient cubic *Pm-3m* structure. Interestingly, heating the material in O_2 atmosphere restores oxygen lost, confirming that the reduction-oxidation process is totally reversible. The sSOFC with LSCT/LDC//LSGM//LSCT configuration (LDC: $La_{0.4}Ce_{0.6}O_{2-\delta}$ used as buffer layer) rendered a power density of 110 mW cm^{-2} at 800 °C in pure H_2. However, the TECs obtained were higher than that of the most commonly used electrolytes, with values of 17.25 and 16.29×10^{-6} K^{-1} (300-900 °C) in air and 5% H_2/N_2, respectively [177].

Several lanthanum strontium ferrites $(La,Sr)FeO_{3\pm\delta}$ have also been proved to be suitable as SOFC electrode materials. In these structures, the mixed valence state of iron favors the formation of oxygen vacancies, which positively affect the conduction properties. Among them, $La_{0.8}Sr_{0.2}FeO_{3-\delta}$ (LSF) is reported for its stability both in air and moist pure H_2 (800 °C, 3% H_2O), with values of electrical conductivity of 141.1 and 0.138 S cm^{-1}, respectively. In addition, the addition of a GDC buffer layer in the LSF/GDC//YSZ//GDC/LSF symmetrical cell leads to an increased performance, achieving a maximum power density of 400 mW cm^{-2} at 800 °C [178]. On the other hand, the Ruddlesden-Popper $La_{0.8}Sr_{1.2}FeO_4$ phase was also investigated as prospective symmetrical electrode. This phase exhibited good stability up to 850 °C in reducing atmosphere (5% H_2/Ar), that involved the iron

reduction accompanied by an oxide ion loss with retention of its K_2NiF_4-type structure. The electrical conductivities were 22 and 0.02 S cm^{-1} in air and 5% H_2/Ar, respectively. Using $La_{0.8}Sr_{1.2}FeO_4$-LSGM as electrode and LSGM as electrolyte, the cell displayed a maximum power density of 73 mW cm^{-2} at 800 °C using pure H_2 as the fuel [179].

In the same way, doping in the perovskite B-site has been proved to be a promising option to enhance the electrical and catalytic properties. For example, $La_{0.5}Sr_{0.5}Fe_{0.8}Cu_{0.2}O_{3-\delta}$ (LSFC) initially investigated as a cathode material, was proposed by Lu *et al.* as potential symmetrical electrode operating both with hydrogen or syngas fuel. LSCF in reducing atmosphere (humidified pure H_2 at 900 °C) showed a reversible structural transition of cubic perovskite to K_2NiF_4-type $SrFeLaO_4$, metallic Cu and minor phase of $LaFeO_3$. The maximum power densities of LSFC/SDC//ScSZ//SDC/LSFC cell were 1054 and 895 mW cm^{-2} at 900 °C using H_2 and syngas fuel, respectively. Nevertheless, a slight degradation in current and power density was observed during long-time operating (100 h), which was partially attributed to the non-uniformity of the exsolved Cu particles and the thermal mismatch of the electrodes with interlayer and electrolyte, although no crack or delamination were observed [180].

In recent years, several materials exhibiting rather promising properties have been reported, including perovskite materials substituted at the A or B-site, double perovskites and Ruddlesden Popper phases. Likewise, the properties were improved by the use of composites, thin-film electrolytes and infiltration or exsolution methods [181]. Table 2 summarized the maximum power densities obtained for some symmetrical solid oxide fuel cells (sSOFC).

Table 2. Selected performances of sSOFC (typically air is used as oxidant).

Cell	Power Density (mW cm^{-2})		T (°C)	Ref.
	100% H_2	CH_4		
LSCM-YSZ//YSZ//LSCM-YSZ	546	347	950	[171]
LSCM-(YSZ-GDC)//YSZ//LSCM-(YSZ-GDC)	400	110	950	[182]
LSTF60-(YSZ-CeO_2)//YSZ//LSTF60-(YSZ-CeO_2)	100	40	950	[175]
LSCT/LDC//LSGM//LSCT	110		800	[177]
LSF/GDC//YSZ//GDC/LSF	400		800	[178]
LSFO4-LSGM//LSGM//LSFO4-LSGM	73		800	[179]
LSFC/SDC//ScSZ//SDC/LSFC	1054	895*	900	[180]
SFM//LSGM//SFM	835	230	900	[183]
LSFN-YSZ//YSZ//LSFN-YSZ	280	230	750	[184]
LSCM-YSZ//YSZ//LSCM-YSZ^{ł}	559	547	900	[185]
LNO4-LSGM//LSGM//LNO4-LSGM^{ł}	520		800	[186]
LNO4-SDC//LSGM//LNO4-SDC^{ł}	500		800	[186]
SSFR//SDC//SSFR	120		800	[187]
PSFNM /GDC//LSGM//GDC/PSFNM	500		800	[188]
LSMO4(NiO)-SDC//SDC//LSMO4(NiO)-SDC^{ł}	714	108	800	[189]

$La_{0.8}Sr_{1.2}FeO_4$ (LSFO4), $Sr_2Fe_{1.5}Mo_{0.5}O_{6-\delta}$ (SFM), $La_{0.6}Sr_{0.4}Fe_{0.9}Ni_{0.1}O_{3-\delta}$ (LSFN), La_2NiO_4 (LNO4), $Sm_{0.9}Sr_{0.1}Fe_{0.9}Ru_{0.1}O_{3-\delta}$ (SSFR), $Pr_{0.6}Sr_{0.4}Fe_{0.8}Ni_{0.2}O_{3-\delta}$ (PSFNM), $La_{0.6}Sr_{1.4}MnO_{4+\delta}$ (LSMO4).

* Syngas.

^{ł} Prepared by infiltration or impregnation

1.5 REFERENCES

[1] A. B. Gallo, J. R. Simoes-Moreira, H. K. M. Costa, M. M. Santos, and E. Moutinho dos Santos, "Energy storage in the energy transition context: A technology review," *Renew. Sustain. Energy Rev.*, vol. 65, pp. 800–822, 2016.

[2] D. C. Y. Foo and R. R. Tan, "A review on process integration techniques for carbon emissions and environmental footprint problems," *Process Saf. Environ. Prot.*, vol. 103, pp. 291–307, 2016.

[3] Robert Polack, S. Wood, and K. N. Smith, "An analysis of fossil-fuel dependence in the United States with implications for community social work," *Crit. Soc. Work*, vol. 11, no. 3, pp. 140–154, 2010.

[4] "International Energy Agency (IEA)," *https://www.iea.org*, 2014.

[5] E. Dlugokencky and Pieter Tans, "NOAA/ESRL," *www.esrl.noaa.gov/gmd/ccgg/trends*, 2017

[6] "Banco Mundial," *http://datos.bancomundial.org*, 2017.

[7] A. Hussain, S. M. Arif, and M. Aslam, "Emerging renewable and sustainable energy technologies: State of the art," *Renew. Sustain. Energy Rev.*, vol. 71, no. July 2016, pp. 12–28, 2017.

[8] C. M. V. B. Almeida, F. Agostinho, D. Huisingh, and B. F. Giannetti, "Cleaner Production towards a sustainable transition," *J. Clean. Prod.*, vol. 142, pp. 1–7, 2017.

[9] Y. D. Lee, K. Y. Ahn, T. Morosuk, and G. Tsatsaronis, "Environmental impact assessment of a solid-oxide fuel-cell-based combined-heat-and-power-generation system," *Energy*, vol. 79, no. C, pp. 455–466, 2015.

[10] A. B. Stambouli, "Fuel cells: The expectations for an environmental-friendly and sustainable source of energy," *Renew. Sustain. Energy Rev.*, vol. 15, no. 9, pp. 4507–4520, 2011.

[11] P. P. Kundu and K. Dutta, "Hydrogen fuel cells for portable applications," in *Compendium of Hydrogen Energy*, 2016, pp. 111–131.

[12] T. Elmer, M. Worall, S. Wu, and S. B. Riffat, "Fuel cell technology for domestic built environment applications: State of-the-art review," *Renew. Sustain. Energy Rev.*, vol. 42, pp. 913–931, Feb. 2015.

[13] P. Nikolaidis and A. Poullikkas, "A comparative overview of hydrogen production processes," *Renew. Sustain. Energy Rev.*, vol. 67, pp. 597–611, 2017.

[14] G. Marbán and T. Valdés-Solís, "Towards the hydrogen economy?," *Int. J. Hydrogen Energy*, vol. 32, no. 12, pp. 1625–1637, 2007.

[15] M. Conte, A. Iacobazzi, M. Ronchetti, and R. Vellone, "Hydrogen economy for a sustainable development: State-of-the-art and technological perspectives," *J. Power Sources*, vol. 100, no. 1–2, pp. 171–187, 2001.

[16] A. Midilli and I. Dincer, "Hydrogen as a renewable and sustainable solution in reducing global fossil fuel consumption," *Int. J. Hydrogen Energy*, vol. 33, no. 16, pp. 4209–4222, 2008.

[17] IHS Market, "Chemical Economics Handbook Hydrogen," 2015.

[18] T. Lipman, “An Overview of Hydrogen Production and Storage Systems with Renewable Hydrogen Case Studies,” *Clean Energy States Alliance*, p. 32, 2011.

[19] FreedomCAR & Fuel Partnership, “Hydrogen production overview of technology options,” *Available from: https://www1.eere.energy.gov/hydrogenandfuelcells/pdfs/h2_tech_roadmap*, 2017

[20] R. Moliner, M. J. Lázaro, and I. Suelves, “Analysis of the strategies for bridging the gap towards the Hydrogen Economy,” *Int. J. Hydrogen Energy*, vol. 41, no. 43, pp. 19500–19508, 2016.

[21] P. E. Dodds, I. Staffell, A. D. Hawkes, F. Li, P. Grünewald, W. McDowall, and P. Ekins, “Hydrogen and fuel cell technologies for heating: A review,” *Int. J. Hydrogen Energy*, vol. 40, no. 5, pp. 2065–2083, 2015.

[22] S. Mekhilef, R. Saidur, and A. Safari, “Comparative study of different fuel cell technologies,” *Renew. Sustain. Energy Rev.*, vol. 16, no. 1, pp. 981–989, 2012.

[23] A. Kirubakaran, S. Jain, and R. K. Nema, “A review on fuel cell technologies and power electronic interface,” *Renew. Sustain. Energy Rev.*, vol. 13, no. 9, pp. 2430–2440, 2009.

[24] D. Shekhawat, J. J. Spivey, and D. A. Berry, Eds., *Fuel Cells: Technologies for fuel processing*. Elsevier, 2011.

[25] N. Q. Minh and T. Takahashi, *Science and Technology of Ceramic Fuel Cells*. New York: Elsevier, 1995.

[26] S. Kakaç, A. Pramuanjaroenkij, and X. Y. Zhou, “A review of numerical modeling of solid oxide fuel cells,” *Int. J. Hydrogen Energy*, vol. 32, no. 7, pp. 761–786, 2007.

[27] B. Timurkutluk, C. Timurkutluk, M. D. Mat, and Y. Kaplan, “A review on cell/stack designs for high performance solid oxide fuel cells,” *Renew. Sustain. Energy Rev.*, vol. 56, pp. 1101–1121, 2016.

[28] K. Wincewicz and J. Cooper, “Taxonomies of SOFC material and manufacturing alternatives,” *J. Power Sources*, vol. 140, no. 2, pp. 280–296, Feb. 2005.

[29] A. B. Stambouli and E. Traversa, “Solid oxide fuel cells (SOFCs): a review of an environmentally clean and efficient source of energy,” *Renew. Sustain. Energy Rev.*, vol. 6, no. 5, pp. 433–455, Oct. 2002.

[30] S. C. Singhal and K. Kendall, *High Temperature Solid Oxide Fuel Cells. Fundamentals, Design ans Applications*. Oxford: Elsevier, 2003.

[31] N. Mahato, A. Banerjee, A. Gupta, S. Omar, and K. Balani, “Progress in material selection for solid oxide fuel cell technology: A review,” *Prog. Mater. Sci.*, vol. 72, pp. 141–337, 2015.

[32] I. Pilatowsky, R. J. Romero, C. A. Isaza, S. A. Gamboa, P. J. Sebastian, and W. Rivera, “Thermodynamics of Fuel Cells,” in *Cogeneration Fuel Cell-Sorption Air Conditioning Systems*, 2011, pp. 25–36.

[33] J. Zhang, Z. Xia, and L. Dai, “Carbon-based electrocatalysts for advanced energy conversion and storage,” *Sci. Adv.*, vol. 1, no. 7, pp. 1–19, 2015.

[34] A. V. Virkar, J. Chen, C. W. Tanner, and J. W. Kim, “Role of electrode microstructure on activation and concentration polarizations in solid oxide fuel cells,” *Solid State Ionics*, vol. 131, no. 1, pp. 189–198, 2000.

[35] J. A. Kilner, J. Druce, and T. Ishihara, “Electrolytes,” in *High-Temperature Solid Oxide Fuel Cells for the 21st Century*, Second Edi., 2016, pp. 85–132.

[36] T. Van Gestel, D. Sebold, and H. P. Buchkremer, “Processing of 8YSZ and CGO thin film electrolyte layers for intermediate- and low-temperature SOFCs,” *J. Eur. Ceram. Soc.*, vol. 35, no. 5, pp. 1505–1515, 2015.

[37] J. W. Fergus, “Electrolytes for solid oxide fuel cells,” *J. Power Sources*, vol. 162, no. 1, pp. 30–40, 2006.

[38] Z. Naiqing, S. Kening, Z. Derui, and J. Dechand, “Study on properties of LSGM electrolyte made by tape casting method and applications in SOFC,” *J. Rare Earths*, vol. 24, pp. 90–92, 2006.

[39] H. Hayashi, T. Saitou, N. Maruyama, H. Inaba, K. Kawamura, and M. Mori, “Thermal expansion coefficient of yttria stabilized zirconia for various yttria contents,” *Solid State Ionics*, vol. 176, no. 5–6, pp. 613–619, 2005.

[40] Hyun Jun Ko, J.-J. Lee, and S.-H. Hyun, “Structural stability of the GDC electrolyte for low temperature SOFCs depending on fuels,” *ECS Trans.*, vol. 25, no. 2, pp. 1611–1616, 2009.

[41] B. C. H. Steele, “Appraisal of $Ce_{1-y}Gd_yO_{2-y}$ electrolytes for IT-SOFC operation at 500°C,” *Solid State Ionics*, vol. 129, pp. 95–110, 2000.

[42] N. P. Brandon, A. Blake, D. Corcoran, D. Cumming, A. Duckett, K. El-Koury, D. Haigh, C. Kidd, R. Leah, G. Lewis, C. Matthews, N. Maynard, N. Oishi, T. McColm, R. Trezona, A. Selcuk, M. Schmidt, and L. Verdugo, “Development of Metal Supported Solid Oxide Fuel Cells for Operation at 500–600 °C,” *J. Fuel Cell Sci. Technol.*, vol. 1, no. 1, p. 61, 2004.

[43] D. Szymczewska, J. Karczewski, A. Chrzan, and P. Jasinski, “CGO as a barrier layer between LSCF electrodes and YSZ electrolyte fabricated by spray pyrolysis for solid oxide fuel cells,” *Solid State Ionics*, vol. Article in, 2016.

[44] M. Morales, J. J. Roa, J. Tartaj, and M. Segarra, “A review of doped lanthanum gallates as electrolytes for intermediate temperature solid oxides fuel cells: From materials processing to electrical and thermomechanical properties,” *J. Eur. Ceram. Soc.*, vol. 36, pp. 1–16, 2016.

[45] T. Kawada and T. Horita, “Cathodes,” in *High-Temperature Solid Oxide Fuel Cells for the 21st Century*, K. Kendall and M. Kendall, Eds. 2016, pp. 161–193.

[46] M. Irshad, K. Siraj, R. Raza, A. Ali, P. Tiwari, B. Zhu, A. Rafique, A. Ali, M. Kaleem Ullah, and A. Usman, “A brief description of high temperature solid oxide fuel cell’s operation, Materials, Design, Fabrication Technologies and Performance,” *Appl. Sci.*, vol. 6, no. 3, p. 75, 2016.

[47] J. A. Kilner and M. Burriel, “Materials for Intermediate-Temperature Solid-Oxide Fuel Cells,” *Annu. Rev. Mater. Res.*, vol. 44, no. 1, pp. 365–393, 2014.

[48] W. Zhou, R. Ran, and Z. Shao, “Progress in understanding and development of $Ba_{0.5}Sr_{0.5}Co_{0.8}Fe_{0.2}O_{3-\delta}$ based cathodes for intermediate-temperature solid-oxide fuel cells: A review,” *J. Power Sources*, vol. 192, pp. 231–246, 2009.

[49] J. Sunarso, S. Baumann, J. M. Serra, W. A. Meulenberg, S. Liu, Y. S. Lin, and

J. C. Diniz da Costa, “Mixed ionic-electronic conducting (MIEC) ceramic-based membranes for oxygen separation,” *J. Memb. Sci.*, vol. 320, no. 1–2, pp. 13–41, 2008.

[50] C. Sun, R. Hui, and J. Roller, “Cathode materials for solid oxide fuel cells: a review,” *J. Solid State Electrochem.*, vol. 14, no. 7, pp. 1125–1144, Oct. 2010.

[51] J. Fleig, “Solid Oxide Fuel Cell Cathodes: Polarization mechanisms and modeling of the electrochemical performance,” *Annu. Rev. Mater. Res.*, vol. 33, pp. 361–382, 2003.

[52] A. J. Samson, M. Søgaard, and P. Hendriksen, “Model for solid oxide fuel cell cathodes,” *Electrochim. Acta*, vol. 229, pp. 73–95, 2017.

[53] J. Kim, W. Seo, J. Shin, M. Liu, and G. Kim, “Composite cathodes composed of $NdBa_{0.5}Sr_{0.5}Co_2O_{5+\delta}$ and $Ce_{0.9}Gd_{0.1}O_{1.95}$ for intermediate-temperature solid oxidefuel cells,” *J. Mater. Chem. A*, vol. 1, no. 3, pp. 515–519, 2013.

[54] R. A. De Souza, “Ph.D. Thesis,” Imperial College of Science, Technology and Medicine, 1996.

[55] S. B. Adler, J. A. Lane, and B. C. H. Steele, “Electrode kinetics of porous mixed-conducting oxygen electrodes,” *J. Electrochem. Soc*, vol. 143, no. 11, p. 3554, 1996.

[56] S. B. Adler, “Mechanism and kinetics of oxygen reduction on porous $La_{1-x}Sr_xCoO_{3-\delta}$ electrodes,” *Solid State Ionics*, vol. 111, pp. 125–134, 1998.

[57] C. Endler-Schuck, J. Joos, C. Niedrig, A. Weber, and E. Ivers-Tiffée, “The chemical oxygen surface exchange and bulk diffusion coefficient determined by impedance spectroscopy of porous $La_{0.58}Sr_{0.4}Co_{0.2}Fe_{0.8}O_{3-\delta}$ (LSCF) cathodes,” *Solid State Ionics*, vol. 269, pp. 67–79, 2015.

[58] C. Sun, R. Hui, and J. Roller, “Cathode materials for solid oxide fuel cells: a review,” *J. Solid State Electrochem.*, vol. 14, no. 7, pp. 1125–1144, Oct. 2010.

[59] Tatsumi Ishihara, “Structure and Properties of Perovskite Oxides,” *Perovskite Oxide for Solid Oxide Fuel Cells*, T. Ishihara, Ed. New York: Springer, pp. 1–16, 2009.

[60] L. Zhu, R. Ran, M. Tadé, W. Wang, and Z. Shao, “Perovskite materials in energy storage and conversion,” *Asia-Pacific J. Chem. Eng.*, vol. 11, pp. 338–369, 2016.

[61] J. M. Ralph, a C. Schoeler, and M. Krumpelt, “Materials for lower temperature solid oxide fuel cells,” *Electrochem. Technol.*, vol. 6, no. 5, pp. 1161–1172, 2001.

[62] J. Mizusaki, Y. Yonemura, H. Kamata, K. Ohyam, and T. Hashimoto, “Electronic conductivity, Seebeck coefficient, defect and electronic structure of nonstoichiometric $La_{1-x}Sr_xMnO_3$,” *Solid State Ionics*, vol. 132, no. 3–4, pp. 167–180, 2000.

[63] A. Mitterdorfer and L. J. Gauckler, “$La_2Zr_2O_7$ formation and oxygen reduction kinetics of the $La_{0.85}Sr_{0.15}Mn_yO_3$, O_2(g)|YSZ system,” *Solid State Ionics*, vol. 111, no. 3–4, pp. 185–218, 1998.

[64] G. Stonchnio, E. Syskakis, and A. Naomidis, “Chemical reactivity between Strontium-Doped Lanthanum Manganite and Yttria-Stabilized Zirconia,” *J. Am. Ceram. Soc.*, vol. 78, pp. 929–932, 1995.

[65] Y. Chen, W. Zhou, D. Ding, M. Liu, F. Ciucci, M. Tade, and Z. Shao, "Advances in cathode materials for solid oxide fuel cells: complex oxides without alkaline earth metal elements," *Adv. Energy Mater.*, vol. 5, no. 18, pp. 1–34, 2015.

[66] F. Tietz, I. Arul Raj, M. Zahid, and D. Stöver, "Electrical conductivity and thermal expansion of $La_{0.8}Sr_{0.2}(Mn,Fe,Co)O_{3-\delta}$ perovskites," *Solid State Ionics*, vol. 177, pp. 1753–1756, 2006.

[67] I. Yasuda, K. Ogasawara, M. Hishinuma, T. Kawada, and M. Dokiya, "Oxygen tracer diffusion coefficient of (La, Sr)$MnO_{3+\delta}$," *Solid State Ionics*, vol. 86–88, pp. 1197–1201, 1996.

[68] S. P. Jiang, "A comparison of O_2 reduction reactions on porous (La,Sr)MnO_3 and (La,Sr)(Co,Fe)O_3 electrodes," *Solid State Ionics*, vol. 146, pp. 1–22, 2002.

[69] T. Kenjo and M. Nishiya, "$LaMnO_3$ air cathodes containing ZrO_2 electrolyte for high temperature solid oxide fuel cells," *Solid State Ionics*, vol. 57, no. 3–4, pp. 295–302, 1992.

[70] M. J. L. Østergard, C. Clausen, C. Bagger, and M. Mogensen, "Manganite-zirconia composite cathodes for SOFC: Influence of structure and composition," *Electrochim. Acta*, vol. 40, no. 12, pp. 1971–1981, 1995.

[71] S. Wang, Y. Jiang, Y. Zhang, J. Yan, and W. Li, "Promoting effect of YSZ on the electrochemical performance of YSZ+LSM composite electrodes," *Solid State Ionics*, vol. 113–115, pp. 291–303, 1998.

[72] J. D. Kim, G. D. Kim, J. W. Moon, Y. il Park, W. H. Lee, K. Kobayashi, M. Nagai, and C. E. Kim, "Characterization of LSM-YSZ composite electrode by ac impedance spectroscopy," *Solid State Ionics*, vol. 143, no. 3–4, pp. 379–389, 2001.

[73] A. Jun, J. Kim, J. Shin, and G. Kim, "Perovskite as a cathode material: a review of its role in solid-oxide fuel cell technology," *ChemElectroChem*, vol. 3, no. 4, pp. 511–530, 2016.

[74] R. Pelosato, G. Cordaro, D. Stucchi, C. Cristiani, and G. Dotelli, "Cobalt based layered perovskites as cathode material for intermediate temperature Solid Oxide Fuel Cells: A brief review," *J. Power Sources*, vol. 298, pp. 46–67, 2015.

[75] D. Marinha, L. Dessemond, and E. Djurado, "Comprehensive review of current developments in IT-SOFCs," *Curr. Inorg. Chem.*, vol. 3, no. 1, pp. 2–22, 2013.

[76] E. Lima Fernandes, Antonio de Pádua Marsalha Garcia, R. Moreira de Almeida, H. A. Taroco, E. P. Campos Silva, R. Zacarias Domingues, and T. Matencio, "Influence of cathode functional layer composition on electrochemical performance of solid oxide fuel cells," *J. Solid State Electrochem.*, vol. 20, pp. 2575–2580, 2016.

[77] J. Laurencin, M. Hubert, K. Couturier, T. Le Bihan, P. Cloetens, F. Lefebvre-Joud, and E. Siebert, "Reactive mechanisms of LSCF single-phase and LSCF-CGO composite electrodes operated in anodic and cathodic polarisations," *Electrochim. Acta*, vol. 174, pp. 1299–1316, 2015.

[78] J. Sar, L. Dessemond, and E. Djurado, "Electrochemical properties of graded and homogeneous $Ce_{0.9}Gd_{0.1}O_{2-\delta}$-$La_{0.6}Sr_{0.4}Co_{0.2}Fe_{0.8}O_{3-\delta}$ composite electrodes for intermediate-temperature solid oxide fuel cells," *Int. J. Hydrogen Energy*, vol. 41, pp. 17037–17043, 2016.

[79] J.-C. Grenier, J.-M. Bassat, and F. Mauvy, “Novel cathodes for solid oxide fuel cells,” in *Functional Materials for Sustainable Energy Applications*, pp. 402–444, 2012.

[80] A. Petric, P. Huang, and F. Tietz, “Evaluation of La– Sr–Co– Fe– O perovskites for solid oxide fuel cells and gas separation membranes,” *Solid State Ionics*, vol. 135, pp. 719–725, 2000.

[81] A. Esquirol, N. P. Brandon, J. A. Kilner, and M. Mogensen, “Electrochemical characterization of $La_{0.6}Sr_{0.4}Co_{0.2}Fe_{0.8}O_3$ cathodes for intermediate-temperature SOFCs,” *J. Electrochem. Soc.*, vol. 151, no. 11, pp. A1847–A1855, 2004.

[82] H. A. Taroco, J. A. F. Santos, R. Z. Domingues, and T. Matencio, “Ceramic materials for solid oxide fuel cells,” in *Advances in Ceramics - Synthesis and Characterization, Processing and Specific Applications*, Costas Sikalidi, Ed. Minas Gerais, Brasil: InTech, 2011.

[83] E. V. Tsipis and V. V. Kharton, “Electrode materials and reaction mechanisms in solid oxide fuel cells: a brief review,” *J. Solid State Electrochem.*, vol. 12, no. 11, pp. 1367–1391, 2008.

[84] T. Matsui, M. Komoto, H. Muroyama, K. Kishida, H. Inui, and K. Eguchi, “Degradation factors in $(La,Sr)(Co,Fe)O_{3-\delta}$ cathode/Sm_2O_3-CeO_2 interlayer/Y_2O_3-ZrO_2 electrolyte system during operation of solid oxide fuel cells,” *J. Power Sources*, vol. 312, pp. 80–85, 2016.

[85] J. C. De Vero, K. Develos-Bagarinao, H. Kishimoto, T. Ishiyama, K. Yamaji, T. Horita, and H. Yokokawa, “Influence of $La_{0.6}Sr_{0.4}Co_{0.2}Fe_{0.8}O_{3-\delta}$ microstructure on GDC Interlayer stability and cation diffusion across the LSCF/GDC/YSZ Interfaces,” *J. Electrochem. Soc.*, vol. 163, pp. F1463–F1470, 2016.

[86] R. Kiebach, W. Zhang, M. Chen, K. Norrman, H. J. Wang, J. R. Bowen, R. Barfod, P. V. Hendriksen, and W. Zhang, “Stability of $La_{0.6}Sr_{0.4}Co_{0.2}Fe_{0.8}O_3$/$Ce_{0.9}Gd_{0.1}O_2$ cathodes during sintering and solid oxide fuel cell operation,” *J. Power Sources*, vol. 283, pp. 151–161, 2015.

[87] D. Beckel, U. P. Muecke, T. Gyger, G. Florey, A. Infortuna, and L. J. Gauckler, “Electrochemical performance of LSCF based thin film cathodes prepared by spray pyrolysis,” *Solid State Ionics*, vol. 178, no. 5–6, pp. 407–415, 2007.

[88] W. G. Wang and M. Mogensen, “High-performance lanthanum-ferrite-based cathode for SOFC,” *Solid State Ionics*, vol. 176, no. 5–6, pp. 457–462, 2005.

[89] G. Constantin, C. Rossignol, P. Briois, A. Billard, L. Dessemond, and E. Djurado, “Efficiency of a dense thin CGO buffer layer for solid oxide fuel cell operating at intermediate temperature,” *Solid State Ionics*, vol. 249–250, pp. 98–104, 2013.

[90] F. Shen and K. Lu, “Perovskite-type $La_{0.6}Sr_{0.4}Co_{0.2}Fe_{0.8}O_3$, $Ba_{0.5}Sr_{0.5}Co_{0.2}Fe_{0.8}O_3$, and $Sm_{0.5}Sr_{0.5}Co_{0.2}Fe_{0.8}O_3$ cathode materials and their chromium poisoning for solid oxide fuel cells,” *Electrochim. Acta*, vol. 211, pp. 445–452, 2016.

[91] L. Wang, R. Merkle, J. Maier, T. Acartürk, and U. Starke, “Oxygen tracer diffusion in dense $Ba_{0.5}Sr_{0.5}Co_{0.8}Fe_{0.2}O_{3-\delta}$ films,” *Appl. Phys. Lett.*, vol. 94, no. 7, pp. 2012–2015, 2009.

[92] Z. Shao and S. M. Haile, “A high-performance cathode for the next generation of solid-oxide fuel cells.,” *Nature*, vol. 431, pp. 170–173, Sep. 2004.

[93] F. Shen and K. Lu, “Comparative study of $La_{0.6}Sr_{0.4}Co_{0.2}Fe_{0.8}O_3$, $Ba_{0.5}Sr_{0.5}Co_{0.2}Fe_{0.8}O_3$ and $Sm_{0.5}Sr_{0.5}Co_{0.2}Fe_{0.8}O_3$ cathodes and the effect of $Sm_{0.2}Ce_{0.8}O_2$ block layer in solid oxide fuel cells,” *Int. J. Hydrogen Energy*, vol. 40, no. 46, pp. 16457–16465, 2015.

[94] Z. Duan, M. Yang, A. Yan, Z. Hou, Y. Dong, Y. Chong, M. Cheng, and W. Yang, “$Ba_{0.5}Sr_{0.5}Co_{0.8}Fe_{0.2}O_{3-\delta}$ as a cathode for IT-SOFCs with a GDC interlayer,” *J. Power Sources*, vol. 160, no. 1, pp. 57–64, Sep. 2006.

[95] S. P. N. Nair and P. Murugavel, “Oxides: their properties and uses,” in *Comprehensive Inorganic Chemistry II*, Second Edi., Jan Reedijk and K. Poeppelmeier, Eds. Elsevier, pp. 47–72, 2014.

[96] Shriver and Atkins, “Solid-state and materials chemistry,” in *Inorganic Chemistry*, Fifth Edit., P. Atkins, T. Overton, J. Rourke, M. Weller, F. Armstrong, and M. Hagerman, Eds. Oxford, pp. 601–651, 2010.

[97] V. V Kharton, A. P. Viskup, A. V Kovalevsky, and E. N. Naumovich, “Ionic transport in oxygen-hyperstoichiometric phases with K_2NiF_4-type structure,” *Solid State Ionics*, vol. 143, pp. 337–353, 2001.

[98] A. Das, E. Xhafa, and E. Nikolla, “Electro- and thermal-catalysis by layered, first series Ruddlesden-Popper oxides,” *Catal. Today*, vol. 277, pp. 214–226, 2016.

[99] S. J. Skinner and J. A. Kilner, “Oxygen diffusion and surface exchange in $La_{2-x}Sr_xNiO_{4+\delta}$,” *Solid State Ionics*, vol. 135, pp. 709–712, 2000.

[100] J. D. Jorgensen, B. Dabrowski, S. Pei, D. R. Richards, and D. G. Hinks, “Structure of the interstitial oxygen defect in $La_2NiO_{4+\delta}$,” *Phys. Rev. B*, vol. 40, no. 4, pp. 2187–2199, 1989.

[101] L. Minervini, R. W. Grimes, J. a. Kilner, and K. E. Sickafus, “Oxygen migration in $La_2NiO_{4+\delta}$,” *J. Mater. Chem.*, vol. 10, pp. 2349–2354, 2000.

[102] J. Bassat, “Anisotropic ionic transport properties in $La_2NiO_{4+\delta}$ single crystals,” *Solid State Ionics*, vol. 167, pp. 341–347, 2004.

[103] D. P. Huang, Q. Xu, F. Zhang, W. Chen, H. X. Liu, and J. Zhou, “Synthesis and electrical conductivity of $La_2NiO_{4+\delta}$ derived from a polyaminocarboxylate complex precursor,” *Mater. Lett.*, vol. 60, no. 15, pp. 1892–1895, 2006.

[104] E. Boehm, J. M. Bassat, P. Dordor, F. Mauvy, J. C. Grenier, and P. Stevens, “Oxygen diffusion and transport properties in non-stoichiometric $Ln_{2-X}NiO_{4+\delta}$ oxides,” *Solid State Ionics*, vol. 176, pp. 2717–2725, 2005.

[105] E. Boehm, J. M. Bassat, M. C. Steil, P. Dordor, F. Mauvy, and J. C. Grenier, “Oxygen transport properties of $La_2Ni_{1-x}Cu_xO_{4+\delta}$ mixed conducting oxides,” *Solid State Sci.*, vol. 5, pp. 973–981, 2003.

[106] A. M. Hernández, L. Mogni, and A. Caneiro, “$La_2NiO_{4+\delta}$ as cathode for SOFC: Reactivity study with YSZ and CGO electrolytes,” *Int. J. Hydrogen Energy*, vol. 35, no. 11, pp. 6031–6036, Jun. 2010.

[107] T. Inprasit, S. Wongkasemjit, S. J. Skinner, M. Burriel, and P. Limthongkul, “Effect of Sr substituted $La_{2-x}Sr_xNiO_{4+\delta}$ (x= 0, 0.2, 0.4, 0.6, and 0.8) on oxygen stoichiometry and oxygen transport properties,” *RSC Adv.*, vol. 5, pp. 2486–

2492, 2015.

[108] V. V Vashook, S. P. Tolochko, I. I. Yushkevich, L. V Makhnach, I. F. Kononyuk, H. Altenburg, J. Hauck, and H. Ullmann, "Oxygen nonstoichiometry and electrical conductivity of the solid solutions $La_{2-x}Sr_xNiO_y$ (0≤x≤0.5)," *Solid State Ionics*, vol. 110, pp. 245–253, 1998.

[109] T. Inprasit, P. Limthongkul, and S. Wongkasemjit, "Property Study of $La_{2-x}Sr_xNiO_4$ (x ≤ 0.8) for IT-SOFCs Cathode," *ECS Trans.*, vol. 25, no. 2, pp. 2581–2588, 2009.

[110] M. Al Daroukh, V. V Vashook, H. Ullmann, F. Tietz, and I. Arual Raj, "Oxides of the AMO_3 and A_2MO_4 -type: structural stability , electrical conductivity and thermal expansion," *Solid State Ionics*, vol. 158, pp. 141–150, 2003.

[111] C. Munnings, S. Skinner, G. Amow, P. Whitfield, and I. Davidson, "Structure, stability and electrical properties of the $La_{(2-x)}Sr_xMnO_{4\pm\delta}$ solid solution series," *Solid State Ionics*, vol. 177, no. 19–25, pp. 1849–1853, Oct. 2006.

[112] S. Liping, H. Lihua, Z. Hui, L. Qiang, and C. Pijolat, "La substituted Sr_2MnO_4 as a possible cathode material in SOFC," *J. Power Sources*, vol. 179, pp. 96–100, Apr. 2008.

[113] S. LiPing, L. Qiang, H. Li-Hua, Z. Hui, Z. Guo-Ying, L. Nan, J.-P. Viricelle, and C. Pijolat, "Synthesis and performance of $Sr_{1.5}La_xMnO_4$ as cathode materials for intermediate temperature solid oxide fuel cell," *J. Power Sources*, vol. 196, no. 14, pp. 5835–5839, Jul. 2011.

[114] M. Cassidy, P. A. Connor, J. T. S. Irvine, and C. D. Savaniu, "Anodes," in *High-Temperature Solid Oxide Fuel Cells for the 21st Century*, Second Edi., Kevin Kendall and M. Kendall, Eds. Elsevier, pp. 133–160, 2016.

[115] M. Mukhopadhyay, J. Mukhopadhyay, and R. N. Basu, "Functional Anode Materials for Solid Oxide Fuel Cell – A Review," *Trans. Indian Ceram. Soc.*, vol. 72, no. 3, pp. 145–168, 2013.

[116] L. S. Mahmud, A. Muchtar, and M. R. Somalu, "Review on anode material development in solid oxide fuel cells," *Am. Inst. Phys.*, vol. 1, p. 070095–1,5, 2015.

[117] M. D. Gross, J. M. Vohs, and R. J. Gorte, "Recent progress in SOFC anodes for direct utilization of hydrocarbons," *J. Mater. Chem.*, vol. 17, pp. 3071–3077, 2007.

[118] B. Shri Prakash, S. Senthil Kumar, and S. T. Aruna, "Properties and development of Ni/YSZ as an anode material n solid oxide fuel cell: A review," *Renew. Sustain. Energy Rev.*, vol. 36, pp. 149–179, 2014.

[119] A. C. Müller, P. B. Pei, A. Weber, and E. Ivers-Tiffée, "Properties of Ni/YSZ Cermets depending on their microstructure," *Proc. 10th Int. Conf. High Temp. Mater. Chem.*, pp. 731–734, 2000.

[120] D. Sarantaridis and A. Atkinson, "Redox cycling of Ni-based solid oxide fuel cell anodes: a review," *Fuel Cells*, vol. 7, no. 3, pp. 246–258, Jun. 2007.

[121] S. K. Pratihar, A. Dassharma, and H.S. Maiti, "Processing microstructure property correlation of porous Ni-YSZ cermets anode for SOFC application," *Mater. Res. Bull.*, vol. 40, pp. 1936–1944, 2005.

[122] M. Kogler, E. M. Köck, M. Stöger-Pollach, S. Schwarz, T. Schachinger, B.

Klötzer, and S. Penner, “Distinct carbon growth mechanisms on the components of Ni/YSZ materials,” *Mater. Chem. Phys.*, vol. 173, pp. 508–515, 2016.

[123] H. Chen, F. Wang, W. Wang, D. Chen, S. D. Li, and Z. Shao, “H_2S poisoning effect and ways to improve sulfur tolerance of nickel cermet anodes operating on carbonaceous fuels,” *Appl. Energy*, vol. 179, no. 5, pp. 765–777, 2016.

[124] T. Klemenso, C. Chung, P. H. Larsen, and M. Mogensen, “The mechanism behind redox instability of anodes in high-temperature SOFCs,” *J. Electrochem. Soc.*, vol. 152, no. 11, p. A2186, 2005.

[125] A. Faes, A. Hessler-Wyser, A. Zryd, and J. Van Herle, “A review of RedOx cycling of solid oxide fuel cells anode,” *Membranes (Basel).*, vol. 2, no. 3, pp. 585–664, 2012.

[126] G. Xiao and F. Chen, “Redox stable anodes for solid oxide fuel cells,” *Front. Energy Res.*, vol. 2, pp. 1–13, 2014.

[127] M. Ettler, H. Timmermann, J. Malzbender, A. Weber, and N. H. Menzler, “Durability of Ni anodes during reoxidation cycles,” *J. Power Sources*, vol. 195, no. 17, pp. 5452–5467, 2010.

[128] M. Pihlatie, A. Kaiser, and M. Mogensen, “Redox stability of SOFC: thermal analysis of Ni-YSZ composites,” *Solid State Ionics*, vol. 180, pp. 1100–1112, 2009.

[129] Y. Zhang, Z. Yang, and M. Wang, “Understanding on the carbon deposition on the Nickel/Yttrium-Stabilized Zirconia anode caused by the CO containing fuels,” *J. Power Sources*, vol. 279, pp. 759–765, 2015.

[130] J. Mirzababaei and S. Chuang, “$La_{0.6}Sr_{0.4}Co_{0.2}Fe_{0.8}O_3$ Perovskite: A sStable anode catalyst for direct methane solid oxide fuel cells,” *Catalysts*, vol. 4, no. 2, pp. 146–161, 2014.

[131] J. Koh, “Carbon deposition and cell performance of Ni-YSZ anode support SOFC with methane fuel,” *Solid State Ionics*, vol. 149, no. 3–4, pp. 157–166, Aug. 2002.

[132] Y. Lin, Z. Zhan, J. Liu, and S. A. Barnett, “Direct operation of solid oxide fuel cells with methane fuel,” *Solid State Ionics*, vol. 176, no. 23–24, pp. 1827–1835, Jul. 2005.

[133] V. Alzate-Restrepo and J. M. Hill, “Carbon deposition on Ni/YSZ anodes exposed to CO/H_2 feeds,” *J. Power Sources*, vol. 195, no. 5, pp. 1344–1351, Mar. 2010.

[134] P. Boldrin, E. Ruiz-Trejo, J. Mermelstein, J. M. Bermúdez Menéndez, T. Ramírez Reina, and N. P. Brandon, “Strategies for carbon and sulfur tolerant solid oxide fuel cell materials, incorporating lessons from heterogeneous catalysis,” *Chem. Rev.*, vol. 116, no. 22, pp. 13633–13684, 2016.

[135] J. Hanna, W. Y. Lee, Y. Shi, and A. F. Ghoniem, “Fundamentals of electro- and thermochemistry in the anode of solid-oxide fuel cells with hydrocarbon and syngas fuels,” *Prog. Energy Combust. Sci.*, vol. 40, no. 1, pp. 74–111, 2014.

[136] D. Lee, J. Myung, J. Tan, S.-H. Hyun, J. T. S. Irvine, J. Kim, and J. Moon, “Direct methane solid oxide fuel cells based on catalytic partial oxidation

enabling complete coking tolerance of Ni-based anodes," *J. Power Sources*, vol. 345, pp. 30–40, 2017.

[137] W. Y. Lee, J. Hanna, and A. F. Ghoniem, "On the predictions of carbon deposition on the nickel anode of a SOFC and Its Impact on open-cCircuit Conditions," *J. Electrochem. Soc.*, vol. 160, no. 2, p. F94-105, 2013.

[138] Y. Matsuzaki, "The poisoning effect of sulfur-containing impurity gas on a SOFC anode: Part I. Dependence on temperature, time, and impurity concentration," *Solid State Ionics*, vol. 132, no. 3–4, pp. 261–269, Jul. 2000.

[139] C. H. Bartholomew, "Mechanisms of catalyst deactivation," *Appl. Catal. A Gen.*, vol. 212, no. 1–2, pp. 17–60, 2001.

[140] K. Sasaki, K. Susuki, A. Iyoshi, M. Uchimura, N. Imamura, H. Kusaba, Y. Teraoka, H. Fuchino, K. Tsujimoto, Y. Uchida, and N. Jingo, "H_2S poisoning of solid oxide fuel cells," *J. Electrochem. Soc.*, vol. 153, no. 11, pp. A2023–A2029, 2006.

[141] S. Zha, Z. Cheng, and M. Liu, "Sulfur poisoning and regeneration of Ni-based anodes in solid oxide fuel cells," *J. Electrochem. Soc.*, vol. 154, no. 2, p. B201, 2007.

[142] S. P. S. Shaikh, A. Muchtar, and M. R. Somalu, "A review on the selection of anode materials for solid-oxide fuel cells," *Renew. Sustain. Energy Rev.*, vol. 51, pp. 1–8, 2015.

[143] P. Vernoux, E. Djurado, and M. Guillodo, "Catalytic and electrochemical Properties of Doped Lanthanum Chromites as new anode materials for solid oxide fuel cells," *J. Am. Ceram. Soc.*, vol. 95, no. 188915, pp. 2289–2295, 2001.

[144] S. Tao and J. T. S. Irvine, "A redox-stable efficient anode for solid-oxide fuel cells.," *Nat. Mater.*, vol. 2, no. 5, pp. 320–323, 2003.

[145] S. Tao and J. T. S. Irvine, "Synthesis and characterization of $(La_{0.75}Sr_{0.25})Cr_{0.5}Mn_{0.5}O_{3-\delta}$ a redox-stable, efficient perovskite anode for SOFCs," *J. Electrochem. Soc*, vol. 151, no. 2, pp. A252-259, 2004.

[146] S. Zha, P. Tsang, Z. Cheng, and M. Liu, "Electrical properties and sulfur tolerance of $La_{0.75}Sr_{0.25}Cr_{1-x}Mn_xO_3$ under anodic conditions," *J. Solid State Chem.*, vol. 178, pp. 1844–1850, 2005.

[147] D. M. Bastidas, S. Tao, and J. T. S. Irvine, "A symmetrical solid oxide fuel cell demonstrating redox stable perovskite electrodes," *J. Mater. Chem.*, vol. 16, no. 17, p. 1603, 2006.

[148] E. Lay, G. Gauthier, and L. Dessemond, "Preliminary studies of the new Ce-doped La/Sr chromo-manganite series as potential SOFC anode or SOEC cathode materials," *Solid State Ionics*, vol. 189, no. 1, pp. 91–99, May 2011.

[149] D. Luo, W. Xiao, F. Lin, C. Luo, and X. Li, "Effects of A-site deficiency on the electrical conductivity and stability of (La, Co) co-doped $SrTiO_3$ anode materials for intermediate temperature solid oxide fuel cells," *Adv. Powder Technol.*, vol. 27, no. 2, pp. 481–485, 2016.

[150] X. Li, H. Zhao, N. Xu, X. Zhou, C. Zhang, and N. Chen, "Electrical conduction behavior of La, Co co-doped $SrTiO_3$ perovskite as anode material for solid oxide fuel cells," *Int. J. Hydrogen Energy*, vol. 34, no. 15, pp. 6407–6414,

2009.

[151] X. Zhou, N. Yan, K. T. Chuang, and J. Luo, “Progress in La-doped $SrTiO_3$ (LST)-based anode materials for solid oxide fuel cells,” *RSC Adv.*, vol. 4, no. 1, pp. 118–131, 2014.

[152] C. Périllat-Merceroz, P. Roussel, R.-N. Vannier, P. Gélin, S. Rosini, and G. Gauthier, “Lamellar titanates: a breakthrough in the search for new solid oxide fuel cell anode materials Operating on Methane,” *Adv. Energy Mater.*, vol. 1, no. 4, pp. 573–576, 2011.

[153] C. Périllat-Merceroz, G. Gauthier, P. Roussel, M. Huvé, P. Gélin, and R.-N. Vannier, “Synthesis and study of a Ce-d La/Sr titanate for solid oxide fuel cell anode operating directly on methane,” *Chem. Mater.*, vol. 23, pp. 1539–1550, 2011.

[154] J. Canales-Vázquez, S. W. Tao, and J. T. S. Irvine, “Electrical properties in $La_2Sr_4Ti_6O_{19-\delta}$: A potential anode for high temperature fuel cells,” *Solid State Ionics*, vol. 159, no. 1–2, pp. 159–165, 2003.

[155] D. Marrero-López, J. Peña-Martínez, J. C. Ruiz-Morales, M. Gabás, P. Núñez, M. A. G. Aranda, and J. R. Ramos-Barrado, “Redox behaviour, chemical compatibility and electrochemical performance of $Sr_2MgMoO_{6-\delta}$ as SOFC anode,” *Solid State Ionics*, vol. 180, no. 40, pp. 1672–1682, 2010.

[156] K. Zheng and K. Świerczek, “Physicochemical properties of rock salt-type ordered Sr_2MMoO_6 (M=Mg, Mn, Fe, Co, Ni) double perovskites,” *J. Eur. Ceram. Soc.*, vol. 34, no. 16, pp. 4273–4284, 2014.

[157] P. K. Dager, C. M. ChanquÍa, L. Mogni, and A. Caneiro, “Synthesis of pure-phase Sr_2MgMoO_6 nanostructured powder by the combustion method,” *Mater. Lett.*, vol. 141, pp. 248–251, 2015.

[158] E. Quenneville, M. Meunier, A. Yelon, and F. Morin, “Electronic transport by small polarons in $La_{0.5}Sr_{0.5}MnO_3$,” *J. Appl. Phys.*, vol. 90, no. 4, pp. 1891–1897, 2001.

[159] A. Jun, S. Yoo, O. Gwon, J. Shin, and G. Kim, “Thermodynamic and electrical properties of $Ba_{0.5}Sr_{0.5}Co_{0.8}Fe0.2O_{3-\delta}$ and $La_{0.6}Sr_{0.4}Co_{0.2}Fe_{0.8}O_{3-\delta}$ for intermediate-temperature solid oxide fuel cells,” *Electrochim. Acta*, vol. 89, pp. 372–376, 2013.

[160] R. Li, L. Ge, S. He, H. Chen, and L. Guo, “Effect of B_2O_3-Bi_2O_3-PbO frit on the performance of $LaBaCo_2O_{5+\delta}$ cathode for intermediate-temperature solid oxide fuel cells,” *Int. J. Hydrogen Energy*, vol. 37, no. 21, pp. 16117–16122, 2012.

[161] K. Zhang, L. Ge, R. Ran, Z. Shao, and S. Liu, “Synthesis , characterization and evaluation of cation-ordered $LnBaCo_2O_{5+\delta}$ as materials of oxygen permeation membranes and cathodes of SOFCs,” *Acta Mater.*, vol. 56, pp. 4876–4889, 2008.

[162] Q. Zhou, F. Wang, Y. Shen, and T. He, “Performances of $LnBaCo_2O_{5+x}$-$Ce_{0.8}Sm_{0.2}O_{1.9}$ composite cathodes for intermediate-temperature solid oxide fuel cells,” *J. Power Sources*, vol. 195, no. 8, pp. 2174–2181, 2010.

[163] J. Lee, H. Moon, H. Lee, J. Kim, and K. Yoon, “Quantitative analysis of microstructure and its related electrical property of SOFC anode, Ni–YSZ

cermet," *Solid State Ionics*, vol. 148, pp. 15–26, 2002.

[164] J. C. Ruiz-Morales, J. Canales-Vázquez, D. Marrero-López, J. T. S. Irvine, and P. Núñez, "Improvement of the electrochemical properties of novel solid oxide fuel cell anodes, $La_{0.75}Sr_{0.25}Cr_{0.5}Mn_{0.5}O_{3-\delta}$ and $La_4Sr_8Ti_{11}Mn_{0.5}Ga_{0.5}O_{37.5-\delta}$, using Cu–YSZ-based cermets," *Electrochim. Acta*, vol. 52, pp. 7217–7225, 2007.

[165] E. Lay, L. Dessemond, and G. Gauthier, "Synthesis and characterization of $Ce_xSr_{1-x}Cr_{0.5}Mn_{0.5}O_{3-\delta}$ perovskites as anode materials for solid oxide fuel cells (SOFC)," *Electrochimica Acta*, vol. 216. pp. 420–428, 2016.

[166] A. A. Yaremchenko, A. V. Kovalevsky, and V. V. Kharton, "Mixed conductivity, stability and electrochemical behavior of perovskite-type $(Sr_{0.7}Ce_{0.3})_{1-x}Mn_{1-y}Cr_yO_{3-\delta}$," *Solid State Ionics*, vol. 179, no. 38, pp. 2181–2191, 2008.

[167] Z. Han, Y. Wang, Y. Yang, L. Li, Y. Zhibin, and M. Han, "High-performance SOFCs with impregnated $Sr_2Fe_{1.5}Mo_{0.5}O_{6-\delta}$ anodes toward sulfur resistance," *J. Alloys Compd.*, vol. 703, pp. 258–263, 2017.

[168] Z. Yang, Y. Yang, Y. Chen, Y. Liu, T. Zhu, M. Han, and F. Chen, "Low temperature co-sintering of $Sr_2Fe_{1.5}Mo_{0.5}O_{6-\delta}$ – $Gd_{0.1}Ce_{0.9}O_{2-\delta}$ anode-supported solid oxide fuel cells with Li_2O–$Gd_{0.1}Ce_{0.9}O_{2-\delta}$ electrolyte," *J. Power Sources*, vol. 297, pp. 271–275, 2015.

[169] J. C. Ruiz-Morales, D. Marrero-López, J. Canales-Vázquez, and J. T. S. Irvine, "Symmetric and reversible solid oxide fuel cells," *RSC Adv.*, vol. 1, pp. 1403–1414, 2011.

[170] J. C. Ruiz-Morales, J. Canales-Vázquez, D. Marrero-López, D. Pérez-Coll, J. Peña-Martínez, and P. Núñez, "An all-in-one flourite-based symmetrical solid oxide fuel cell," *J. Power Sources*, vol. 177, no. 1, pp. 154–160, 2008.

[171] J. C. Ruiz-Morales, J. Canales-Vázquez, J. Peña-Martínez, D. M. López, and P. Núñez, "On the simultaneous use of $La_{0.75}Sr_{0.25}Cr_{0.5}Mn_{0.5}O_{3-\delta}$ as both anode and cathode material with improved microstructure in solid oxide fuel cells," *Electrochim. Acta*, vol. 52, no. 1, pp. 278–284, 2006.

[172] J. C. Ruiz-Morales, J. Canales-Vázquez, C. Savaniu, D. Marrero-López, W. Zhou, and J. T. S. Irvine, "Disruption of extended defects in solid oxide fuel cell anodes for methane oxidation.," *Nature*, vol. 439, pp. 568–571, 2006.

[173] E. C. Miller, Z. Gao, and S. A. Barnett, "Fabrication of solid oxide fuel cells with a thin $(La_{0.9}Sr_{0.1})_{0.98}(Ga_{0.8}Mg_{0.2})O_{3-\delta}$ electrolyte on a Sr0.8La0.2TiO 3 support," *Fuel Cells*, vol. 13, no. 6, pp. 1060–1067, 2013.

[174] D. P. Fagg, V. V Kharton, J. R. Frade, and a a L. Ferreira, "Stability and mixed ionic- electronic conductivity of (Sr,La)(Ti, Fe)$O_{3-\delta}$ (LSTF) perovskites," *Solid State Ionics*, vol. 156, pp. 45–57, 2003.

[175] J. Canales-Vázquez, J. C. Ruiz-Morales, D. Marrero-López, J. Peña-Martínez, P. Núñez, and P. Gómez-Romero, "Fe-substituted (La,Sr)TiO_3 as potential electrodes for symmetrical fuel cells (SFCs)," *J. Power Sources*, vol. 171, no. 2, pp. 552–557, 2007.

[176] F. Napolitano, A. L. Soldati, J. Geck, D. G. Lamas, and A. Serquis, "Electronic and structural properties of $La_{0.4}Sr_{0.6}Ti_{1-y}Co_yO_{3\pm\delta}$ electrode materials for symmetric SOFC studied by hard X-ray absorption spectroscopy," *Int. J.*

Hydrogen Energy, vol. 38, no. 21, pp. 8965–8973, 2013.

[177] R. Martínez-Coronado, A. Aguadero, D. Pérez-Coll, L. Troncoso, J. A. Alonso, and M. T. Fernández-Díaz, "Characterization of $La_{0.5}Sr_{0.5}Co_{0.5}Ti_{0.5}O_{3-\delta}$ as symmetrical electrode material for intermediate-temperature solid-oxide fuel cells," *Int. J. Hydrogen Energy*, vol. 37, pp. 18310–18318, Dec. 2012.

[178] D. Tian, B. Lin, Y. Yang, Y. Chen, X. Lu, Z. Wang, W. Liu, and E. Traversa, "Enhanced performance of symmetrical solid oxide fuel cells using a doped ceria buffer layer," *Electrochim. Acta*, vol. 208, pp. 318–324, 2016.

[179] J. Zhou, Y. Chen, G. Chen, K. Wu, and Y. Cheng, "Evaluation of $La_xSr_{2-x}FeO_4$ layered perovskite as potential electrode materials for symmetrical solid oxide fuel cells," *J. Alloys Compd.*, vol. 647, pp. 778–783, 2015.

[180] J. Lu, Y. M. Yin, J. Li, L. Xu, and Z. F. Ma, "A cobalt-free electrode material $La_{0.5}Sr_{0.5}Fe_{0.8}Cu_{0.2}O_{3-\delta}$ for symmetrical solid oxide fuel cells," *Electrochem. commun.*, vol. 61, pp. 18–22, 2015.

[181] C. Su, W. Wang, M. Liu, M. O. Tadé, and Z. Shao, "Progress and prospects in symmetrical solid oxide fuel cells with two identical electrodes," *Adv. Energy Mater.*, vol. 5, no. 14, pp. 1–19, 2015.

[182] J. C. Ruiz-Morales, J. Canales-Vázquez, B. Ballesteros-Pérez, J. Peña-Martínez, D. Marrero-López, J. T. S. Irvine, and P. Núñez, "LSCM-(YSZ-CGO) composites as improved symmetrical electrodes for solid oxide fuel cells," *J. Eur. Ceram. Soc.*, vol. 27, no. 13–15, pp. 4223–4227, 2007.

[183] Q. Liu, X. Dong, G. Xiao, F. Zhao, and F. Chen, "A novel electrode material for symmetrical SOFCs," *Adv. Mater.*, vol. 22, no. 48, pp. 5478–5482, 2010.

[184] Z. Ma, C. Sun, C. Ma, H. Wu, Z. Zhan, "Ni doped $La_{0.6}Sr_{0.4}FeO_{3-\delta}$ symmetrical electrode for solid oxide fuel cells," *Chinese J. Catal.*, vol. 37, no. 8, pp. 1347–1353, 2016.

[185] X. Zhu, Z. Lü, B. Wei, X. Huang, Y. Zhang, and W. Su, "A symmetrical solid oxide fuel cell prepared by dry-pressing and impregnating methods," *J. Power Sources*, vol. 196, no. 2, pp. 729–733, 2011.

[186] G. Yang, C. Su, R. Ran, M. O. Tade, and Z. Shao, "Advanced symmetric solid oxide fuel cell with an infiltrated K_2NiF_4-type La_2NiO_4 electrode," *Energy & Fuels*, vol. 28, no. 1, pp. 356–362, 2014.

[187] W. Fan, Z. Sun, J. Zhou, K. Wu, and Y. Cheng, "Characterization of Sr/Ru co-doped ferrite based perovskite as a symmetrical electrode material for solid oxide fuel cells," *J. Power Sources*, vol. 348, pp. 94–106, 2017.

[188] X. Lu, Y. Yanga, Y. Ding, Y. Chen, Q. Gu, D. Tian, W. Yuc, and B. Lin, "Mo-doped $Pr_{0.6}Sr_{0.4}Fe_{0.8}Ni_{0.2}O_{3-\delta}$ as potential electrodes for intermediate-temperature symmetrical solid oxide fuel cells," *Electrochim. Acta*, vol. 227, pp. 33–40, 2017.

[189] J. Shen, G. Yang, Z. Zhang, M. O. Tadé, W. Zhou, and Z. Shao, "Improved performance of a symmetrical solid oxide fuel cell by swapping the roles of doped ceria and $La_{0.6}Sr_{1.4}MnO_{4+\delta}$ in the electrode," *J. Power Sources*, vol. 342, pp. 644–651, 2017.

CHAPTER 2

PRELIMINARY STUDY OF THE RUDDLESDEN-POPPER $RE_xA_{2-x}MnO_{4\pm\delta}$ FAMILY (RE: La, Nd AND A: Sr, Ca)

The materials considered in this chapter have the general formula $RE_xA_{2-x}MnO_{4\pm\delta}$ (RE: La, Nd and A: Sr, Ca); they are n=1 members of the Ruddlesden-Popper manganites of general stoichiometry $A_{n+1}Mn_nO_{3n+1}$ (A being a rare earth or an alkaline earth) and present the K_2NiF_4-type structure (see Chapter 1, section 1.3.2). These compounds will be studied as possible electrode materials for symmetrical Solid Oxide Fuel Cells (SOFCs). Indeed, finding a material able to withstand both oxidizing and highly reducing atmospheres and, at the same time, to satisfy properties such as sufficient electronic conductivity, compatibility with electrolyte material, and good electrochemical activity is a real challenge.

2.1 INTRODUCTION

In recent years, the interest in developing symmetrical solid oxide fuel cells (SOFCs) has motivated the exploration of new materials, with preferably MIEC behavior in oxidizing and reducing conditions (cathodic and anodic) [1]. A MIEC material presents the advantage to make the SOFC reactions extend over the entire surface of the electrode [2][3]; this is basically an electron conductor in which the formation of oxygen defects (oxygen vacancies or extra-framework oxygen atoms) enables the conduction of ionic charge carriers. Famous examples of MIEC materials that have been developed for SOFC cathode and anode are doped $LaCoO_3$ [4], $(Ba,Sr)(Co,Fe)O_3$ [5], $RE_2NiO_{4+\delta}$ (RE=La, Nd, Pr) [6][7] or $REBaCo_2O_{5+\delta}$ (RE = Nd, Gd,…) [8] on one hand, and pure or doped $La_{0.75}Sr_{0.25}Cr_{0.5}Mn_{0.5}O_{3-\delta}$ (LSCM) [9][10], on the other hand.

The materials described in this chapter are the first term (n=1) of the RP series, which can be described as the succession of *n* ABO_3 perovskite layers separated by a single rock salt-like AO layer (Figure 12). This structure can accommodate a significant amount of non-stoichiometric oxygen, which could favor the transport properties, in particular of oxide ions [11].

Figure 12. Crystal structure of A_2MnO_4, depicting atomic positions and bonds.

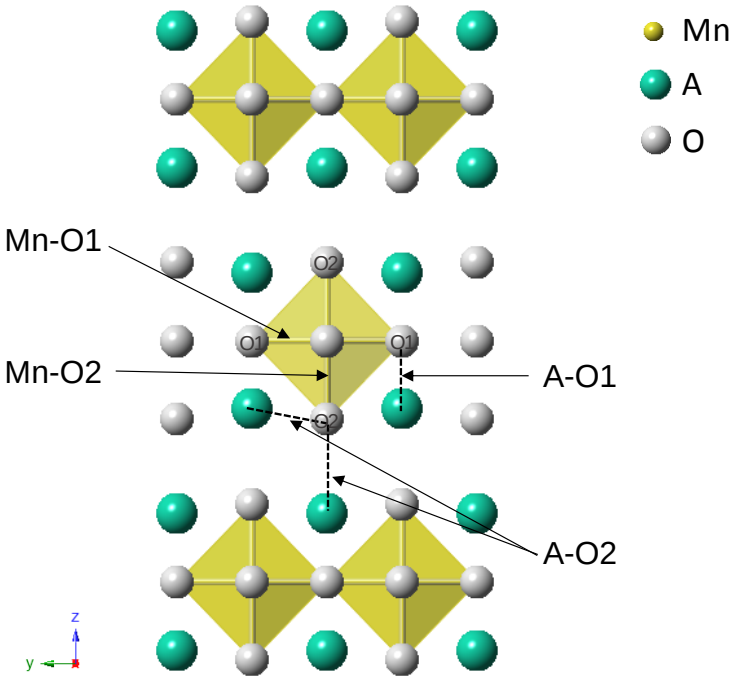

Our interest for the Ruddlesden-Popper manganites derived from their improved stability under reducing conditions, compared to that of the parent perovskites [10][12]. For example, based on neutron diffraction studies, it has been found that manganites such as $La_{0.8}Sr_{1.2}Co_{0.5}Mn_{0.5}O_{4-\delta}$ [13] and $Pr_{0.5}Sr_{1.5}Cr_{0.5}Mn_{0.5}O_{4-\delta}$ [14] heated in a reducing atmosphere can create oxygen ion vacancies via manganese reduction, keeping the crystal structure unchanged (*I4/mmm*).

The $La_xSr_{2-x}MnO_{4\pm\delta}$ series ($0 \leq x \leq 1.4$) has been recently studied by Munnings *et al.* as cathode materials, reporting good stability until 800 °C in air, thermal expansion coefficients comparable with yttria-stabilized zirconia (YSZ) and gadolinium-doped ceria (GDC) electrolytes and a moderate electrical conductivity with a maximum of ~ 6 S cm^{-1} for x=0.2 at 900 °C in air [15]. In addition, different members of the $La_xSr_{2-x}MnO_{4\pm\delta}$ (x= 0.4, 0.5, 0.6) [16] and $La_xSr_{1.5}MnO_4$ (x=0.35, 0.4, 0.45) [17] series revealed suitable electrochemical properties for use as cathode materials. For example, using $La_{0.35}Sr_{1.5}MnO_4$ as cathode and GDC as electrolyte, the polarization

resistance value obtained at 750 °C was 0.25 Ω cm^2. Very recently, it was also demonstrated that $La_{0.6}Sr_{1.4}MnO_{4\pm\delta}$ compound could be considered as a good candidate for electrode application in intermediate-temperature symmetrical solid oxide fuel cells (IT-SSOFCs), due to sufficient stability in both oxidizing and reducing atmospheres, thermo-mechanically compatibility with $Sm_{0.2}Ce_{0.8}O_{1.9}$ (SDC) and $La_{0.8}Sr_{0.2}Ga_{0.83}Mg_{0.17}O_{3-\delta}$ (LSGM) electrolytes and acceptable electrochemical properties in air and hydrogen, with a polarization resistance in air of about 0.87 Ω cm^2, against 2.07 Ω cm^2 in 5% H_2 [18][19][20].

On the other hand, the studies concerning $RE_xCa_{2-x}MnO_{4\pm\delta}$ materials (RE = Pr, Nd, Sm, Gd, Ho) that also exhibit a K_2NiF_4-type structure, have been focused mainly on the evaluation of their magnetic, electrical, magnetoresistance and charge ordering properties [21][22][23]. The structural description of some of these compounds has been reported: Tlili *et al.* described that $Pr_xCa_{2-x}MnO_4$ ($0 \leq x \leq 0.2$) compounds possesses a tetragonal structure for Ca_2MnO_4 that turns orthorhombic with Pr-doping [24]. Besides, the structure of $Gd_xCa_{2-x}MnO_4$ ($0 \leq x \leq 0.45$) [25] and $Nd_xCa_{2-x}MnO_4$ ($0 \leq x \leq 0.45$) [26] presents also different types of orthorhombic distortion, depending on the degree of substitution at the Ca site. However, to the best of our knowledge, neither the stability of those substituted materials in reducing atmosphere at high temperature nor they application as SOFC electrode has been extensively studied.

In this chapter, we report on the synthesis and preliminary study of the $RE_xA_{2-x}MnO_{4\pm\delta}$ compounds (RE: La, Nd and A: Sr, Ca) to define a range of compositions that could be used for a future optimization of composition vs. performance as electrode materials for symmetrical SOFC. In addition, the different substitutions at the A-site were aimed either to improve the stability in reducing conditions or to diminish the eventual reactivity with the electrolyte materials, since according to the literature such reactivity can partly depends on the characteristics of rare-earth element [27][28][29]. Considering the influence of heat treatments on the cost of the

cells, the materials synthesis was always carried out in air at the lowest temperature and the structural characterizations were performed by Rietveld refinement using X-ray Powder Diffraction data (XRPD). The stability in reducing atmosphere (3% H_2/N_2) of the as-obtained compounds was studied to select the candidates that fulfill the basic requirements for use as anode and thus as electrode for symmetrical cells. The redox and thermomechanical behavior of those materials was further examined by HT-XRD in both cathodic and anodic conditions. The total electrical conductivity in air and hydrogen were measured. In addition, we used thermogravimetrical analyses and *in situ* Neutron Powder Diffraction (NPD) to extract detailed information concerning changes in Mn oxidation state and oxygen vacancies formation during reduction.

2.2 SYNTHESIS AND CHARACTERIZATION

The main goal of this section is to study the limit of solubility of lanthanum and neodymium in the $(Sr/Ca)_2MnO_{4\pm\delta}$ matrices. The materials have been synthesized in air using solid state reaction or sol-gel method. The initial structural characterizations were performed by X-ray Powder Diffraction (XRPD), looking for the formation of single phases at the lowest temperature.

2.2.1 EXPERIMENTAL SECTION

2.2.1.1 Materials Synthesis

The oxide materials derived from the perovskite structure can be synthesized using different preparative routes, which play a critical role on the physical and chemical properties of the reaction products, controlling the structure and microstructure (morphology, grain size and surface area) of the obtained materials. There are

several methods available to prepare the target compounds: coprecipitation, sol gel, Pechini method, etc [30].

The solid-state reaction (SS) is the most widely used method for the synthesis of polycrystalline bulk manganites. It consists in directly reacting the precursors (oxides and/or carbonates) using one or several successive high temperature heat treatments to obtain a single compound, after intermediately homogenization and grain size reduction steps using mechanical grinding. This method is environmentally friendly (except for the high energy consumption it sometimes requires) and, generally, no toxic or unwanted waste is produced after the reaction is complete. The disadvantage of this method is that it usually requires several steps of grinding and calcination at high temperature and leads generally to large size of particles (a few tens of microns). In the case of the wet chemical synthetic methods such as sol-gel (SG), the main aim is the accelerating the single phase formation. Thus, the goal is achieved due to the liquid media which permits a perfect mixing of the elements at the atomic level resulting in lower firing temperatures. Other advantages of SG method are the possibility of having controlled particle size, morphology and improvement of the surface area [31][32][33][34].

In this work, we used two types of synthesis route; SS technique was first chosen for reasons of simplicity and allows to define the range of compositions obtainable in air within the $Sr_{2-x}La_xMnO_{4\pm\delta}$ series. Nevertheless, SG route was used afterwards due to limitations of sintering, especially considering that the RP manganites were presenting a limit of temperature beyond which a chemical decomposition was occurring. Moreover, the SG technique was selected to obtain powders with low particle size that would facilitate the subsequent steps of cell preparation as well as favor the electrocatalytic properties of the materials.

In both cases, before using, La_2O_3 and Nd_2O_3 precursors were calcined at 1000°C, $SrCO_3$ at 500°C and $CaCO_3$ at 200°C for 1 hour. Such pre-treatments were

performed to remove hydration products (and carbonation in the case of lanthanum and neodymium oxides) in order to facilitate the weighing of the precursors in stoichiometric proportions.

Solid-State Reaction Method

$La_xSr_{2-x}MnO_{4\pm\delta}$ (0, 0.25, 0.4, 0.5, 0.6 and 0.7) powders were prepared by traditional solid state reaction. The range of compositions was chosen in order to obtain materials that can be easily prepared in air, phases with higher lanthanum content requiring reducing conditions (more complex, expensive, dangerous…) such as flowing diluted hydrogen to be prepared [35]. Stoichiometric amounts of La_2O_3 (Alfa Aesar 99.99%), $SrCO_3$ (Sigma Aldrich 99.9%) and $MnCO_3$ (Sigma Aldrich 99.9%) were mixed and milled in an agate mortar for 2 hours. The resulting powders were uniaxially pressed into pellets of approximately 10 mm diameter. The powders were calcined using three successive heating cycles at 1300 °C for 6h for the compositions where x≥0.25, and at 1500°C for 12h for x=0, performing intermediate grinding steps in all cases.

Sol Gel synthesis using Citrate-Nitrate technique

$RE_xA_{2-x}MnO_{4\pm\delta}$ (RE: La, Nd and A: Sr, Ca) powders were also prepared by the citric acid sol gel method (also referred to as the citrate-nitrate sol-gel method), using Nd_2O_3 (Alfa Aesar 99.9%), $CaCO_3$ (Alfa Aesar 99.5%) and the same precursors as mentioned above. These precursors were dissolved in an excess (two times the amounts corresponding to the stoichiometric conversion of oxides/carbonate into nitrates) of nitric acid HNO_3 (Merck ≥65%) and citric acid (CA, Merck ≥99.5%) added in a molar ratio of CA:(metal) = 3:1. The process is illustrated graphically in Figure 13.

Figure 13. Synthesis process by sol gel method.

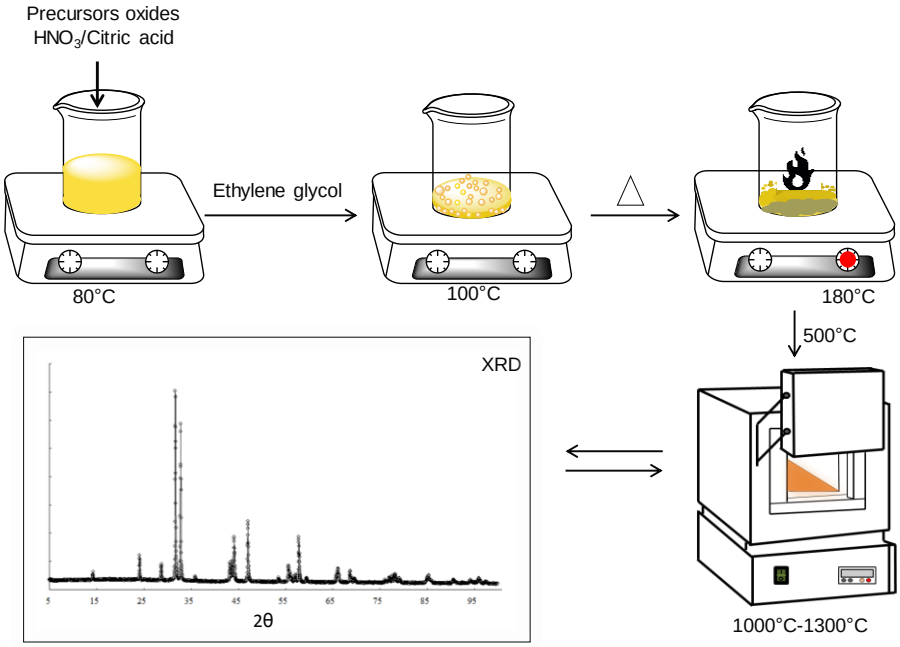

The solution was stirred and heated at 90°C, and, subsequently, polyethylene glycol (≥99%, Panreac) was added as polymerization agent, in a proportion of 1.5 mL per gram of targeted product. The heating was kept over several hours until all water has been evaporated and the polymerized complex started to form. The resulting mixture was heated at 180 °C and a viscous gel was obtained which was subsequently calcined at ~300 °C in air for about 3 h, then brought to ~500 °C to ensure total organic matter decomposition. Finally, the samples were pressed into a pellet, and then sintered in air at 1100°C during 6 h using two successive heating cycles, with intermediate grinding and pelletizing steps.

2.2.1.2 Structural Characterization

The samples were characterized by powder X-ray diffraction (XRD) using a Bruker D8 ADVANCE powder diffractometer working in Bragg Brentano geometry with Cu-$K_{\alpha 1,2}$ radiation and Lineal LynxEye detector. The diffractometer was operated over the angular range 2θ=2°-70° for qualitative analysis and 2θ=2°-90° for Rietveld

analysis, using a step size of 0.02° in 2θ and acquisition time of 1 s/step. The qualitative identification of crystalline phases was performed by comparing the measured profile reflections with the diffraction profiles reported in the Powder Diffraction File (PDF-2) database of the International Center of Diffraction Data (ICDD), using Crystallographica Search-Match Software [36]. Based on those XRD data, structural information was extracted by LeBail or Rietveld refinement using the FullProf Suite program and its graphical interface WinPLOTR [37] or Jana-2006 program [38].

2.2.1.3 Iodometric Titration

In iodometric titrations, the analyte/powder (an oxidizing agent) reacts with an unmeasured excess of iodide to produce iodine (I_2). The iodine produced in this reaction is stoichiometrically related to the amount of analyte originally present in the sample. The iodine may then be titrated to determine the analyte concentration in the sample. The nearly universal titrant for iodine is thiosulfate; the stoichiometry equation of the iodometric reaction is as follows (Figure 14):

$$2S_2O_3^{2-}{}_{(aq)} + I_2 \rightarrow S_4O_6^{2-}{}_{(aq)} + 2I^-{}_{(aq)} \quad (2\text{-}16)$$

Figure 14. Iodometric titration assembly.

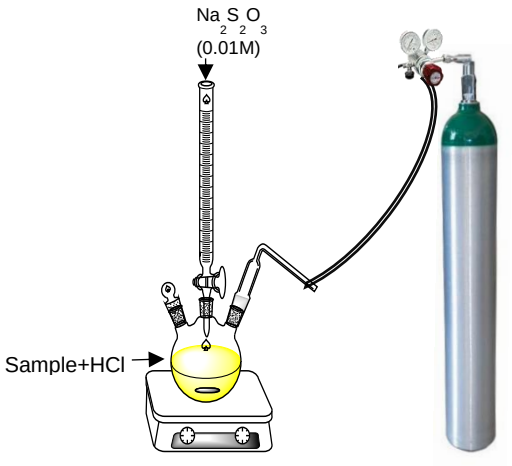

The titration procedure is used according to the following description [39]. Initially, 40 mL of concentrated HCl solution is introduced in a three-neck angled round bottom flask, to allow the use of argon flow during the reaction and avoid contact with the atmosphere while maintaining a constant bubbling, 0.3 g of KI is introduced. Posteriorly, 0.02 g of powder (dried at 150°C) is added and completely dissolved (the solution turns yellow). Later, the standard 0.01 M $Na_2S_2O_3$ solution is added dropwise until the solution turns pale yellow. Finally, 0.03 g of starch (the solution turns faint blue) is added to continue the titration with higher precision, a complete discoloration indicating the equilibrium point. Such procedure was performed in triplicate for each composition. With the previously results, the oxygen stoichiometry and the manganese oxidation state were determined.

2.2.2 RESULTS

2.2.2.1 $La_xSr_{2-x}MnO_{4\pm\delta}$ series

The powder XRD patterns of $La_xSr_{2-x}MnO_{4\pm\delta}$ (0, 0.25, 0.4, 0.5, 0.6 and 0.7) synthesized by solid state reaction are shown in Figure 15. The $0.25 \leq x \leq 0.6$ compositions were obtained as single phases by heating at 1300°C in air. However, the x=0 and x=0.7 compositions were not obtained as single phases under these conditions. For x=0, even after increasing the temperature up to 1500 °C, a small impurity of $Sr_7Mn_4O_{15}$ was still observed. Beyond the x=0.6 composition, all synthesis attempts were found unsuccessful in air and the x=0.7 sample already presents peaks of $(La,Sr)_3Mn_2O_7$ impurity.

Figure 15. XRD patterns of $La_xSr_{2-x}MnO_{4\pm\delta}$ (x=0, 0.25, 0.4, 0.5, 0.6, 0.7) after synthesis in air. In inset, zoom on (1) $Sr_7Mn_4O_{15}$ and (2) $(La,Sr)_3Mn_2O_7$ impurities for x=0 and 0.7, respectively.

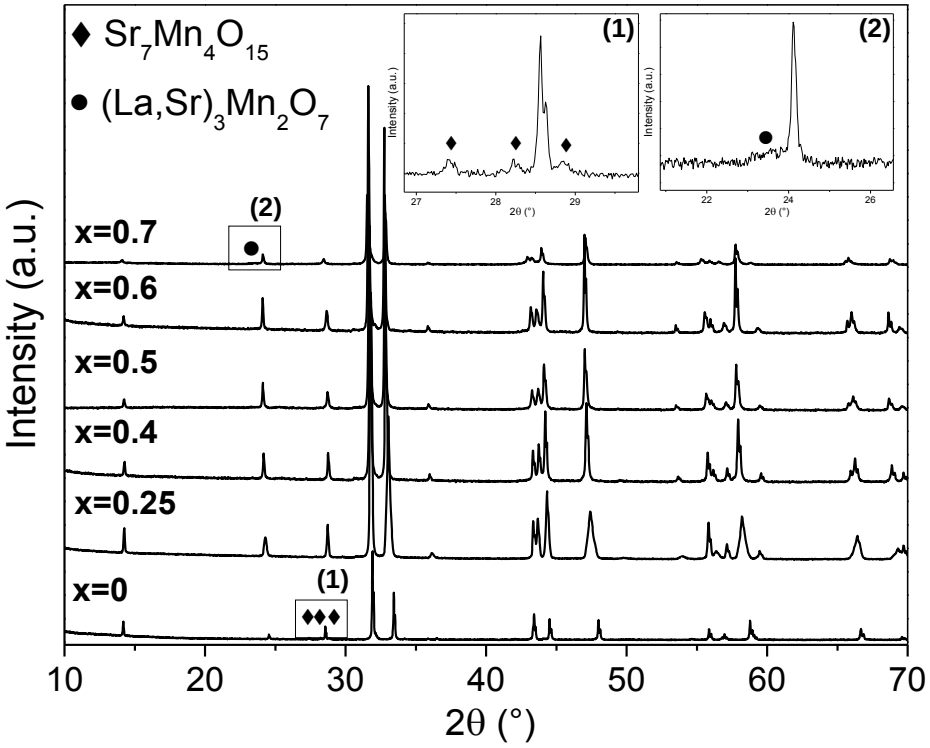

The XRD patterns were indexed in a tetragonal unit cell with *I4/mmm* space group and Rietveld refinements were carried out using the easiest structural model of RP n=1 materials (The graphical results of refinements are shown in Annex 1). The evolution of the cell parameters and oxidation state of manganese are displayed in Figure 16. The results of refinements are shown in Table *3*. The values for the as-synthesized powders are in acceptable agreement with literature, for example, for x=0.5 the parameters reported are a= 3.863 Å and 12.421 Å and the obtained here 3.8616(2) Å and 12.4211(11) Å [16][17][40].

Figure 16. Evolution of cell parameters of $La_xSr_{2-x}MnO_{4\pm\delta}$ (x= 0, 0.25, 0.4, 0.5, 0.6) synthesized by solid state reaction.

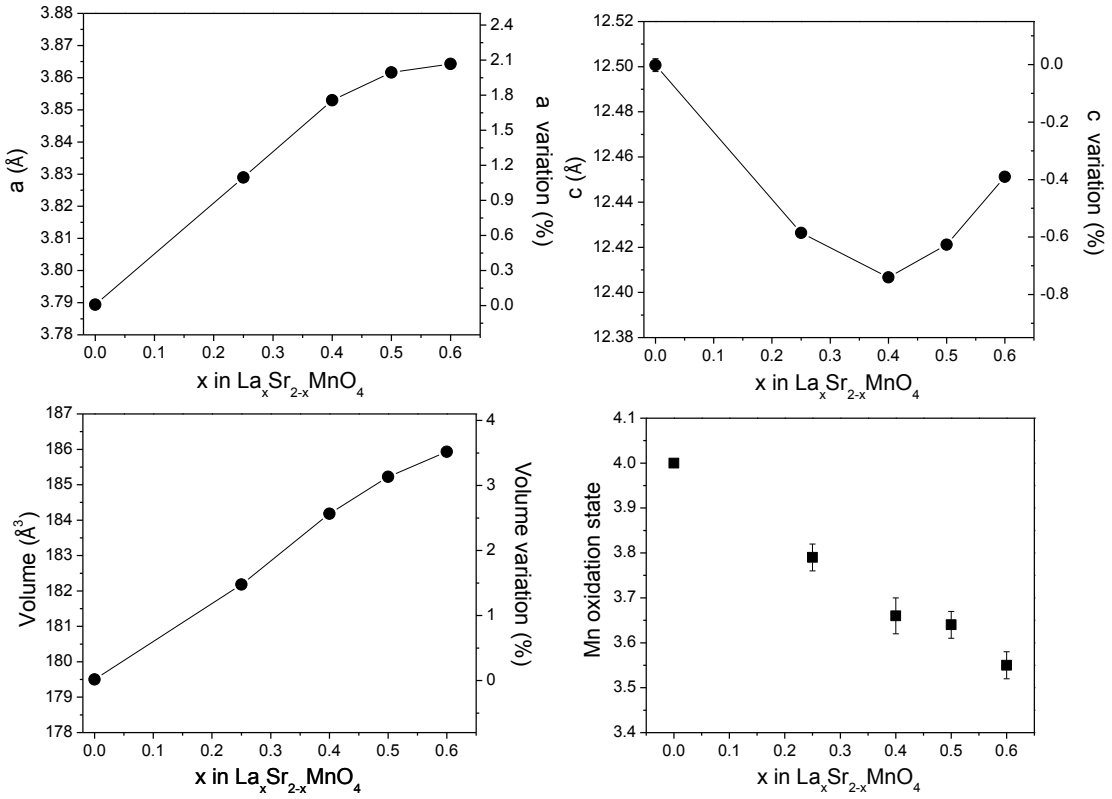

As observed in Table 3 and Figure 16, the *a* parameter and lattice volume progressively increase with the lanthanum concentration, what can be explained by the fact that the substitution of La^{3+} for Sr^{2+} is compensated by a decrease of the average oxidation state of Mn, changed from Mn^{4+} ($R^{VI}_{Mn^{4+}}$= 0.53 Å [41]) to Mn^{3+} ($R^{VI}_{Mn^{3+}}$= 0.645 Å [41]), as confirmed by iodometric titration. The large ionic radius of Mn^{3+} generates a significant variation of the *a* parameter (~1.8%) between x=0 and x=0.4, associated to the increase of the Mn-O1 bond length (Table 3) [42]. For x≥0.4, the *a* parameter variation is less pronounced, probably due to the similarity in the average oxidation state of manganese that remains *ca.* +3.6. The behavior of the *c* parameter is less evident along the series with a decrease of ~0.8% between x=0 and x=0.4, while for x>0.4 it begins to increase again. Such variation is indeed the convolution of at least two effects (i) the decrease of the average oxidation state of

Mn and concomitant increase of Mn-O2 bond length and (ii) the substitution of the Sr^{2+} cation ($R^{IX}_{Sr^{2+}}$= 1.31 Å [41]) by the smaller La^{3+} cation ($R^{IX}_{La^{3+}}$= 1.216 Å [41]) that leads to a decrease of the La/Sr-O2 bond length or shrinking of the rock salt layer.

Table 3. Structural parameters and selected bond lengths (Å) for $La_xSr_{2-x}MnO_{4\pm\delta}$ (x=0, 0.25, 0.4, 0.5, 0.6) calculated by Rietveld refinement from powder X-ray diffraction data (space group *I*4/*mmm*); estimated Mn oxidation states deduced from iodometric titration.

Sample	**S2MSS**	**L25S175MSS**	**L25S175MSS**	**L5S15MSS**	**L6S14MSS**
x	**0**	**0.25**	**0.4**	**0.5**	**0.6**
a (Å)	3.7894(7)	3.8289(3)	3.8529(1)	3.8616(2)	3.8643(2)
c (Å)	12.5007(28)	12.4263(13)	12.4067(5)	12.4211(11)	12.4511(10)
V(Å^3)	179.50(6)	182.18(3)	184.18(1)	185.22(2)	185.93(3)
R_p	5.58	6.19	3.18	4.07	3.87
R_{wp}	7.71	8.07	4.17	5.60	5.16
χ^2	2.1	1.8	2.3	2.0	1.8
Atom	Refined atomic positions (*x,y,z*)				
La/Sr	0, 0, 0.3566(2)	0, 0, 0.3563(1)	0, 0, 0.3571(6)	0, 0, 0.3570(1)	0, 0, 0.3574(7)
Mn	0, 0, 0	0, 0, 0	0, 0, 0	0, 0, 0	0, 0, 0
O1	0, 0.5, 0	0, 0.5, 0	0, 0.5, 0	0, 0.5, 0	0, 0.5, 0
O2	0, 0, 0.1560(1)	0, 0, 0.1602(7)	0, 0, 0.1608(4)	0, 0, 0.1617(5)	0, 0, 0.1605(5)
Mn-O1	1.89466(2) x 4	1.91448(2) x 4	1.92649(5) x 4	1.93080(10) x 4	1.93215(5) x 4
Mn-O2	1.950(10) x 2	1.991(10) x 2	1.995(5) x 2	2.009(7) x 2	1.999(6) x 2
La/Sr-O1	2.6081(13) x 4	2.6179(12) x 4	2.6181(5) x 4	2.6235(7) x 4	2.6233(6) x 4
La/Sr-O2	2.5078(19) x 1	2.437(10) x 1	2.435(5) x 1	2.426(7) x 1	2.452(6) x1
	2.6841(11) x 4	2.7153(7) x 4	2.7335(4) x4	2.7404(6) x 4	2.7417(5) x 4
Mn-O1/Mn-O2	0.972	0.962	0.966	0.961	0.967
Mn oxidation state	+4	+3.79(3)	+3.66(4)	+3.64(3)	+3.55(3)

As mentioned earlier, to obtain the single phases $La_xSr_{2-x}MnO_{4\pm\delta}$ (0.25, 0.4, 0.5, 0.6) a high synthesis temperature (1300°C) was required. However, the high temperature preparation may afterward complicate the sintering and cell preparation. In order to decrease this temperature, we used also the citrate sol-gel method, described above. This methodology allows to obtain single phases using only two consecutive heating steps; at 1000 and 1100°C during 6 h. As seen in Figure 17, regardless of the method used, the compounds obtained exhibit the same structural parameters.

This procedure was finally used for the synthesis of all materials presented in this work (Table 7).

Figure 17. Evolution of cell parameters of $La_xSr_{2-x}MnO_{4\pm\delta}$ (x= 0.25, 0.4, 0.5, 0.6) synthesized by sol gel and solid-state method.

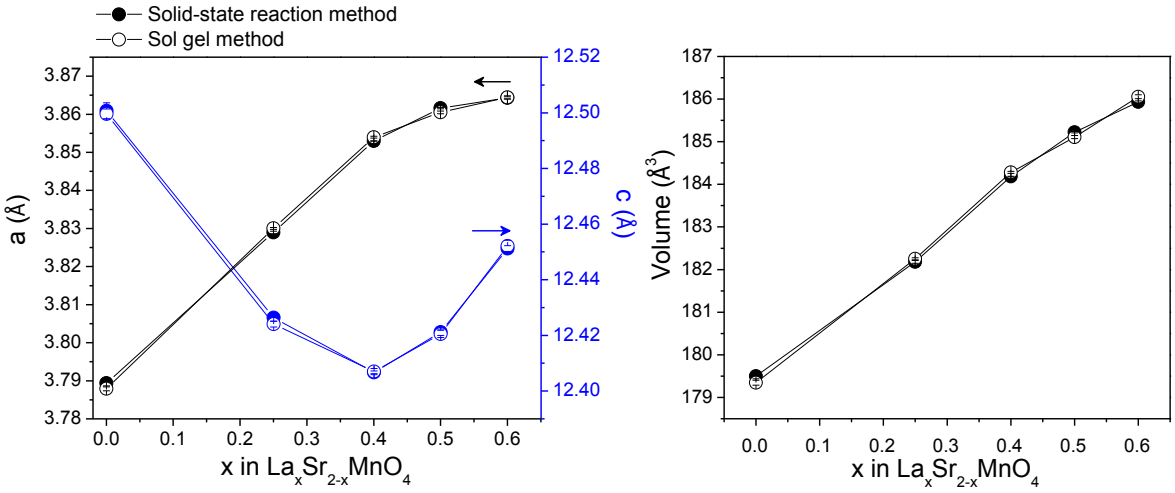

2.2.2.2 $Nd_xSr_{2-x}MnO_{4\pm\delta}$ series

Following the success of its use with the $La_xSr_{2-x}MnO_{4\pm\delta}$ series, the $Nd_xSr_{2-x}MnO_{4\pm\delta}$ manganites with x=0.25, 0.4, 0.5 and 0.6 were prepared by sol-gel reaction. According to the literature, $Nd_xSr_{2-x}MnO_{4\pm\delta}$ compounds with $0\leq x\leq 0.5$ have been prepared in the past by the coprecipitation technique using citric acid. However, to obtain single phases by such synthesis route, a heat treatment temperature of 1500°C for 24 h in O_2 atmosphere had been required [43][44][45]. In this work, we tried to prepare all the phases in air at lower temperature that would make the cell preparation easier.

Figure 18 shows the XRD patterns of the as-synthesized $Nd_xSr_{2-x}MnO_{4\pm\delta}$ powders obtained after two consecutive thermal cycles at 1000 and 1100°C for 6 h. Single phase $Nd_{0.4}Sr_{1.6}MnO_{4\pm\delta}$ (x= 0.4) and $Nd_{0.5}Sr_{1.5}MnO_{4\pm\delta}$ (x= 0.5) can be obtained after a heat treatment at 1100 °C. For x=0.25 and x=0.6, some impurities are detected in

the same conditions. Quantitative Rietveld refinement was used in all cases, the structure of the main RP phase being refined in the I4/*mmm* tetragonal space group, using the Jana-2006 program [38].

Figure 18. XRD patterns of $Nd_xSr_{2-x}MnO_{4\pm\delta}$ (x= 0.25, 0.4, 0.5, 0.6) after synthesis in air. In inset, zoom on Nd_2O_3 impurity in x=0.6 sample.

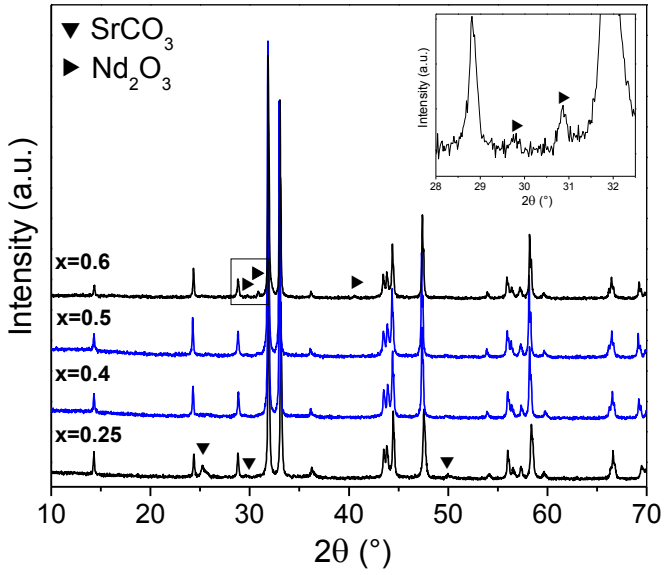

The results are all given in Table 4 (the graphical results of refinements are shown in Annex 1). The sample x= 0.25 contains a large amount of $SrCO_3$ impurity (~ 10.8 wt.%), even with increasing the temperature to 1200 °C. For x= 0.6, Nd_2O_3 is detected as a minor impurity (~0.9 wt.%). Thus, the solubility range of Nd^{3+} in $Nd_xSr_{2-x}MnO_{4\pm\delta}$ is found as $0.25 < x < 0.6$ using synthesis in air, the lower and upper limits being probably not far from x=0.25 and x=0.6 themselves, especially for the upper limit.

As observed in Table 4, the substitution of strontium by neodymium leads to a smooth increase in the *a* parameter, while the *c* parameter first decreases then increases as a function of x, in a similar way as it makes in the case of La-substitution. The comparison of the lattice parameters of $La_xSr_{2-x}MnO_{4\pm\delta}$ and Nd_xSr_{2-}

$_xMnO_{4\pm\delta}$ series (Table 4) makes it evident that both series show the same kind of behavior, independently of the ionic size of lanthanide at the A-site, as demonstrated for the $R_{0.5}Sr_{1.5}MnO_{4\pm\delta}$ (R: La, Pr, and Nd) compounds [45].

Table 4. Structural parameters and selected bond lengths (Å) for $Nd_xSr_{2-x}MnO_{4\pm\delta}$ (x= 0.25, 0.4, 0.5, 0.6) calculated by Rietveld refinement from powder X-ray diffraction data (space group *I*4/*mmm*).

Sample	**N25S175M**	**N4S16M**	**N5S15M**	**N6S14M**
x	**0.25#**	**0.4**	**0.5**	**0.6***
Crystal system	Tetragonal	Tetragonal	Tetragonal	Tetragonal
Space group	*I*4/*mmm*	*I*4/*mmm*	*I*4/*mmm*	*I*4/*mmm*
Z	2	2	2	2
a (Å)	3.8233(2)	3.8359(2)	3.8395(2)	3.8389(2)
c (Å)	12.3923(7)	12.3659(8)	12.3779(9)	12.4087(10)
V (Å^3)	181.14(2)	181.96(2)	182.47(2)	182.86(2)
R_p	3.86	4.11	4.76	3.74
R_{wp}	4.85	5.19	6.27	5.28
χ^2	1.24	1.33	1.60	1.48
Impurity amount (wt.%)	$SrCO_3$ 10.8(4)			Nd_2O_3 0.9(3)
Atom	Refined atomic positions (*x,y,z*)			
Nd/Sr	0, 0, 0.3568(2)	0, 0, 0.3570(2)	0, 0, 0.3565(3)	0, 0, 0.3568(3)
Mn	0, 0, 0	0, 0, 0	0, 0, 0	0, 0, 0
O1	0, 0.5, 0	0, 0.5, 0	0, 0.5, 0	0, 0.5, 0
O2	0, 0, 0.1575(10)	0, 0, 0.1610(14)	0, 0, 0.1619(16)	0, 0, 0.164(2)
Mn-O1	1.9116(2) x 4	1.9180(2) x 4	1.9198(2) x 4	1.9194(2) x 4
Mn-O2	1.946(12) x 2	1.991(12) x 2	2.010(13) x 2	2.041(12) x 2
Nd/Sr-O1	2.6084(17) x 4	2.6088(17) x 4	2.615(3) x 4	2.616(3) x 4
Nd/Sr-O2	2.476(13) x 1	2.424(13) x 1	2.410(11) x 1	2.401(14) x 1
	2.7089(8) x 4	2.7216(10) x 4	2.725(2) x 4	2.727(2) x 4
Mn-O1/Mn-O2	0.982	0.963	0.955	0.940

$SrCO_3$ impurity

* Nd_2O_3 impurity

Figure 19. Evolution of cell parameters of $La_xSr_{2-x}MnO_{4\pm\delta}$ and $Nd_xSr_{2-x}MnO_{4\pm\delta}$ (x= 0.25, 0.4, 0.5, 0.6).

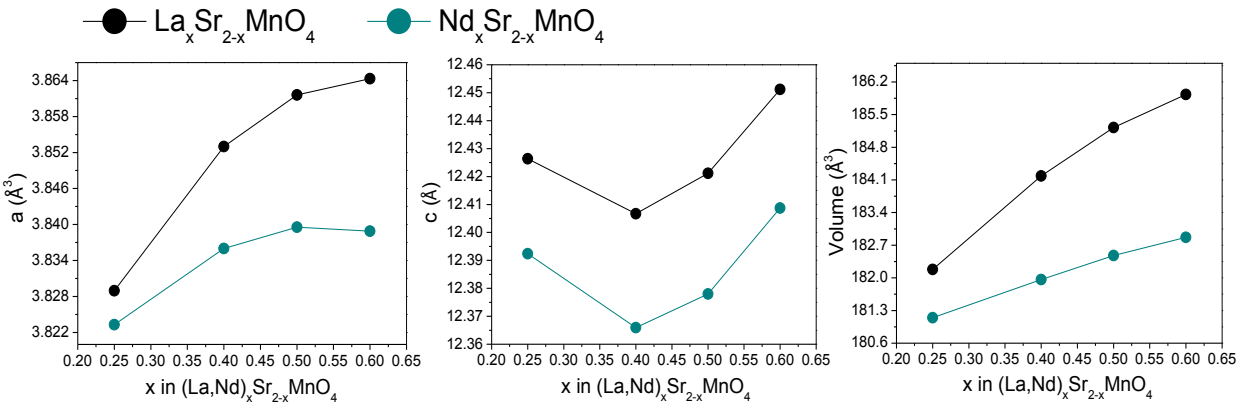

The only difference remains in the fact that the substitution of Sr by the smaller Nd^{3+} ($R^{IX}_{Nd^{3+}}$= 1.163 Å [41]) compared to La^{3+} ($R^{IX}_{La^{3+}}$= 1.216 Å [41]) tends to reduce the cell parameter values. Consequently, the substitution with La^{3+} alters more drastically the *a*-parameter than the substitution with Nd^{3+}, what could be also related to a lower degree of reduction of manganese for Nd (latter case) and not only an effect of ionic size. Nevertheless, the oxidation states of Mn was determined by iodometric titration and, for example, values of +3.64(3) and +3.67(4) were found for $La_{0.5}Sr_{1.5}MnO_{4\pm\delta}$ and $Nd_{0.5}Sr_{1.5}MnO_{4\pm\delta}$, respectively. So, it seems that the effect is mainly steric. In addition, the increase in the neodymium concentration or substitution of the small Nd^{3+} cation ($R^{IX}_{Nd^{3+}}$= 1.163 Å [41]) by the larger Sr^{2+} ($R^{IX}_{Sr^{2+}}$= 1.31 Å [41]) generates a notably decrease in the Nd/Sr-O2 bond lengths, which leads to the deformation of [MnO_6] octahedra, evidenced with the variation of Mn-O1/Mn-O2 ratio.

2.2.2.3 $La_xCa_{2-x}MnO_{4\pm\delta}$ series

Several studies of equilibrium systems have been used to explain the formation of the solid solutions of lanthanum and/or calcium manganese oxides. It is known that

in the La–Mn–O system (1200 °C) several phases are formed: La_2MnO_4, $LaMnO_3$ and $LaMn_7O_{12}$; however, La_2MnO_4 is stabilized only at low oxygen partial pressure [46]. On the other hand, in the Ca–Mn–O system many more compounds are evidenced: Ca_2MnO_4 (<1600 °C), $Ca_3Mn_2O_7$ (<1500 °C), $Ca_4Mn_3O_{10}$ (<1480 °C), $CaMnO_3$ (<1400 °C), $CaMn_2O_4$ (<1400 °C) and $CaMn_3O_6$ (<860 °C) [47]. The solubility of lanthanum has been considered in several studies of La–Ca–Mn–O phase diagrams [48][49][50]. The substitution of La for Ca takes place not only in $CaMnO_3$, but also in Ca_2MnO_4 and $Ca_3Mn_2O_7$, with a wide variety of compounds that coexist in equilibrium, including $LaMnO_3$ and different solid solutions of $La_{1-x}Ca_{1+x}MnO_4$ ($0.65 \leq x \leq 1.0$), and $La_{2-2x}Ca_{1+2x}Mn_2O_7$ ($0.50 \leq x \leq 1.0$) [48][49]. It is worth noting that these compounds have been generally prepared using solid state reaction. Using this information, attempts were made to confirm or improve the range of solubility of lanthanum in $La_xCa_{2-x}MnO_{4\pm\delta}$ using the sol gel method, for which the compositions with x= 0.15, 0.25 and 0.5 were prepared. Figure 20 shows the XRD patterns obtained after synthesis in air using two consecutive heating at 1000 and 1100 °C for 6 hours.

The XRD results reveal that for x= 0.15 and 0.25 the main phase is $La_xCa_{2-x}MnO_{4\pm\delta}$ with K_2NiF_4 structure. However, the sample with x=0.15 contains also $CaCO_3$ impurity (~1.7 wt %), whereas La_2O_3 impurity (~1 wt %) is detected in the sample with x=0.25. In the case of x=0.5, a single phase was not obtained; instead, several phases such as $(La,Ca)_3Mn_2O_7$, $La_{1-x}Ca_xMnO_3$ and CaO were identified.

Figure 20. XRD patterns of $La_xCa_{2-x}MnO_{4\pm\delta}$ (x= 0.15, 0.25, 0.5) after synthesis in air. In inset, zoom on (1) $CaCO_3$ and (2) La_2O_3 impurities in x=0.15 and 0.25 compositions, respectively.

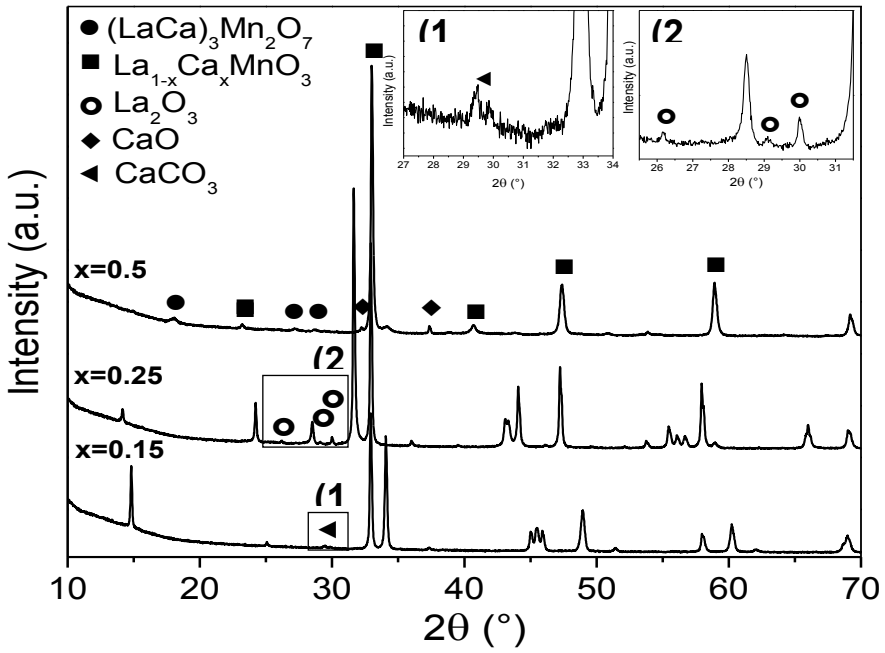

Considering that the materials were almost single phases, a Rietveld refinement for x=0.15 and 0.25 was performed to confirm the crystal structure of the main phase and quantify the impurities (Table 5). In the case of x=0.25, the structure was refined in the *I*4*/mmm* space group, with $a \approx 3.8472$ Å and $c \approx 12.5266$ Å. For x=0.15, initially, the refinement was carried out using a tetragonal cell with *I*4/*mmm* space group. However, convergence difficulties were observed using this model. Therefore, considering that the lanthanum substitution was low, the space group was changed to $I4_1/acd$ (a= 5.2631(2) Å and *c*= 23.9237(4) Å), which corresponds to the space group of the Ca_2MnO_4 phase [51]. Using the latter space group, the refinements quickly converged and a good fit was obtained. It confirms that the compound with low La content (x=0.15) has the same crystal structure than Ca_2MnO_4 ($I4_1/acd$), *i.e.* a doubling of the *c* parameter ($c \approx 23.9237$ Å) with respect to the non-distorted *I*4*/mmm* space group, *and* lattice parameters $a \approx b \approx a_p\sqrt{2}$ (a_p being the parameter of the perovskite unit cell). This doubling of the *c* parameter has been attributed to a

rotation of the octahedra in opposite directions around the *c*-axis, between two successive perovskite layers, as shown in Figure 21 [52]. This behavior has been reported also for other phases with low trivalent lanthanide content such as $RE_{0.08}Ca_{1.92}MnO_4$ series (with RE=La, Pr, Ho and Y) [53].

Table 5. Structural parameters for $La_xCa_{2-x}MnO_{4\pm\delta}$ (x= 0.15, 0.25) calculated by Rietveld refinement from powder X-ray diffraction data.

Sample	**L15C185M**	**L25C175M**
x	**0.15**	**0.25**
Crystal system	Tetragonal	Tetragonal
Space group	*I*4$_1$/*acd*	*I*4/*mmm*
Z	8	4
a (Å)	5.2631(2)	3.8472(2)
c (Å)	23.9237(4)	12.5266(9)
V (Å^3)	662.70(6)	185.41(2)
R_p	2.79	3.49
R_{wp}	3.81	4.81
χ^2	1.37	1.40
Impurity amount (wt. %)	$CaCO_3$ 1.7(5)	La_2O_3 1.0(2)
Atom	Refined atomic positions (x,y,z)	
La/Ca	0, 0, 0.1766(1)	0, 0, 0.3583(2)
Mn	0, 0, 0	0, 0, 0
O1	0, 0, 0.0847(4)	0, 0.5, 0
O2	0.221(2), 0.221(2), 0.25	0, 0, 0.1677(15)

Figure 21. View along [001] of (a) Ca_2MnO_4 (*I*4$_1$/*acd*) and (b) $La_{0.25}Ca_{1.75}MnO_4$ (*I*4/*mmm*).

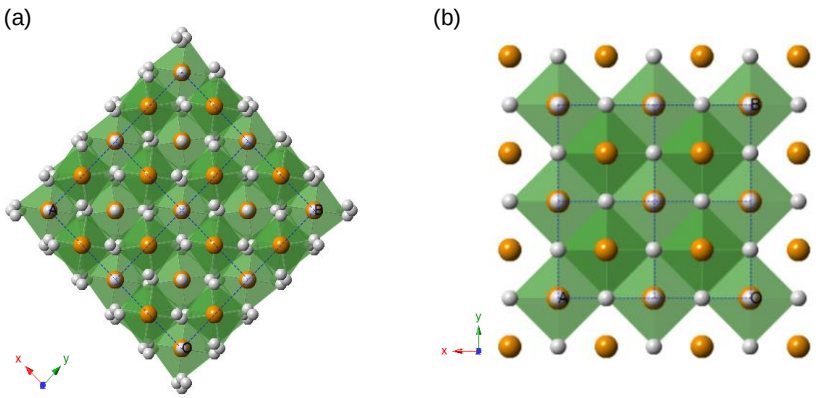

On the other hand, the composition with x=0.5 was far from being a single phase after synthesis in air, even increasing the temperature until 1200 °C. In this case, a mixture of three phases $(LaCa)_3Mn_2O_7$, $La_{1-x}Ca_xMnO_3$ and CaO was obtained. This result is different from the case of the $La_xSr_{2-x}MnO_{4\pm\delta}$ series that can be obtained as a single phase in a larger range of composition. La-doping seems more difficult in calcium manganites due to the large ionic size of La^{3+} ($R^{IX}_{La^{3+}}$= 1.216 Å) compared to Ca^{2+} ($R^{IX}_{Ca^{2+}}$= 1.18 Å), contrary to the case of Nd^{3+} ($R^{IX}_{Nd^{3+}}$= 1.163 Å) or Pr^{3+} ($R^{IX}_{Pr^{3+}}$= 1.179 Å) [41], with higher solubility limit. For example, it has been possible to obtain $Nd_xCa_{2-x}MnO_4$ for 0 ≤ x ≤ 0.45 at 1250 °C [26] and $Pr_xCa_{2-x}MnO_4$ for 0 ≤ x ≤ 0.5 at 1200 °C [54]. In summary, despite changing the synthesis technique from solid state reaction to sol-gel method, it was not only difficult to synthesize completely single phases of the $La_xCa_{2-x}MnO_{4\pm\delta}$ family at low temperature (1100 °C) in the reported range of solubility (0 ≤ x ≤ 0.35) but also impossible to extend the range of compositions to higher La content. A solution would have been to increase the temperature of synthesis, but we preferred changing La for Nd as substituting element for Ca, hopping easier synthesis at low temperature.

2.2.2.4 $Nd_xCa_{2-x}MnO_{4\pm\delta}$ series

For $Nd_xCa_{2-x}MnO_{4\pm\delta}$, several authors have demonstrated the formation of single phases in air at 1300°C in the range of 0 ≤x≤0.4, using solid state reaction [26][42]. In this work, we prepared $Nd_xCa_{2-x}MnO_{4\pm\delta}$ (x= 0.25, 0.4, 0.5 and 0.6) compounds by sol gel method at 1100 °C, to evaluate the solubility limit of neodymium at the A-site of Ca_2MnO_4 using another synthesis technique. The XRD patterns obtained after synthesis are shown in Figure 22.

Figure 22. XRD patterns of $Nd_xCa_{2-x}MnO_{4\pm\delta}$ (x= 0.25, 0.4, 0.5, 0.6) after synthesis in air. In inset, zoom on x=0.6.

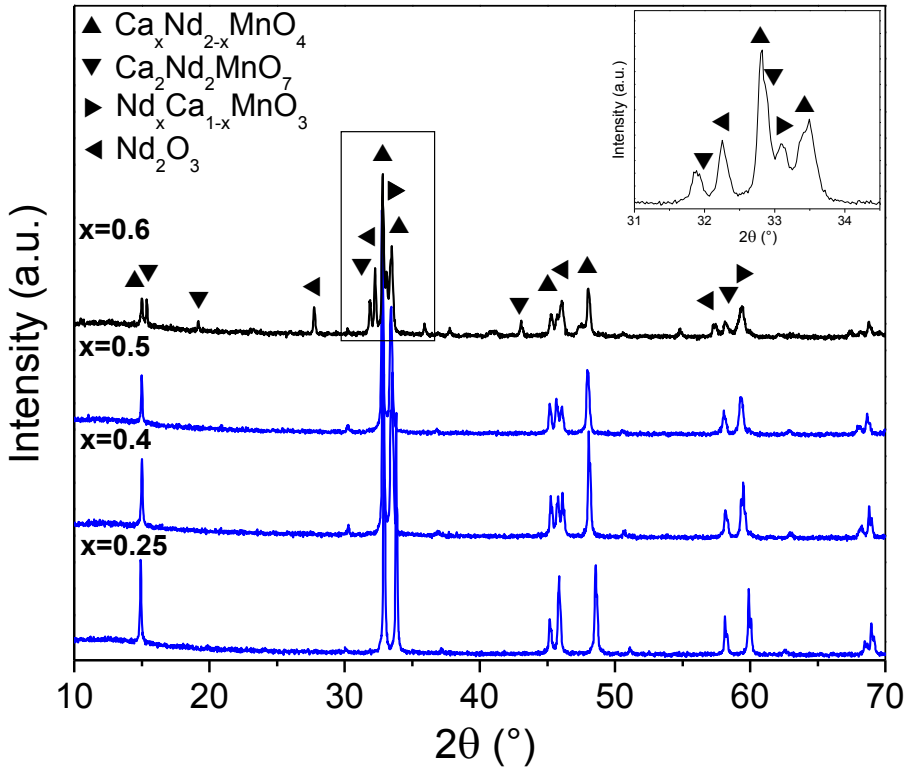

At the difference of the La series, XRD analysis shows the formation of single phases for x= 0.25, 0.4 and 0.5. On the contrary, for x=0.6, the secondary phases $Ca_2Nd_2MnO_7$, $Nd_xCa_{1-x}MnO_3$ and Nd_2O_3 are detected. The RE solubility is favored by the smaller ionic radii of Nd^{3+} ($R^{IX}_{Nd^{3+}}$= 1.163 Å) with respect to La^{3+} ($R^{IX}_{La^{3+}}$= 1.216 Å), in better agreement with Ca^{2+} ($R^{IX}_{Ca^{2+}}$= 1.18 Å). These results agree well with the previous reports concerning the fact that $Nd_xCa_{2-x}MnO_{4\pm\delta}$ form a solid solution for $0\leq x\leq 0.5$ [26][55][56]. It is worth mentioning that this series exhibits a distorted K_2NiF_4 structure at room temperature that depends on x value, as will be discussed below, on the base of the Rietveld refinement results (Table 6). The corresponding graphical results of refinements are shown in Annex 1.

Table 6. Structural parameters for $Nd_xCa_{2-x}MnO_{4\pm\delta}$ (x= 0.25, 0.4, 0.5) calculated by Rietveld refinement from powder X-ray diffraction data.

Sample	**N25C175**	**N4C16**	**N5C15**
x	**0.25**	**0.4**	**0.5**
Crystal system	Tetragonal	Orthorhombic	Orthorhombic
Space group	*I*4$_1$/*acd*	*Fmmm*	*Fmmm*
Z	8	4	4
a (Å)	5.2993(1)	5.3424(1)	5.3584(3)
b (Å)		5.3613(1)	5.3707(3)
c (Å)	23.7495(8)	11.8047(4)	11.8203(7)
V (Å^3)	666.94(3)	338.11(2)	340.17(4)
R_p	2.95	2.40	2.42
R_{wp}	3.86	3.10	3.16
χ^2	1.30	1.24	1.27
Atom	Refined atomic positions (*x,y,z*)		
Nd/Ca	0, 0, 0.55172(11)	0, 0, 0.35551(13)	0, 0, 0.35601(17)
Mn	0, 0, 0	0, 0, 0	0, 0, 0
O1	0.229(4), 0.479(4), 0.125	0.25, 0.25, 0	0.25, 0.25, 0
O2	0, 0.25, 0.4609(4)	0, 0, 0.1687(7)	0, 0, 0.1679(9)
Mn-O1	1.88(2) x 4	1.89216(7) x 4	1.89667(15) x 4
Mn-O2	2.040(10) x 2	1.991(8) x 2	1.985(11) x 2
Nd/Ca1-O1	2.445(15) x 2	2.5475(8) x 4	2.5484(16) x 4
	2.675(16) x 2		
Nd/Ca1-O2	2.156(10) x 1	2.205(8) x 1	2.223(11) x 1
	2.6665(11) x 4	2.6958(9) x 2	2.7002(12) x 2
		2.6864(9) x 2	2.6941(12) x 2
Mn-O1/Mn-O2	0.92	0.95	0.96

The refinements were initially attempted using the space group *I*4$_1$/*acd* for all compounds, considering that this space group has been reported for Ca_2MnO_4 and for compositions with low neodymium content (x≤0.2) [26]. The x=0.25 composition was successfully refined in the space group *I*4$_1$/*acd*; however, a poor match between model and experimental reflections and convergence difficulties were observed when using this model for the x=0.4 and 0.5 compounds (See Annex 2). Based on the results reported by Taguchi *et al.* [56], in which $Nd_xCa_{2-x}MnO_{4\pm\delta}$ presents an orthorhombic *Fmmm* structure for x=0.3 and x=0.4, this space group was used for carried out the Rietveld refinement of the x=0.4 and x=0.5 compounds. As seen in Table 6, in all cases, good values of goodness-of-fit and R-factors were obtained with such structural model. The lattice parameters obtained for $Nd_xCa_{2-x}MnO_{4\pm\delta}$ (x=

0.25, 0.4 and 0.5) series were in agreement with those reported for the similar compositions prepared using a flow of oxygen at 1100 °C [56]. Globally, the variation of *a* and *b* parameters shows a pronounced increase with increasing value of x, whereas *c* parameter decreases between x=0 and x=0.5 (Figure 23), taking into account that above x=0.25 the symmetry changes from tetragonal to orthorhombic (for x=0 the c-parameter was divided by 2). The resulting evolution of cell volume follows the same trend as for *a* or *b* parameters.

Figure 23. Evolution of cell parameters of $Nd_xCa_{2-x}MnO_{4\pm\delta}$ (x= 0, 0.25, 0.4, 0.5). For x=0 the parameters were taken from [52].

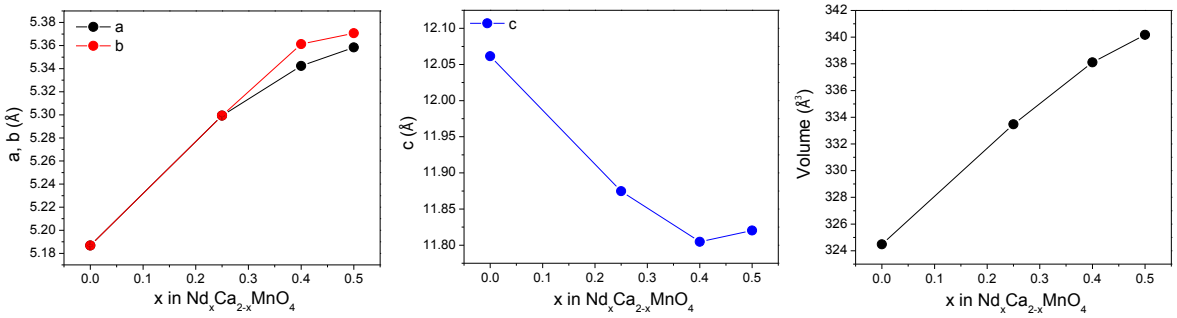

Such behavior is the consequence of the substitution of Ca^{2+} by the slightly smaller cation Nd^{3+}; similarly to the La/Sr manganites described above, the origin of such variation remains in the reduction of Mn^{4+} ($R^{VI}_{Mn^{4+}}$= 0.53 Å [41]) to the larger Mn^{3+} ($R^{VI}_{Mn^{3+}}$=0.645 Å [41]), conducing to the tendency for *a* and *b* parameters, as well as cell volume *V*. On the other side, and although the size of the Mn cations globally increases, the *c* parameter decrease with x can be related in part to the decrease of the mean ionic radius at the A site ($R^{IX}_{Nd^{3+}}$= 1.163 Å and $R^{IX}_{Ca^{2+}}$= 1.18 Å), but also to the Jahn-Teller distortion associated to the increasing concentration of Mn^{3+} cation.

Table 7 summarizes the results obtained for the different compositions that have been prepared in this chapter. All compositions were synthesized in air by solid state reaction in air or sol gel method at 1100 °C for 6 hours.

Table 7. Summary of synthesis for $RE_xA_{2-x}MnO_{4\pm\delta}$ (RE: La, Nd and A: Sr, Ca) family.

Composition	x	Name	Synthesis method	Synthesis temperature	Purity
$La_xSr_{2-x}MnO_{4\pm\delta}$	0	S2MSS	SS	1300°C	No
	0.25	L25S175MSS			Yes
	0.4	L4S16MSS			Yes
	0.5	L5S15MSS			Yes
	0.6	L6S14MSS			Yes
	0.7	LS13MSS			No
	0.25	L25S175M	SG	1100°C	Yes
	0.4	L4S16M			Yes
	0.5	L5S15M			Yes
	0.6	L6S14M			Yes
$Nd_xSr_{2-x}MnO_{4\pm\delta}$	0.25	N25S175M	SG	1100°C	No
	0.4	N4S16M			Yes
	0.5	N5S15M			Yes
	0.6	N6S14M			No
$La_xCa_{2-x}MnO_{4\pm\delta}$	0.15	L15C185M	SG	1100°C	No
	0.25	L25C175M			No
	0.5	L5C15M			No
$Nd_xCa_{2-x}MnO_{4\pm\delta}$	0.25	N25C175M	SG	1100°C	Yes
	0.4	N4C16M			Yes
	0.5	N5C15M			Yes
	0.6	N6C14M			No

Our study allows to confirm that $La_xSr_{2-x}MnO_{4\pm\delta}$ ($0.25 \leq x \leq 0.5$), $Nd_xSr_{2-x}MnO_{4\pm\delta}$ (x= 0.4 and 0.5) and $Nd_xCa_{2-x}MnO_{4\pm\delta}$ ($0.25 \leq x \leq 0.5$) can be obtained as single phase materials, compositions that will be studied now with more details in the scope of a possible use as symmetrical SOFC electrode. In this sense, we will now focus on the materials stability, possible structural changes and measurement of the total conductivity in oxidizing and reducing conditions. As a first selection criterion, the following part is dedicated to the thermal stability of the materials in reducing atmosphere.

2.3 STABILITY IN REDUCING ATMOSPHERE

2.3.1 EXPERIMENTAL SECTION

2.3.1.1 Reduction in diluted hydrogen

To rapidly assess the stability in SOFC anode conditions of the materials successfully prepared in air, approximately 0.5 grams of the as-synthesized powders were first reduced in a tubular furnace at 850 °C for 16 h in dry 3% H_2/Ar using a heating rate of 10 °C min^{-1} and a flux of 6 L/h. The resulting materials were characterized by XRD to study their stability in typical anode conditions.

2.3.1.2 Thermogravimetric analysis in reducing atmosphere

To understand the material reduction, in particular with respect to Mn reduction and oxygen vacancy formation, thermogravimetric analyses were carried out in reducing atmosphere using a gravimetric analyzer (Hiden-Isochema model IGA-003), applying a first cycle in N_2 (at 5 °C min^{-1}) that aims to suppress any further influence of moisture and/or adsorbed species, then a second slower cycle (at 2 °C min^{-1}) in 3% H_2/N_2, both cycles from Room Temperature (RT) to 1000 °C.

2.3.2 RESULTS

2.3.2.1 Thermal stability of $La_xSr_{2-x}MnO_{4\pm\delta}$ series in reducing atmosphere

The thermal stability of $La_xSr_{2-x}MnO_{4\pm\delta}$ materials for x=0, 0.25, 0.4, 0.5, 0.6 was evaluated in 3% H_2/Ar at 850 °C during 16 h. Figure 24 shows that the ordered K_2NiF_4-type structure remains stable after reduction for x≥0.25 as no extra peaks corresponding to impurities are present in the XRD patterns. The composition x=0 is not stable under such reducing conditions [57], showing the destruction of the phase

with formation of MnO and $SrCO_3$, the latter being likely a product of re-carbonation reaction when the sample contacts the air at room temperature. A partial conclusion is that Sr_2MnO_4 can be hardly used at the anode side of an SOFC. In view of the application as dual electrode material, this composition will be discarded of the rest of the study.

Figure 24. XRD patterns of $La_xSr_{2-x}MnO_{4-\delta}$ (x=0, 0.25, 0.4, 0.5, 0.6) after reduction at 850 °C in diluted hydrogen. Except for x=0, all compositions are stable.

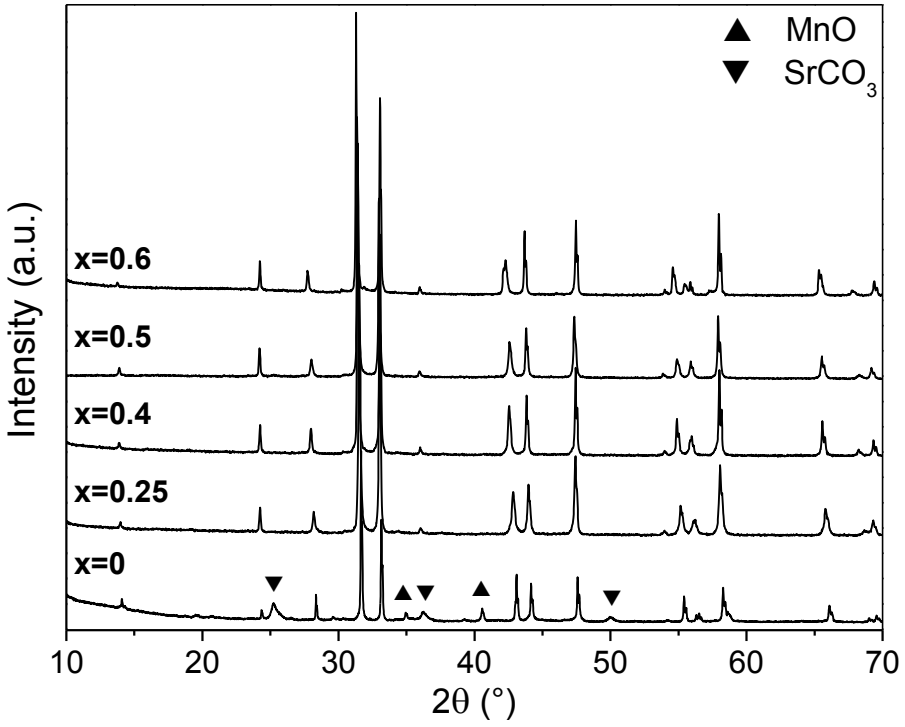

As an example, the graphical result of Rietveld refinement using the XRD pattern collected at room temperature after reduction (for x=0.5) is shown in Figure 25; the other members of the series with x=0.25, 0.4 and 0.6 present a similar profile (See Annex 3). All the Rietveld structural refinements were carried out successfully using the tetragonal cell (S.G. *I4/mmm*) characteristic of the RP n=1 structure, like the as-synthesized samples.

Figure 25. Graphical result of Rietveld refinement of x=0.5 after reduction in 3% H_2/Ar at 850 °C for 16 h.

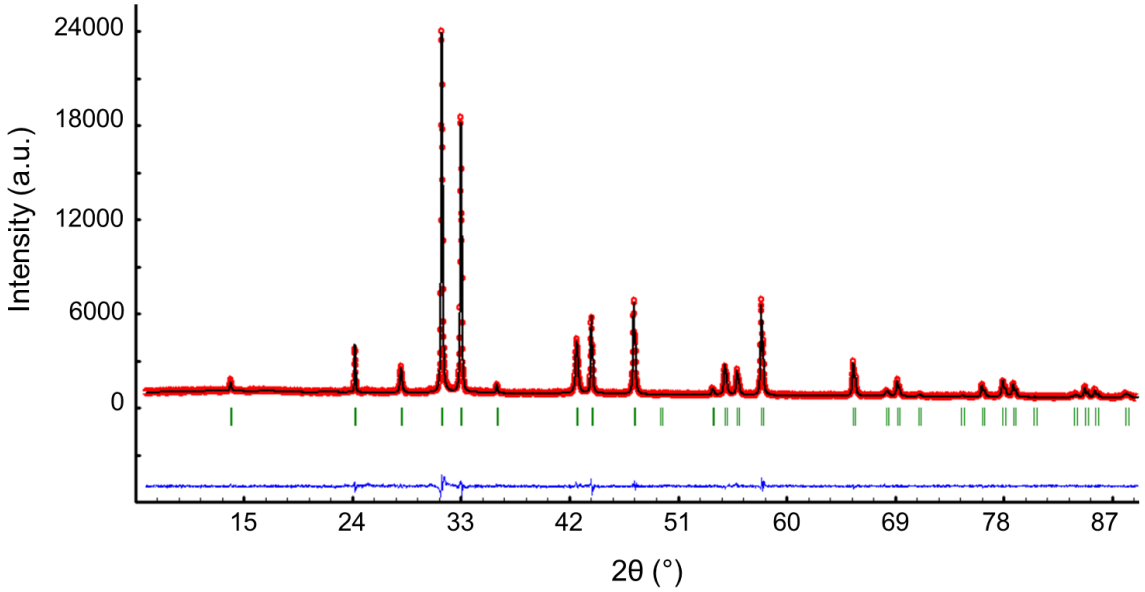

The refined structural parameters and bond distances are listed in Table 8 (the suffix H indicates the sample has been reduced). In general, the data reveal an expansion of both the *c* parameter and the lattice volume after reduction (Figure 26). Although the volume increase is slightly lower at higher La content, *(*~1.9% for x=0.25 and ~1.2% for x=0.6), the difference between oxidized and reduced phases for the *c* parameter is stronger at higher La content with ~1.9% for x=0.25 against ~3.4% for x=0.6. Such behavior is reflected in the Mn-O2 bond length that follows the same trend as for *c* parameter (+4.2% for x=0.25 to 6.0% for x=0.6). On the other hand, for x=0.25, the *a* parameter is surprisingly the same after reduction and remains nearly constant throughout the series. The net result is an [MnO_6] octahedra deformation that can be evidenced analyzing the evolution of Mn-O1/Mn-O2 ratio.

Table 8. Structural parameters and selected bond lengths (Å) of reduced $La_xSr_{2-x}MnO_{4-\delta}$ (x=0.25, 0.4, 0.5, 0.6) calculated by Rietveld refinement using powder X-ray diffraction data (space group *I*4/*mmm*).

Sample	**L25S175M-H**	**L4S16M-H**	**L5S15M-H**	**L6S14M-H**
x	**0.25**	**0.4**	**0.5**	**0.6**
a (Å)	3.8318(5)	3.8310(4)	3.8378(3)	3.8274(4)
c (Å)	12.6456(17)	12.7479(15)	12.7286(13)	12.8461(14)
V(Å^3)	185.67(4)	187.10(4)	187.48(3)	188.18(4)
R_p	3.09	3.48	3.32	3.85
R_{wp}	4.08	4.64	4.39	5.37
χ^2	2.8	2.9	2.0	1.9
Atom	Refined atomic positions (*x,y,z*)			
La/Sr	0, 0, 0.3540(9)	0, 0, 0.3544(9)	0, 0, 0.3570(1)	0, 0, 0.3574(7)
Mn	0, 0, 0	0, 0, 0	0, 0, 0	0, 0, 0
O1	0, 0.5, 0	0, 0.5, 0	0, 0.5, 0	0, 0.5, 0
O2	0, 0, 0.1606(4)	0, 0, 0.1620(6)	0, 0, 0.1617(5)	0, 0, 0.1605(5)
Mn-O1	1.91593(3) x 4	1.91553(20) x 4	1.91894(2) x 4	1.91370(2) x 4
Mn-O2	2.031(6) x 2	2.066(7) x 2	2.087(7) x 2	2.119(8) x 2
La/Sr-O1	2.6605(9) x 4	2.6667(9) x 4	2.6672(7) x 4	2.6683(9) x 4
La/Sr-O2	2.446(6) x 1	2.453(7) x 1	2.449(9) x 1	2.445(8) x 1
	2.7159(4) x 4	2.7171(6) x 4	2.724(9) x 4	2.7188(8) x 4
Mn-O1/Mn-O2	0.943	0.927	0.919	0.903

Figure 26. Evolution of the cell parameters of $La_xSr_{2-x}MnO_{4-\delta}$ (x=0, 0.25, 0.4, 0.5, 0.6) (●) as-synthesized in air and (●) reduced in 3% H_2/Ar at 850°C for 16 h.

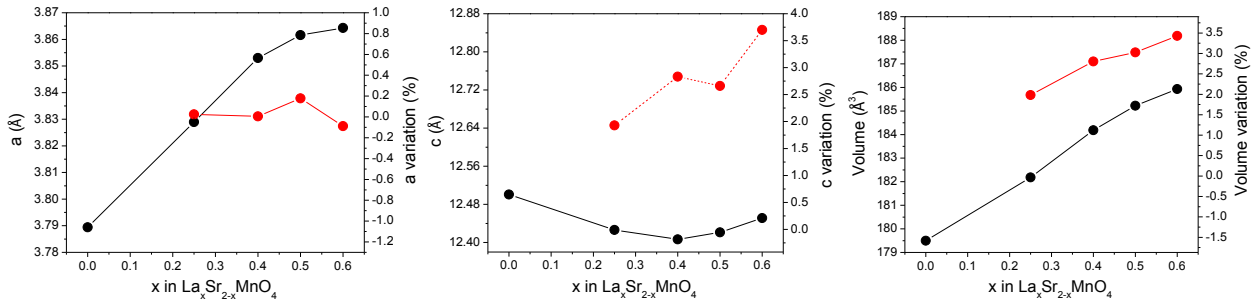

To try to understand such behavior, thermogravimetrical analyses (TGA) in diluted hydrogen have been performed from RT until 1000°C (Figure 27). In

Table 9, the temperatures associated to the different weight losses are reported along with the corresponding evolution of manganese oxidation state and oxygen stoichiometry in the $La_xSr_{2-x}MnO_{4-\delta}$ series.

Figure 27. Thermogravimetric analysis (TG) in 3% H_2/N_2 of $La_xSr_{2-x}MnO_{4\pm\delta}$ (x=0, 0.25, 0.4, 0.5, 0.6).

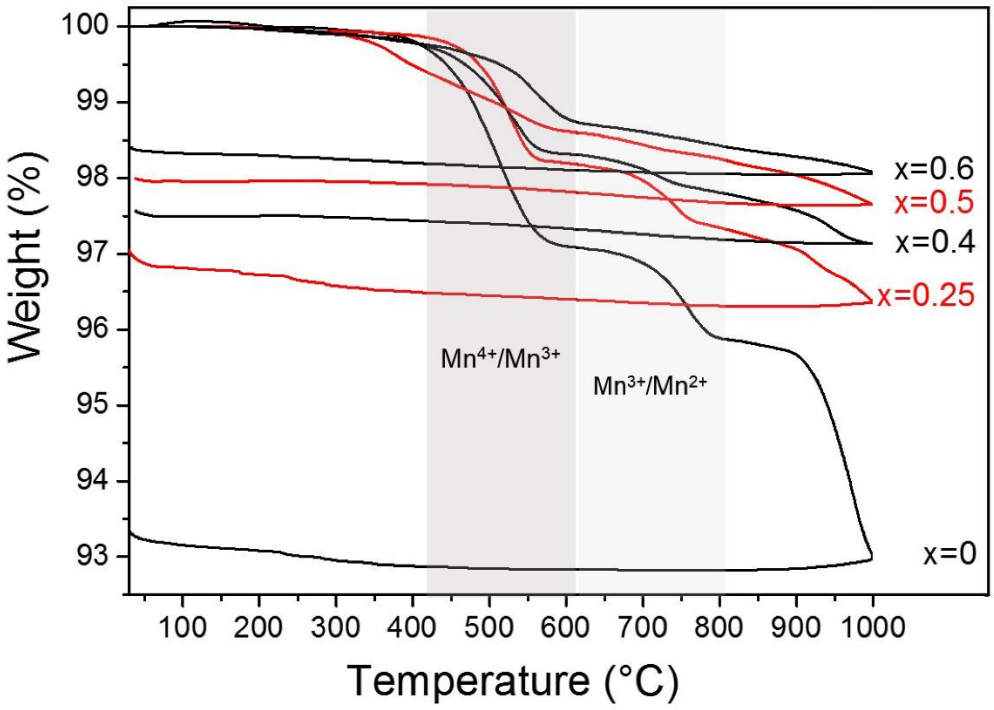

As shown in Figure 27, the TGA reduction profiles are similar for all compositions but the lower the x value, the stronger and sharpener the different weight changes. Between around 400 and 600 °C, a first consequent weight loss is observed. Interestingly, while x increases, the transition temperature also increases and the weight change becomes smaller (see Table 9).

Table 9. Weight losses and stoichiometries estimated from iodometric titration and TGA data (reducing atmosphere).

		x=0	**x=0.25**	**x=0.4**	**x=0.5**	**x=0.6**
As-synthesized		Sr_2MnO_4	$La_{0.25}Sr_{1.75}Mn^{+3.79(3)}O_{4.07}$	$La_{0.4}Sr_{1.6}Mn^{+3.66(4)}O_{4.03}$	$La_{0.5}Sr_{1.5}Mn^{+3.64(3)}O_{4.07}$	$La_{0.6}Sr_{1.4}Mn^{+3.55(3)}O_{4.08}$
First loss	T_1 (°C)	**500**	**520**	**530**	**540**	**557**
	Stoichiometry (at T °C)	$Sr_2Mn^{+2.96}O_{3.48}$ (at 570°C)	$La_{0.25}Sr_{1.75}Mn^{+3.22}O_{3.74}$ (568°C)	$La_{0.4}Sr_{1.6}Mn^{+3.01}O_{3.70}$ (575°C)	$La_{0.5}Sr_{1.5}Mn^{+3.09}O_{3.79}$ (595°C)	$La_{0.6}Sr_{1.4}Mn^{+3.03}O_{3.81}$ (620°C)
	Weight loss (%)	2.8	1.8	1.6	1.4	1.3
Second loss	T_2 (°C)	**750**	**740**	**725**	*	*
	Stoichiometry (at T °C)	$Sr_2Mn^{+2.49}O_{3.25}$ (795°C)	$La_{0.25}Sr_{1.75}Mn^{+2.91}O_{3.58}$ (770°C)	$La_{0.4}Sr_{1.6}Mn^{+2.84}O_{3.62}$ (750°C)		
	Weight loss (%)	4.1	2.6	2.1		
Anode conditions	T(°C)			**850**		
	Stoichiometry (at T °C)	$Sr_2Mn^{+2.46}O_{3.23}$	$La_{0.25}Sr_{1.75}Mn^{+2.82}O_{3.54}$	$La_{0.4}Sr_{1.6}Mn^{+2.76}O_{3.58}$	$La_{0.5}Sr_{1.5}Mn^{+2.90}O_{3.70}$	$La_{0.6}Sr_{1.4}Mn^{+2.85}O_{3.72}$
	Weight loss (%)	4.2	2.8	2.3	1.9	1.7
Final state	T(°C)			**1000**		
	Stoichiometry (at T °C)	$Sr_2Mn^{+1.42}O_{2.71}$	$La_{0.25}Sr_{1.75}Mn^{+2.51}O_{3.38}$	$La_{0.4}Sr_{1.6}Mn^{+2.54}O_{3.47}$	$La_{0.5}Sr_{1.5}Mn^{+2.71}O_{3.60}$	$La_{0.6}Sr_{1.4}Mn^{+2.76}O_{3.68}$
	Weight loss (%)	7.0	3.6	2.9	2.3	1.9

* Weight loss difficult to clearly assigned

This first weight loss is probably related to two simultaneous effects: (i) the reduction of Mn^{4+} to Mn^{3+}, and (ii) the creation of oxygen vacancies δ. The behavior is similar for all phases, suggesting that up to 600°C the phases have not been destabilized, in agreement with the first stability results described above. In the range of 630-800 °C, a second loss is observed, that can be associated to the reduction of Mn^{3+} to Mn^{2+}. Well defined for low La content, this second weight loss is broader as the lanthanum concentration increases, what can be attributed to better stability for the corresponding materials. Indeed, except for x=0, all the compositions remain with high Mn^{3+} content, *i.e.* a stoichiometry slightly above the critical formula $La_xSr_{2-x}MnO_{3.5}$. On the other hand, the x=0 composition fixes its oxygen stoichiometry around $Sr_2MnO_{3.25}$ with a formal Mn oxidation state of 2.5. This is beyond the scope of the present study to examine if such composition really exists or is already decomposed in several oxides, in particular MnO. Indeed, it has been demonstrated in previous work than $Sr_2MnO_{3.55(1)}$ composition, obtained at 550 °C, is the limit of a stable RP phase with the lowest well-defined oxygen content [58]. It means that $Sr_2MnO_{3.25}$ compound is probably already decomposed, at least partially, into binary oxides. Between 900 and 1000°C, a third weight loss is clearly observed for the compositions x=0 and 0.25, being larger for x=0 with a corresponding value of ~2.7%.

The XRD pattern taken after thermogravimetric analysis reveals the fully decomposition of Sr_2MnO_4, forming MnO, SrO, Mn_3O_4 and $SrCO_3$, while for x=0.25 only a partial decomposition is observed (Figure 28). In this latter case, the calculated composition of the material at 1000 °C would be $La_{0.25}Sr_{1.75}MnO_{3.38}$. On the other hand, the x=0.4, 0.5 and 0.6 phases remain stable after TG analysis, with respective stoichiometries of $La_{0.4}Sr_{1.6}MnO_{3.47}$, $La_{0.5}Sr_{1.5}MnO_{3.60}$ and $La_{0.6}Sr_{1.4}MnO_{3.68}$, suggesting that both a small Mn^{2+} content and an oxygen content

greater than the critical value of 3.50 allows the RP structure to remain stable in reducing conditions. For a practical use of the materials at anodic side of an SOFC, we confirm the results described above (Figure 24), *i.e.* all the compositions for x≥0.25 are stable and globally fulfill the same stoichiometry conditions (see Table 9).

Figure 28. XRD patterns of $La_xSr_{2-x}MnO_{4\pm\delta}$ (x=0, 0.25, 0.4, 0.5, 0.6) after TGA in 3% H_2/N_2.

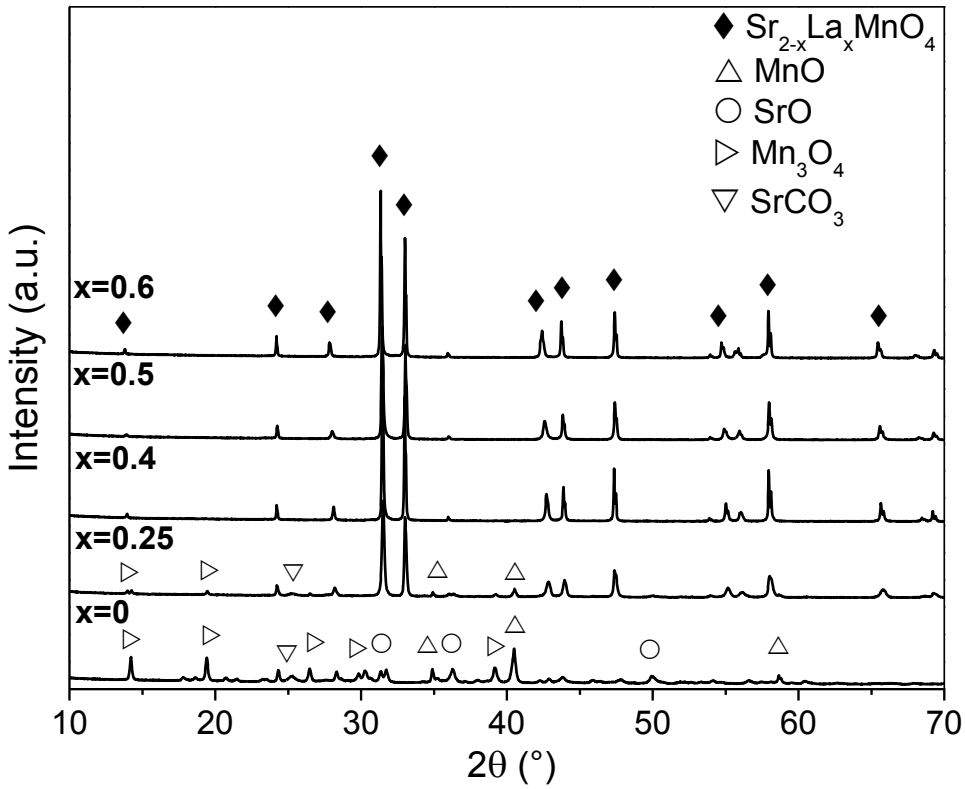

As a consequence of TG analysis, the difference of behavior between the *a* and *c* parameters, and the corresponding decrease of Mn-O1/O2 ratio in hydrogen, *i.e.* the elongation of [MnO_6] octahedral in the z direction, can stem from the electronic state of Mn cations, since during reduction process, Mn^{4+} shifts to Mn^{3+}, the latter being

an active Jahn-Teller cation. Such common feature of manganites has already been observed for example in $La_{1.2}Sr_{0.8}MnO_{3.94}$ [59], $La_{0.8}Sr_{1.2}Co_{0.5}Mn_{0.5}O_{3.6}$ [13] and $Pr_{0.5}Sr_{1.5}Cr_{0.5}Mn_{0.5}O_{4-\delta}$ [14]. The structural behavior induced by the change from an oxidizing to a reducing atmosphere will be discussed in section 2.4, using the results obtained by high temperature *in situ* XRD.

2.3.2.2 Thermal stability of $Nd_xSr_{2-x}MnO_{4\pm\delta}$ in reducing atmosphere

In order to evaluate the materials stability under reducing condition, $Nd_xSr_{2-x}MnO_{4\pm\delta}$ (x= 0.25, 0.4, 0.5, 0.6) samples were also heated in flowing 3% H_2/Ar at 850 °C for 16 h. Figure 29 shows the XRD patterns after the reduction process.

Figure 29. XRD patterns of $Nd_xSr_{2-x}MnO_{4-\delta}$ (x= 0.25, 0.4, 0.5, 0.6) after reduction at 850 °C in 3% H_2/Ar.

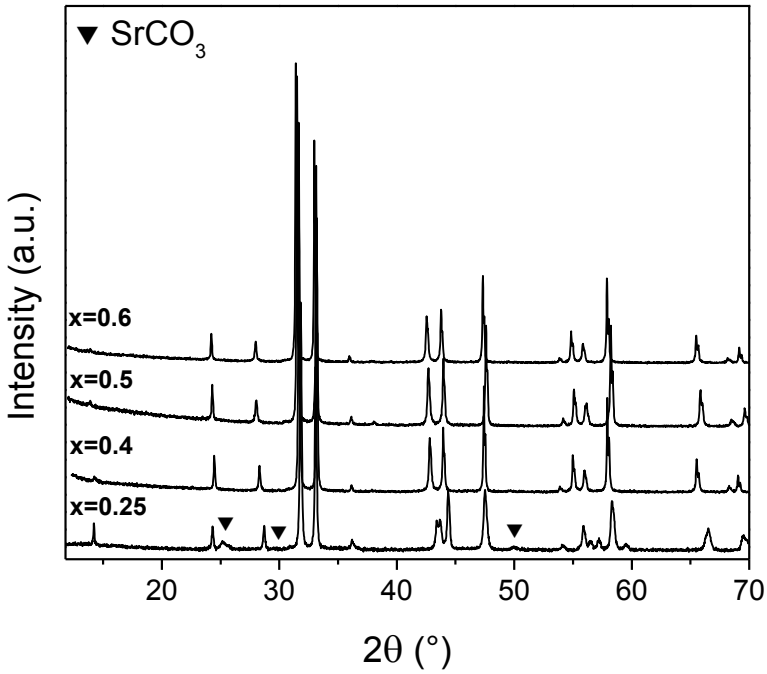

In the previous section 2.2.2, it has been established that the solid solubility limit of Nd in $Nd_xSr_{2-x}MnO_{4\pm\delta}$ system is $0.25 < x < 0.6$, obtaining single phases when x= 0.4 and 0.5. However, the reduction was carried out for all prepared samples. As shown

in Figure 29, under reducing atmosphere the compositions x=0.4 and 0.5 maintain their initial ordered K_2NiF_4-type structure with tetragonal structure (*I*4/*mmm*), in a similar way as for La-doped manganites. Rietveld refinement using the XRD data were carried out without any major difficulty; the refined structural parameters and bond distances are listed in Table 10 (the suffix (H) stands for reduced sample) and the graphical result of Rietveld refinement using the XRD patterns are displayed in Annex 4. In the case of the composition x= 0.25, $SrCO_3$ is once again observed as impurity and, after Rietveld refinement, the amount of carbonate remains nearly the same as after synthesis, *i.e.* 10.8(4) wt.% in the as-synthesized sample and 10.9(3) wt.% in the reduced sample (see Table 4 andTable *10*). Interestingly, for x= 0.6, the heat treatment in reducing atmosphere suppresses the impurity of Nd_2O_3 present in the powder that has been prepared in air. Such result can be explained by considering that at 850 °C (similar to $La_xSr_{2-x}MnO_{4\pm\delta}$) the manganese oxidation state change from Mn^{4+}/Mn^{3+} to Mn^{3+}/Mn^{2+}, what can find a charge compensation if Nd^{3+} cations is present at the A-site, therefore forming a reduced single phase.

Table 10. Structural parameters and selected bond lengths (Å) of reduced $Nd_xSr_{2-x}MnO_{4-\delta}$ (x=0.25, 0.4, 0.5, 0.6) calculated by Rietveld refinement using powder X-ray diffraction data (space group *I*4/*mmm*).

Sample	**N25S175M-H**	**N4S16M-H**	**N5S15M-H**	**N6S14M-H**
x	**0.25**	**0.4**	**0.5^+**	**0.6^+**
Space group	I4/*mmm*	I4/*mmm*	I4/*mmm*	I4/*mmm*
a (Å)	3.8227(2)	3.8217(2)	3.8142(2)	3.8109(2)
b (Å)				
c (Å)	12.4179(10)	12.6425(9)	12.6884(10)	12.7454(10)
V(Å^3)	181.46(2)	184.64(2)	184.59(2)	185.10(2)
R_p	4.25	6.97	6.64	8.48
R_{wp}	5.42	9.09	8.76	8.18
χ^2	1.29	1.70	1.76	1.70
Phase amount (wt %)	$SrCO_3$ 10.9(3)			
Atom	Refined atomic positions (*x*,*y*,*z*)			
Nd/Sr	0, 0, 0.3565(2)	0, 0, 0.3539(5)	0, 0, 0.3540(4)	0, 0, 0.3535(5)
Mn	0, 0, 0	0, 0, 0	0, 0, 0	0, 0, 0

O1	0, 0.5, 0	0, 0.5, 0	0, 0.5, 0	0, 0.5, 0
O2	0, 0, 0.1609(11)	0, 0, 0.164(2)	0, 0, 0.166(2)	0, 0, 0.164(3)
Mn-O1	1.9113(2) x 4	1.9063(2) x 4	1.9071(2) x 4	1.9137(2) x 4
Mn-O2	1.997(12) x 2	2.09(3) x 2	2.11(3) x 2	2.15(4) x 2
Nd/Sr-O1	2.6132(17) x 4	2.685(4) x 4	2.659(4) x 4	2.678(4) x 4
Nd/Sr-O2	2.428(13) x 1 2.7117(10) x 4	2.43(3) x 1 2.739(2) x 4	2.39(3) x 1 2.709(2) x 4	2.42(4) x 1 2.729(3) x 4
Mn-O1/Mn-O2	0.96	0.91	0.90	0.89

The variation in the lattice parameters after reduction is observed in Figure 30 (green symbols). For the single phases, the refined structural parameters reveal a decrease of the *a* parameter and an expansion of both the *c* parameter and the lattice volume after reduction. On the one hand, the decrease of *a* parameter is more noticeable when increasing the Nd content (for x= 0.25 it decreases of only ~0.02% while for x=0.6 the drop is around 0.7%). On the other hand, the *c* parameter increases markedly after reduction for the compounds with high Nd content, (~2.2% for x=0.25 and ~2.7% for x=0.5), possibly due to the presence of Mn^{3+}, which is a Jahn-Teller cation that induces octahedral distortion, as in the case of $La_xSr_{2-x}MnO_{4\pm\delta}$ family. Likewise, this is reflected in the behavior of the Mn-O2 bond lengths, which expansion is around 4.9%, whereas Mn-O1 bond lengths contraction is only 0.66% for x=0.5. In addition, the difference in the volume between oxidized and reduced phases for any phases do not exceed 1.4%, which is small compared to the volume change occurring in conventional Ni/YSZ cermet during the reduction and oxidation processes. In general, the small volumetric expansion observed for the neodymium phases is on the same order as the obtained for $La_xSr_{2-x}MnO_{4\pm\delta}$ series, suggesting that any studied member of these families could be used as hydrogen electrode material.

Figure 30. Evolution of cell parameters of $Nd_xSr_{2-x}MnO_{4\pm\delta}$ (x=0, 0.25, 0.4, 0.5, 0.6) (•) as-synthesized in air and (•) reduced in 3% H_2/Ar at 850°C for 16 h. For x=0.6, the phase is pure after reduction process.

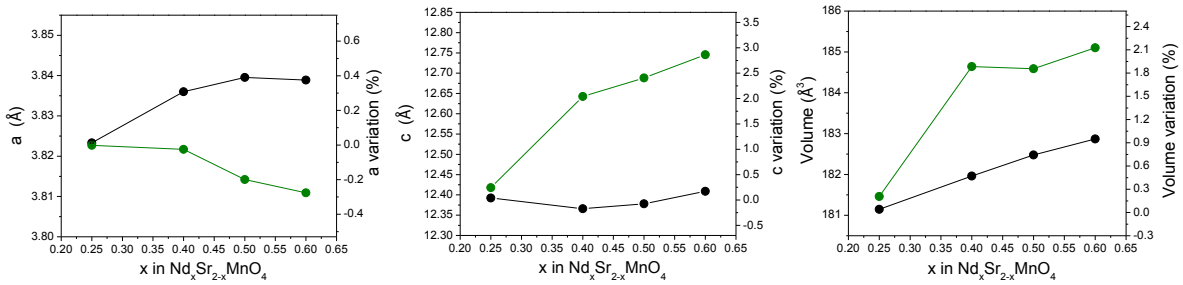

Thermogravimetric analysis (TGA) of the as-synthesized $Nd_{0.5}Sr_{1.5}MnO_{4\pm\delta}$ (Figure 31) was conducted in 3 % H_2/N_2 from room temperature to 1000 °C with a heating rate of 2 °C/min (see section 2.3.1.2 for the experimental details). This experiment was carried out in order to determine the oxygen stoichiometry and Mn oxidation states changes with temperature. The oxidation state of manganese and the oxygen content for the as-synthesized sample was determined by iodometric titration (see section 2.2.1). In Table 11, the temperatures associated to the different weight losses are reported along with the corresponding calculated manganese oxidation states and oxygen stoichiometry for $Nd_{0.5}Sr_{1.5}MnO_{4\pm\delta}$ compared to $La_{0.5}Sr_{1.5}MnO_{4\pm\delta}$.

Figure 31. Thermogravimetric analysis (TG) in 3% H_2/N_2 of $Nd_{0.5}Sr_{1.5}MnO_{4\pm\delta}$ in comparison to $La_{0.5}Sr_{1.5}MnO_{4\pm\delta}$.

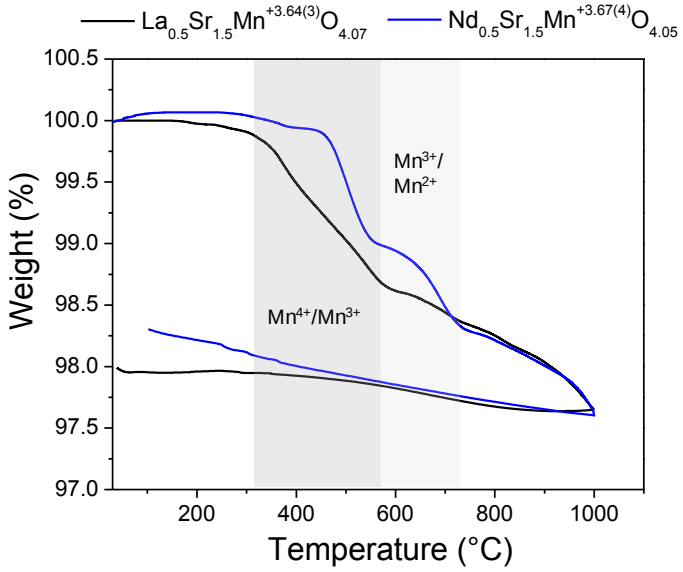

The TGA profile for as-synthesized $Nd_{0.5}Sr_{1.5}MnO_{4\pm\delta}$ (N5S15M) exhibits three well identified weight changes. We observe a first weight loss of ~1.0 % between 450 and 550 °C. In comparison with L5S15M, this weight loss in N5S15M begins at higher temperature and ends at lower temperature. Interestingly, the manganese oxidation state calculated at the end of this loss is slightly different for the two materials, showing a more severe reduction in L5S15M (+3.09(3)) than in N5S15M (+3.29(4)).

Table 11. Weight losses and stoichiometries estimated from iodometric titration and TGA data.

Sample		**L5S15M**	**N5S15M**
As-synthesized		$La_{0.5}Sr_{1.5}Mn^{+3.64(3)}O_{4.07}$	$Nd_{0.5}Sr_{1.4}Mn^{+3.67(4)}O_{4.05}$
First loss	T_1 (°C)	540	500
	Stoichiometry (at T °C)	$La_{0.5}Sr_{1.5}Mn^{+3.09(3)}O_{3.79}$ (595)	$Nd_{0.5}Sr_{1.5}Mn^{+3.29(4)}O_{3.85}$ (550)
	Weight loss (%)	1.4	1.0
Second loss	T_2 (°C)	*	690
	Stoichiometry (at T °C)		$Nd_{0.5}Sr_{1.5}Mn^{+3.00(4)}O_{3.70}$ (730)
	Weight loss (%)		1.7
Anode conditions	T(°C)	850	
	Stoichiometry (at T °C)	$La_{0.5}Sr_{1.5}Mn^{+2.90(3)}O_{3.70}$	$Nd_{0.5}Sr_{1.5}Mn^{+2.93(4)}O_{3.66}$
	Weight loss (%)	1.9	1.9
Final state	T(°C)	1000	
	Stoichiometry (at T °C)	$La_{0.5}Sr_{1.5}Mn^{+2.71(3)}O_{3.60}$	$Nd_{0.5}Sr_{1.5}Mn^{+2.76(4)}O_{3.58}$
	Weight loss (%)	2.3	2.3

* Weight loss difficult to clearly assign

According to the previous results, this weight loss is associated to two simultaneous effects of the reduction of Mn^{4+} to Mn^{3+} and of creation of oxygen vacancies. The second weight change between 600 and 730 °C corresponds to a loss of ~8.6 % of oxygen, resulting in the $Nd_{0.5}Sr_{1.5}Mn^{+3.00(4)}O_{3.70}$ composition. Surprisingly, when the temperature reaches 850 °C, both the weight loss and the manganese oxidation state are the same in both compounds, with a limited concentration of Mn^{2+}. Because the behavior in reducing atmosphere is similar for L5S15M and N5S15M, it can be inferred that the expansion of the *c* parameter observed after reduction of N5S15M

is also related to the Jahn-Teller effect provided by Mn^{3+} cation, confirming the previous discussion.

In order to examine the impact of heating at high temperature on the structural stability, the XRD pattern was recorded for the N5S15M sample after the thermogravimetric test (Figure 32).

Figure 32. XRD pattern of $Nd_{0.5}Sr_{1.5}MnO_{4\pm\delta}$ after TGA in 3% H_2/N_2.

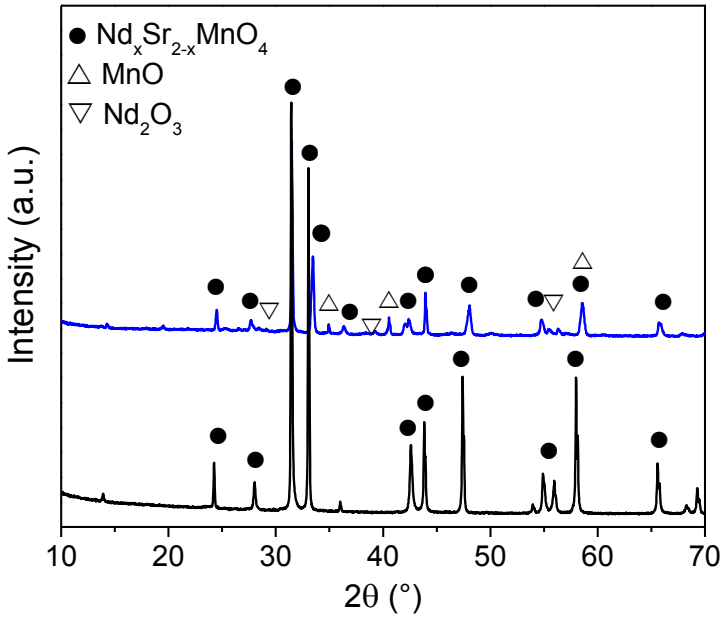

As seen in Figure 32, the XRD pattern of N5S15M after TG analysis shows that the heat treatment up to 1000 °C in hydrogen led to partial decomposition of the phase, as MnO and Nd_2O_3 are identified as additional phases. Unlike L5S15M, which was completely stable after such thermal treatment (see Figure 28), N5S15M begins to be unstable when exposed for a long time to temperatures higher than 850 °C in dry reducing conditions.

2.3.2.3 Thermal stability of $Nd_xCa_{2-x}MnO_{4\pm\delta}$ in reducing atmosphere.

The stability in reducing atmosphere of the $Nd_xCa_{2-x}MnO_{4\pm\delta}$ phases with x= 0.25, 0.4, 0.5, 0.6 was also evaluated in 3% H_2/Ar (using the conditions described in section 2.3.1). Figure 33 shows the XRD patterns after reduction at 850 °C during 16 h.

Figure 33. XRD patterns of $Nd_xCa_{2-x}MnO_{4-\delta}$ (x= 0.25, 0.4, 0.5, 0.6) after reduction at 850 °C.

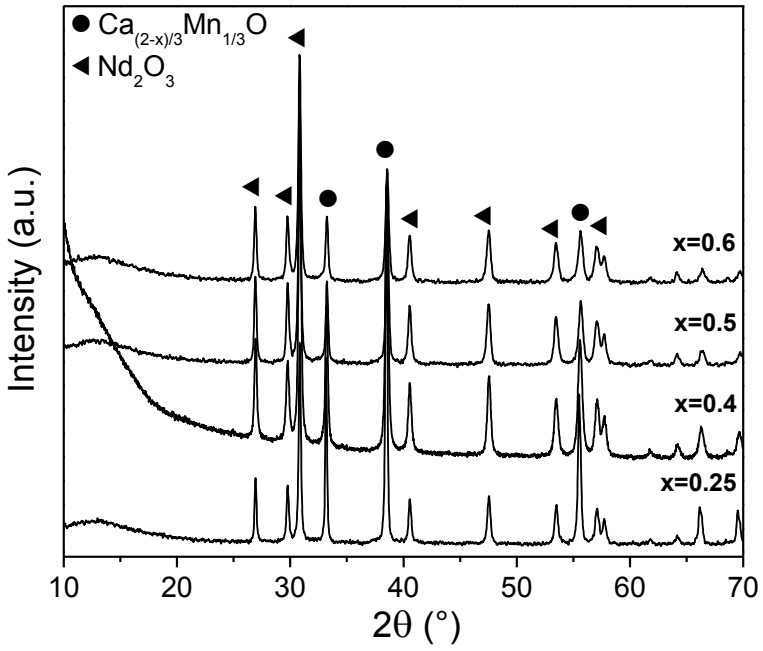

Considering that Sr_2MnO_4 is unstable in reducing atmosphere, but can be stabilized with the substitution of La, Nd or Pr onto the A-site [14][18], we expected that the substitution of Nd by Ca into Ca_2MnO_4 would improve its stability in reducing atmosphere. However, the results were not satisfactory; regardless of the degree of Nd substitution at the A-site, $Nd_xCa_{2-x}MnO_{4-\delta}$ materials are unstable in diluted hydrogen. As observed in Figure 33, all samples were decomposed into a mixture of the two phases Nd_2O_3 and $Ca_{2/3}Mn_{1/3}O$. Indeed, the presence of $Ca_{2/3}Mn_{1/3}O$

phase is reasonable considering the behavior of Ca_2MnO_4 in reducing conditions reported in the literature. Using diluted hydrogen Ca_2MnO_4 is initially reduced to $Ca_2MnO_{3.5}$ in the narrow temperature range 300-325°C. Afterwards, above 700°C, the thermogravimetric reduction and subsequent XRD analysis shows that the sample is reduced to the cubic rock-salt structure of $Ca_{2/3}Mn_{1/3}O$. This transformation can be expressed as follows [60][61][62]:

$$Ca_2MnO_4 \xrightarrow[300\text{-}325\ ^\circ C]{H_2} Ca_2MnO_{3.5} \xrightarrow[700\ ^\circ C]{H_2} 3Ca_{2/3}Mn_{1/3}O + 1/2H_2O \quad (2\text{-}17)$$

In our case, the above equation can be expressed as:

$$Nd_xCa_{2-x}MnO_4 + (1\text{-}3x/2)H_2 \xrightarrow{850\ ^\circ C} x/2\ Nd_2O_3 + 3Ca_{(2-x)/3}Mn_{1/3}O + (1\text{-}3x/2)H_2O \quad (2\text{-}18)$$

The neutron powder diffraction study, carried out by Poeppelmeier *et al.,* showed that the reduction of Mn^{4+} to Mn^{3+} generates oxygen vacancies in the MnO_2 plane of the Ca_2MnO_4 ($I4_1/acd$) structure, giving $Ca_2MnO_{3.5}$ (*Bbam*) at 300 °C, which is a layer structure of interconnected distorted square-pyramidal Mn^{3+} coordination that retains perovskite-like connectivity along the *z*-axis but tends to be unstable above 500 °C [60][63][64]. If we compare the results of these authors to the thermogravimetric reduction carried out for the $La_xSr_{2-x}MnO_{4-\delta}$ ($0 \leq x \leq 0.6$) series, the barrier of reduction is lower for Ca_2MnO_4 than for Sr_2MnO_4; in the calcium phase, the full Mn^{3+} stoichiometry $Ca_2MnO_{3.5}$ is reached at very low temperature (300 °C) while, for the strontium manganite, the $Mn^{+2.96}$ is formed at 570 °C conducing to $Sr_2MnO_{3.48}$ composition. In this way, even using Nd substitution, which allows to already form a high concentration of Mn^{3+} oxidation state after synthesis and then reduce the concentration of oxygen vacancies due to reduction process, the RP Ca manganite series cannot be stabilized in reducing atmosphere and always decomposes.

According to the previous results, we focused our interest on the study of the strontium phases ($La_xSr_{2-x}MnO_{4\pm\delta}$ and $Nd_xSr_{2-x}MnO_{4\pm\delta}$), those families being the only ones for which stable compositions can be found in both air and reducing conditions, with possible application as electrode material for symmetrical SOFC.

2.4 STRUCTURAL BEHAVIOR OF THE $RE_xSr_{2-x}MnO_{4\pm\delta}$ (RE: La, Nd) SERIES DURING REDOX CYCLING

Structural changes induced by the shift from an oxidizing to a reducing atmosphere are of primary importance for an SOFC anode material (and even more for a symmetrical SOFC electrode); redox stability is considered as one of the main issues to be solved for the state-of-the-art Ni-based cermets [65]. For that purpose, high temperature *in situ* redox cycling between air and diluted H_2 was followed by XRD for all the La-substituted compounds and a representative composition of the Nd series (x=0.5). Finally, an in-depth study by *in situ* HT neutron diffraction of one characteristic composition of the whole family was performed, with the objective to get a further insight into the formation of oxygen vacancies in reducing conditions, with a special focus on their position and concentration in the crystal structure.

2.4.1 EXPERIMENTAL SECTION

The structural behavior during redox cycling was studied for several members of the $RE_xSr_{2-x}MnO_{4\pm\delta}$ series (RE: La, Nd) using High Temperature (HT) XRD technique following a sequence of three continuous cycles of heating and cooling from RT to 800 °C in air, then diluted hydrogen (3% H_2/N_2) and, finally, air (re-oxidation). The data were collected every 50 °C and the heating and cooling rates were 5 °C min^{-1}. The experiments were carried out using a D8 Bruker diffractometer equipped with an Anton Paar XRK900 reaction chamber, a Cu-$K_{\alpha1,2}$ incident radiation and a

Lynxeye detector. The evolution with temperature of the cell parameters was determined with the “cyclic refinement” option of FullProf software [37], using a profile matching approach.

In order to study the possible evolution of oxygen stoichiometry of the materials in air as a function of temperature, thermogravimetric (TG) measurements were conducted on a Discovery TGA 5500 thermobalance using artificial air with a flow rate of 5 mL/min. During the TG experiments, about 30 mg of the powder material was placed on a Pt holder. Measurements were performed in two cycles of heating and cooling from RT to 1000 °C. A first cycle with a 3 °C/min ramp rate and a second cycle with a 1 °C/min ramp rate. Due to the strong similarities between La and Nd series, those measurements were carried out only on $La_xSr_{2-x}MnO_{4\pm\delta}$ materials.

The thermo-mechanical compatibility with the electrolyte materials was evaluated from the comparison of Thermal Expansion Coefficients (TEC). TEC values were deduced from HT-XRD data analysis during cooling. The materials being of tetragonal symmetry, two independent coefficients of linear expansion were calculated, α_a and α_c, normal and parallel to *c*-axis, respectively. Assuming an isotropic repartition of grain orientation during electrode elaboration, the mean average linear Thermal Expansion Coefficients (TEC) were calculated as TEC = 1/3 ($2\alpha_a + \alpha_c$).

To complete the study in particular concerning the formation of oxygen vacancies in reducing conditions, we undertook *in situ* neutron diffraction experiments on only one composition, representative of both series, $La_{0.5}Sr_{1.5}MnO_{4\pm\delta}$. Indeed, if X-rays are well suited to follow the structural evolution of compounds with high Z atoms, in our case, the strong contrast between O (Z=8) and La (Z=56) does not play in favor of oxygen, which study is precisely one of the key points of MIEC compounds, *i.e.* electrode materials. For neutron radiation, O and La have similar weight (the neutron

coherent scattering length, *b*, are 5.803 fm and 8.24 fm for O and La, respectively, thus of the same order of magnitude).

Neutron powder diffraction (NPD) experiments were carried out at the Orphée reactor of the Léon Brillouin Laboratory (CEA/Saclay-France) on the high resolution 3T2 diffractometer using a Ge(335) monochromator to select a wavelength of 1.22763 Å. The x=0.5 composition was selected as representative of the whole $La_xSr_{2-x}MnO_{4\pm\delta}$ series in the studied range, since it has been previously demonstrated that all the compositions have a similar behavior. About 20 g of sample were prepared by sol-gel method using the conditions described above (section 2.2), and then encapsulated in a quartz tube and introduced in the furnace. Diffraction patterns were collected in the 4.5-120° 2θ range with a step of 0.05°, on heating under 3%H_2/Ar from 200°C to 850°C. The data analysis was performed by the Rietveld method using the Jana-2006 program [38].

2.4.2 RESULTS

The redox behavior of $La_xSr_{2-x}MnO_{4\pm\delta}$ materials (x= 0.25, 0.4 and 0.6) is presented in Figure 34 to 37. In all cases, there is no evidence of additional phase formation during all the cycles and the materials remain in their K_2NiF_4-type structure with *I*4/*mmm* space group during the change of atmosphere in the studied temperature range. The hydrogen treatment leads to clear shifts for the (0 0 4), (1 0 3) (1 1 0) (1 1 4) and (2 0 0) reflections, slight shifts of (1 0 1) and (1 1 2) reflections and finally an overlap of the (1 0 5) and (0 0 6) reflections, which return to their initial positions during re-oxidation.

The cell parameters evolution for the series are given in Figure 38. For all the compounds, the first heating in air shows an anisotropic thermal expansion with the *c* parameter increasing much more rapidly with temperature than the *a* parameter

[66]. Both *a* and *c* (then *V*) parameters do not deviate from the linear behavior and are reversibly restored upon cooling.

Figure 34. *In situ* HT-XRD patterns of as-prepared $La_{0.5}Sr_{1.5}MnO_{4\pm\delta}$ (x=0.25) from Room Temperature to 800 °C in air (grey), 3% H_2/N_2 (red) then air again (blue).

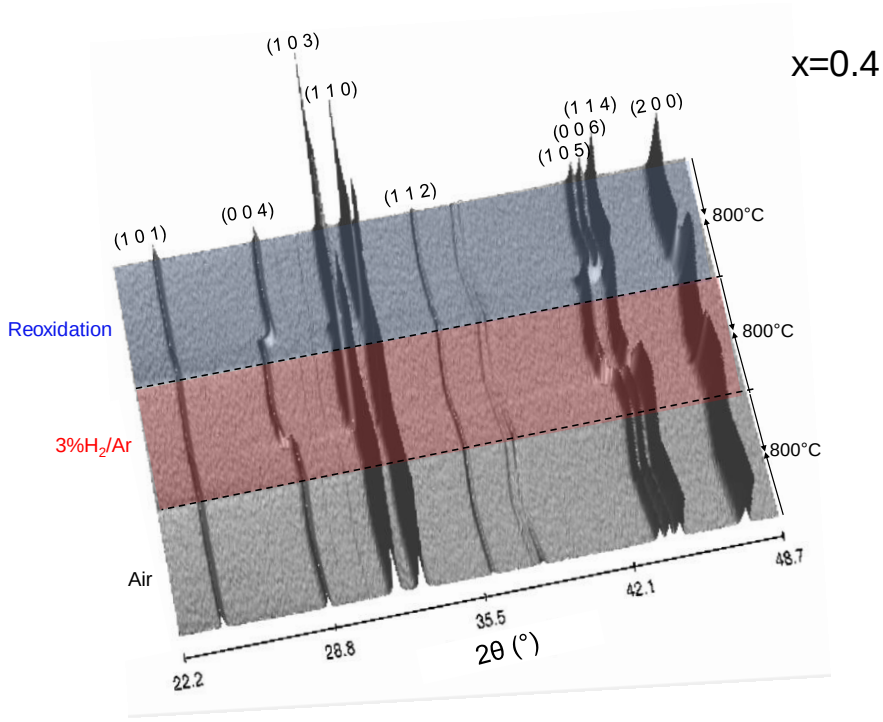

Figure 35. *In situ* HT-XRD patterns of as-prepared $La_xSr_{2-x}MnO_{4\pm\delta}$ (x=0.5) from Room Temperature to 800 °C in air (grey), 3% H_2/N_2 (red) then air again (blue).

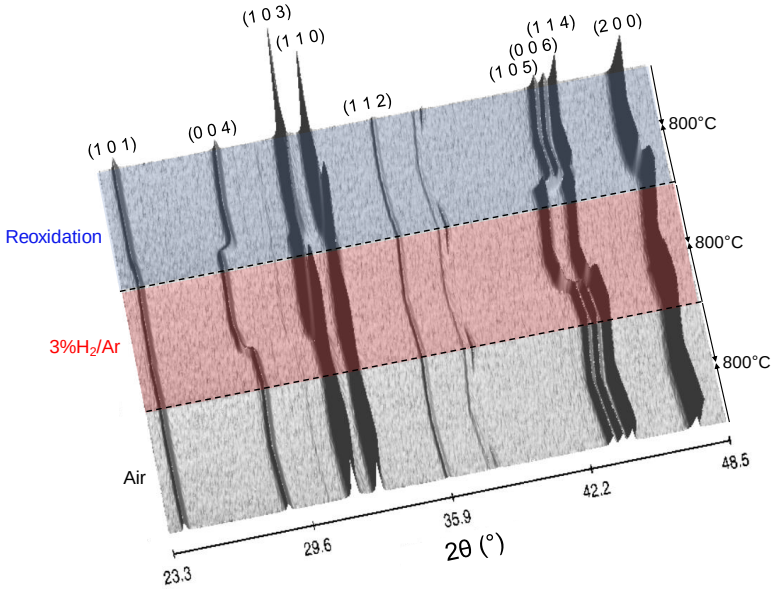

Figure 36. In situ HT-XRD patterns of as-prepared $La_xSr_{2-x}MnO_{4\pm\delta}$ (x=0.6) from Room Temperature to 800 °C in air (grey), 3% H_2/N_2 (red) then air again (blue).

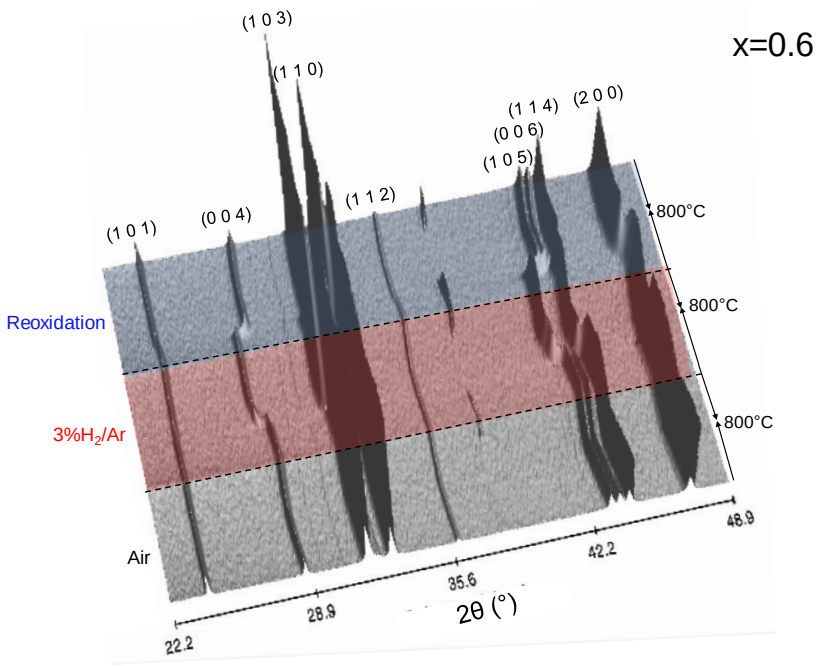

In addition, Figure 37 shows the TG curves in air for $La_xSr_{2-x}MnO_{4\pm\delta}$ (x= 0.25 and 0.5) compounds, the other compositions are shown in Annex 5. In all cases, during the first heating, the materials experience several limited weight losses between RT

and 700-750 °C, that are not reproduced during the second heating/cooling cycle. Such losses are attributed to the desorption of physi-/chemisorbed species, typically H_2O and CO_2 that don´t correspond to the intrinsical behavior of the materials.

Figure 37. Thermogravimetric profiles for $La_xSr_{2-x}MnO_{4\pm\delta}$ (x=0.25 and 0.5) in air.

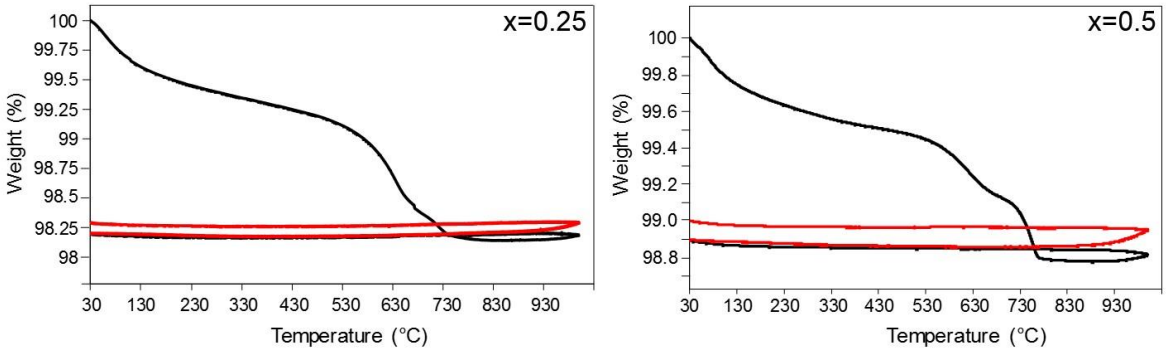

The second cycle in air up to 1000 °C does not generate significant changes in weight; therefore, it is concluded that no major variation of oxygen stoichiometry (resp. Mn oxidation state) occurs in the series in cathode conditions and that the oxygen contents of the as-synthesized materials, obtained by iodometry, remain the same at high temperature in air. The absence of any “accident” in the TG curves in air is in agreement with the thermal behavior during the first cycle in air, *i.e.* a pure dilatation phenomenon. Unlike $La_2NiO_{4+\delta}$ (δ=0.17-0.19) [7], in which the overall expansion of the lattice volume (~3.5% in air up to 800 °C) is not purely due to the thermal expansion but instead, is associated with the loss of interstitial oxygen [67]. In fact, for this nickelates the thermogravimetric curves show weight losses between 0.20 and 0.25% during the heating in air [68][69], contrary to the absence of weight loss observed in the $La_xSr_{2-x}MnO_{4\pm\delta}$ series.

Figure 38. Evolution of the cell parameters during redox cycling for $La_xSr_{2-x}MnO_{4\pm\delta}$ (x=0.25, 0.4, 0.5, 0.6)

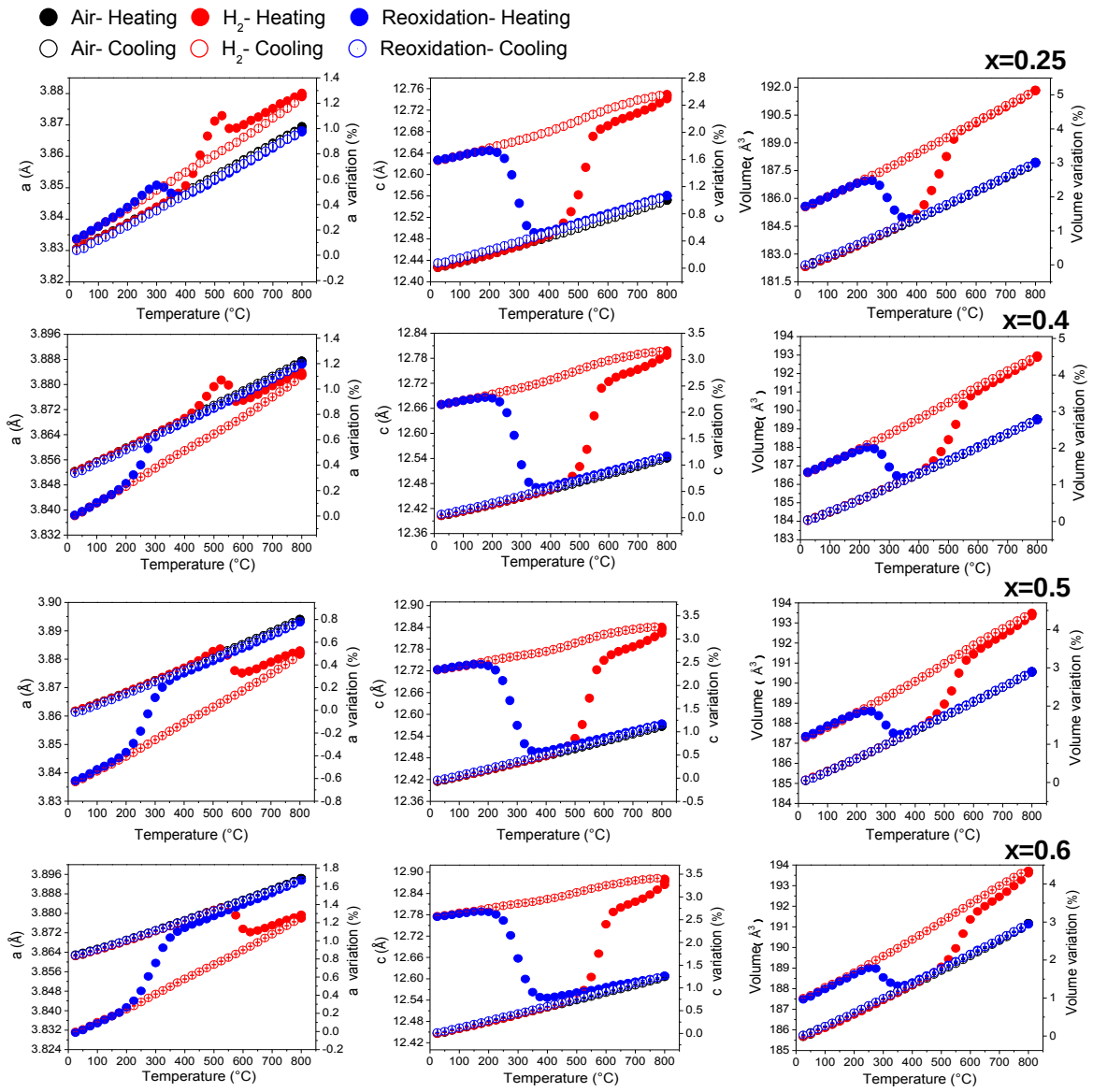

The heating in reducing atmosphere causes a two-step evolution of the cell volume: (i) a fast evolution between 400 and *ca.* 550 °C and (ii) a smoother one between 600 and 800 °C. This behavior can be even better evidenced by comparing the heating and cooling curves, the linear behavior of the latter being only associated to classical thermal contraction.

(i) Based on TG measurements, it is clear that the strong volume increase between 400 and 550 °C, in addition to classical thermal expansion, is

associated to the first Mn reduction from Mn^{4+} to Mn^{3+} that systematically induces a strong increase of the *c* parameter (for x=0.5, the change of *c*-parameter around 500 °C is *ca.* 1.7 %). Meanwhile, the *a* parameter follow a peculiar behavior in which it begins to increase between 400 and 500°C, strongly for x=0.25 and, as the La content increases, the phenomenon becomes less pronounced to be nearly inexistent for x=0.6. By comparison with TG results, such phenomenon seems associated to the appearance of a sufficient amount of Mn^{3+} in the low La containing compounds. Since, for x>0.25, the Mn^{3+} concentration is already high after synthesis, it doesn´t create such a strong expansion along *a* (see Table 3). As far as the first reduction step continues, the *a* parameter rapidly drops between 500 and 550 °C. Intriguingly, the higher the La content, the stronger the decrease, whereas it is this time very weak for the compounds with low La content. It is worth noting that the decrease of *a* parameter corresponds with the stronger increase of *c* parameter after 500 °C. Such change in the *a* parameter evolution could be the proof that the Jahn Teller (JT) effect, already mentioned, is of Q_3-type, using the notation described by Kanamori [70], for which the four equatorial Mn-O bond lengths decrease as the axial Mn-O distances become longer, the predominant mode of JT deformation. The behavior of the manganese oxidation state and the variation of bond lengths during reduction will be confirmed by *in situ* neutron diffraction experiments (see below).

(ii) During the second reduction step, identified by TGA as the Mn^{3+} ($R^{VI}_{Mn^{3+}}$=0.645 Å [41]) to Mn^{2+} reduction ($R^{VI}_{Mn^{2+}}$= 0.67 Å [41]), *c* and *V* parameters smoothly increase, independently of the composition. On the other side, *a* parameter slowly drops in comparison to the thermal expansion curve that corresponds to cooling, once again related to the anisotropy of the chemical expansion phenomenon.

For all the composition, the re-oxidation proceeds in only one step, between 200 and 350 °C, a temperature range in which the lattice parameters return to their initial values, demonstrating that reduction process is reversible. It is also interesting to note that the redox cycling generates a small volumetric change, that is known to be detrimental since it could induce stress and cracking in the cell [71]. However, this ~1.5% variation (for x=0.5 for instance), is relatively small compared to that of Ni in Ni/YSZ cermet, where volume decreases ~41.6% during reduction and increases ~69% during reoxidation [72][73].

The compatibility of an electrode material with the electrolyte concerns possible mismatch from the chemical as well as the thermomechanical point of view. Thermal expansion coefficients (TECs) calculated from the change of the cell parameters during cooling in air and hydrogen (Figure 38), are presented in Table 12.

Table 12. Thermal expansion coefficients of $La_xSr_{2-x}MnO_{4\pm\delta}$ (x= 0.25, 0.4, 0.5, 0.6).

x in $La_xSr_{2-x}MnO_{4\pm\delta}$	**TEC (25-800 °C) x 10^6 K^{-1}**	
	Air	3% H_2/Ar
0.25	12.9(2)	13.8(3)
0.4	12.6(1)	13.7(3)
0.5	12.3(1)	13.7(6)
0.6	12.3(2)	13.7(3)

For all the probed compositions, the TECs obtained are about 12.5x10^{-6} K^{-1} in air and 13.7x10^{-6} K^{-1} in reducing atmosphere, lower than those already reported values for the $La_xSr_{2-x}MnO_{4\pm\delta}$ ($0\leq x\leq 1.4$) series (TEC=15.1-16.5x10^{-6} K^{-1}) between room temperature and 800 °C [15]. Compared to other materials, the TECs obtained in air throughout the $La_xSr_{2-x}MnO_{4\pm\delta}$ series are close to those reported for RP nickelates as $La_2NiO_{4-\delta}$ and $La_{1.6}Sr_{0.4}NiO_{4-\delta}$ with TEC of 11.9x10^{-6} K^{-1} and 13.2x10^{-6} K^{-1}, respectively, in the temperature range 30-1000 °C [12]. Those values are

comparable with those of LSGM ($11.4x10^{-6}$ K^{-1}), YSZ ($10.1\text{-}10.5x10^{-6}$ K^{-1}) and GDC ($12\text{-}13x10^{-6}$ K^{-1}) electrolytes [74][75][76].

The difference between the TEC values measured in hydrogen and in air is not easy to explain but may be due to the change of oxidation state of manganese [77]. According to the literature, in manganese oxides, the most important bonding orbitals are the σ-bonding e_g and the π-bonding t_{2g}, which are composed of manganese 3*d* and oxygen 2*p* atomic orbitals. In this way, with the decrease in the oxidation state of the manganese atom, these orbitals become more antibonding in character insofar as they donate less electron density to the Mn atom and become more instable, which could lead to an increase in the expansion coefficients [78].

In situ High Temperature (HT) XRD for $Nd_{0.5}Sr_{1.5}MnO_{4\pm\delta}$ compound

The *in situ* High Temperature (HT) XRD analyzes in oxidizing and reducing atmosphere were also carried out for $Nd_{0.5}Sr_{1.5}MnO_{4\pm\delta}$ compound, in order to observe the structural evolution and compare its behavior with that observed for the $La_xSr_{2-x}MnO_{4\pm\delta}$ series. Figure 39 depicts the XRD patterns using three cycles of heating from RT to 800 °C and cooling back to RT in air, diluted hydrogen, then air for the material re-oxidation. As in the case of La manganites, no phase transitions or additional peaks formation are evidenced during redox cycling, whereas the reduction leads to a shift of some diffraction peaks, especially the (0 0 4), (1 0 3) (1 1 0) (1 1 4) and (2 0 0) reflections, and to the overlapping of the (1 0 5) and (0 0 6) reflections. The reoxidation process allowed the movement of all reflections to their initial positions, suggesting that N5S15M presents a nearly perfect reversibility, besides a good stability both in oxidizing and reducing atmosphere. All XRD data obtained could be indexed in the tetragonal *I*4/*mmm* space group. The evolution of the lattice parameters as a function of temperature is shown in Figure 40.

Figure 39. In situ HT-XRD patterns of as-prepared $Nd_{0.5}Sr_{1.5}MnO_{4\pm\delta}$ from Room Temperature to 800 °C in air (grey), 3% H_2/N_2 (red) then air again (cyan).

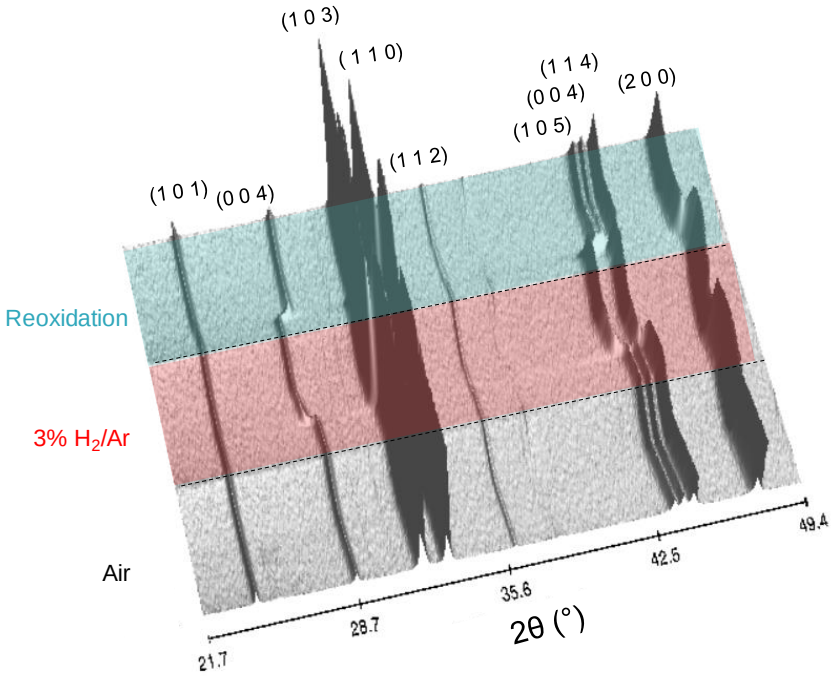

Figure 40. Evolution of the cell parameters during redox cycling for $Nd_{0.5}Sr_{1.5}MnO_{4\pm\delta}$

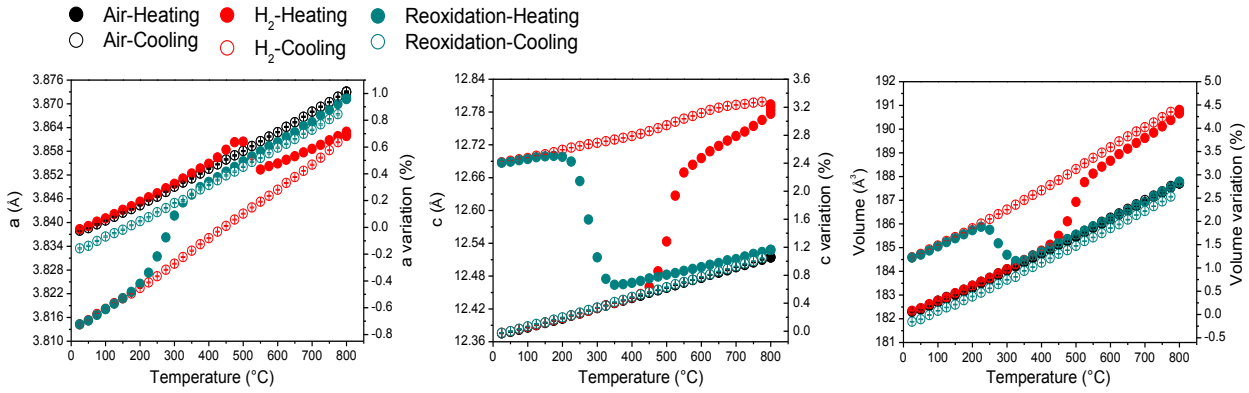

N5S15M shows a redox behavior similar to the $La_xSr_{2-x}MnO_{4\pm\delta}$ series. The first heating in air generate an increase of 1% and 1.1% of the *a* and *c* parameters, respectively, in comparison to 0.8% and 1.25 % for $La_{0.5}Sr_{1.5}MnO_{4\pm\delta}$ (L5S15M). As a consequence, N5S15M presents a slightly lower anisotropy in the thermal

expansion, with a volume change of 2.75%, which is smaller than for L5S15M (3%). During cooling the lattice parameters return linearly to the initial values.

The evolution of cell parameters during heating in reducing atmosphere occurs also in two steps, which are related to the weight losses observed during thermogravimetric experiment (Figure 31). The most notable evolution between 450 and 550 °C, is attributed to the Mn reduction from Mn^{4+} to Mn^{3+}, which induces a strong increase of the *c* parameter, while the *a* parameter decreases. Unlike the lanthanum phase, in the N5S15M phase, the latter decrease is slighter, what can be related to the fact that at the end of this drop the manganese has not been converted totally to Mn^{3+} ($Nd_{0.5}Sr_{1.5}Mn^{+3.29(4)}O_{3.85}$ at 550 °C), whereas in L5S15M the same reduction step leads to $Mn^{+3.09(3)}$ (590 °C). Between 550 and 800 °C, both *a* and *c* parameters smoothly increase, generating a whole volume change of ~1.5%, which is of the same magnitude as that obtained for L5S15M, but once again much smaller that of Ni in Ni/YSZ cermet. As in the case of L5S15M, the evolution of *a* and *c* parameters is associated to a Jahn Teller (JT) effect, where the stretching along *c*-axis is predominant with respect to the contraction along *a,b* axis, generating octahedral distortion. Finally, during reoxidation the lattice parameters return to their initial values, demonstrating the perfect reversibility of the reduction processes.

Thermal expansion coefficient (TEC) values obtained from the lattice parameter variation during cooling in air and hydrogen are $12.7(4) \times 10^{-6}\,K^{-1}$ and $14.4(2) \times 10^{-6}\,K^{-1}$ (25 - 800 °C), respectively. These values are in the same range of magnitude as for L5S15M, being in both cases comparable with those of the common LSGM, YSZ and GDC electrolytes (TEC~ 10-13 $x10^{-6}\,K^{-1}$) [74][75][79].

In situ Neutron Powder Diffraction (NPD)

All the NPD patterns of $La_{0.5}Sr_{1.5}MnO_{4\pm\delta}$ were refined in the space group *I4/mmm*. Beside profile parameters, the structural Rietveld refinements at each temperature included the *z* coordinate of the (La/Sr) site and axial oxygen atom (O2) and the anisotropic displacement parameters. During first test of the refinements, the oxygen occupancy of O2 (axial) was refined and since no significant change was observed, it was therefore fixed to full occupancy. Hence, to decrease the numbers of parameters and the potential correlation problems, only the occupancy of the equatorial oxygen site (O1) was refined. In addition, as for X-ray, no additional peaks or structural changes were detected during the experiment, indicating that no major changes concerning the oxygen sublattice was happening. Such refinement procedure gave good fits and acceptable R-factors; an example of graphical result of refinement at 850°C is given in Figure 41. Table 13 summarizes the refined oxygen occupancy, anisotropic thermal parameters for O1 and manganese oxidation state calculated from NPD data obtained during reduction (3%H_2/Ar). The bond lengths for all atoms are shown in Table 14. The variation of the lattice parameters, atomic coordinates and thermal parameters are shown in the Annex 6 (Table S1).

Figure 41. Neutron diffraction pattern for $La_{0.5}Sr_{1.5}MnO_{4\pm\delta}$ at 850°C in 3% H_2/Ar.

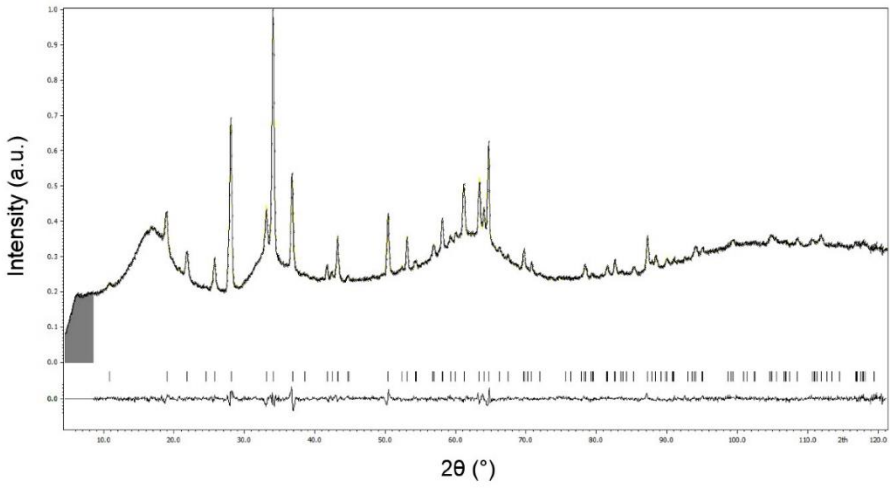

Table 13. Occupancies and anisotropic thermal parameters of O1, oxidation state of Mn for $La_{0.5}Sr_{1.5}MnO_{4\pm\delta}$ derived from *in situ* neutron diffraction data collected upon heating in 3% H_2/Ar.

Temperature (°C)	**O1**				Mn oxidation state	R_p	R_{wp}	χ^2
	Occupancy	U_{11}	U_{22}	U_{33}				
200	0.98(3)	0.008(4)	0.013(4)	0.007(4)	3.42(6)	3.23	4.20	1.24
250	0.96(3)	0.012(5)	0.015(5)	0.006(5)	3.34(6)	3.20	4.05	1.24
300	0.97(4)	0.022(5)	0.013(4)	0.003(4)	3.38(6)	3.15	4.07	1.21
350	0.96(4)	0.034(6)	0.006(4)	0.008(4)	3.34(6)	3.04	3.87	1.15
400	0.88(3)	0.037(7)	0.010(5)	0.010(5)	3.02(6)	3.14	4.08	1.20
410	0.88(3)	0.035(7)	0.006(5)	0.011(5)	3.02(6)	3.09	3.92	1.16
430	0.89(3)	0.048(8)	0.008(5)	0.006(6)	3.06(6)	3.25	4.12	1.21
450	0.92(3)	0.055(9)	0.009(5)	0.015(6)	3.18(6)	3.18	4.05	1.19
470	0.87(3)	0.059(9)	0.002(4)	0.009(6)	2.98(6)	3.25	4.14	1.22
490	0.86(3)	0.066(10)	0.001(5)	0.003(6)	2.94(6)	3.27	4.17	1.23
510	0.89(3)	0.064(9)	0.005(4)	0.009(6)	3.06(6)	3.11	3.95	1.16
530	0.86(3)	0.065(10)	0.001(5)	0.003(7)	2.94(6)	3.19	4.17	1.23
550	0.88(3)	0.062(9)	0.002(4)	0.016(6)	3.02(6)	3.15	4.00	1.18
570	0.89(3)	0.055(10)	0.001(5)	0.014(7)	3.06(6)	3.11	3.98	1.17
590	0.88(2)	0.053(10)	0.002(2)	0.011(6)	3.02(4)	2.94	3.75	1.10
610	0.86(3)	0.056(10)	0.008(5)	0.024(7)	2.94(6)	2.92	3.74	1.11
630	0.88(3)	0.055(9)	0.003(5)	0.012(6)	3.02(6)	2.97	3.79	1.12
650	0.84(3)	0.064(11)	0.001(5)	0.011(7)	2.86(6)	3.29	4.13	1.22
670	0.86(3)	0.074(11)	0.001(4)	0.020(7)	2.94(6)	2.97	3.78	1.10
690	0.88(3)	0.066(11)	0.003(5)	0.019(7)	3.02(6)	2.97	3.80	1.12
710	0.87(3)	0.074(12)	0.002(5)	0.015(8)	2.98(6)	3.12	3.93	1.15
730	0.85(4)	0.071(15)	0.003(8)	0.010(9)	2.90(8)	3.20	4.15	1.22
750	0.82(3)	0.063(12)	0.008(6)	0.015(7)	2.78(6)	2.99	3.84	1.13
770	0.84(3)	0.071(12)	0.001(5)	0.019(8)	2.86(6)	3.14	3.96	1.16
790	0.84(3)	0.079(13)	0.008(5)	0.019(8)	2.86(6)	3.17	3.97	1.16
810	0.83(3)	0.077(13)	0.007(6)	0.016(8)	2.82(6)	2.94	3.72	1.10
830	0.83(2)	0.072(11)	0.001(7)	0.017(8)	2.82(6)	3.02	3.91	1.14
850	0.81(3)	0.072(14)	0.011(7)	0.025(9)	2.74(6)	3.03	3.87	1.15

As can be seen in Figure 42, the evolution of the oxygen occupancies during reduction indicates an oxygen loss of ~25 % from 200 to 850°C, which generates a change in the mean oxidation state of Mn from +3.42(6) to +2.74(6) (See Table 13). The NPD results confirm that the mixed valence Mn^{4+}/Mn^{3+} is present up to 550°C

(+3.02(3)), changing to Mn^{3+}/Mn^{2+} when the temperature increase up to 850°C (+2.74), in agreement with the TG results mentioned above.

Figure 42. Occupancy factors of the equatorial oxygen sites (O1) of $La_{0.5}Sr_{1.5}MnO_{4\pm\delta}$ upon heating in 3% H_2/Ar, refined from neutron data under H_2 flow.

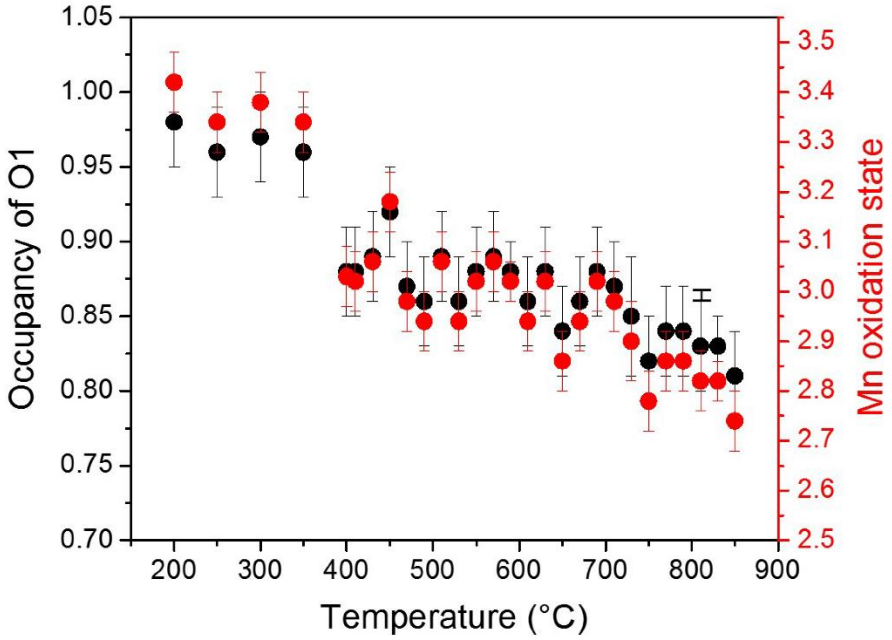

Previous studies have demonstrated that the reduction of oxidation state of the metal art the B-site of n=1 RP phases is linked to oxygen removal, leading to vacancy formation [58][13][80][81]. For example, the redox chemistry of $Pr_{0.5}Sr_{1.5}Cr_{0.5}Mn_{0.5}O_{4-\delta}$ reported by Bahout *et al.* [14] showed that when the sample was heated up to 700°C under 5% H_2/He, the fractional occupancy of equatorial oxygen (*4c* site) decreased to 0.90(2), generating at the same time an expansion of the *a* and *c* parameters (by ~1.2 % and ~1.6 %, respectively). In the present work, the analysis of the neutron diffraction data for $La_{0.5}Sr_{1.5}MnO_{4\pm\delta}$ in 3%H_2/Ar up to 850°C indicates also the formation of vacancies on the equatorial sites (O1) in the "MnO_2" layers, similar to what is reported for analogous structures such as $La_{0.8}Sr_{1.2}Co_{0.5}Mn_{0.5}O_{4-\delta}$ [13], $La_{1.2}Sr_{0.8}MnO_{3.94(2)}$ [59] or $Sr_2MnO_{4-\delta}$ [58]. The

fractional occupancy of O1 decreases from 0.98(3) to 0.81(3) between 200 and 850°C in hydrogen, accompanied by an increase of ~0.45 % of the *a* parameter and ~3.3 % of the *c* parameter (see Figure 38).

The formation of these oxygen vacancies (valence change) has a greater effect on the Mn-O2 bond length that on the Mn-O1 bond length, since this latter expands only by ~0.4 % during reduction (Figure 43a). Clearly the strong variation of the Mn-O2 apical bond causes a decrease of Mn-O1/Mn-O2 ratio upon heating in hydrogen, confirming the [MnO_6] octahedra deformation predominantly along *c*-direction (see Table 14). As already discussed, the Jahn-Teller nature of the Mn^{3+} cation induces an axial distortion effect, which is reflected in the increase of the axial Mn-O2 bond length (Figure 43b), resulting in an expansion of the *c* parameter and lattice volume. The heating in hydrogen induces a significant increase (~3.7 %) of the Mn-O2 bond between 200 and 550°C, which, after this temperature remains almost constant at ~2.09 Å (see Figure 43b and Table 14).

Figure 43. Variation of (a) Mn-O1 and (b) Mn-O2 bond lengths in $La_{0.5}Sr_{1.5}MnO_{4\pm\delta}$ during reduction.

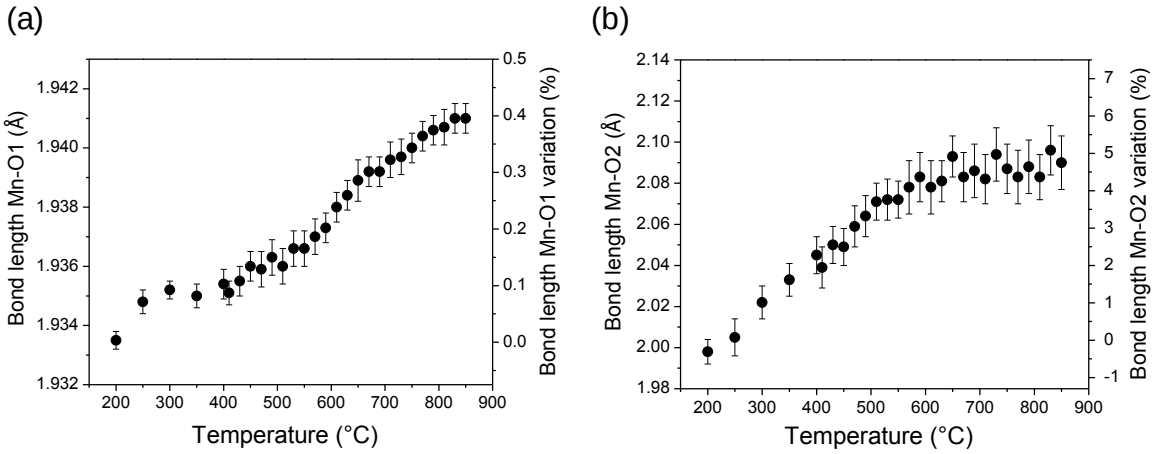

In addition, La/Sr-O2 bond length does not show any significant variation during reduction, suggesting that the perovskite layers are mainly responsible of the

expansion along the *c* axis, the rock-salt layers contribution being negligible (see Figure 44 and Table 14 and Annex 6). This behavior is similar to that obtained for the *c* parameter by HT-XRD, where a pronounced increase was evidenced between 400 and 550 °C (see Figure 38).

Figure 44. Variation of (a) La/Sr-O1 and La/Sr-O2 bond lengths in $La_{0.5}Sr_{1.5}MnO_{4\pm\delta}$ during reduction.

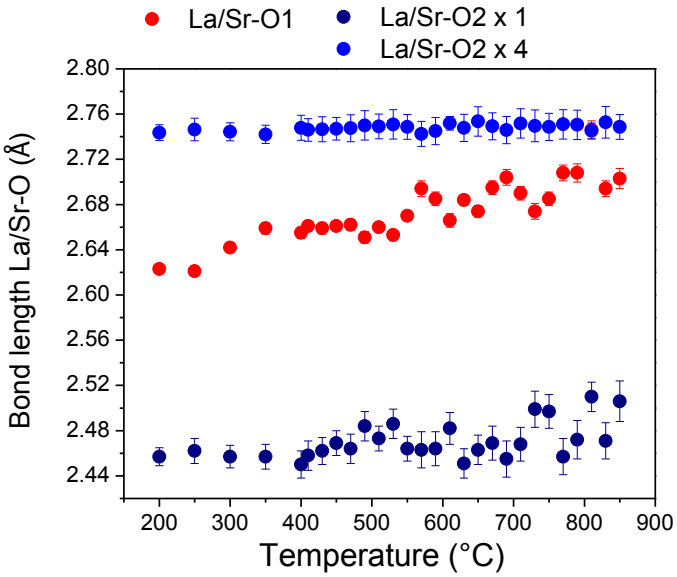

Table 14. Selected bond lengths (Å) in $La_{0.5}Sr_{1.5}MnO_{4\pm\delta}$ derived from *in situ* neutron diffraction data collected upon heating in 3% H_2/Ar.

Temperature (°C)	La/Sr-O1	La/Sr-O2 x 1	La/Sr-O2 x 4	Mn-O1	Mn-O2	Mn-O1/Mn-O2
200	2.623(3)	2.457(8)	2.7436(7)	1.9335(3)	1.998(6)	0.968
250	2.621(4)	2.462(11)	2.7464(10)	1.9348(4)	2.005(9)	0.965
300	2.642(4)	2.457(10)	2.7444(8)	1.9352(3)	2.022(8)	0.957
350	2.659(5)	2.457(11)	2.7421(8)	1.9350(4)	2.033(8)	0.952
400	2.655(5)	2.450(12)	2.7479(11)	1.9354(5)	2.045(9)	0.946
410	2.661(5)	2.458(13)	2.7460(10)	1.9351(4)	2.039(10)	0.949
430	2.659(5)	2.462(12)	2.7466(11)	1.9355(5)	2.050(9)	0.944
450	2.661(4)	2.469(11)	2.7470(10)	1.9360(5)	2.049(9)	0.945
470	2.662(5)	2.464(13)	2.7475(12)	1.9359(6)	2.059(10)	0.940
490	2.651(5)	2.484(13)	2.7500(13)	1.9363(6)	2.064(10)	0.938
510	2.660(4)	2.473(11)	2.7491(11)	1.9360(6)	2.071(9)	0.935

530	2.653(5)	2.486(13)	2.7509(13)	1.9366(6)	2.072(10)	0.935
550	2.670(4)	2.464(11)	2.7486(11)	1.9366(6)	2.072(9)	0.935
570	2.694(7)	2.463(16)	2.7425(11)	1.9370(6)	2.078(13)	0.932
590	2.685(6)	2.464(15)	2.7450(12)	1.9373(5)	2.083(12)	0.930
610	2.666(6)	2.522(14)	2.7518(6)	1.9380(5)	2.078(13)	0.933
630	2.684(5)	2.451(13)	2.7478(12)	1.9384(5)	2.081(10)	0.931
650	2.674(5)	2.463(13)	2.7535(13)	1.9389(7)	2.093(10)	0.926
670	2.695(6)	2.469(15)	2.7492(12)	1.9392(5)	2.083(12)	0.931
690	2.704(7)	2.455(16)	2.7459(12)	1.9392(5)	2.086(13)	0.930
710	2.690(6)	2.468(15)	2.7517(13)	1.9396(6)	2.082(12)	0.932
730	2.674(7)	2.519(16)	2.7496(14)	1.9397(6)	2.094(13)	0.926
750	2.685(6)	2.497(15)	2.7487(12)	1.9400(5)	2.087(12)	0.930
770	2.708(7)	2.457(16)	2.7510(13)	1.9404(5)	2.083(13)	0.932
790	2.708(8)	2.472(17)	2.7505(13)	1.9406(5)	2.088(13)	0.929
810	2.746(8)	2.510(3)	2.7452(7)	1.9407(6)	2.083(11)	0.932
830	2.694(7)	2.471(16)	2.7527(14)	1.9410(5)	2.096(12)	0.926
850	2.703(9)	2.526(18)	2.7486(11)	1.9410(5)	2.090(13)	0.929

The variation of the anisotropic atomic displacement parameters (ADP) upon heating in hydrogen are shown in Figure 45 and Table 13.

Figure 45. Anisotropic displacement parameters U_{11}, U_{22} and U_{33} for O1 in $La_{0.5}Sr_{1.5}MnO_{4\pm\delta}$ upon heating in 3% H_2/Ar. Note the anomalous behavior of U_{11}.

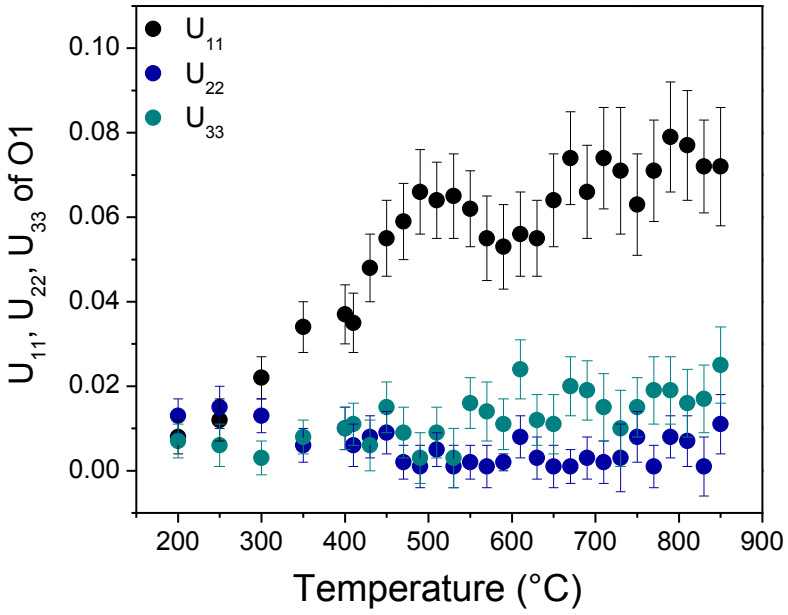

If, on one hand, the evolution of the U_{ii} components for the apical (O2) site is conform to what is expected for a classical thermal expansion, the behavior for the equatorial oxygen (O1) is clearly anomalous (see Figure 45). Indeed, the U_{11} component of this atom is i) much larger than U_{22} or U_{33}, indicating a kind of disorder in the direction perpendicular to the Mn-O1 bond ii) not regular with temperature, with a change of scheme around 500°C. It is difficult to conclude about the nature of this disorder (static or dynamic) since attempts to refine the ADP using anharmonic model [82] were not significantly better than harmonic ones. However, in oxide conductors, it is well known that this disorder is dynamic (with anharmonic ADP) and the anomalous behavior of ADP for O1 seems to indicate such behavior.

2.5 COMPATIBILITY BETWEEN ELECTRODE AND ELECTROLYTE MATERIALS

Possible chemical reactivity between $RE_xSr_{2-x}MnO_{4\pm\delta}$ (RE: La, Nd) and YSZ, GDC or LSGM was studied initially in air at high temperature, aiming to detect the undesirable formation of secondary phases during the electrode elaboration step (and, incidentally, in cathode conditions). The $RE_{0.5}Sr_{1.5}MnO_{4\pm\delta}$ composition was selected as representative of each series. Preliminarily, a powder of as-synthesized $RE_{0.5}Sr_{1.5}MnO_{4\pm\delta}$ material was mixed with a powder of YSZ ($Zr_{0.85}Y_{0.15}O_{1.925}$, Nextech Materials, USA, # 312005), GDC ($Ce_{0.9}Gd_{0.1}O_{1.95}$ Nextech Materials, USA, # 112101, pre-sintered at 1000 °C) or LSGM ($La_{0.8}Sr_{0.2}Ga_{0.8}Mg_{0.2}O_{3-\delta}$, Nextech Materials, USA, # 121501) in a 50:50 weight ratio, pressed into pellets and heat treated at 1200 °C for 10 h in the case of YSZ and GDC and at 900 °C for 10 h for LSGM (only for La-substituted manganite). Some additional treatment temperatures were considered in the case of GDC, in agreement with the studied range of temperature for electrode sintering, as described in the next section. The resulting samples were analyzed by X-ray diffraction (XRD) using a Bruker D8 ADVANCE

powder diffractometer working in Bragg Brentano geometry with Cu-$K_{\alpha1,2}$ radiation equipped with 1D Bruker LynxEye detector.

Figure 46a shows the XRD patterns for each electrode/electrolyte mixture before and after heat treatments in air. In the case of YSZ (Figure 46a), $La_{0.5}Sr_{1.5}MnO_{4\pm\delta}$ reacts to form the insulating phase $SrZrO_3$ with lanthanum strontium manganite ($La_{1-x}Sr_xMnO_3$) by-product. Apparently, an $La_xSr_{2-x}MnO_{4\pm\delta}$-type phase remains after heating but in a very low proportion. The formation of $SrZrO_3$ as secondary phase has been previously reported between LSCF cathode and YSZ electrolyte. This high reactivity begins around 800 °C after 200 h of heating, and is more evident above 1100 °C when $La_2Zr_2O_7$ begins to form concomitantly [83][84].

Even if the sintering temperature in air was lower with respect to other electrolytes, the chemical reactivity of $La_{0.5}Sr_{1.5}MnO_{4\pm\delta}$ with LSGM electrolyte is also high, resulting in the formation of additional phases such as $LaSrGaO_4$ and La_2O_3 with partial decomposition of the initial RP manganite (Figure 46b). Such result is in disagreement with what was recently described by J. Zhou *et al.* [19], who reported that $La_{0.6}Sr_{1.4}MnO_{4\pm\delta}$ is chemically compatible with LSGM.

The chemical compatibility between $La_{0.5}Sr_{1.5}MnO_{4\pm\delta}$ and GDC in air shows that, after a heat treatment up to 1250 °C, both materials remain unchanged and no major modification of XRD patterns or additional peaks are evidenced (Figure 46c). This stability with GDC electrolyte has also been proven for LSM [85] and $La_xSr_{2-x}MnO_{4\pm\delta}$ (x= 0.4, 0.5, 0.6) synthesized in different conditions, but tested at lower temperature (1000 °C) [16][17]. At 1200 and 1250 °C, structure refinements using XRD data show a slight variation of the lattice parameters of each phase (Table 15), possibly due to cation interdiffusion.

Figure 46. XRD patterns after reactivity test of $La_{0.5}Sr_{1.5}MnO_{4\pm\delta}$ in air with (a) YSZ at 1200 °C, (b) LSGM at 900 °C, (c) GDC at 1200, 1250 and 1300 °C.

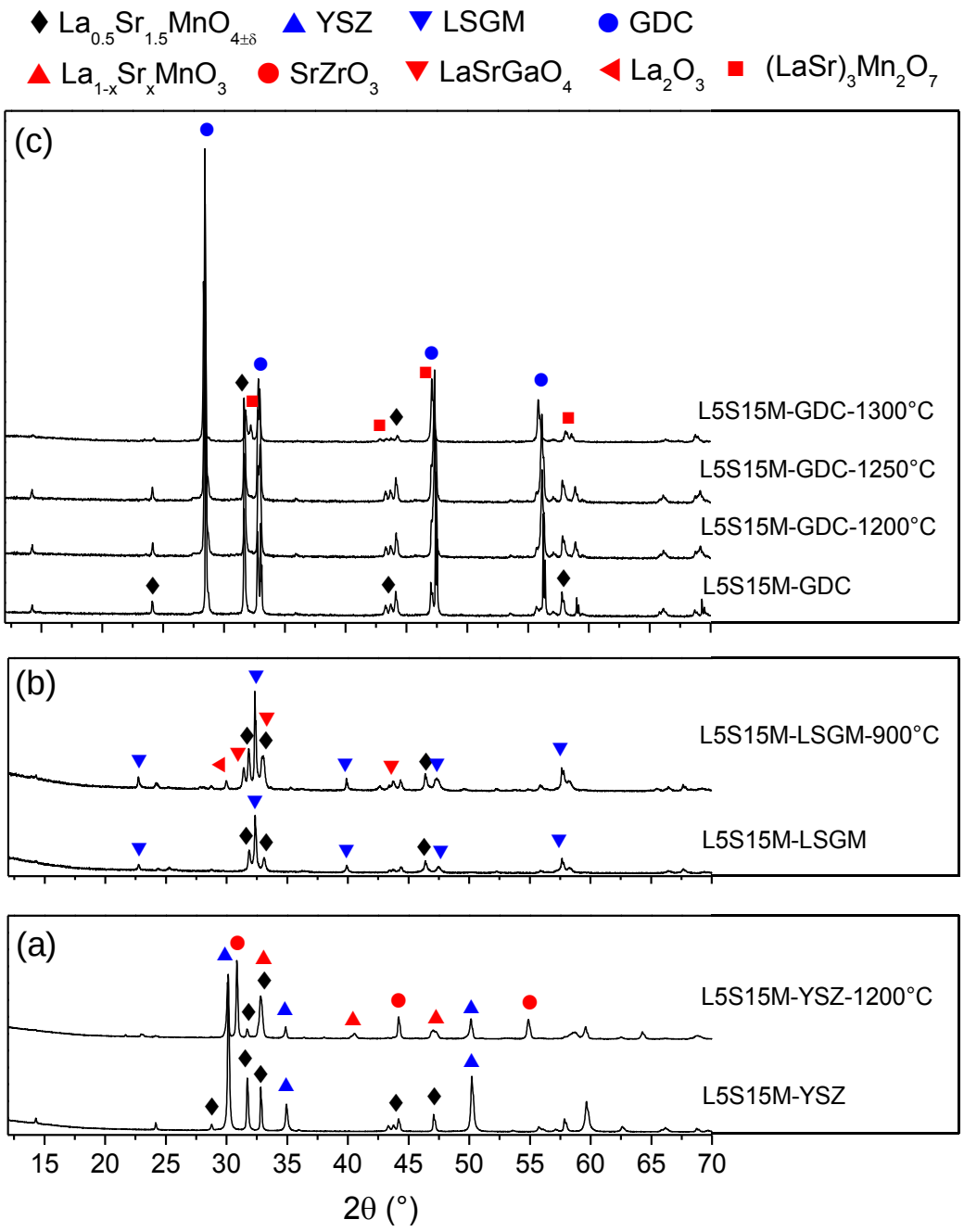

The decrease of $La_{0.5}Sr_{1.5}MnO_{4\pm\delta}$ cell volume after heating can be due to the substitution of the small Ce^{4+} or Gd^{3+} cations ($R^{IX}_{Ce^{4+}}$= 1.02 Å, $R^{IX}_{Gd^{3+}}$= 1.107 Å [41]) at the position of larger La^{3+} or Sr^{2+} cations ($R^{IX}_{La^{3+}}$ = 1.216 Å, $R^{IX}_{Sr^{2+}}$= 1.31 Å [41]), compensated by La/Sr diffusion into ceria, as suggested by the increase of GDC lattice parameter [86][87]. Nevertheless, an additional $(La,Sr)_3Mn_2O_7$ phase is formed after a heating at 1300 °C, possibly due to the fact that the high temperature begins to destabilize the n=1 RP structure in favor of higher terms of the RP series. In this precise case, it is worth mentioning that during the synthesis of $LaSr_2Mn_2O_7$, such phase only begins to form at 1200 °C in coexistence with a Sr_2MnO_4 phase, and becomes single phase at 1400 °C [88].

Table 15. Structural parameters of $La_{0.5}Sr_{1.5}MnO_{4\pm\delta}$-GDC mixture before and after the reactivity tests in air, calculated by Rietveld refinement using powder X-ray diffraction data.

	Before treatment		After treatment at high temperature			
			1200 °C/10 h		**1250 °C/10 h**	
	L5S15M	GDC	L5S15M	GDC	L5S15M	GDC
a (Å)	3.8614(1)	5.4187(6)	3.8585(6)	5.4309(4)	3.8471(8)	5.4599(6)
c (Å)	12.4201(7)		12.4212(32)		12.4042(9)	
V (Å^3)	185.18(3)	159.11(2)	184.93(2)	160.19(6)	183.58(6)	162.76(9)
R_p	4.64		5.04		6.53	
R_{wp}	5.94		6.42		9.09	
X^2	1.3		1.6		1.8	

The chemical reactivity test of $Nd_{0.5}Sr_{1.5}MnO_{4\pm\delta}$ with YSZ and GDC electrolytes was also carried out, in order to analyze the influence of the rare earth element on the chemical reaction between the two components. Figure 47 shows a comparison of the XRD patterns of the electrode/electrolyte mixture before and after heat treatments in air.

Figure 47. XRD patterns after reactivity test of $Nd_{0.5}Sr_{1.5}MnO_{4\pm\delta}$ in air with (a) YSZ at (b) GDC at 1200 °C.

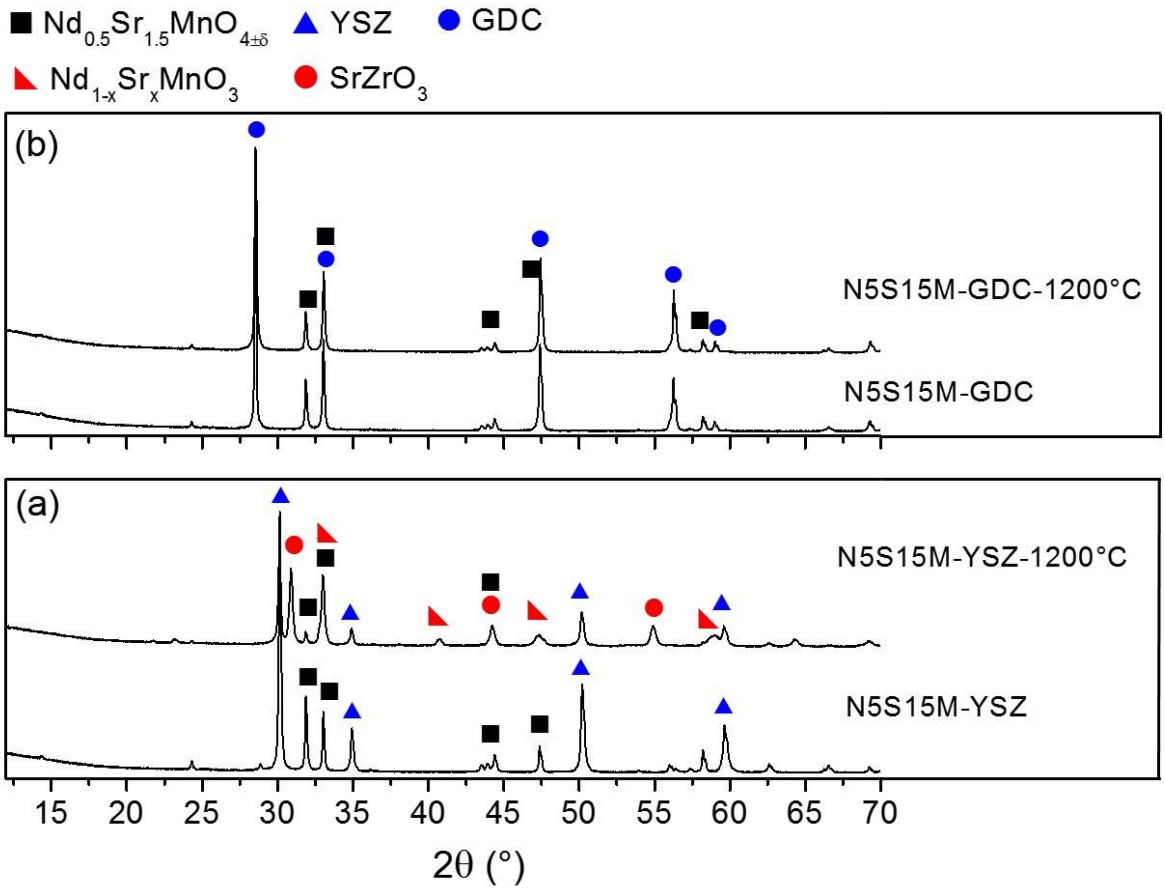

As for L5S15M, N5S15M highly reacts with YSZ electrolytes, showing a partial decomposition of N5S15M with formation of $SrZrO_3$ and $Nd_{1-x}Sr_xMnO_3$ phases (Figure 47a). On the other side, and as depicted in Figure 47b, no reaction occurs between N5S15M and GDC, confirming the good chemical compatibility of these oxides at high temperature. According to those results, the result of the chemical reactivity test does not really depend on the rare earth at the A-site, what would have been probably the case if the formation of an La zirconate would have occurred between L5S15M and YSZ, instead of $SrZrO_3$. Considering the latter result, L5S15M manganite was finally selected for the rest of the study.

Considering it of high importance for the cell tests in anode conditions, the reactivity of L5S15M with GDC was also evaluated in reducing atmosphere by treating the same powder mixture in 3% H_2/Ar at 850°C for 16 h. The XRD patterns before and after treatment are shown in Figure 48. After heating, the presence of the same indexed peaks is observed corresponding to (reduced) L5S15M and GDC without any other additional phases.

Figure 48. XRD patterns before and after reactivity test of $La_{0.5}Sr_{1.5}MnO_{4\pm\delta}$ with GDC in diluted hydrogen at 850 °C.

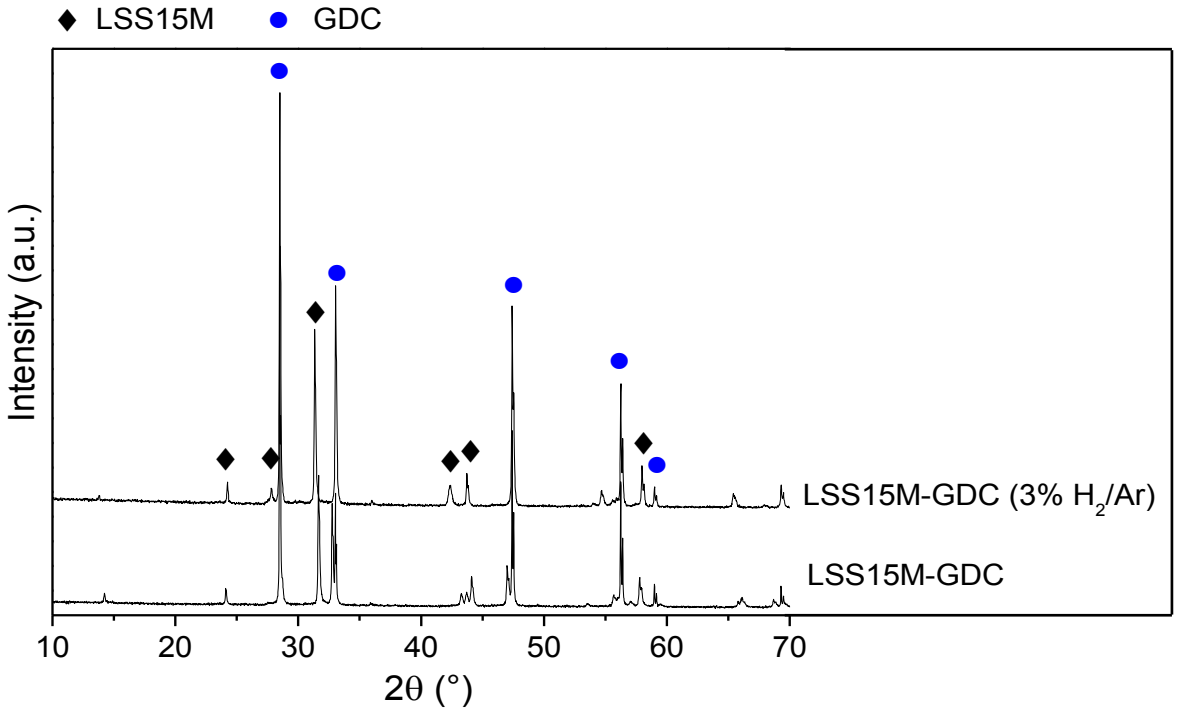

As observed in Table 16, the heat treatment in reducing atmosphere leads to a remarkable decrease of a-parameter and increase of c-parameter for the $La_{0.5}Sr_{1.5}MnO_{4\pm\delta}$ phase. The obtained values are in complete agreement with those of reduced L5S15M single phase presented above. The behavior is associated to reduction from Mn^{4+} to Mn^{3+}, which induce octahedron deformation that is related both to the Jahn-Teller effect and the formation of oxide-ion vacancies (see Chapter

2, sections 2.3.2 and 2.4.2). Additionally, the similarity of GDC lattice parameter before and after treatment in hydrogen confirm that, in such conditions, no noticeable cation cross diffusion is evidenced.

Table 16. Structural parameters of $La_{0.5}Sr_{1.5}MnO_{4\pm\delta}$ -GDC mixture before and after the reactivity tests in reducing atmosphere, calculated by Rietveld refinement using powder X-ray diffraction data.

	Before treatment		After treatment	
			3% H_2/Ar	
	L5S15M	GDC	L5S15M	GDC
a (Å)	3.8614(1)	5.4187(6)	3.8284(1)	5.4187(1)
c (Å)	12.4201(7)		12.8158(7)	
V (Å^3)	185.18(3)	159.11(2)	187.83(1)	159.10(2)
R_p	4.64		4.54	
R_{wp}	5.94		5.93	
c^2	1.3		1.42	

These results allow us to conclude that $La_{0.5}Sr_{1.5}MnO_{4\pm\delta}$ is chemically compatible with GDC electrolyte both in oxidizing and reducing atmosphere under the conditions investigated here. It is worth remembering that the material presented thermal expansion coefficients (TEC) of 12.3(1)x10^{-6} K^{-1} in air and 13.7(6)x10^{-6} in reducing atmosphere between RT to 850 °C. These values are comparable with the range of TEC values for doped ceria (12-13x10^{-6} K^{-1}), ensuring good thermomechanical compatibility between L5S15M and GDC electrolyte [74][75][76].

2.6 ELECTRICAL CONDUCTIVITY OF THE $RE_xSr_{2-x}MnO_{4\pm\delta}$ (RE: La, Nd) SERIES

In the course of the chapter, we have shown which members of the family fulfill the requirement of stability in oxidizing and reducing medium as the first condition to be used as symmetrical electrodes. In this way $La_xSr_{2-x}MnO_{4\pm\delta}$ (x= 0.25, 0.4, 0.5 and 0.6) series was chosen to evaluate the electrical properties in oxidizing and reducing

atmosphere. Preliminarily, the dilatometric analyses were performed in order to know the optimal conditions of sintering and therefore to form dense pellets.

2.6.1 EXPERIMENTAL SECTION

2.6.1.1 Dilatometric analysis

The thermal behavior of the materials was studied by dilatometry. Dilatometry measurements were carried out in air on pellets that were previously pressed at 1700 bar. The tests were performed using a Netzsch DIL 402C system in horizontal geometry. The treatment performed is as follows:

$$50°C \xrightarrow{5°C/min} 1600°C(10\ min) \xrightarrow{5°C/min} 50°C \qquad (2\text{-}19)$$

These experiments made it possible to determine the optimum sintering temperatures, for preparing the pellets and bars for conductivity measurements, by identifying the temperature at which the sintering speed (or withdrawal speed) is maximum. In addition, it is generally possible to calculate the thermal expansion coefficients during cooling, according to the following equation:

$$\propto = \frac{dL}{L_0} x \frac{1}{dT} \qquad (2\text{-}20)$$

Where L_0 is the initial length of the bar and dL/dT is the rate of change of that linear dimension per unit change in temperature.

2.6.1.2 Electrical conductivity measurements

The electrical properties of the $La_xSr_{2-x}MnO_{4\pm\delta}$ (x= 0.25, 0.4, 0.5 and 0.6) series as well as $Nd_{0.5}Sr_{1.5}MnO_{4\pm\delta}$ were evaluated by measurement of (total) electrical conductivity using four-point probe DC technique in air and reducing atmosphere at

variable temperature. The cylindrical pellets/bars (~4 mm in diameter and ~8 mm in thickness) were prepared by densification of the powders, which were uniaxially then isostatically pressed at a pressure of 190 and 1700 bar, respectively. The cylindrical samples were sintered at 1400 °C (see section 2.5.2.1) to obtain bars with ~85% relative density. Figure 49 shows the schematic representation of the sample, where the contact points are the two opposite sides (points 1, 4) and the two rings (gold wire) separated by a L distance (points 2, 3). The measurement method then includes a forced current through the outer points 1 and 4 and a measurement of the voltage drop over points 2 and 3, using a very high Ohmic measurement device, so that the current flowing through pin 2 and 3 is nearly zero.

Figure 49. Schematic representation of the sample for four-point probe DC measurement of electrical conductivity.

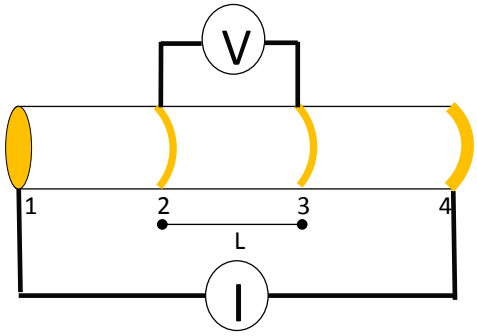

The measurements were carried out with a cell consisting of alumina support tubes through which pass the collectors of gold (Figure 50). A thermocouple is placed next to the sample to measure the temperature. The experiments were performed in two different atmospheres: air (for cathode applications) and 3% H_2/Ar (for anode applications), from 800°C to ~ 100°C. A direct current between 5 and 100mA in air and between 0.5 and 2 mA in 3% H_2/Ar was passed through the two outside terminals, and the voltage was measured between the two inside terminals, using a BioLogic SP-300 Potentiostat-Galvanostat.

Figure 50. Experimental measuring device for four-point probe DC measurement of electrical conductivity.

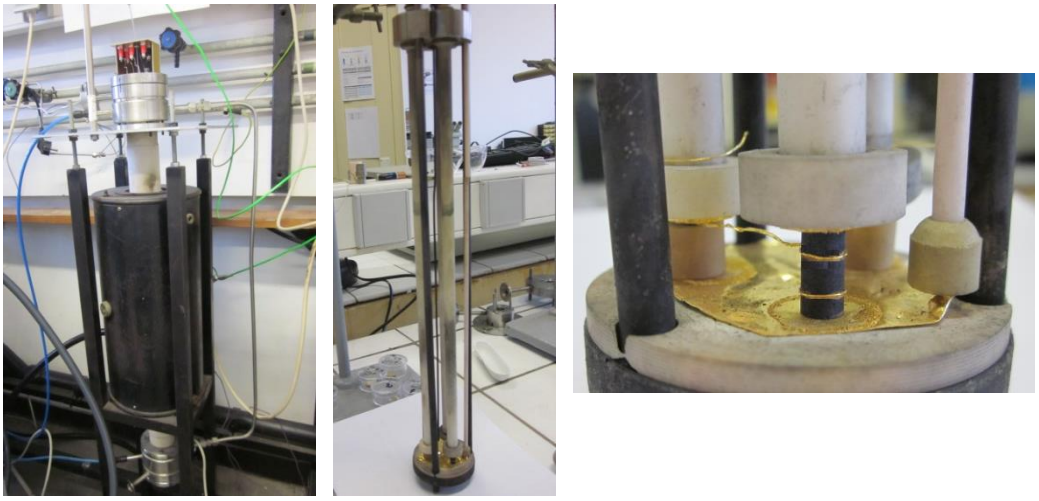

The total conductivity was estimated following the Ohm's Law, where the electrical resistance of a circuit component or device is defined as the ratio of the applied voltage to the electric current which flows through the sample:

$$R = \frac{V}{I} \qquad (2\text{-}21)$$

Where *R* is the resistance (ohms), V is the voltage (volts) and *I* is the current (amperes).

The resistance is dependent on the resistivity *ρ* multiplied by *L*, the wire length divided by the area *A* of the section of the resistor, and the conductivity (*σ*) is the inverse of the resistivity, according to:

$$R = \rho\left(\frac{L}{A}\right), \quad \sigma = \frac{1}{R}\left(\frac{L}{A}\right) \qquad (2\text{-}22)$$

Where *σ* is the conductivity (Siemens*cm^{-1}), *R* is the resistance (Ω), *L* is the length between points 2 and 3 (cm) and *A* is the area (circle) of the cross section (cm^2)

The conductivity was corrected for the influence of porosity, according to the following equation [89]:

$$\sigma_{corrected} = \frac{\sigma_{measured}}{\left[1-\left(\frac{\prod_{total}}{100}\right)\right]^2} \qquad (2\text{-}23)$$

Where $\prod_{total}$ is the porosity (%)

The activation energy of conduction was calculated by the standard Arrhenius model:

$$\sigma = \frac{A}{T} exp\left(\frac{-Ea}{kT}\right) \qquad (2\text{-}24)$$

Where E_a is the activation energy (eV), A is the pre-exponential factor, K is the Boltzmann constant and T is the absolute temperature (K)

2.6.2 RESULTS

2.6.2.1 Thermal behavior – Dilatometry test

Before dilatometry analysis, it is necessary to evaluate the thermal stability of materials at very high temperature in air, in order to avoid destruction or structural changes in the material due to sintering process. This test was performed on $La_{0.5}Sr_{1.5}MnO_{4\pm\delta}$, taken as the intermediate composition in $La_xSr_{2-x}MnO_{4\pm\delta}$ series. Figure 51 shows the XRD patterns of powders heating in air from 1350°C to 1450°C during 48 h. $La_{0.5}Sr_{1.5}MnO_{4\pm\delta}$ does not show any change in the XRD patterns up to 1400°C. This indicates that the sample is thermodynamically stable at such temperature. On the contrary, above 1425°C, additional peaks assigned to the $LaSr_2Mn_2O_7$ (RP n=2) phase are observed [90][91].

Figure 51. Thermal stability of $La_{0.5}Sr_{1.5}MnO_{4\pm\delta}$, between 1350 and 1450°C in air.

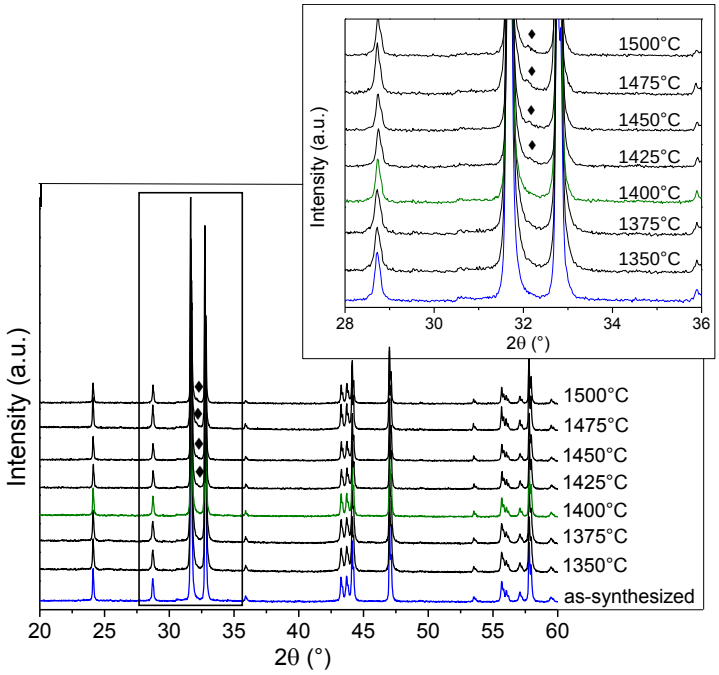

The dilatometry test to determinate optimal sintering temperature was initially performed on $La_{0.5}Sr_{1.5}MnO_{4\pm\delta}$ phase, prepared by solid state reaction at 1300°C (section 2.2.1). The dilatometric curve shows that the shrinkage starts at 1375°C, and the contraction or sintering is maximum at 1455°C (Figure 52).

Figure 52. Dilatometric curve of $La_{0.5}Sr_{1.5}MnO_{4\pm\delta}$ prepared by solid state reaction. The derivative curve (red) was normalized for easier comparison.

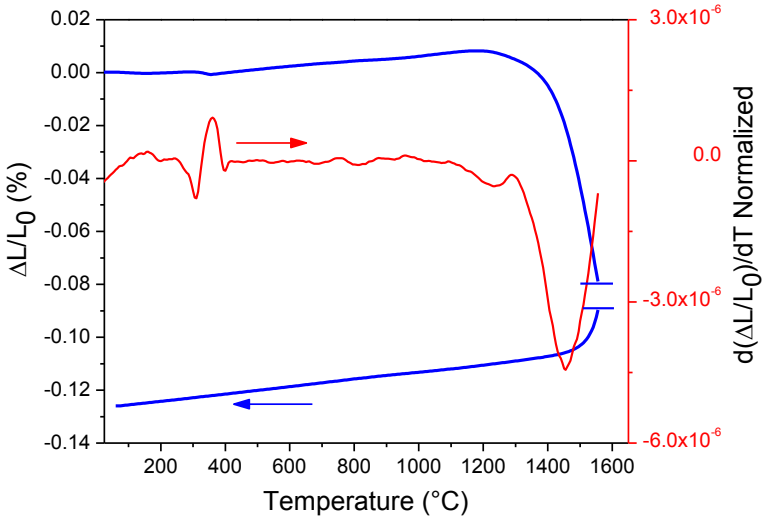

Using this information, and with the aim of preparing the sample for the conductivity test, dense bars were prepared at different temperatures (Table 17). The theoretical density (d_{cal}) was calculated according to the equation (2-10):

$$d_{cal} = \frac{M*Z}{N_A V} \qquad (2\text{-}25)$$

Where M is the molar mass, Z is the number of formula units per unit cell, N_A is the Avogadro's number and V is the cell volume. The theoretical density for $La_{0.5}Sr_{1.5}MnO_{4\pm\delta}$ is 5.78 g/cm^3.

Table 17. Sintering treatments and compacity for $La_{0.5}Sr_{1.5}MnO_{4\pm\delta}$ prepared by solid state reaction.

Test	d_{exp}	Sintering (°C) -Time (h)	Compacity (%) d_{exp}/d_{cal}
1	3.99	1350 – 24	69.1
2	4.08	1350 – 48	70.7
3	4.13	1400 – 24	71.6
4	4.20	1400 – 48	72.7

All sintering tests from powder prepared at 1300°C by solid state reaction generated porous or cracked bars. Therefore, to obtain dense bars for the conductivity test, it was necessary to use the powders prepared by sol-gel method, which produces a material with a smaller grain size that can be generally sintered more easily. Figure 53 shows the dilatometric curves of $La_xSr_{2-x}MnO_{4\pm\delta}$ prepared by sol-gel method at 1100°C (section 2.2.2.1). The pellet contraction or sintering shifts to lower temperature, *i.e.* for x=0.5, it decreases from 1455 °C (SS) to around 1400 °C (SG). Based on these results, several sintering tests were performed (
Table 18), using $La_{0.5}Sr_{1.5}MnO_{4+\delta}$ synthesized by sol gel method (as an example of the $La_xSr_{2-x}MnO_{4\pm\delta}$ series). Under these conditions, it was possible to obtain bars with compacity greater than 85%.

Figure 53. Dilatometric curves of $La_xSr_{2-x}MnO_{4\pm\delta}$ prepared by sol-gel method. The derivative (dotted curves) was standardized for easier comparison.

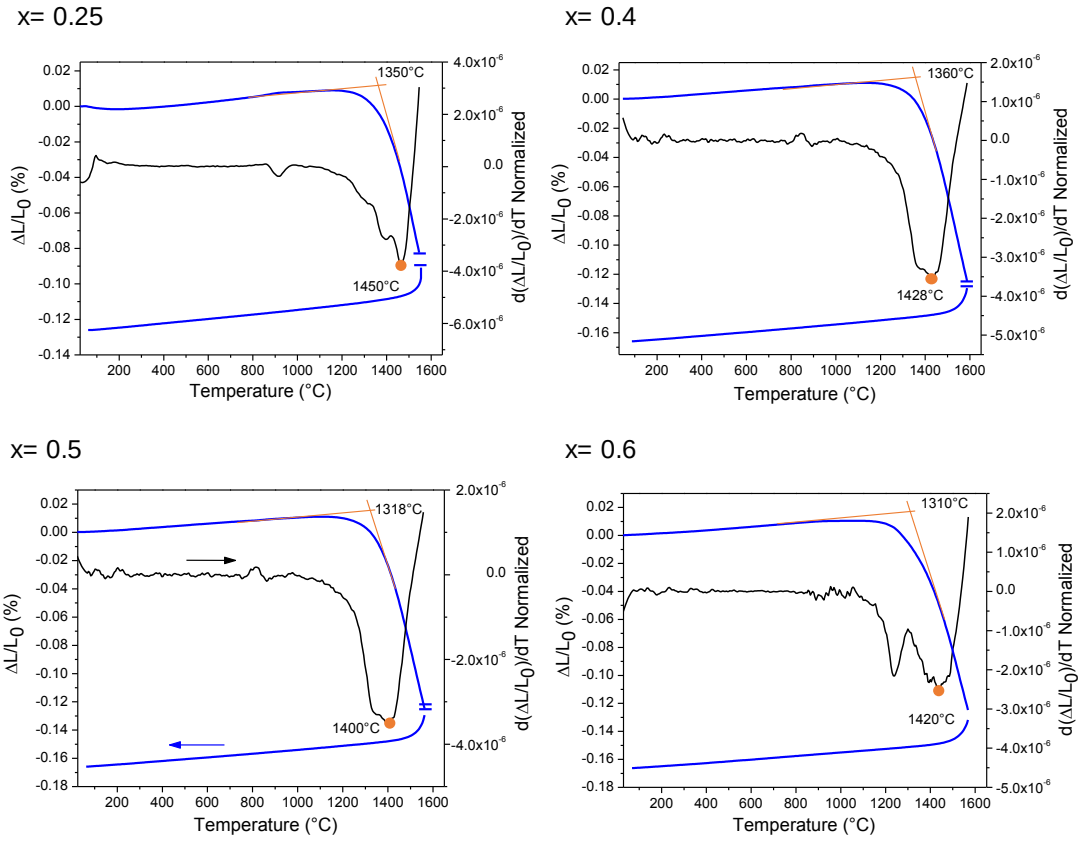

Table 18. Sintering treatments and compacity for $La_{0.5}Sr_{1.5}MnO_{4\pm\delta}$ prepared by sol-gel method.

Test	d_{exp}	Sintering (°C) -Time (h)	Compacity (%) d_{exp}/d_{cal}
1	4.70	1350 - 24	81.3
2	4.74	1350 - 48	82.1
3	5.06	1400 - 24	87.6
4	5.08	1400 - 48	87.8

For the other compositions, the sintered bars for conductivity measurements were prepared using the powders synthesized by sol-gel method. The exact sintering conditions that have been applied to prepare all samples for conductivity

measurements were T=1400 °C for 24 h in air. The compacity values were 86.5, 87.2, 87.6, 86.9 and 91.3% for $La_xSr_{2-x}MnO_{4\pm\delta}$ (x= 0.25, 0.4, 0.5, 0.6) and $Nd_{0.5}Sr_{1.5}MnO_{4\pm\delta}$, respectively.

2.6.2.2 Electrical conductivity measurements

For all compositions and atmospheres of measurements, the conductivity is found of semiconducting-type with a clear increase of σ when the temperature is raised. The evolution of electrical conductivity as a function of temperature for $La_xSr_{2-x}MnO_{4\pm\delta}$ (x≥0.25) and $Nd_{0.5}Sr_{1.5}MnO_{4\pm\delta}$, measured in air and diluted hydrogen, is represented in Figure 54 using an Arrhenius plot.

Table *19* shows the maximum conductivity at 800 °C and the activation energies (E_a) calculated from the slope of the Ln(σT) vs. 1000/T curves.

Figure 54. Arrhenius plot of the total conductivity of $La_xSr_{2-x}MnO_{4\pm\delta}$ (x=0.25, 0.4, 0.5, 0.6) in air and 3% H_2/Ar.

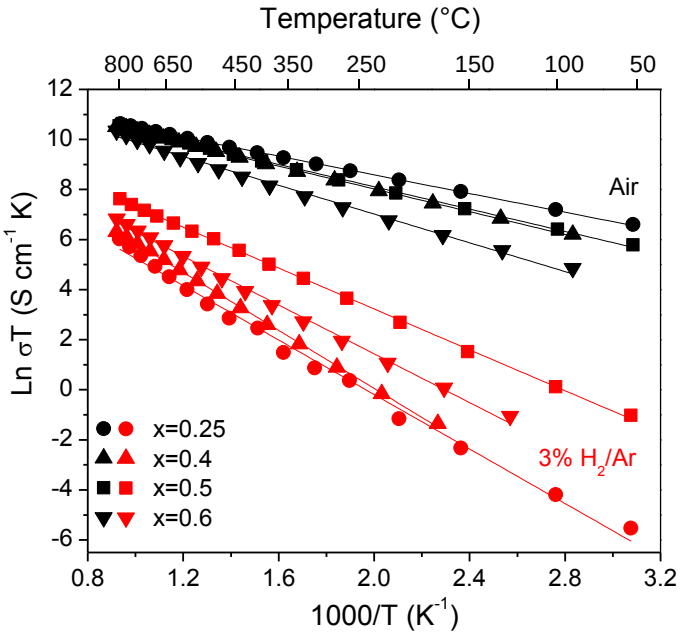

Table 19. Conductivity values at 800 °C and activation energy values for $La_xSr_{2-x}MnO_{4\pm\delta}$ (x=0.25, 0.4, 0.5, 0.6) in air and 3% H_2/Ar. A comparison to literature values for RP manganites and LSCM is made.

Sample	**x**	Temperature	Conductivity (S cm^{-1})		Activation Energy (eV)	
			Air	3% H_2/Ar	Air	3% H_2/Ar
L25S175M	**0.25**	800 °C	38.6	0.4	0.16(1)	0.46(1)
L4S16M	**0.4**		33.5	0.5	0.19(2)	0.49(4)
L5S15M	**0.5**		35.6	1.9	0.19(2)	0.35(2)
L6S14M	**0.6**		28.8	0.8	0.24(6)	0.41(7)
$La_xSr_{2-x}MnO_4$	0.5 [2]		10.0		0.15	
	0.5 [15]		<5.7		0.29	
	0.6 [17]		5.5	0.004	0.11	1.395
	0.6 [15]		5.7		0.28	
	0.6 [18]*		2.5	0.13		
	LSCM [80]	900 °C	38.6	1.49	0.21	0.56

*porous electrode

For the $La_xSr_{2-x}MnO_{4\pm\delta}$ compounds, the conductivity values at 800 °C in air varies from 28.8 S cm^{-1} to 38.6 S cm^{-1}, the maximum value being obtained for the composition x=0.25, higher than the previously reported values for $La_{0.5}Sr_{1.5}MnO_{4\pm\delta}$ (σ ~ 8 S cm^{-1}) [12] or $La_{0.6}Sr_{1.4}MnO_{4\pm\delta}$ (σ = 5.5 S cm^{-1}) [15][16][19] at the same temperature, possibly due to both the compacity difference and the sintering conditions. Even if the difference is not very pronounced between x=0.4 and 0.5 compositions, it seems clear from Figure 54 that the higher the La content, the lower the conductivity. Such phenomenon was already reported by C.N. Munnings *et al.* [15] for the same RP manganites and by H. Taguchi *et al.* for the analogue $Nd_xCa_{2-x}MnO_{4\pm\delta}$ materials, *i.e.* with a global decrease of the conductivity along the series for x>0.1 [42].

Based on the values of activation energy, from 0.16 to 0.24 eV, the evolution with temperature of conductivity can be explained by a small polaron mechanism, in agreement with what is generally observed for numerous perovskite or RP manganites and chromo-manganites and mainly associated with the presence of mixed valent Mn cations at the B-site [12][92]. Concerning the conduction

mechanism in those RP manganite materials, several authors report that the electronic conduction occurs due to the hopping of electrons (e') or electron holes ($\dot{h}$) from one Mn cation to the neighboring Mn cation ion, through the σ or π-bonds [19][42]. In this sense, the conductivity is affected both by the number of charge carriers as by the crystal structure. In this latter case, and as already described in literature, the Mn-O-Mn conduction path makes particularly critical the possible changes of basal Mn-O1 distances (strictly speaking, the angle Mn-O1-Mn would be also worth considering but in our case no structural distortion is evidenced in the studied materials that remain tetragonal with *I*4/*mmm* space group, so that such angle values remain constant at 180°, *i.e.* the ideal situation for Mn and O orbital overlap) [19][92][93].

In air, and as described above, all the materials studied in this work have a mixed valence Mn^{4+}/Mn^{3+}, and are consequently much more active than Sr_2MnO_4 [15] (that contains only Mn^{4+}), since the electron transfer is enhanced through the Mn^{4+}-O-Mn^{3+} path. Indeed, in the $Nd_xCa_{2-x}MnO_{4\pm\delta}$ series, Taguchi *et al.* could determine the Seebeck coefficients and conclude that the materials are n-type semiconductors in air with carriers being electrons [42]. Nevertheless, and even if the carrier concentration is found to slightly improve with x in the latter series, the carrier mobility seems much strongly affected and drops because of the increase of the equatorial Mn-O bond length. Indeed, according to Munnings *et al.*, the conductivity decrease within the $La_xSr_{2-x}MnO_{4\pm\delta}$ series for $x \geq 0.2$ is only explained by the enlargement of the equatorial Mn-O1 distance [15], a phenomenon also evidenced in the present study, as already discussed before (see sections 2.2.2.1, 2.3.2.1).

As can be seen in Figure 54, a significant drop in conductivity is observed in reducing atmosphere as well as a raise in activation energies. Such phenomenon is relatively common in all those perovskite-like manganites, and values are in the same range than for LSCM (0.56 eV) [94] or $Ce_{0.1}La_{0.65}Sr_{0.25}Cr_{0.5}Mn_{0.5}O_{3-\delta}$ (0.56 eV) [10] reference anode materials. The conductivity values range from 0.4 S cm^{-1} to 1.9 S

cm^{-1} at 800 °C for the entire series. Such results are in agreement with longer Mn-O bond length along the a/b basal planes in reducing atmosphere (Table 8 and 14); an additional explanation, proposed by J. Zhou et al., would be the presence of oxygen vacancies in the reduced samples, that would block the carrier hopping through the Mn-O1-Mn path [19]. Nevertheless, contrary to the measurements in air, the conductivity in diluted hydrogen is notably higher for $La_{0.5}Sr_{1.5}MnO_{4\pm\delta}$, a phenomenon that is not completely understood but could be related to the stoichiometry of this phase, $La_{0.5}Sr_{1.5}Mn^{+2.90(3)}O_{3.70}$, with the lowest Mn^{2+} concentration in anode conditions for the whole series (see Table 9).

2.7 CONCLUSIONS

In this chapter, the n=1 Ruddlesden-Popper manganites of general formula $RE_xA_{2-x}MnO_{4\pm\delta}$ (RE: La, Nd and A: Sr, Ca) have been studied. The first series $La_xSr_{2-x}MnO_{4\pm\delta}$ can be successfully synthesized in the range of compositions $0.25\leq x\leq 0.6$. In this case, all materials present a K_2NiF_4 structure with space group *I*4/*mmm* and a mixed valence Mn^{4+}/Mn^{3+} that varies from +3.79(3) to +3.55(3), depending on the lanthanum concentration. For the second family, $Nd_xSr_{2-x}MnO_{4\pm\delta}$, the Nd solubility range, after synthesis sol-gel in air at 1100°C, is found a bit narrower with $0.25<x<0.6$, the composition below and above those limits presenting $SrCO_3$ and Nd_2O_3 impurities, respectively. The members of the third series, $La_xCa_{2-x}MnO_{4\pm\delta}$, cannot be obtained as single phases, regardless the degree of lanthanum substitution tested (x= 0.15, 0.25 and 0.5). If it is perhaps related to the synthesis method and the voluntarily low temperature of synthesis for the two former substitution level, the x=0.5 composition is definitely a mixture of oxides after synthesis in air. For the fourth series $Nd_xCa_{2-x}MnO_{4\pm\delta}$, single samples are obtained when x=0.25, 0.4 and 0.5, in all cases with a slightly distorted K_2NiF_4-type structure depending on the neodymium content.

The stability in reducing atmosphere of $RE_xA_{2-x}MnO_{4\pm\delta}$ materials has been investigated. The prepared $Nd_xCa_{2-x}MnO_{4\pm\delta}$ materials are all unstable in reducing environment, being decomposed into an oxide mixture, which does not make them useful as SOFC anode materials. Focusing on both $RE_xSr_{2-x}MnO_{4\pm\delta}$ series (RE: La, Nd), we can conclude that the La-substituted materials with $0.25\leq x\leq 0.6$ and the Nd-substituted materials with $0.4\leq x\leq 0.6$ are completely stable without strong structural modification upon heating in reducing atmosphere, *i.e.* maintaining their K_2NiF_4-type structure with *I4/mmm* symmetry.

From thermogravimetric (TG), high temperature (HT)XRD and neutron powder diffraction (NPD) analysis, carried out for $La_{0.5}Sr_{1.5}MnO_{4\pm\delta}$ material, it can be inferred that the ability of manganese to reversibly change its oxidation state between Mn^{4+}, Mn^{3+} and, to some extent, to Mn^{2+} within the Ruddlesden-Popper strontium manganites confers to the material an excellent redox stability even after long exposure times in 3% H_2/N_2. The reduction process generates i) a decrease of the Mn oxidation state, ii) oxygen vacancies mainly located in equatorial oxygen site in the perovskite layers and iii) a Jahn-Teller distortion of the [MnO_6] octahedron. Likewise, the reducing atmosphere generates a complex change in the cell parameters, mainly due to thermal expansion and elongation of the Mn-O2 bond length. Nevertheless, the volume change is not drastic, which may not induce considerable stress in the electrode layer or at the electrode-electrolyte interface during redox process. Moreover, the average TECs of the $La_xSr_{2-x}MnO_{4\pm\delta}$ series determined were around 12.6(2) and 13.7(3) x 10^{-6} K^{-1} in air and hydrogen, respectively. In the case of $Nd_{0.5}Sr_{1.5}MnO_{4\pm\delta}$ the TECs measured in air was 12.7(4) $\times$ 10^{-6} K^{-1} and in hydrogen 14.4(2) $\times$ 10^{-6} K^{-1}. These values are comparable to those of commercial electrolytes, making this material a good candidate for symmetrical cells.

The chemical compatibility of $La_{0.5}Sr_{1.5}MnO_{4\pm\delta}$ (L5S15M) and $Nd_{0.5}Sr_{1.5}MnO_{4\pm\delta}$ (N5S15M) materials with the common SOFC electrolytes was studied. Both materials highly react with YSZ electrolyte forming secondary phases. The main reaction products obtained at 1100 °C were $SrZrO_3$ and $La_{1-x}Sr_xMnO_3$ or $Nd_{1-x}Sr_xMnO_3$. Conversely, no chemical reaction was detected between L5S15M or N5S15M and GDC electrolyte at temperature up to 1250 °C in air. Since changing La by Nd did not provide an improvement with respect to reactivity, the following studies were performed using the lanthanum compounds. In addition, L5S15M material yield no reaction product with GDC electrolyte when sintered at 850 °C in reducing atmosphere.

For the $La_xSr_{2-x}MnO_{4\pm\delta}$ series ($0.25\leq x\leq 0.6$), the total conductivity values were around 34 S cm^{-1} in air and beyond 0.8 S cm^{-1} in diluted hydrogen at 800 °C. These values are judged to be sufficient for an active layer of symmetrical SOFC electrodes. Within the La-series, the best compromise based on electrical behavior was obtained for $La_{0.5}Sr_{1.5}MnO_{4\pm\delta}$ material, which showed a total conductivity of 35.6 S cm^{-1} and 1.9 S cm^{-1} at 800°C in air and 3% H_2/Ar, respectively.

As a final conclusion of the chapter, the RE solubility limit, the thermal stability in oxidizing and reducing atmospheres and, for selected compositions, the total conductivity was widely studied within the $RE_xAE_{2-x}MnO_{4\pm\delta}$ family. The good redox stability and acceptable conductivity in both oxidizing and reducing atmosphere suggest $La_{0.5}Sr_{1.5}MnO_{4\pm\delta}$ (L5S15M) as a promising candidate for electrode material of Symmetrical Solid Oxide Fuel Cell. This composition has been therefore selected for the analysis of its properties electrochemical properties as both SOFC cathode and anode, what will be the object of the following chapter.

2.8 REFERENCES

[1] J. C. Ruiz-Morales, D. Marrero-López, J. Canales-Vázquez, and J. T. S. Irvine, "Symmetric and reversible solid oxide fuel cells," *RSC Adv.*, vol. 1, pp. 1403–1414, 2011.

[2] S. B. Adler, "Factors governing oxygen reduction in solid oxide fuel cell cathodes," *Chem. Rev.*, vol. 104, no. 10, pp. 4791–4843, 2004.

[3] S. B. Adler, J. A. Lane, and B. C. H. Steele, "Electrode kinetics of porous mixed-conducting oxygen electrodes," *J. Electrochem. Soc*, vol. 143, no. 11, p. 3554, 1996.

[4] S. B. Adler, "Mechanism and kinetics of oxygen reduction on porous $La_{1-x}Sr_xCoO_{3-\delta}$ electrodes," *Solid State Ionics*, vol. 111, pp. 125–134, 1998.

[5] W. Zhou, R. Ran, and Z. Shao, "Progress in understanding and development of $Ba_{0.5}Sr_{0.5}Co_{0.8}Fe_{0.2}O_{3-\delta}$ based cathodes for intermediate-temperature solid-oxide fuel cells: A review," *J. Power Sources*, vol. 192, pp. 231–246, 2009.

[6] V. V Kharton, A. P. Viskup, E. N. Naumovich, and F. M. B. Marques, "Oxygen ion transport in La_2NiO_4 -based ceramics," *J. Mater. Chem.*, vol. 9, pp. 2623–2629, 1999.

[7] S. J. Skinner and J. A. Kilner, "Oxygen diffusion and surface exchange in $La_{2-x}Sr_xNiO_{4+\delta}$," *Solid State Ionics*, vol. 135, pp. 709–712, 2000.

[8] N. Li, Z. Lü, B. Wei, X. Huang, K. Chen, Y. Zhang, and W. Su, "Characterization of $GdBaCo_2O_{5+\delta}$ cathode for IT-SOFCs," *J. Alloys Compd.*, vol. 454, pp. 274–279, 2008.

[9] S. Zha, P. Tsang, Z. Cheng, and M. Liu, "Electrical properties and sulfur tolerance of $La_{0.75}Sr_{0.25}Cr_{1-x}Mn_xO_3$ under anodic conditions," *J. Solid State Chem.*, vol. 178, pp. 1844–1850, 2005.

[10] E. Lay, G. Gauthier, and L. Dessemond, "Preliminary studies of the new Ce-doped La/Sr chromo-manganite series as potential SOFC anode or SOEC cathode materials," *Solid State Ionics*, vol. 189, no. 1, pp. 91–99, 2011.

[11] H. Nie, T. Wen, S. Wang, Y. Wang, U. Guth, and V. Vashook, "Preparation, thermal expansion, chemical compatibility, electrical conductivity and polarization of $A_{2-\alpha}A'_{\alpha}MO_4$ (A=Pr, Sm; A′=Sr; M=Mn, Ni; α=0.3, 0.6) as a new cathode for SOFC," *Solid State Ionics*, vol. 177, pp. 1929–1932, 2006.

[12] M. Al Daroukh, V. V Vashook, H. Ullmann, F. Tietz, and I. Arual Raj, "Oxides of the AMO_3 and A_2MO_4-type: structural stability , electrical conductivity and thermal expansion," *Solid State Ionics*, vol. 158, pp. 141–150, 2003.

[13] H. El Shinawi, J. F. Marco, F. J. Berry, and C. Greaves, "Synthesis and characterization of $La_{0.8}Sr_{1.2}Co_{0.5}M_{0.5}O_{4-\delta}$ (M=Fe, Mn)," *J. Solid State Chem.*, vol. 182, no. 8, pp. 2261–2268, 2009.

[14] M. Bahout, F. Tonus, C. Prestipino, D. Pelloquin, T. Hansen, E. Fonda, and P. D. Battle, "High-temperature redox chemistry of $Pr_{0.5}Sr_{1.5}Cr_{0.5}Mn_{0.5}O_{4-\delta}$ investigated in situ by neutron diffraction and X-ray absorption spectroscopy under reducing and oxidizing gas flows," *J. Mater. Chem.*, vol. 22, p. 10560, 2012.

[15] C. Munnings, S. Skinner, G. Amow, P. Whitfield, and I. Davidson, "Structure, stability and electrical properties of the $La_{(2-x)}Sr_xMnO_{4\pm\delta}$ solid solution series," *Solid State Ionics*, vol. 177, no. 19–25, pp. 1849–1853, 2006.

[16] S. Liping, H. Lihua, Z. Hui, L. Qiang, and C. Pijolat, "La substituted Sr_2MnO_4 as a possible cathode material in SOFC," *J. Power Sources*, vol. 179, pp. 96–100, 2008.

[17] S. LiPing, L. Qiang, H. Li-Hua, Z. Hui, Z. Guo-Ying, L. Nan, J.-P. Viricelle, and C. Pijolat, "Synthesis and performance of $Sr_{1.5}La_xMnO_4$ as cathode materials for intermediate temperature solid oxide fuel cell," *J. Power Sources*, vol. 196, no. 14, pp. 5835–5839, 2011.

[18] C. Jin, Z. Yang, H. Zheng, C. Yang, and F. Chen, "$La_{0.6}Sr_{1.4}MnO_4$ layered perovskite anode material for intermediate temperature solid oxide fuel cells," *Electrochem. commun.*, vol. 14, no. 1, pp. 75–77, 2012.

[19] J. Zhou, G. Chen, K. Wu, and Y. Cheng, "The performance of $La_{0.6}Sr_{1.4}MnO_4$ layered perovskite electrode material for intermediate temperature symmetrical solid oxide fuel cells," *J. Power Sources*, vol. 270, pp. 418–425, 2014.

[20] J. Shen, G. Yang, Z. Zhang, W. Zhou, W. Wang, and Z. Shao, "Tuning layer-structured $La_{0.6}Sr_{1.4}MnO_{4+\delta}$ into a promising electrode for intermediate-temperature symmetrical solid oxide fuel cells through surface modification," *J. Mater. Chem. A*, no. 5, pp. 1–4, 2016.

[21] F. Issaoui, M. T. Tlili, M. Bejar, E. Dhahri, and E. K. Hlil, "Structural and magnetic studies of $Ca_{2-x}Sm_xMnO_4$ compounds (x=0–0.4)," *J. Supercond. Nov. Magn.*, vol. 25, no. 4, pp. 1169–1175, 2011.

[22] A. Maignan, C. Martin, V. Tendeloo, M. Hervieu, and B. Raveaua, "Ferromagnetism and magnetoresistance in monolayered manganites $Ca_{2-x}Ln_xMnO_4$," vol. 8, no. 11, pp. 2411–2416, 1998.

[23] C. Autret, R. Retoux, M. Hervieu, and B. Raveau, "Charge ordering in a 2D manganite, $Pr_{0.25}Ca_{1.75}MnO_4$," *Chem. Mater.*, vol. 13, no. 12, pp. 4745–4752, 2001.

[24] M. T. Tlili, N. Chihaoui, M. Bejar, E. Dhahri, M. a. Valente, and E. K. Hlil, "Charge ordering analysis by electrical and dielectric measurements in $Ca_{2-x}Pr_xMnO_4$ (x=0–0.2) compounds," *J. Alloys Compd.*, vol. 509, pp. 6447–6451, 2011.

[25] J. Takahashi, H. Nakada, H. Satoh, and N. Kamegashira, "Orthorhombic distortion in $Ca_{2-x}Gd_xMnO_4$," *J. Alloys Compd.*, vol. 408–412, pp. 598–602, 2006.

[26] T. Nagai, A. Yamazaki, K. Kimoto, and Y. Matsui, "Synthesis and structural properties of n=1 Ruddlesden–Popper manganites $Nd_{1-x}Ca_{1+x}MnO_4$," *J. Alloys Compd.*, vol. 453, pp. 247–252, 2008.

[27] G. C. Kostogloudis, G. Tsiniarakis, and C. Ftikos, "Chemical reactivity of perovskite oxide SOFC cathodes and yttria stabilized zirconia," *Solid State Ionics*, vol. 135, no. 1–4, pp. 529–535, 2000.

[28] L. Qiu, T. Ichikawa, A. Hirano, N. Imanishi, and Y. Takeda, "$Ln_{1-x}Sr_xCo_{1-y}Fe_yO_{3-\delta}$ (Ln=Pr, Nd, Gd; X=0.2, 0.3) for the electrodes of solid oxide fuel cells,"

Solid State Ionics, vol. 158, no. 1–2, pp. 55–65, 2003.

[29] A. Montenegro-Hernández, J. Vega-Castillo, L. Mogni, and A. Caneiro, "Thermal stability of $Ln_2NiO_{4+\delta}$ (Ln: La, Pr, Nd) and their chemical compatibility with YSZ and CGO solid electrolytes," *Int. J. Hydrogen Energy*, vol. 36, no. 24, pp. 15704–15714, 2011.

[30] C. N. R. Rao and L. Gopalakrishnan, *New Directions in Solid State Chemistry*. 1997.

[31] M. P. Pechini and N. Adams, "Method of preparing lead and alkaline earth titanates and niobates and coating method using the same to form a capacitor," *United states patent office*. pp. 01–07, 1967.

[32] F. Deganello, G. Marcì, and G. Deganello, "Citrate-nitrate auto-combustion synthesis of perovskite-type nanopowders: A systematic approach," *J. Eur. Ceram. Soc.*, vol. 29, no. 3, pp. 439–450, 2009.

[33] A. Ecija, K. Vidal, A. Larrañaga, L. Ortega San Martin, and M. I. Arriortua, "Synthethic methods for perovskite materials: structure and morphology," *Adv. Cryst. Process.*, pp. 485–506, 2012.

[34] M. Mori, N. M. Sammes, and G. A. Tompsett, "Fabrication processing condition for dense sintered $La_{0.6}AE_{0.4}MnO_3$ perovskites synthesized by the coprecipitation method (AE= Ca and Sr)," *J. Power Sources*, vol. 86, pp. 395–400, 2000.

[35] T. Broux, C. Prestipino, M. Bahout, O. Hernandez, D. Swain, S. Paofai, T. C. Hansen, and C. Greaves, "Unprecedented high solubility of oxygen interstitial defects in $La_{1.2}Sr_{0.8}MnO_{4+\delta}$ up to $\delta\sim0.42$ revealed by in situ high temperature Neutron Powder Diffraction in flowing O_2," *Chem. Mater.*, vol. 25, pp. 4053–4063, 2013.

[36] "Crystallographica - A software toolkit for crystallography," *J. Appl. Crystallogr.*, vol. 30, pp. 418–419, 1997.

[37] J. Rodríguez-Carvajal, "References," in *A program for rietveld refinement and pattern matching analysis. Abstracts of the Satellite Meeting on Powder Diffraction of the XV Congress of the IUCr*, 1990.

[38] V. Petricek, M. Dusek, and L. Palatinus, "JANA2006." Institute of Physics, Academy of Sciences, Praha, Czech Republic, Institute of Physics, Praha, Czech Republic, 2006 (http://jana.fzu.cz/)., 2006.

[39] D. Cachau-Herreillat, *Des experiences de la famille Réd-Ox*. Paris: De Boeck and Larcier, 2007.

[40] D. Senff, P. Reutler, M. Braden, O. Friedt, D. Bruns, A. Cousson, F. Bourée, M. Merz, B. Büchner, and A. Revcolevschi, "Crystal and magnetic structure of $La_{1-x}Sr_{1+x}MnO_4$: Role of the orbital degree of freedom," *Physical Review B - Condensed Matter and Materials Physics*, vol. 71, no. 2. pp. 24425–1, 2005.

[41] R. D. Shannon, "Revised effective ionic radii and systematic studies of interatomic distances in Halides and Chalcogenides," *Acta Cryst.*, vol. 32, pp. 751–945, 1976.

[42] H. Taguchi, H. Kido, and K. Hirota, "The relationship between the crystal structure and electrical properties of K_2NiF_4-type $(Ca_{2-x}Nd_x)MnO_4$," *Solid State Sci.*, vol. 25, pp. 22–27, 2013.

[43] W. Norimatsu and Y. Koyama, "Stability of electronic states in the layered perovskite $Sr_{2-x}Nd_xMnO_4$," *Phys. C-Superconductivity Its Appl.*, vol. 463, pp. 115–119, 2007.

[44] W. Norimatsu and Y. Koyama, "Evolution of orthorhombic domain structures during the tetragonal-to-orthorhombic phase transition in the layered perovskite $Sr_{2-x}La_xMnO_4$," *Phys. Rev. B*, vol. 74, no. 8, p. 85113, 2006.

[45] C. S. Hong, E. O. Chi, W. S. Kim, N. H. Hur, K. W. Lee, and C. H. Lee, "Magnetic Properties and Structural Evolution in $Nd_{0.5}Sr_{1.5}MnO_4$," *Chem. Mater.*, vol. 13, p. 945, 2001.

[46] M. L. Borlera and F. Abbattista, "Investigations of the La-Mn-O system," *October*, vol. 92, pp. 55–65, 1983.

[47] H. S. Horowitz and J. M. Longo, "Phase relations in the Ca-Mn-O system," *Mater. Res. Bull.*, vol. 13, no. 12, pp. 1359–1369, Dec. 1978.

[48] B. V. Slobodin, L. L. Surat, and E. V. Vladimirova, "Phase relationships in 'MO-$LaMnO_3$-manganese oxides' systems where M=Ca, Ba," *J. Alloys Compd.*, vol. 335, no. 1–2, pp. 115–119, 2002.

[49] Y. X. Wang, Y. Du, R. W. Qin, B. Han, J. Du, and J. H. Lin, "Phase Equilibrium of the La-Ca-Mn-O System," *J. Solid State Chem.*, vol. 156, no. 1, pp. 237–241, 2001.

[50] P. Majewski, L. Epple, and F. Aldinger, "Phase-diagram studies in the La_2O_3-SrO-CaO-Mn_3O_4 system at 1200°C in air," *J. Am. Ceram. Soc.*, vol. 17, no. 189381, pp. 1513–1517, 2000.

[51] N. Chihaoui, M. Bejar, E. Dharhi, M. a. Valente, and M. P. F. Graça, "Effect of the oxygen deficiency on the physical properties of $Ca_2MnO_{4-\delta}$ compounds," *J. Alloys Compd.*, vol. 509, pp. 8965–8969, 2011.

[52] C. Autret, C. Martin, M. Hervieu, R. Retoux, B. Raveau, G. André, and F. Bourée, "Structural investigation of Ca_2MnO_4 by neutron powder diffraction and electron microscopy," *J. Solid State Chem.*, vol. 177, pp. 2044–2052, 2004.

[53] C. Autret, C. Martin, R. Retoux, a. Maignan, B. Raveau, G. André, F. Bourée, and Z. Jirak, "Coexistence of ferromagnetism and antiferromagnetism in the $L_{0.08}Ca_{1.92}MnO_4$ series," *J. Magn. Magn. Mater.*, vol. 284, pp. 172–180, 2004.

[54] A. Castro-Couceiro, M. Sánchez-Andújar, B. Rivas-Murias, J. Mira, J. Rivas, and M. A. Señarís-Rodríguez, "Dielectric response in the charge-ordered $Ca_{2-x}Pr_xMnO_4$ phases," *Solid State Sci.*, vol. 7, no. 8, pp. 905–911, 2005.

[55] A. Daoudi and G. Le Flem, "Sur une série de solutions solides de formule $Ca_{2-x}Ln_xMnO_4$, (Ln = Pr, Nd, Sm, Eu, Gd)," *J. Solid State Chem.*, vol. 5, pp. 57–61, 1972.

[56] H. Taguchi, H. Kido, and K. Hirota, "The relationship between the crystal structure and electrical properties of K_2NiF_4-type $(Ca_{2-x}Nd_x)MnO_4$," *Solid State Sci.*, vol. 25, pp. 22–27, 2013.

[57] C. N. Munnings, R. Sayers, P. A. Stuart, and S. J. Skinner, "Structural transformation and oxidation of $Sr_2MnO_{3.5+x}$ determined by in-situ neutron powder diffraction," *Solid State Sci.*, vol. 14, pp. 48–53, 2012.

[58] T. Broux, M. Bahout, O. Hernandez, F. Tonus, S. Paofai, T. Hansen, and C.

Greaves, "Reduction of Sr_2MnO_4 investigated by high temperature in situ neutron powder diffraction under Hydrogen Flow," *Inorg. Chem.*, vol. 52, pp. 1009–1017, 2013.

[59] R. K. Li and C. Greaves, "Synthesis and Characterization of the electron-doped single-layer manganite $La_{1.2}Sr_{0.8}MnO_{4-\delta}$ and its oxidized phase $La_{1.2}Sr_{0.8}MnO_{4+\delta}$," *J. Solid State Chem.*, vol. 153, no. 1, pp. 34–40, 2000.

[60] K. R. Poeppelmeier, M. E. Leonowicz, and J. M. Longo, "$CaMnO_{2.5}$ and $Ca_2MnO_{3.5}$: New oxygen-defect perovskite-type oxides," *J. Solid State Chem.*, vol. 44, pp. 89–98, 1982.

[61] Y. Surace, M. Simoes, J. Eilertsen, L. Karvonen, S. Pokrant, and A. Weidenkaff, "Functionalization of $Ca_2MnO_{4-\delta}$ by controlled calcium extraction: Activation for electrochemical Li intercalation," *Solid State Ionics*, vol. 266, pp. 36–43, 2014.

[62] J. Takahashi and N. Kamegashira, "X-ray structural study of calcium manganese oxide by rietveld analysis at high temperatures $Ca_2MnO_{4.00}$," *Mat. Res. Bull.*, vol. 28, no. 139, pp. 565–573, 1993.

[63] M. E. Leonowicz, K. R. Poeppelmeier, and J. M. Longos, "Structure Determination Neutron Methods of Ca_2MnO_4 and $Ca_2MnO_{3.5}$ by X-Ray and Neutron Methods," *Solid State Chem.*, vol. 59, pp. 71–80, 1985.

[64] K. R. Poeppelmeier, H. S. Horowitz, and J. M. Longo, "Oxide solid solutions derived from homogeneous carbonate precursors: The CaO-MnO solid solution," *J. Less-Common Met.*, vol. 116, no. 1, pp. 219–227, 1986.

[65] D. Waldbillig, A. Wood, and D. G. Ivey, "Electrochemical and microstructural characterization of the redox tolerance of solid oxide fuel cell anodes," *J. Power Sources*, vol. 145, pp. 206–215, 2005.

[66] A. C. Tomkiewicz, M. Tamimi, A. Huq, and S. McIntosh, "Oxygen transport pathways in Ruddlesden–Popper structured oxides revealed via in situ neutron diffraction," *J. Mater. Chem. A*, vol. 3, no. 43, pp. 21864–21874, 2015.

[67] S. J. Skinner, "Characterisation of $La_2NiO_{4+\delta}$ using in-situ high temperature neutron powder diffraction," *Solid State Sci.*, vol. 5, no. 3, pp. 419–426, 2003.

[68] G. Amow, I. J. Davidson, and S. J. Skinner, "A comparative study of the Ruddlesden-Popper series, $La_{n+1}Ni_nO_{3n+1}$ (n = 1, 2 and 3), for solid-oxide fuel-cell cathode applications," *Solid State Ionics*, vol. 177, no. 13–14, pp. 1205–1210, 2006.

[69] A. Aguadero, J. A. Alonso, M. . Martínez-Lope, F.-D. M. T., M. J. Escudero, and L. Daza, "In situ high temperature neutron powder diffraction study of oxygen-rich $La_2NiO_{4+\delta}$ in air: Correlation with the electrical behavior," *J. Mater. Chem.*, vol. 16, pp. 3402–3408, 2006.

[70] J. Kanamori, "Crystal distortion in magnetic compounds," *J. Appl. Phys.*, vol. 31, no. 5, pp. S14–S23, 1960.

[71] Q. X. Fu, F. Tietz, P. Lersch, and D. Stöver, "Evaluation of Sr- and Mn-substituted $LaAlO_3$ as potential SOFC anode materials," *Solid State Ionics*, vol. 177, no. 11–12, pp. 1059–1069, 2006.

[72] A. Faes, A. Nakajo, A. Hessler-Wyser, D. Dubois, A. Brisse, S. Modena, and J. Van herle, "RedOx study of anode-supported solid oxide fuel cell," *J. Power*

Sources, vol. 193, pp. 55–64, 2009.

[73] D. Waldbillig, A. Wood, and D. G. Ivey, “Thermal analysis of the cyclic reduction and oxidation behaviour of SOFC anodes,” *Solid State Ionics*, vol. 176, no. 9–10, pp. 847–859, 2005.

[74] Z. Naiqing, S. Kening, Z. Derui, and J. Dechand, “Study on properties of LSGM electrolyte made by tape casting method and applications in SOFC,” *J. Rare Earths*, vol. 24, pp. 90–92, 2006.

[75] H. Hayashi, T. Saitou, N. Maruyama, H. Inaba, K. Kawamura, and M. Mori, “Thermal expansion coefficient of yttria stabilized zirconia for various yttria contents,” *Solid State Ionics*, vol. 176, no. 5–6, pp. 613–619, 2005.

[76] G. A. Tompsett and N. M. Sammes, “Ceria – Yttria-Stabilized Zirconia Composite Ceramic Systems for Applications as low-temperature electrolytes,” *J. Am. Ceram. Soc.*, vol. 80, no. 12, pp. 3181–3186, 1997.

[77] C. Chatzichristodoulou, C. Schönbeck, a. Hagen, and P. V. Hendriksen, “Defect chemistry, thermomechanical and transport properties of $(RE_{2-x}Sr_x)_{0.98}(Fe_{0.8}Co_{0.2})_{1-y}Mg_yO_{4-\delta}$ (RE=La, Pr),” *Solid State Ionics*, vol. 232, pp. 68–79, 2013.

[78] D. M. Sherman, “The electronic structures of manganese oxide minerals,” *Am. Miner.*, vol. 69, pp. 788–799, 1984.

[79] G. A. Tompsett, N. M. Sammes, and O. Yamamoto, “Ceria – yttria-stabilized zirconia composite ceramic systems for applications as low-temperature Electrolytes,” *J. Am. Ceram. Soc.*, vol. 80, no. 12, pp. 3181–3186, 1997.

[80] A. J. Jennings, S. J. Skinner, and Ö. Helgason, “Structural properties of $La_xSr_{2-x}FeO_{4\pm\delta}$ at high temperature and under reducing conditions,” *J. Solid State Chem.*, vol. 175, pp. 207–217, 2003.

[81] H. El Shinawi and C. Greaves, “Synthesis and characterization of the K_2NiF_4 phases $La_{1+x}Sr_{1-x}Co_{0.5}Fe_{0.5}O_{4-\delta}$ (x=0, 0.2),” *J. Solid State Chem.*, vol. 181, pp. 2705–2712, 2008.

[82] B. T. M. Willis and A. W. Pryor, *Thermal vibrations in crystallography*. London UK: Cambridge University Press, 1975.

[83] W. H. Kim, H. S. Song, J. Moon, and W. H. Lee, “Intermediate temperature solid oxide fuel cell using (La,Sr)(Co,Fe)O_3-based cathodes,” *Solid State Ionics*, vol. 177, no. 35–36, pp. 3211–3216, 2006.

[84] A. Mai, M. Becker, W. Assenmacher, F. Tietz, D. Hathiramani, E. Ivers-Tiffée, D. Stöver, and W. Mader, “Time-dependent performance of mixed-conducting SOFC cathodes,” *Solid State Ionics*, vol. 177, no. 19–25 SPEC. ISS., pp. 1965–1968, 2006.

[85] A. Gondolini, E. Mercadelli, P. Pinasco, C. Zanelli, C. Melandri, and A. Sanson, “Alternative production route for supporting $La_{0.8}Sr_{0.2}MnO_{3-\delta}$-$Ce_{0.8}Gd_{0.2}O_{2-\delta}$ (LSM-GDC),” *Int. J. Hydrogen Energy*, vol. 37, pp. 8572–8581, 2012.

[86] A. Rangaswamy, P. Sudarsanam, and B. M. Reddy, “Rare earth metal doped CeO_2-based catalytic materials for diesel soot oxidation at lower temperatures,” *J. Rare Earths*, vol. 33, no. 11, pp. 1162–1169, 2015.

[87] N. Jaiswal, S. Upadhyay, D. Kumar, and O. Parkash, “Ionic conductivity investigation in lanthanum (La) and strontium (Sr) co-doped ceria system,” *J.*

Power Sources, vol. 222, pp. 230–236, 2013.

[88] A. M. Yankin, O. M. Fedorova, I. a. Zvereva, S. G. Titova, and V. F. Balakirev, "Phase formation during synthesis of the $LaSr_2Mn_2O_7$ compound," *Glas. Phys. Chem.*, vol. 32, no. 5, pp. 574–578, 2006.

[89] M. Zahid, I. Arul Raj, F. Tietz, P. Lersch, and D. Stöver, "Electrical conductivity of perovskites in the quasi-ternary system $La_{0.8}Sr_{0.2}MnO_3$ - $La_{0.8}Sr_{0.2}CoO_3$ - $La_{0.8}Sr_{0.2}FeO_3$ for application as cathode-interconnect contact layer in sofc," *Proceedings - Electrochemical Society*, pp. 1708–1716, 2005.

[90] M. H. Ehsani. M. E. Ghazi. P. Kameli, "Effects of pH and sintering temperature on the synthesis and electrical properties of the bilayered $LaSr_2Mn_2O_7$ manganite prepared by the sol – gel process," *J Mater Sci*, pp. 5815–5822, 2012.

[91] A. B. Missyul, I. a. Zvereva, and T. T. M. Palstra, "The formation of the complex manganites $LnSr_2Mn_2O_7$ (Ln=La, Nd, Gd)," *Mater. Res. Bull.*, vol. 47, pp. 4156–4160, 2012.

[92] H. Taguchi, "Metal-insulator transition in orthorhombic perovskite-type $Ca(Mn_{1-x}Nb_x)O_3$," *Phys. B Condens. Matter*, vol. 304, pp. 38–44, 2001.

[93] G. Amow, P. Whitfield, I. Davidson, R. P. Hammond, C. Munnings, and S. J. Skinner, "Structural and physical property trends of the hyperstoichiometric series $La_2Ni_{1-x}Co_xO_{4+\delta}$ ($0.00 \leq x \leq 1.00$)," *Mater Res Soc Symp Proc*, pp. 347–352, 2003.

[94] V. Kharton, E. Tsipis, I. Marozau, a Viskup, J. Frade, and J. Irvine, "Mixed conductivity and electrochemical behavior of $(La_{0.75}Sr_{0.25})_{0.95}Cr_{0.5}Mn_{0.5}O_{3-\delta}$," *Solid State Ionics*, vol. 178, no. 1–2, pp. 101–113, 2007.

CHAPTER 3

PERFORMANCE OF $La_{0.5}Sr_{1.5}MnO_{4\pm\delta}$ AS ELECTRODE MATERIAL FOR SYMMETRICAL SOLID OXIDE FUEL CELL

The study of the $RE_xA_{2-x}MnO_{4\pm\delta}$ (RE: La, Nd and A: Sr, Ca) family presented in Chapter 2 allowed to select the $La_{0.5}Sr_{1.5}MnO_{4\pm\delta}$ (L5S15M) compound as a possible candidate for electrode material of symmetrical SOFC. L5S15M is stable in reducing atmosphere while maintaining the K_2NiF_4-type structure with *I4/mmm* symmetry under redox cycling conditions. In addition, L5S15M presents an acceptable total electrical conductivity in oxidizing and reducing atmosphere as well as thermomechanical and chemical compatibility with Gd-doped ceria that can play the role of electrolyte material or barrier layer in combination with YSZ electrolyte.

After drawing the interest of the Electrochemical Impedance Spectroscopy (EIS) technique for the study of SOFC electrode, this chapter describes the electrochemical performance of $La_{0.5}Sr_{1.5}MnO_{4\pm\delta}$ (L5S15M) as electrode material for symmetrical solid oxide fuel cell. The first part concerns the description of the cell elaboration process. In the second part, the electrochemical impedance spectroscopy (EIS) is used to evaluate the electrochemical behavior of L5S15M in air then in hydrogen as a function of the electrode sintering temperature and electrode composition. In all cases, the impedance data are analyzed in terms of equivalent circuits, in order to extract the contributions associated to each process occurring at the electrodes. SEM and EDXS techniques are also used to study the possible elemental diffusion between the different layers.

3.1 EIS AS A POWERFULL TOOL FOR SOFC DIAGNOSIS

Research on SOFC is vast, and their development has been long and continuous, primarily because such system offers very high efficiency and have a unique scalability in electricity-generation applications. Despite its apparent promise and advantages, the development of SOFC as commercial devices for the energy

generation depends on different factors, which are related to the materials properties, the sintering temperature, the method of manufacture, the fuel, among others [1][2][3]. Thus, to improve and optimize the technology, it is important to understand the losses and degradation mechanisms within SOFCs. Electrochemical impedance spectroscopy (EIS) has proven itself as a powerful technique for breaking down the losses within an SOFC, but also to provide insight into which component and/or process primarily degrade during operation [4][5].

The impedance technique has been extensively used in fuel cell diagnosis since it allows to separate the processes that are believed to occur at the electrodes, which involve charge transfer at the electrode/electrolyte interface, mass diffusion, adsorption/desorption of the reactive and produces species on/from the electrode, and electrochemical and chemical interface reactions. In general, the results extracted from EIS measurements aim to identify the rate-limiting step(s) in the oxygen reduction or hydrogen oxidation reactions occurring at the SOFC cathode or anode, respectively, in all cases in order to optimize the electrode behavior and operating conditions [6][7]. A detailed description of Electrochemical Impedance Spectroscopy (EIS) and its use for the characterization of electrocatalysts is displayed in Annex 7.

The interpretations of the Oxygen Reduction Reaction were initially carried out in LSM-based systems and subsequently extended to Mixed Ionic-Electronic Conductors such as LSCF $(La,Sr)(Co,Fe)O_3$ or $La_2NiO_{4+\delta}$ (LNO) [8][9][10]. A different number of steps have been considered as limiting factors, among them adsorption and/or dissociative adsorption of oxygen on LSM surface [11], electron transfer and oxygen ion transfer through the electrode/electrolyte interface [12]. Each process could be affected by the cathode sintering temperature, cathode composition (composite), electrolyte material, oxygen partial pressure, measurement temperature, etc.

For example, Youngblood *et al*. have investigated the oxygen reduction process at 900-1000°C using a roughened $La_{1-x}Sr_xMnO_{3\pm\delta}$ (x=0.1 or 0.3) electrode in contact with a roughened YSZ surface [13]. Two processes were found to be rate limiting; at high frequency, charge transfer was suggested to be limiting, while oxygen dissociation was indicated to dominate at low frequency. The study carried out by Østergard and Mogensen on $La_{0.85}Sr_{0.15}MnO_3$ cathodes sintered on YSZ at 1300°C suggested that the oxygen dissociation and diffusion steps identified at medium or low frequency are also rate-determining processes under typical reaction conditions [14]. For LSM/YSZ composite electrodes, Murray *et al*. found a high frequency arc in addition to the one or two limiting processes found for porous LSM electrodes, which was ascribed to YSZ grain boundary resistance [15]. Adler *et al*. suggested that the origin of a large arc at low frequency in $La_{0.6}(Ca,Sr)_{0.4}Fe_{0.8}Co_{0.2}O_{3-\delta}$ is due to gas diffusion, this limitation can either be related to the porous electrode structure or a stagnant gas layer above the electrode structure [16]. Revising literature, it is clear that the impedance strongly depends on the nature of the electrode. Various processes may be limiting depending on electrode composition, processing parameters, and the measurement conditions, although there are discrepancies about the nature of the rate-limiting steps of the oxygen reaction mechanism [17].

The replacement of a pure electronic conducting LSM ($La_{0.8}Sr_{0.2}MnO_3$) by a Mixed Ionic Electronic Conducting perovskite such as LSCF led to significantly decrease the polarization resistance, which is seen as a consequence of the fast surface oxygen exchange kinetics and the high diffusivity for oxygen of the LSCF perovskites [18]. At 800 °C, under the same operating conditions, the polarization resistance of LSM cathode (YSZ electrolyte) is ~ 3.8 Ω cm^2 while for LSCF cathode (SDC electrolyte) it is 0.05 Ω cm^2, with activation energies of 2.2 eV and 1.3 eV, respectively [19][20]. The Mixed Ionic Electronic Conductors based on the Ruddlesden-Popper phases have also attracted significant attention as alternative cathodes in place of the conventional perovskites. For $La_2NiO_{4+\delta}$ cathode deposited by screen-printing on GDC electrolyte, the polarization resistance reported at 700 °C

is 0.42 Ω cm^2 [10]. The different members of the $La_xSr_{2-x}MnO_{4\pm\delta}$ (x= 0.4, 0.5, 0.6) [21] and $La_xSr_{1.5}MnO_4$ (x=0.35, 0.4, 0.45) [22] series, similar to the materials object of this work, also showed suitable electrochemical properties for use as cathode materials. Particularly, for $La_{0.6}Sr_{1.4}MnO_{4+\delta}$, the area specific resistance (ASR) at 800 °C is 0.39 Ω cm^2 with an activation energy of 1.39 eV. The impedance measurements carried out at different oxygen partial pressures (pO_2) provided some knowledge of the oxygen reduction mechanism occurring at the electrode. The resistance variation as a function of oxygen partial pressure (pO_2) allowed to associate with certainty the response at high frequency to the charge transfer reaction at the triple-phase boundary. However, the process related to the low frequency contribution was not clearly identified, the authors suggesting that it may be related either to surface diffusion of the dissociative adsorbed oxygen or the gas diffusion phenomenon [21][23]. The different mechanisms and limiting steps associated to oxygen reduction are described into details in Annex 8.

On the other hand, several theoretical and experimental investigations have been performed in order to understand the hydrogen oxidation mechanism; however, there is still very little consensus on the elementary steps that are involved. Most of the studies have been performed with Ni/YSZ cermet, considering that the electrochemical oxidation reactions occur at the Ni-YSZ-gas triple phase boundary (TPB) [24][25][26]. Bieberle *et al.* proposed that the hydrogen dissociated on the Ni surface migrates to the YSZ surface to form OH^- and H_2O in a wet fuel gas atmosphere [27]. Bessler *et al*. summarized the possible charge transfer reaction paths and analyzed these paths using one-dimensional surface reaction-diffusion modeling, proposing several kinetic mechanisms (discussed in Annex 9) [28][29][30]. Many of these limiting steps have been used to explain the behavior of other oxides for the hydrogen oxidation reaction, even if these are potentially Mixed Ionic Electronic Conducting materials [31][32]. As discussed in Sections 1.3.2 and 1.3.3, different MIEC materials have been developed as SOFC anodes, among which LSCM ($La_{0.75}Sr_{0.25}Cr_{0.5}Mn_{0.5}O_{3-\delta}$) perovskite has received considerable

attention due to its excellent stability under reducing atmospheres and favorable electrocatalytic activity not only for fuel oxidation but also as cathode, allowing its development as symmetrical cell electrode. For example, at 950 °C, LSCM shows polarization resistances of 1.62, 1.85, 2.18 and 2.05 Ω cm^2 in air, 5% H_2, 100% H_2 and 100% CH_4, respectively [33]. These values decrease with the use of a LSCM(YSZ-GDC) composite, reaching values of 0.5 Ω cm^2 in air and 0.8 Ω cm^2 in 5% H_2 at the same temperature [34]. $La_{0.6}Sr_{1.4}MnO_{4+\delta}$ Ruddlesden-Popper composition was also proposed as potential electrode for intermediate-temperature symmetrical cell. For this material, an ASR value of 1 Ω cm^2 has been found in wet H_2 using LSGM electrolyte, presenting a maximum power densities (MPD) of 110.9 and 47.3 mW cm^{-2} with H_2 and CH_4 fuels at 800 °C [35][36]. The description of anodic reaction mechanism proposed to Ni-YSZ cermet is displayed in Annex 9.

3.2 CELL PREPARATION FOR EIS MEASUREMENTS

The evaluation of L5S15M as symmetrical electrode comprised, as a first step, the definition of the conditions for the cell preparation, *i.e.* the conditions of electrode layers preparation, including the possible use of a diffusion barrier layer or a composite electrode, as well as the temperature range for the sintering of the electrode active layer, taking into account the results of dilatometric and SEM analyses.

3.2.1 CONDITIONS OF SYMMETRICAL CELL PREPARATION

The symmetrical Solid Oxide Fuel Cell (SSOFC) is a configuration where the same electrode material is used simultaneously as cathode and anode. According to the literature, the choice of the electrolyte material, the preparation of electrode powder, the electrode composition, the sintering temperature, the electrode layer thickness, the current collector, among others, influence the impedance spectroscopy

measurements. In this study, some of the preparation conditions (electrolyte nature, buffer layer, electrode thickness, current collector) were the same for all the cell assemblies [37][38][39]. Nevertheless, the influence of the electrode sintering temperature and the use of a composite instead of a pure phase electrode material were evaluated. On the one hand, the sintering conditions generally have an effect on electrochemical performance, because they can influence the adhesion between the electrode and electrolyte, the electrode microstructure and the percolation paths that must have sufficient open porosity for the free passage of gas [40]. On the other hand, the introduction of an ionic conducting phase such as GDC to form a composite electrode can improve the electrode ionic conductivity, if it is not sufficient, and help maintaining the electrode porosity as blocking the manganite grain growth [9][41]. The electrolyte used in a symmetrical cell must fulfil the same requirements as that of traditional SOFCs; however, in view of the reducibility of GDC electrolyte in anode atmosphere that leads to its mixed electronic/ionic conductivity in such conditions, *i.e.* a loss of performance of the complete cell [42][43], we used a common supporting dense YSZ electrolyte in association with a GDC interlayer (acting as a barrier layer) on each side, before the final electrode deposition.

3.2.1.1 Preparation of the dense YSZ electrolyte

Dense YSZ pellets (15 mm in diameter) were prepared with YSZ commercial powder (Nextech Materials, USA, # 312005). Initially, 2.1 g of YSZ were weighed and placed in a circular holder, applying pressure at 1 Ton for 2 minutes, using a manual die-casted. Subsequently, the pellets were recovered and put in finger gloves, evacuated under vacuum and isostatic pressed at 1700 bar for 15 minutes. The YSZ pellets were sintered at 1400°C for 12 h (heating and cooling 200°C/h), using a sheet of alumina and a few sacrificial powder (YSZ). The last step was the polishing of the as-obtained pellets. The polishing was necessary to ensure the parallelism between both faces and adjust the thickness, because the shim of the screen printer has a

fixed height of 1.8 mm. The polishing was performed with discs of reference MD Piano 220. The relativity density of the electrolytes was, in general, of 96%. Once prepared the electrolytes, the barrier layer and the electrode were deposited using automatic screen printing. The ink preparation and the description of this technique is described in the following section.

3.2.1.2 Ink preparation and deposition by screen printing technique

The inks that were used for screen printing were prepared by mixing the powder with a dispersant and an organic binder. These compounds confer a rheofluidifying and thixotropic character necessary to obtain a homogeneous and cohesive deposition with the substrate. The material (usually 3 g) was mixed with 2% w/w of organic dispersant (T01 Cerlase). The mixture was submitted to planetary milling for 5 h using zirconia jar filled with zirconia balls (1 cm) and covered with ethanol (2/3 volume). Later, the mixture (powder+ethanol) was transferred to a beaker and dried overnight. The resulting powder was mixed with 65% w/w of a terpenoid binder (Mixtion EC3, Ferro Couleurs, France), and homogenized with a three-roll mill (Figure 55a).

Figure 55. (a) three roll mill and (b) screen printer (DEK 248).

(a) (b)

The screen printing technique was introduced by researchers to deposit materials on various substrates and fulfil the demand for reproducible, stable and disposable layers that are suitable for mass production [44]. The screen-printing technique considers the use of a woven mesh to support an ink-blocking stencil, and a roller or squeegee is moved across the screen stencil to force or pump ink. In this case, the inks prepared were then coated on the electrolyte pellets. To form the symmetrical cell, the GDC interlayers or the electrodes (1 cm^2 in diameter) were first deposited on one side and dried at 100°C for 30 minutes. Subsequently, the same procedure was performed on the opposite side of the electrolyte. The depositions were carried out with a DEK 248 screen-printer at a speed of 30 mm s^{-1} and an applied pressure of 4 kg m^{-2} (Figure 55b).

3.2.1.3 GDC buffer layer preparation

As described in previous section, $La_{0.5}Sr_{1.5}MnO_{4+\delta}$ reacts with YSZ and LSGM forming insulating phases. On the other hand, the behavior of GDC electrolyte in anodic atmosphere has been reported by several authors, showing that the stability problems arise from the partial reduction of Ce^{4+} to Ce^{3+}. This is detrimental because: (i) the electrolyte begins to present n-type electronic conductivity which causes a partial internal electronic short circuit in the cell and (ii) it generates nonstoichiometry (with respect to normal valence in air) and expansion of the lattice which can lead to mechanical failure [45][46][42][47]. Considering the above, in this work, YSZ was used as electrolyte and a GDC buffer layer was required on both side of the electrolyte to prevent the formation of secondary phases such as insulating $SrZrO_3$ at the electrode/electrolyte interface.

The GDC interlayer was deposited by screen printing. The GDC ink was prepared according to the procedure described in Section 3.2.2.2, using GDC (HSA Rhodia, Paris, France) with particle size ~0.38 µm (D_{90}). A TGA analysis of the ink was

carried out with the objective to identify the temperature of removal of the organic solvent. Figure 56a shows that the abrupt weight loss corresponding to the elimination of the organic part occur between 30 and 400°C. Consequently, we use a slow heating ramp (40 °C/h) up to 400°C.

The quality of the GDC interlayer depends on its preparation conditions, including the powder pre-sintering temperature, the concentration of the dispersant-organic solvent, the sintering temperature and the deposition process [48]. The final sintering temperature of 1250 °C was chosen based on previous studies, which demonstrated that this is the optimum firing temperature for the GDC layer onto the YSZ film, conducing to a good adhesion of the GDC/YSZ interface without reaction between YSZ and GDC [49][50]. In the present work, as a first parameter study, two options of heating ramp were chosen (40 °C/h and 300 °C/h) up to the sintering temperature, as depicted in Figure 56b,c. After preparation, the GDC surface was observed by scanning electron microscopy (SEM).

Figure 56. a) Thermogravimetric analysis of GDC ink and deduced heat-treatment using b) slow ramp (40 °C/h) or c) fast ramp (300 °C/h).

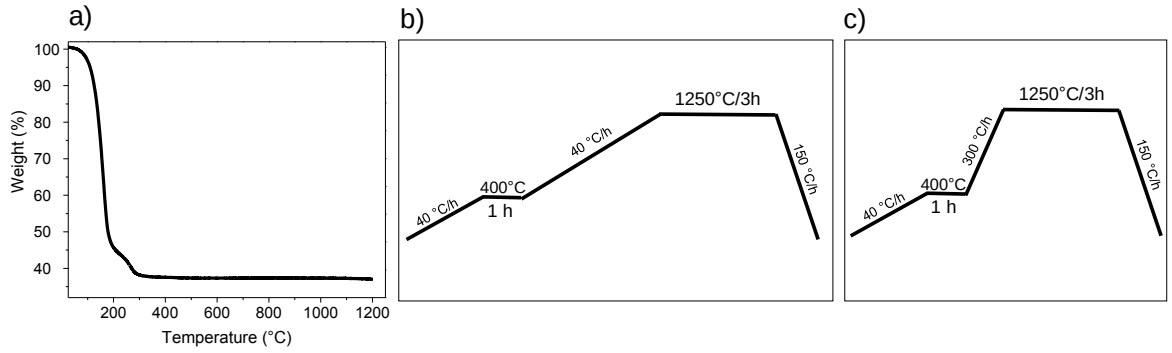

The SEM images (Figure 57) show that the number of cracks and their depth are greater when using a slow ramp. At the same time, the slow heating causes an

excessive grain growth, the average grain size for the fast ramp is ~1µm, while it is ~0.5µm for the slow ramp.

Figure 57. SEM micrographs of GDC surface sintered using a) slow ramp (40 °C/h) and b) fast ramp (300 °C/h).

a)

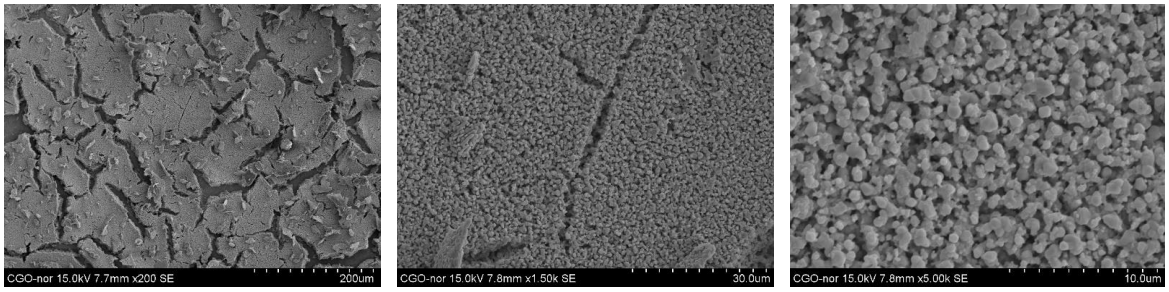

b)

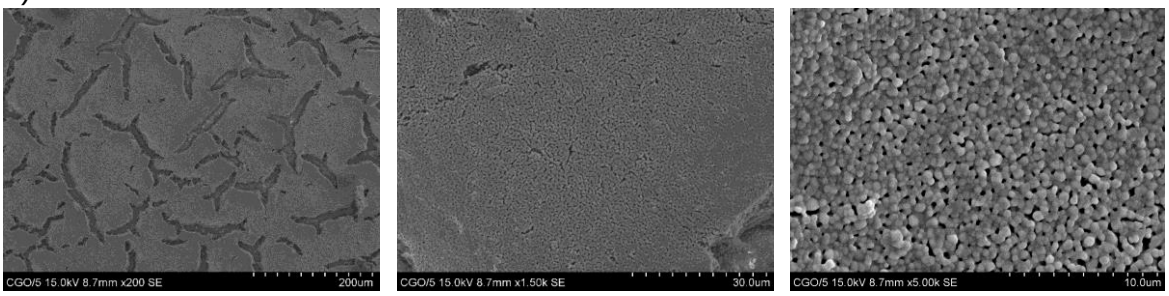

In order to reduce the cracks in the buffer layer and avoid any contact between L5S15M and YSZ, for the subsequent tests, a fast heating ramp (300 °C/h) was chosen and we decided to study the influence of a sintering pretreatment of the GDC powder, since some authors demonstrated that the pre-sintering of GDC powder decrease the formation of agglomerates and cracks when spray coating deposition was used [51]. This crack formation could be due to both the particle size and thermal contraction of GDC. The GDC powder was thus pre-sintered at 900, 1000, 1100, 1200 and 1300 °C during 3 h. Dilatometry studies were carried out on GDC without and with pre-sintering treatment, giving the results shown in Figure 58.

Figure 58. Dilatometric curves in air of GDC without and with pre-sintering treatment at different temperatures for 3 h.

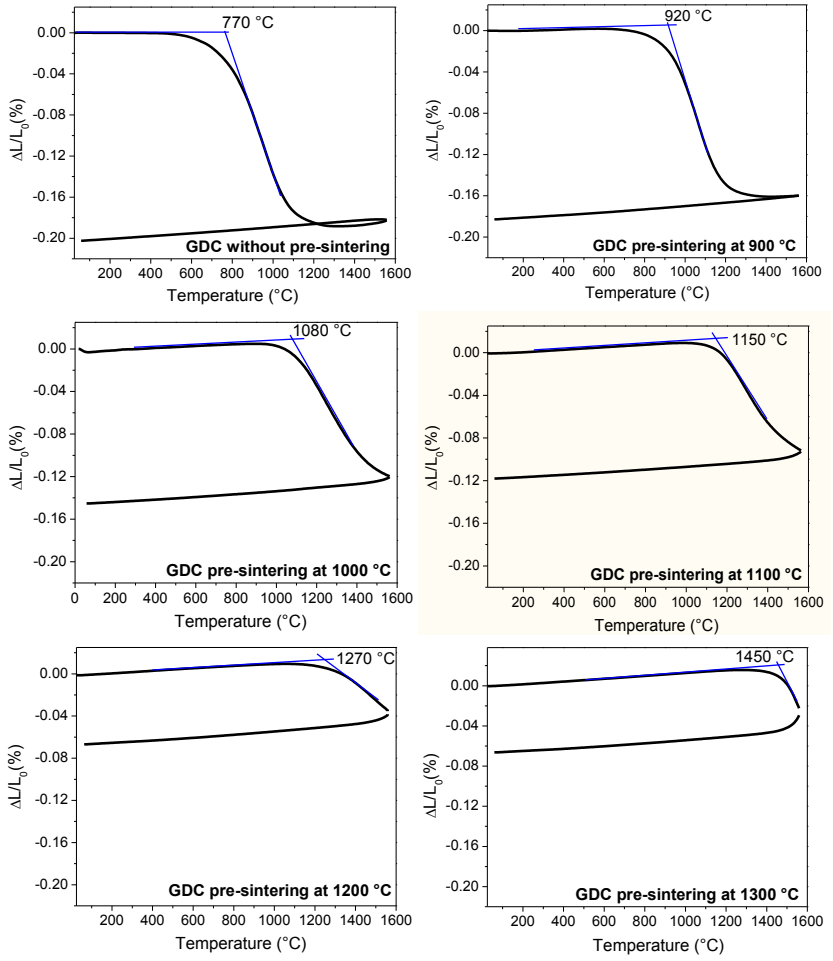

On the dilatometric curves of Figure 58, it is evident that the sintering of GDC has a drastic effect on sample contraction. The early stage of sintering is shifted to higher temperatures with the increase of the pre-sintering temperature of GDC, *i.e.* the stage of sintering begins at 770 °C for GDC without pre-sintering, whereas for the powders that were pre-sintered at 900, 1100, 1200 and 1300 °C, it begins at 920, 1150, 1270 and 1450 °C, respectively. In addition, the shrinkage also decreases with the increase of the pre-sintering temperature, decreasing from 20% for the GDC without pre-sintering to 18, 12 and 7% for the powder that was pre-sintered at 900, 1100 and 1300°C, respectively. In order to evaluate the effect of pre-sintering on the

formation of GDC layer on YSZ electrolyte, GDC layers were deposited using the powders pre-sintered at 900, 1000 and 1100 °C. The pre-sintering temperatures of 1200 and 1300 °C were discarded, since in these cases the shrinkage onset temperature was higher than the final sintering temperature (1250°C). Figure 59 shows SEM images of GDC surface prepared with pre-sintered GDC and fired using the same heating ramp as described in Figure 56c.

Figure 59. SEM micrographs of GDC surface prepared using GDC pre-sintering at a) 900 °C, b) 1000 °C and c) 1100 °C.

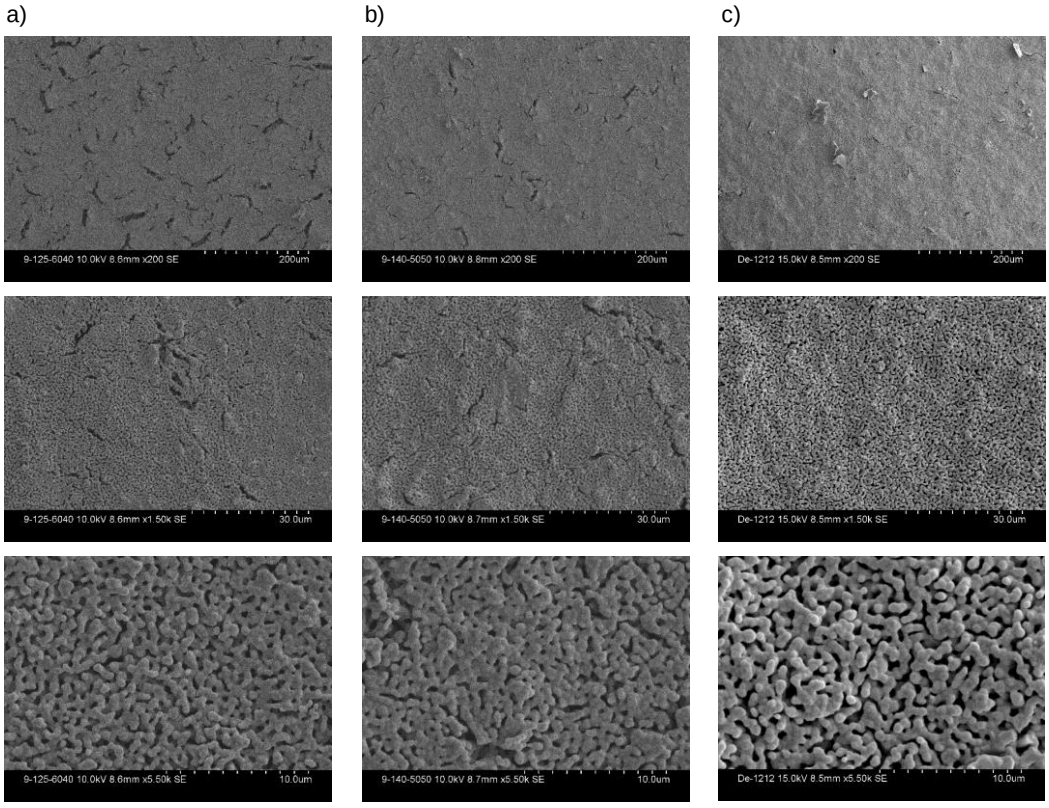

As shown in the micrographs, the number of cracks decreases as the temperature increases from 900 °C to 1100 °C. The layer formed with GDC pre-sintering at 1100 °C is uniform and free of cracks. These results indicate that using the preparation conditions described above, the optimal pre-sintering temperature of GDC powder is 1100 °C. Figure 60 displays the SEM images corresponding to the cross section

of the GDC layer on YSZ substrate after sintering at 1250 °C using a GDC pre-sintering at 1100 °C.

Figure 60. SEM images of the cross-section of the GDC/YSZ interface, sintered at 1250 °C using GDC pre-sintering treatment at 1100 °C.

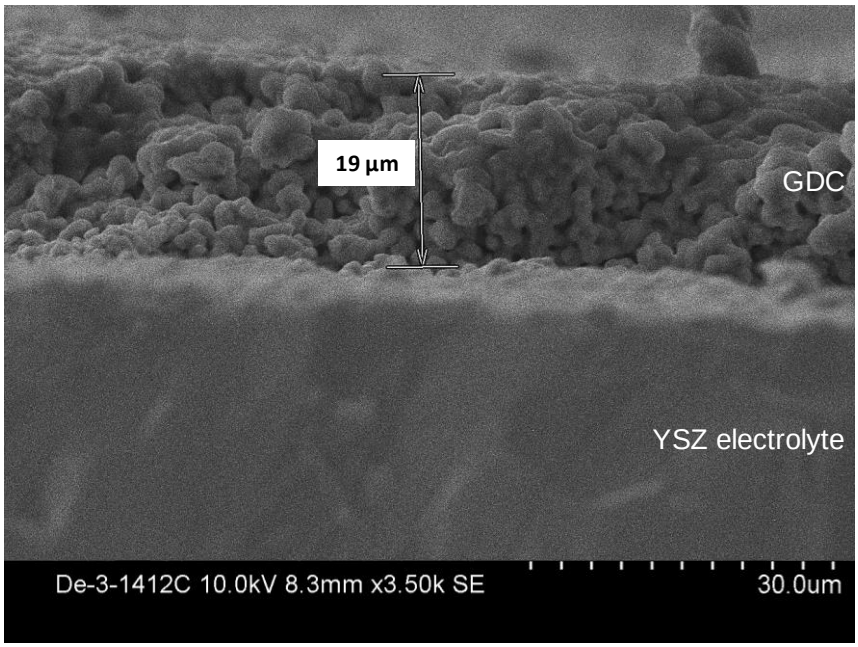

From Figure 60, one can see that the GDC layer is adheres well on YSZ electrolyte without any delamination or cracks. The thickness of the GDC layer is approximately 20 µm. These are the best conditions we could define to elaborate the GDC diffusion barrier protecting the interface between YSZ and the electrode active layer.

3.2.1.4 Electrode active layer preparation

In the electrode layer formation step, the sintering temperature and electrode composition were defined as variables, keeping constant both the heating rate and time of the isothermal heating (3 h). $La_{0.5}Sr_{1.5}MnO_4$ (L5S15M) or L5S15M-GDC50

composite active layer were deposited on each side of the GDC/YSZ/GDC sandwich, using also screen printing technique. In this preliminary study, the composite was made of 50 wt% L5S15M and 50 wt% GDC. The dilatometry technique was used to define the range of sintering temperature of both pure phase and composite active layer (Figure 61).

Figure 61. Dilatometric curves of (a) L5S15M and (b) L5S15M-GDC50 composite.

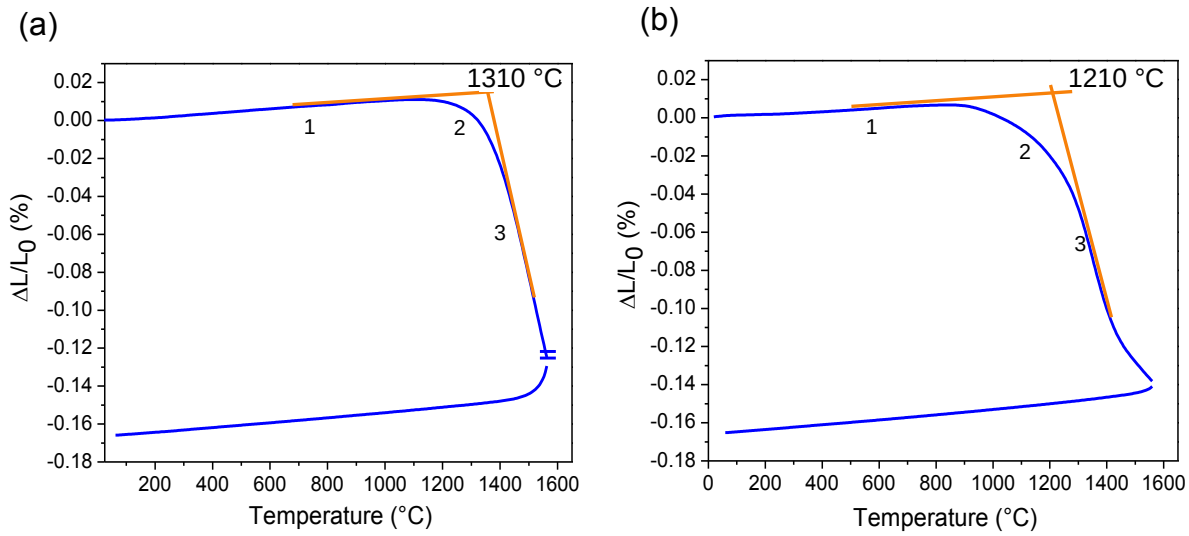

Each curve can be divided into three parts as the temperature increases: the first corresponds to the thermal expansion of the powder grains, the second to the contacts formation (bridges) between grains and the third represents the elimination of porosity related to grain growth, mainly. The tangent method allows determining the range of sintering temperature where the bridges begin to form, that is normally the best choice for the elaboration of the conducting but porous layer. Since the temperature range for both the L5S15M and composite are close, the active layers (electrodes) were prepared in air at the same temperatures of 1150, 1200 or 1250 °C, using the sintering process shown in Figure 62.

Figure 62. Sintering process used for the electrode formation.

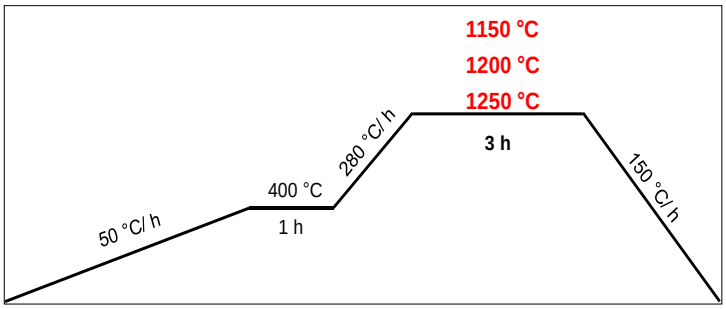

Subsequently, the electrodes were coated with a thin Au layer deposited by sputtering on the top of each electrode. This last layer was added to improve the current collection with the collecting grid of the EIS setup (see below). The sputtering process was performed using 15-20 Amperes and 4 minutes of deposition using a mini sputter coater EMSCOPE model SC500.

3.2.2 EIS - EXPERIMENTAL CONDITIONS FOR EIS MEASUREMENTS

The cells prepared under the above-mentioned conditions were evaluated by EIS (Section 3.3 and 3.4). The Figure 63 shows the assembly used for the EIS measurements. The symmetrical cell was introduced between two gold mesh used as current collector [52].

Figure 63. Experimental set-up for EIS measurements of symmetric cells.

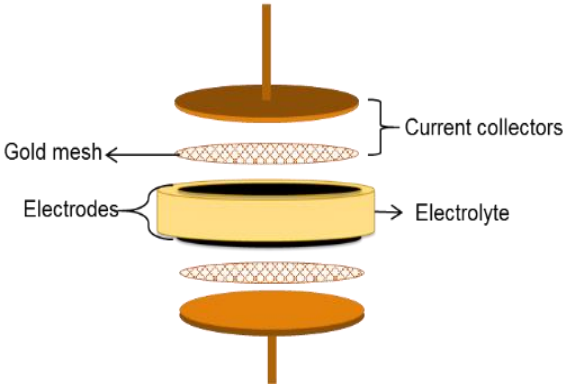

The experiments were carried out with a SI Solartron 1260 frequency response in the 10 mHz and MHz frequency range, using an AC signal of 50 mV amplitude under OCV conditions. Such device allows the simultaneous measurement of three symmetric cells, ensuring identical experimental conditions. The electrochemical measurements were carried out consecutively in air for cathode conditions, then wet 3% H_2/Ar (3 % H_2O), wet 97% H_2 (3 % H_2O) and dry 3% H_2/Ar for anode study, with a flow rate of 150 mL/min in each case. Before starting each measurement, the samples were stabilized at high temperature (~ 850 °C) until there is no variation in the impedance spectra (~ 24 h). Data were collected every 25 °C, from 850°C to 600°C, with a temperature accuracy of a ±1 °C and a stabilization time of two hours at each temperature. The spectra were fitted to equivalent circuits using the ZView software (version 3.4 c) [53]. All impedance data were normalized with the electrode area (1.02 cm^2).

3.3 ELECTROCHEMICAL PROPERTIES IN AIR (OXYGEN REDUCTION)

The electrocatalytic behavior in air of $La_{0.5}Sr_{1.5}MnO_4$ (L5S15M) was evaluated performing electrochemical impedance spectroscopy (EIS) of symmetrical cells (prepared as described in section 3.2). The electrochemical behavior in air was studied as a function of:

i. The sintering temperature of the electrode active layer, using the Au/L5S15M/GDC/YSZ/GDC/L5S15M/Au cell, where the electrode was formed by a layer of pure $La_{0.5}Sr_{1.5}MnO_{4\pm\delta}$ (L5S15M) calcined at 1150, 1200 or 1250 °C for 3 h (see section 3.2.1.4).
ii. The influence of both the use of a composite and the sintering temperature, where the electrode was formed by a layer of composite made of 50 wt% L5S15M and 50 wt% GDC, with heat-treatment at 1150 or 1200 °C for 3 h.

iii. The influence of the GDC content in the composite, using ratio of 40:60 wt%, 50:50 wt%, 60:40 wt% and 70:30 wt % for L5S15M:GDC to form the electrode active layer.

3.3.1 PURE L5S15M - INFLUENCE OF SINTERING TEMPERATURE

The EIS measurements in air were carried out from 850 to 600 °C in the frequency range between 1 MHz and 10 mHz. All the data were then normalized with respect to the surface area (1.02 cm^2). For all impedance spectra presented below, the numbers at the top indicate the frequency logarithms. The impedance spectra of Au/L5S15M/GDC/YSZ/GDC/L5S15M/Au cells sintered at 1150, 1200 y 1250 °C are shown in Figure 64 as a function of the temperature of measurement.

Globally, and as a first approach to those results, the sintering temperature affects noticeably the electrode polarization resistance (R_p)[4]. Such phenomenon is quite common and is generally associate to the following effects of the temperature on the electrode microstructure: a too low temperature allows to keep a large surface area within the porous electrode, but causes a poor adherence between electrode and GDC buffer layer. Increasing the temperature of elaboration of the electrode improves the contact between electrode and electrolyte, but generates an increase in the grain size decreasing the specific surface area of the electrode [54]. Even if such explanation seems reasonable, we decided to embark on a deeper examination of the EIS data in order to try to correlate them to the exact effect of the sintering temperature.

[4] R_p can be extracted graphically from the difference between the high and low frequency intercepts with the real axis of the impedance plot.

Figure 64. Impedance spectra measured in air between 835 °C and 600 °C for L5S15M electrodes sintered at 1150, 1200 or 1250 °C for 3 hours. The numbers indicate the frequency logarithms.

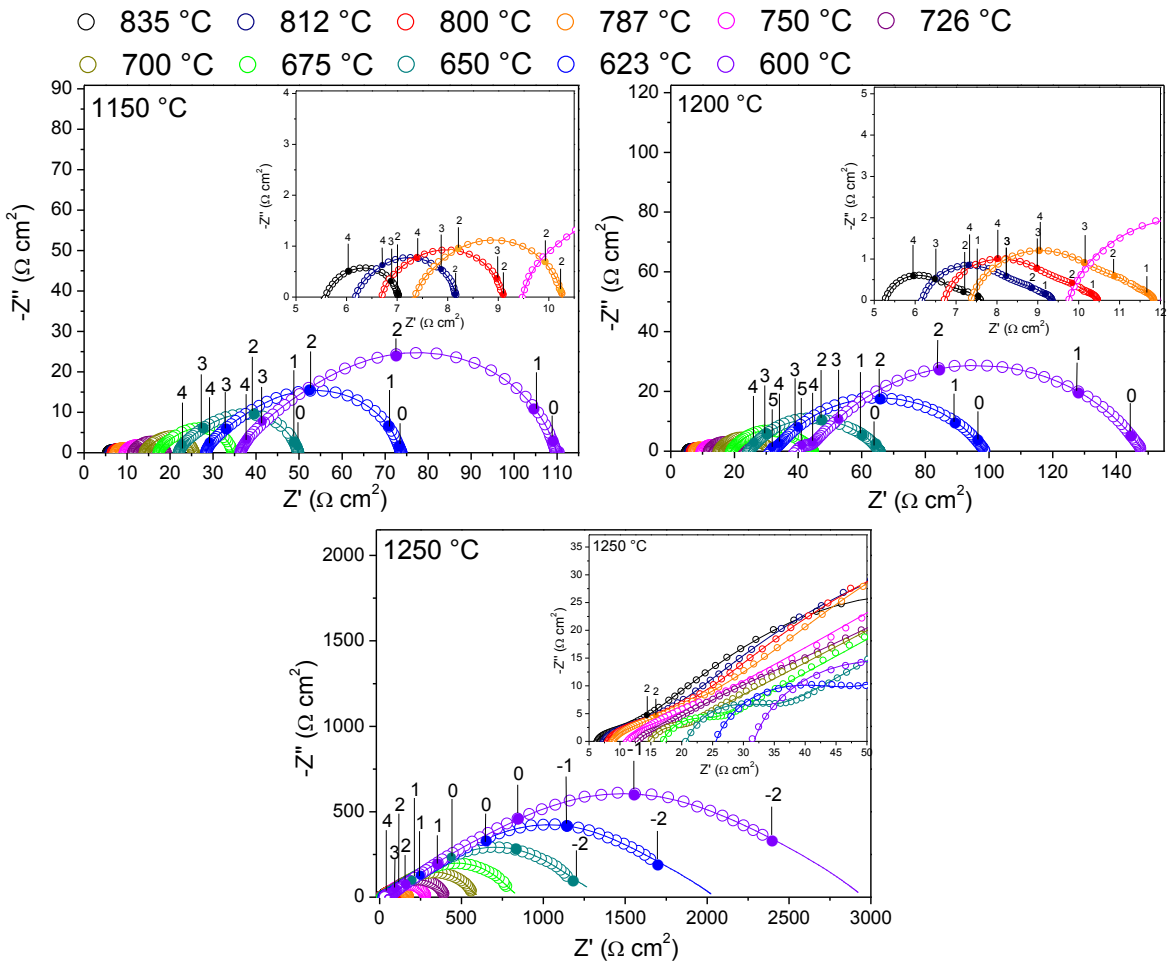

As shown in Figure 64, the shape of the arcs that describe each spectrum is different for each cell, as well as its characteristic frequency range. In order to describe the processes that contribute to the total polarization resistance, the impedance spectra were fitted to equivalent circuits using the ZView® software [53], which allowed to condense the data and to translate them into quantitative parameters describing all the limiting steps of the electrochemical process.

3.3.1.1 Electrode sintered at 1150 °C

The obtained impedance spectra are asymmetric in shape, indicating more than one limiting step for the electrode process. Figure 65 shows an example of spectrum obtained at 800 °C and the corresponding equivalent circuit used to fit the spectra measured in the whole studied temperature range.

Figure 65. Impedance spectrum at 800 °C for L5S15M electrode sintered at 1150 °C and measured in air. The serial resistance has been removed. The numbers indicate the frequency logarithms.

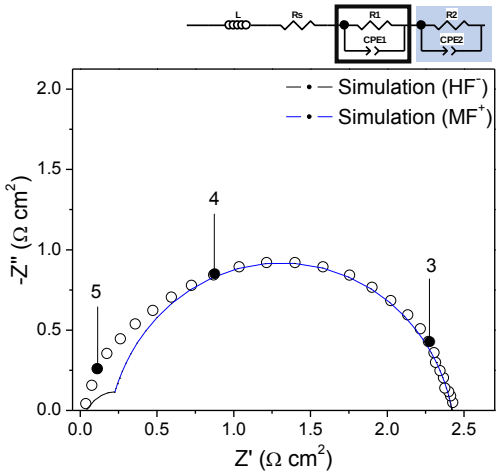

The circuit $LR_s(R_1CPE_1)(R_2CPE_2)$ consists of an inductance (L), an ohmic resistance (R_s) and two (R-CPE) components that refer to the limiting electrode processes. The Constant Phase Element (CPE) is defined by two values CPE-T and CPE-p (see Annex 7). The capacitance values (C) were calculated using the following equation [55]:

$$C = R^{\frac{(1-p)}{p}} Q^{\frac{1}{p}} \qquad (3\text{-}26)$$

where R is the resistance, Q (T) is the pseudo-capacitance and *p* is an exponent. The relaxation frequency *f* of each electrode process corresponding to a specific (R-CPE) component was calculated from:

$$f_{max} = \frac{1}{2\pi RC} \qquad (3\text{-}27)$$

Table 20 lists the electrical parameters for each element derived from spectra fitting. The area specific resistance (ASR) was calculated from the polarization resistance (R_p), which is the sum of the individual resistances:

$$ASR = \frac{R_p S}{2} \qquad (3\text{-}28)$$

where *S* is the electrode surface area (cm^2) and the factor 2 accounts for the fact that the cell is symmetrical.

Table 20. Parameters of elementary contributions for L5S15M electrode prepared at 1150 °C and measured in air.

Temp. (°C)	R_s (Ωcm^2)	HF^-			MF^+			R_p (Ω cm^2)	ASR (Ω cm^2)
		R_1 (Ω cm^2)	C_1 (F cm^{-2})	*f* (Hz)	R_2 (Ω cm^2)	C_2 (F cm^{-2})	*f* (Hz)		
835	5.35	0.19	2.25E-5	37251	1.34	2.10E-5	5648	1.53	0.77
812	5.94	0.27	1.78E-5	33454	1.84	1.84E-5	4710	2.10	1.05
800	6.40	0.32	1.70E-5	29216	2.32	1.86E-5	3695	2.64	1.32
787	7.10	0.41	1.63E-5	23933	2.73	2.01E-5	2904	3.14	1.57
751	9.19	0.80	1.43E-5	13967	4.42	2.29E-5	1577	5.21	2.61
726	11.10	1.23	1.27E-5	10174	6.43	2.48E-5	998	7.66	3.83
700	13.69	1.93	1.25E-5	6605	9.68	2.68E-5	613	11.61	5.80
675	16.54	3.32	1.27E-5	3775	14.09	3.17E-5	356	17.41	8.71
650	21.45	6.22	1.37E-5	1870	21.71	3.80E-5	193	27.93	13.96
623	27.64	10.81	1.49E-5	991	34.74	4.45E-5	103	45.55	22.78
600	35.37	20.46	1.72E-5	452	53.41	4.91E-5	61	73.87	36.94

According to Figure 66 and Table 20, two processes contribute to the polarization resistance. A first arc in the high frequency region (10^5 and 10^3 Hz) and a second one in the ultra-medium frequency region (10^4 and 10^2 Hz), labeled as HF^- and MF^+, respectively. The activation energies of the whole electrode process and of each limiting step were obtained from the Arrhenius plots of the ASR and the individual resistances (limiting steps) as a function of temperature (Figure 66). All Arrhenius plots presented in this work, were plotted using the Log_{10} function.

Figure 66. Arrhenius plot of the (a) area specific resistance (ASR) and (b) individual resistances (limiting steps) for L5S15M electrode prepared at 1150 °C and measured in air.

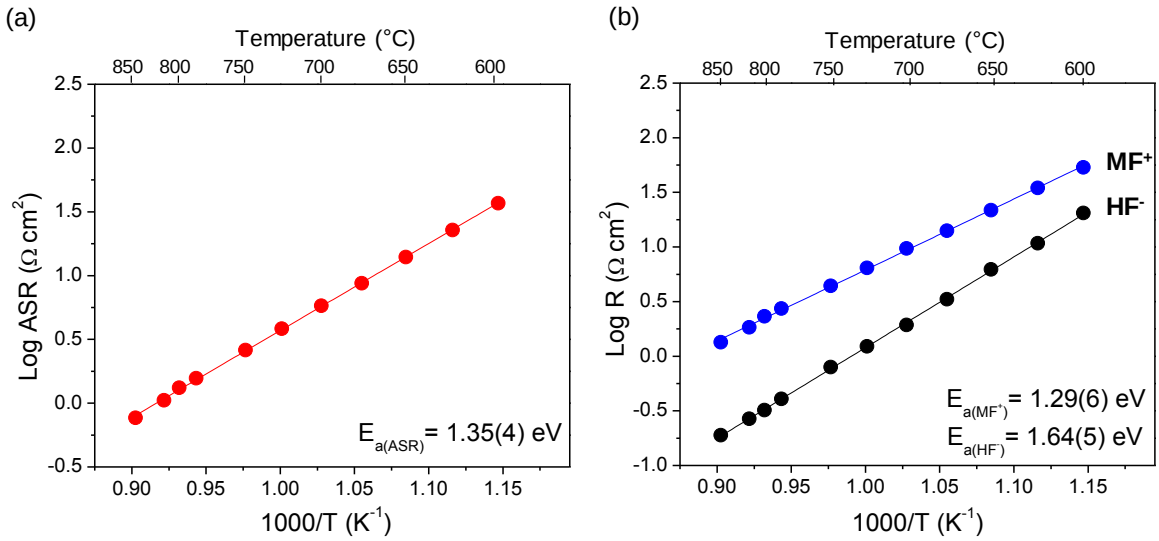

As depicted in Figure 66a, the overall activation energy obtained from the ASR is 1.35(4) eV. This activation energy value is similar to that reported for other mixed ionic-electronic conductors such as LSCF (1.5-1.65 eV) [56][57], La_2NiO_4 (1.07-1.3 eV) [10][58] and $La_{0.6}Sr_{1.4}MnO_{4+\delta}$ (1.39-1.86 eV) [21][36]. In a similar way, the two identified limiting steps are thermally activated; however, the resistive component of the medium frequency arc (MF^+) presents the highest contribution to the polarization resistance (Figure 66b). For example, at 800 °C, the ASR value is equal to 1.32 Ω cm^2, for which R_{MF+} corresponds to ~88 % of the total resistance. This ASR is larger than that reported in air at the same temperature for $La_{0.6}Sr_{1.4}MnO_4$ cathode (0.39 Ω cm^2 [36]) or for LSCM (0.43 Ω cm^2 [17]) symmetrical electrode.

In the same way, the equivalent capacitance and relaxation frequency (Schouler methodology) are characteristic parameters very useful to identify the electrode processes. The Schouler methodology consists in plotting the relaxation frequency (Log_{10}) and capacitance (Log_{10}) of each contribution vs. reciprocal temperature [59].

Figure 67 shows the relaxation frequencies and the corresponding capacitances for each process as a function of the temperature, respectively.

Figure 67. Arrhenius plot of the (a) relaxation frequencies and (b) equivalent capacitances for L5S15M electrode prepared at 1150 °C and measured in air.

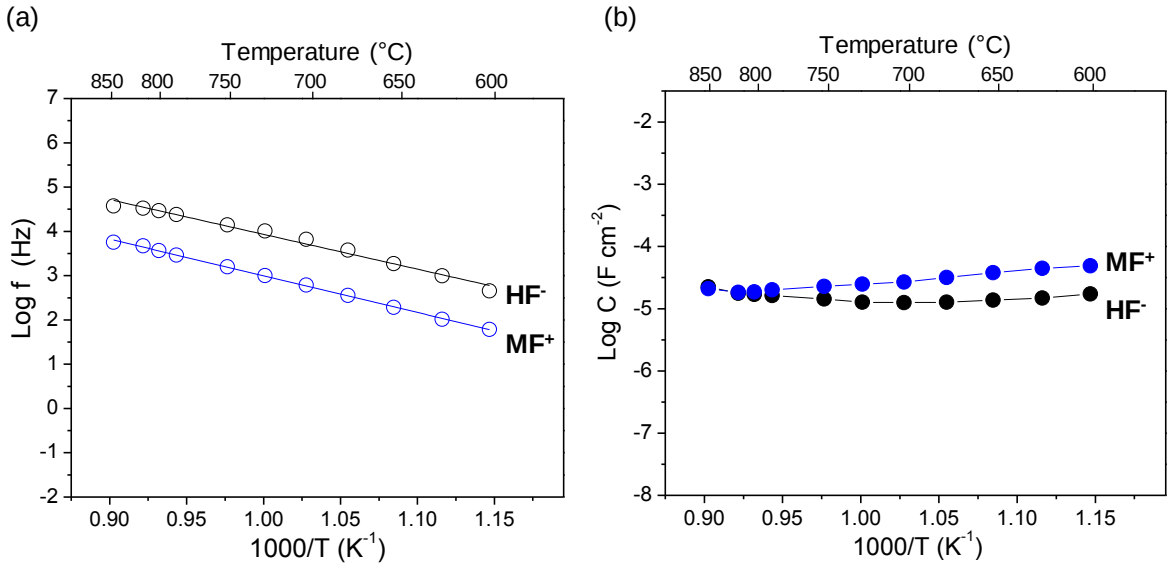

As shown in Figure 67, the capacitances of each process do not vary significantly with the temperature and, in both cases, have similar values (10^{-5} F cm^{-2}), while the relaxation frequencies are decreased by almost two orders of magnitude with decreasing temperature, signifying a thermally activated mechanism. According to the literature, the electrode process corresponding to (HF^-) can be tentatively attributed to the charge transfer of oxygen ions (O^{2-}) at the interface between the electrode and electrolyte [16][60]. This limiting process with equivalent capacitances of 10^{-6}-10^{-5} F cm^{-2} has been identified in LSCF cathode calcined at 800 °C [9], $La_2NiO_{4+\delta}$ calcined at 950 °C [61] and $La_{0.6}Sr_{1.4}MnO_{4+\delta}$ calcined at 1000 °C [21]. The simulations carried out by *Sunde* suggest that this contribution may be related to the lack of connectivity between electrode and electrolyte particles, which is consistent with the low sintering temperature [62]. Nevertheless, the activation energy obtained

for this process (1.64(5) eV) is much higher than the value reported for the same process in $La_2NiO_{4+\delta}$, for example (0.61 eV [61]).

The main contribution to ASR is the medium frequency element (MF^+) with capacitance values around 10^{-5}-10^{-4} F cm^{-2}. It can be assigned to electron transfer between the electrode and oxygen, referring to ionization of oxygen species on the surface and subsequent incorporation into the electrode [63]. A contribution of this type was identified in the electrochemical study of $La_{1.8}Sr_{0.2}NiO_{4+\delta}$ cathode sintered at 950 °C, with an activation energy of 1.11(3) eV [64], similar to that obtained in our case (1.29(6) eV).

Scanning electron microscopy (SEM) and energy dispersive X-ray spectroscopy (EDXS) analyses were performed on the cross-section of the Au/L5S15M/GDC/YSZ/GDC/L5S15M/Au cell prepared at 1150 °C, before EIS test (Figure 68). This analysis was focused on assessing of the efficiency of the GDC layer as a diffusion barrier for hindering the interaction between the cathode and YSZ electrolyte, preventing the formation of insulating phases at the electrode/electrolyte interface. The SEM image with the corresponding atomic concentration mapping for La (Lα, 4.65 keV), Sr (Lα, 1.81 keV), Mn(Kα, 5.89 keV), Ce (Lα, 4.84 keV), Gd (Lα, 6.06 keV), Y (Lα, 1.92 keV) and Zr (Lα, 2.04 keV) is shown in Figure 68.

Figure 68. SEM image and EDXS concentration mapping of the main elements in the cross-section of Au/L5S15M/GDC/YSZ/GDC/L5S15M/Au cell sintered at 1150 °C.

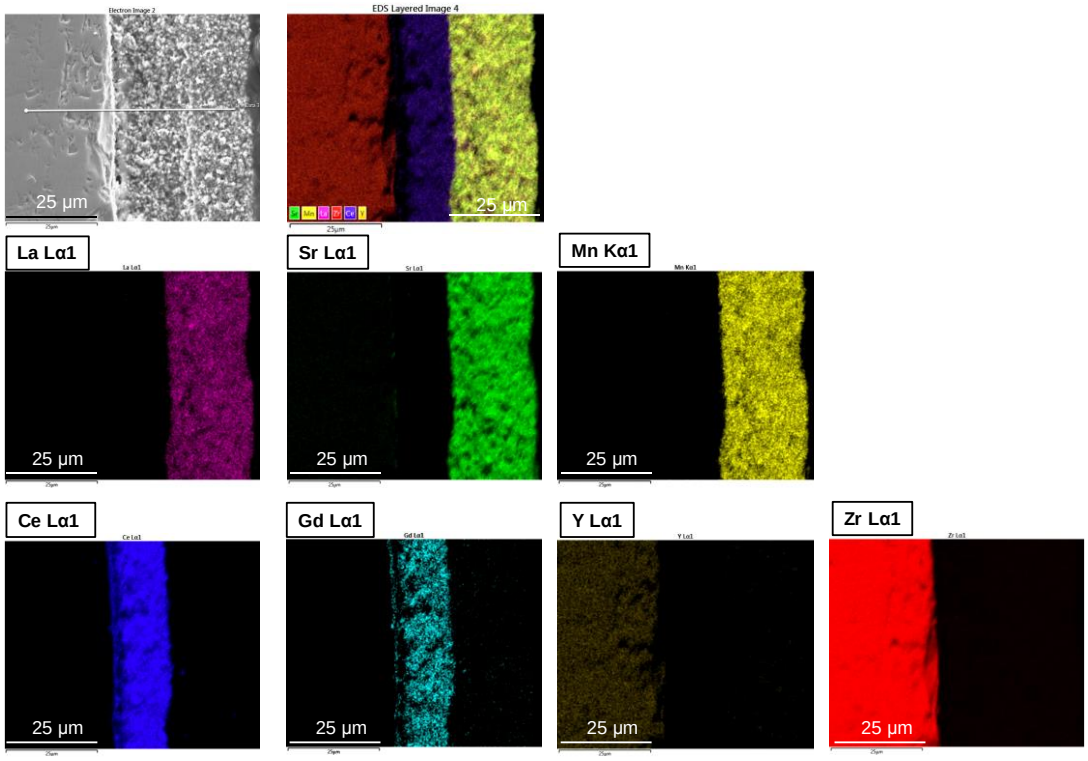

A good interface between the electrode-GDC interlayer and the YSZ-electrolyte is observed, confirming the chemical and thermal compatibility of the materials. EDXS mapping of the elements indicates that globally all the elements are located in the phase where they are expected; nevertheless, it seems to be a very slight diffusion of Sr through the GDC interlayer, indicated by a very thin green line at GDC/YSZ interface on Figure 68. According to the literature the Sr diffusion may occur during the sintering heat treatment of the cell layers [65][66], promoting the formation of $SrZrO_3$ at the GDC/YSZ interface, which somehow leads to a reduction of electrolyte ionic conductivity [67][68][69]. On the other hand, it has been demonstrated that the $SrZrO_3$ formation depends on the electrode sintering temperature; for example, $SrZrO_3$ phase is formed when the LSCF electrode is sintered at 1200 °C, and not at

1100 °C [66][70][71]. In our case, the formation of $SrZrO_3$ at the GDC/YSZ interface seems possible but remains limited at a sintering temperature of 1150 °C.

3.3.1.2 Electrode sintered at 1200 °C

The impedance spectrum obtained at 800 °C under air for Au/L5S15M/GDC/YSZ/GDC/L5S15M/Au cell prepared at 1200 °C is displayed in Figure 69. The inset shows the equivalent circuit used to fit the data.

Figure 69. Impedance spectrum of L5S15M electrode sintered at 1200 °C and measured in air at 800 °C. The serial resistance has been removed. The numbers indicate the frequency logarithms.

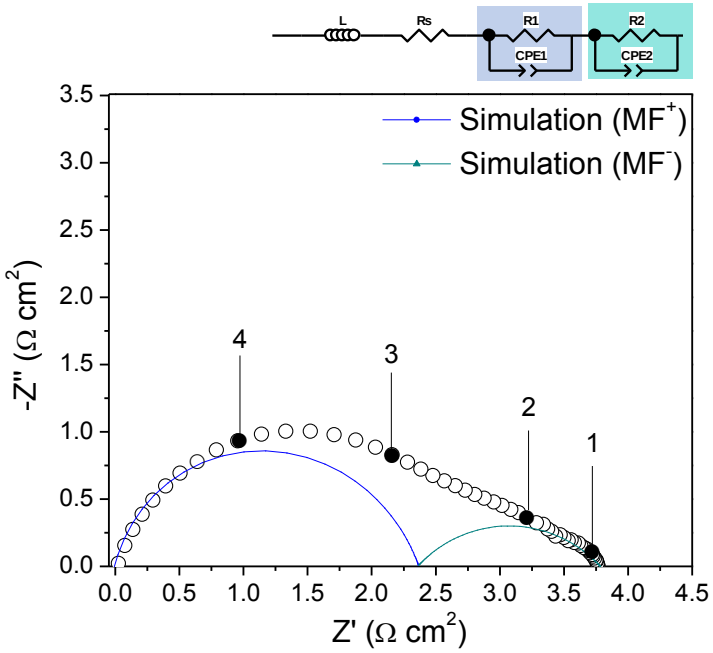

Globally, the increase of the electrode sintering temperature yields an increase of ASR; for example, at 800 °C is 1.32 Ω cm^2 and 1.89 Ω cm^2 for the electrodes sintered at 1150 and 1200 °C, respectively. This behavior has also been reported for the well-known LSCF cathode, for which the ASR cathode was increased sintering at 1000 °C rather than 850°C (Figure 70). In that case, the authors suggested that the high

temperature led to the densification of the electrode, making it more prone to gaseous diffusion limitations [57].

Figure 70. Impedance spectra for LSCF sintered at (a) 850 and (b) 1000°C measured at 800°C in air. Taken from [57].

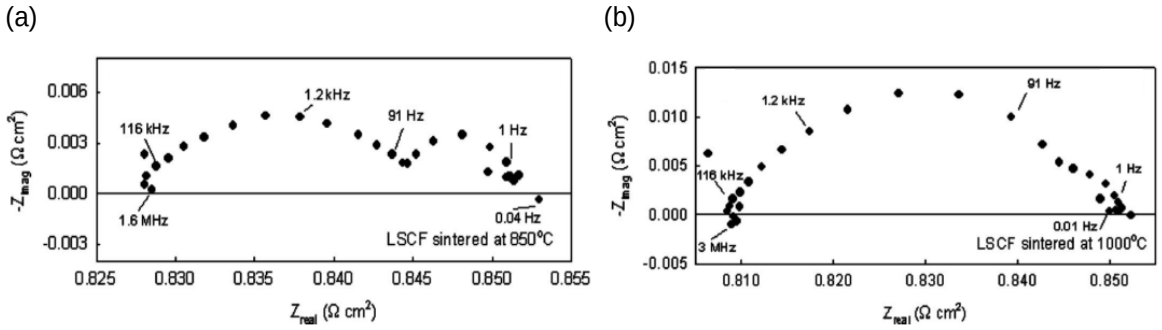

The spectra obtained in the whole range of temperature were deconvoluted into two arcs: a large arc at the ultra-medium frequency (10^4 and 10^2 Hz) and a small one at medium frequency (10^2-10^1), labeled as MF^+ and MF^-, respectively. Table 21 lists the electrical parameters for each element derived from spectra fitting. Figure 71 shows the Arrhenius plots of the resistances, from which the activation energies were calculated.

Table 21. Parameters of elementary contributions for L5S15M electrode sintered at 1200 °C and measured in air.

Temp. (°C)	R_s (Ω cm²)	MF^+			MF^-			R_p (Ω cm²)	ASR (Ω cm²)
		R_1 (Ω cm²)	C_1 (F cm^{-2})	*f* (Hz)	R_2 (Ωcm²)	C_2 (F cm^{-2})	*f* (Hz)		
835	5.13	1.43	1.40E-5	7974	0.96	1.17E-3	142	2.38	1.19
812	6.00	2.00	1.38E-5	5786	1.26	1.01E-3	126	3.25	1.63
800	6.58	2.34	1.35E-5	5040	1.43	1.01E-3	110	3.77	1.89
787	7.19	2.95	1.33E-5	4045	1.59	1.15E-3	87	4.54	2.27
751	9.57	5.71	1.31E-5	2130	2.23	1.81E-3	39	7.93	3.97
725	11.78	8.61	1.35E-5	1372	2.70	2.36E-3	25	11.31	5.66
700	14.78	13.59	1.83E-5	641	3.86	2.46E-3	17	17.45	8.73
675	18.63	20.28	1.76E-5	447	4.88	2.50E-3	13	25.16	12.58
649	24.03	33.01	2.36E-5	205	7.03	2.43E-3	9	40.04	20.02
623	30.78	63.61	2.37E-5	102	9.25	2.62E-3	7	72.86	36.43
600	38.66	105.40	3.14E-5	48	12.03	2.83E-3	6	117.43	58.71

Figure 71. Arrhenius plot of the (a) individual resistances (limiting steps) and (b) area specific resistance (ASR) for L5S15M electrode sintered at 1200 °C and measured in air.

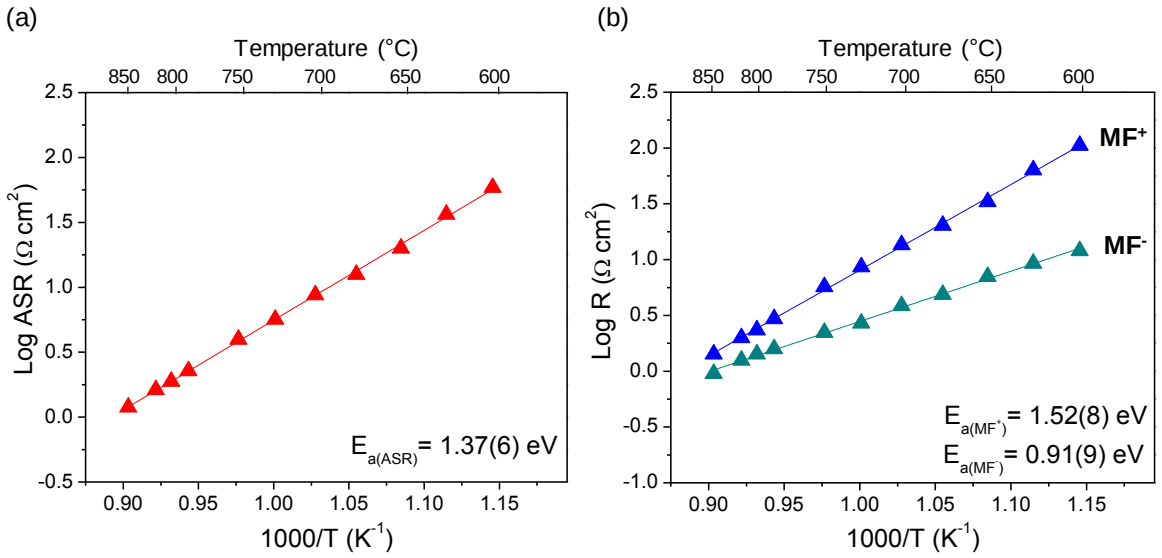

According to those results, the (R_{MF^+}) resistance values are very close to those obtained for the electrode sintered at 1150 °C, representing in both cases the greatest contribution to the total resistance. As previously discussed, with an activation energy of 1.52(8) eV similar to that obtained for the electrode sintered at 1150 °C (1.29(6) eV), the MF^+ response is assigned to the electron transfer between the electrode and oxygen with incorporation of the adsorbed oxygen ion into the electrode. At 1200 °C, there is no apparent high frequency contribution (HF^-), what seems in agreement with a better sintering process of the electrode layer that allows an improved transport of oxygen ions at the electrode/electrolyte interface. However, a new contribution of lower activation energy (0.91(9) eV) appears in the spectra (MF^-). Figure 72 shows the temperature dependence of relaxation frequencies and equivalent capacitances that can be to understand/confirm the origin of the observed phenomena.

Figure 72. Arrhenius plot of the (a) relaxation frequencies and (b) equivalent capacitances for L5S15M electrode sintered at 1200 °C and measured in air.

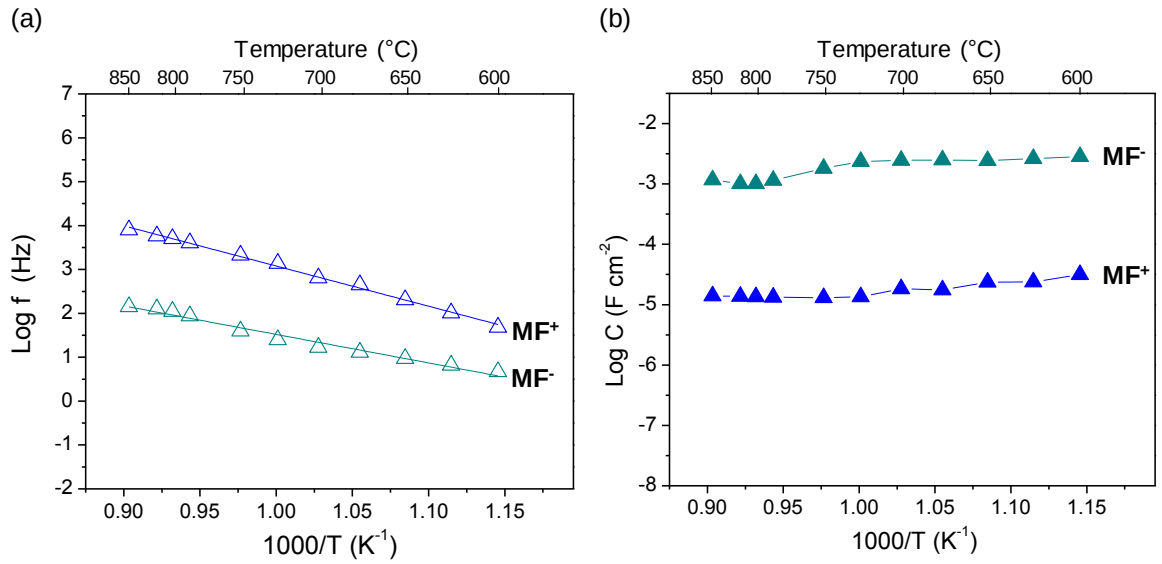

The new contribution at medium frequency (MF^-) with a capacitance of 10^{-3} F cm^{-2} refers to processes occurring on the electrode surface: dissociation of the adsorbed molecular oxygen and/or surface diffusion [72]. This contribution identified at medium frequency (10^2-10^1 Hz) in $La_2NiO_{4+\delta}$ and $Sr_3FeMO_{6+\delta}$ (Fe, Co, Ni) cathodes was described as a rate-limiting step due to oxygen dissociative adsorption on the electrode surface [64][73]. Specifically, for the $Sr_3FeMO_{6+\delta}$ (Fe, Co, Ni) cathode, the impedance study realized as a function of oxygen partial pressure allowed to identify that such process occurs at 700 °C (measured temperature) when pO_2 was less to 10^{-2} atm, varying according to the relation $R_{MF} \alpha pO_2^{-0.5}$ [73]. On the other hand, the impedance spectra obtained for $La_{0.35}Sr_{1.5}MnO_4$ cathode also present a contribution in the range of 10^1 to 10^2 Hz, but in this case, it was related to surface diffusion of adsorbed oxygen (O_{ad}), a study as a function of pO_2 at 750 °C confirming that above 0.03 atm the process presents a relation $R_{MF} \alpha pO_2^{-0.51}$ [22]. Accordingly, we suggest that the contribution observed in our case is due to one or both processes of dissociative adsorption/desorption and/or surface diffusion of adsorbed oxygen. The appearance of this phenomenon by increasing the sintering temperature may be

related to the increase in grain size, *i.e.* to the decrease of specific surface area, which does not favor the dissociative adsorption process that is intimately linked to the surface area of the electrode.

In order to evaluate the influence of the sintering temperature on the elemental diffusion across the GDC interlayer and the quality of adhesion between layers, and also possibly identify another origin to the limiting phenomena that are observed, SEM and EDXS analyses have been performed on the cross-sectional of Au/L5S15M/GDC/YSZ/GDC/L5S15M/Au cell prepared at 1200 °C before EIS measurements (Figure 73).

Figure 73. SEM image and EDXS concentration mapping of the main elements in the cross-section of Au/L5S15M/GDC/YSZ/GDC/L5S15M/Au cell sintered at 1200 °C.

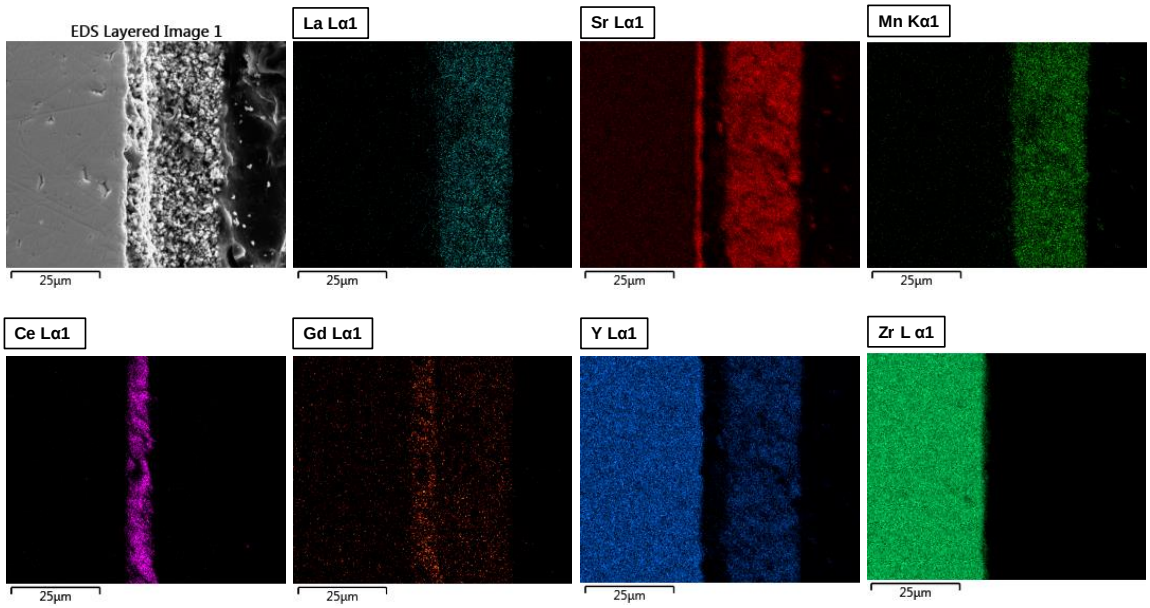

The corresponding EDS mapping reveals that La, Mn, Ce and Zr are homogeneously distributed in their respective layers; however, at the interface YSZ-GDC a Sr concentration is clearly detected. Y is also found at a detectable level in the electrode layer, confirming the diffusion of this element through the GDC interlayer. The Sr

diffusion across the GDC “diffusion” barrier is a phenomenon that has been unequivocally confirmed in the literature, showing that $SrZrO_3$ is formed during sintering of the electrode [66][69]. Such $SrZrO_3$ presence is redhibitory as such compound presents a very low oxygen ion conductivity [74], leading generally to a decrease of the ionic conductivity at the GDC/YSZ interface [19]; nevertheless, such phenomenon seems not to be preponderant in our case as the series resistance of the cell elaborated at 1200 °C are approximately the same as for a sintering temperature of 1150 °C (Figure 69). However, the increase of Sr diffusion from L5S15M to GDC/YSZ interface. by increasing the sintering temperature can also generate a Sr depletion from the manganite, and be an indirect source of performance degradation, as it has been described for LSCF cathodes [75][76]. In our case, such phenomenon, and the related modification of the materials chemistry, can have negatively affected, on the one hand, the R_{MF+} contribution, which is related to the oxygen exchange and diffusion properties of the material, *i.e.* its oxygen exchange (k^*) and/or oxygen diffusion (D^*) coefficients [16][77]. On the other hand, a chemical modification of the material surface associated to Sr depletion could also be one of the source of the R_{MF-} contribution that has been associated to oxygen dissociative adsorption and/or surface diffusion of adsorbed oxygen.

3.3.1.3 Electrode sintered at 1250 °C

Figure 74 shows the impedance spectra obtained at 800 and 600 °C and the equivalent circuits used to fit those data. Figure 75 shows the Arrhenius plot of ASR and the elementary phenomena resistances, from which the activation energies can be calculated. Clearly, the high sintering temperature (1250 °C) has a negative effect on the area specific resistance (ASR), which increased from 1.32 Ω cm^2 to 73.44 Ω cm^2 at 800 °C for the electrode sintered at 1150 °C and 1250 °C, respectively. Between 825 and 600 °C, two arcs can be identified in the spectra; however, with decreasing the temperature further, a third concentration is observed at ultra-high

frequency. In this latter case, the spectra can be simulated using three (R-CPE) elements connected in series, as follows $LR_S(R_1CPE_1)(R_2CPE_2)(R_3CPE_3)$. Table 22 lists the electrical parameters for each element derived from spectra fitting.

Figure 74. Impedance spectra for L5S15M electrode sintered at 1250 °C and measured in air at (a) 800 °C and (b) 600 °C. The serial resistances have been removed. The numbers indicate the frequency logarithms.

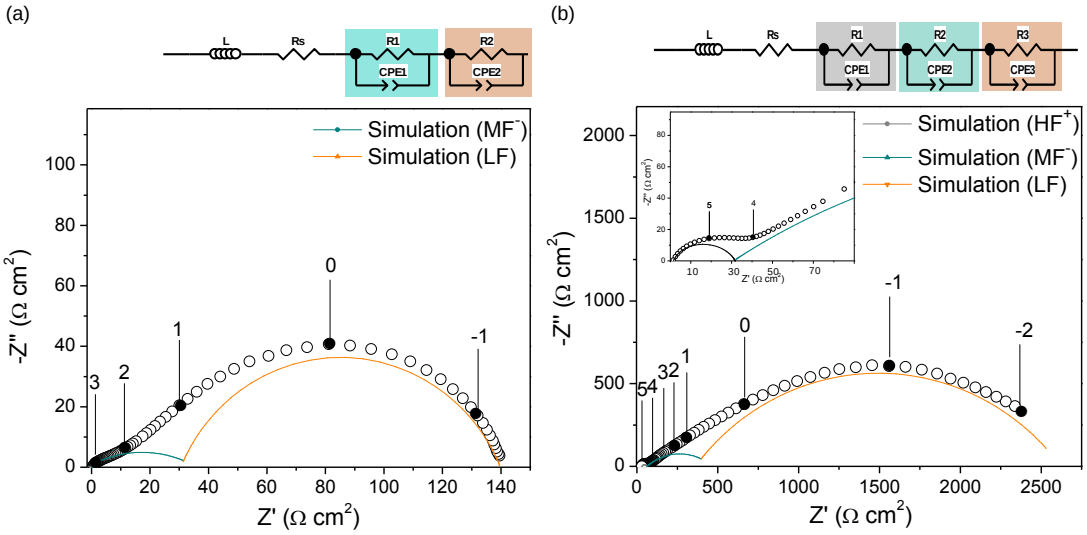

Figure 75. Arrhenius plot of the (a) area specific resistance (ASR) and (b) individual resistances (limiting steps) for L5S15M electrode sintered at 1250 °C and measured in air.

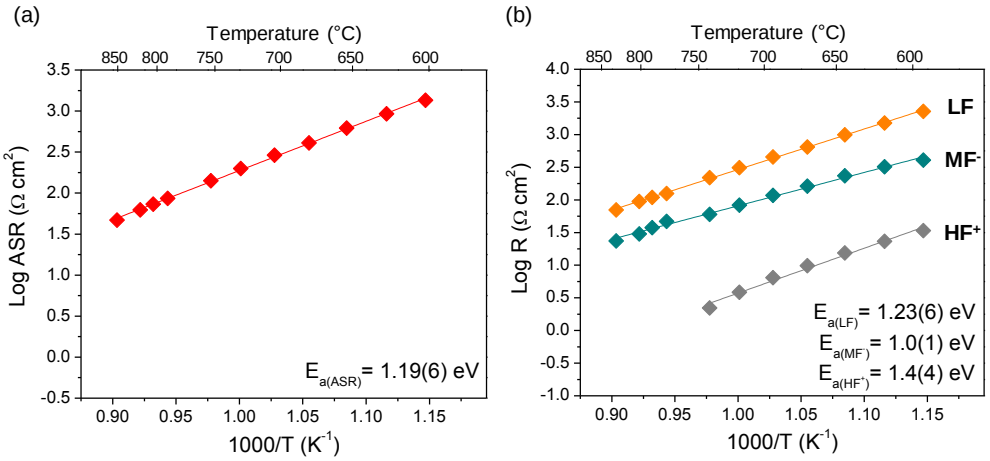

Table 22. Parameters of elementary contributions for L5S15M electrode sintered at 1250 °C and measured in air.

Temp. (°C)	R_s (Ω cm^2)	HF^+			MF^-			LF			R_p (Ω cm^2)	ASR (Ω cm^2)
		R_1 (Ω cm^2)	C_1 (F cm^{-2})	*f* (Hz)	R_2 (Ω cm^2)	C_2 (F cm^{-2})	*f* (Hz)	R_3 (Ω cm^2)	C_3 (F cm^{-2})	*f* (Hz)		
835	6.19				23.54	2.33E-04	29	70.11	1.97E-03	1.2	93.65	46.83
812	7.23				30.13	1.83E-04	29	94.82	1.85E-03	0.9	124.95	62.48
800	7.95				37.57	1.59E-04	27	109.30	1.82E-03	0.8	146.87	73.44
787	8.66				46.77	1.29E-04	26	125.40	1.80E-03	0.7	172.17	86.09
751	11.12	2.17	1.34E-7	545904	60.18	9.93E-05	27	219.50	1.54E-03	0.5	281.85	140.93
726	12.66	3.84	8.71E-8	476122	82.93	8.73E-05	22	312.15	1.43E-03	0.4	398.92	199.46
700	16.75	6.45	6.31E-8	391478	117.10	7.88E-05	17	455.80	1.30E-03	0.3	579.35	289.67
675	22.02	9.82	5.24E-8	309115	162.10	7.65E-05	13	644.10	1.20E-03	0.2	816.02	408.01
649	28.69	15.41	4.52E-8	228605	233.50	7.20E-05	9	991.20	1.04E-03	0.2	1240.11	620.06
623	41.90	23.21	4.24E-8	161594	321.10	6.97E-05	7	1504	8.67E-04	0.1	1848.31	924.16
600	53.34	33.87	4.15E-8	113215	405.90	6.59E-05	6	2261	6.94E-04	0.1	2700.77	1350.39

For an electrode sintering temperature of 1250 °C, around 75% of the ASR is due to the low frequency contribution (10^{-2}-10^{-1} Hz), which is accompanied by a contribution at medium frequency (10^{2}-10^{1} Hz) present in the whole temperature range. Below 750 °C a small additional contribution appears at ultra-high frequency (10^{5}-10^{6} Hz), labeled as HF^{+} (probably masked by the other contributions at lower temperature). Figure 76 depicts the evolution of relaxation frequencies and equivalent capacitances as a function of temperature, helping to deduce the origin of each limiting phenomenon.

Figure 76. Arrhenius plot of the (a) relaxation frequencies and (b) equivalent capacitances for L5S15M electrode prepared at 1250 °C and measured in air.

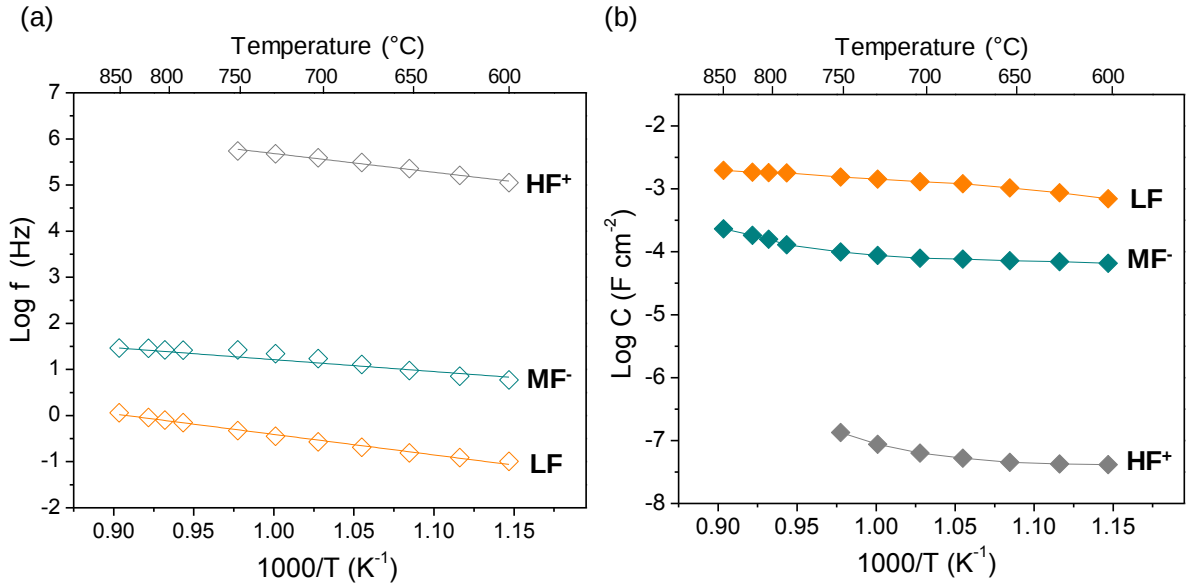

As seen in Figure 76, the arc located at low frequency (LF) side dominates the impedance response and is the most important feature with respect to lower sintering temperatures, with capacitances of the order of 10^{-3}-$10^{-2.5}$ F cm^{-2}. Typically, such low frequency contribution has been associated to gas phase diffusion; however, in this case, the dominant arc cannot be assigned to such process for two reasons: (i) the gas diffusion resistance is temperature-independent, with a very low activation energy ($E_a \approx 0$ eV) [78][79], while in our case the process at LF is thermally activated

$E_{a(LF)}$= 1.23(6) eV and (ii) the capacitance values reported to O_2 gas diffusion into the porous electrode (*e.g.* $PrBaCo_2O_{5+\delta}$ or $Sr_3FeMO_{6+\delta}$ (M=Fe, Co, Ni)) are between 10^{-1}-10^{0} F cm^{-2} [73][80], higher than what we obtained here. According to the literature, such phenomenon has been associated to the formation of secondary phases at electrode/electrolyte interfaces; for example, a contribution of this type (10^{-2}-10^{-1} Hz) has been identified in the spectra of LSM:YSZ/GDC and LSM:YSZ/YSZ cells when the electrodes are sintered at 1180 °C; by contrast, such phenomenon is not present in an LSM:GDC/GDC cell prepared and measured under the same conditions [4]. The formation of a resistive layer could be a consequence of the high reactivity already reported between LSM (or LSCF) and YSZ electrolyte [81][82]. For example, some studies carried out on LSM electrodes report a marked increase in polarization resistance after electrode sintering above 1100 °C, which is interpreted as an effect of the formation of $La_2Zr_2O_7$ and/or $SrZrO_3$ (depending on Sr content) at the LSM/YSZ interface [83][84]. In order to overcome this problem, a thin buffer layer based on gadolinia doped ceria (GDC) has been deposited between the electrolyte (YSZ) and the cathode [85][86]. However, other parallel studies performed on cells consisting of LSCF cathode and YSZ electrolyte protected by a GDC buffer layer show the formation of an insulating $SrZrO_3$ barrier between GDC and YSZ, due to Sr and Zr diffusion through the interlayer when the electrode is sintered above 1100 °C [75][70].

The element distribution on polished cross sections of the Au/L5S15M/GDC/YSZ/GDC/L5S15M/Au cell sintered at 1250 °C was examined by EDXS before EIS measurements (Figure 77 and 79).

Figure 77. SEM image and EDXS concentration mapping of the main elements in the cross-section of Au/L5S15M/GDC/YSZ/GDC/L5S15M/Au cell sintered at 1250 °C (before EIS test).

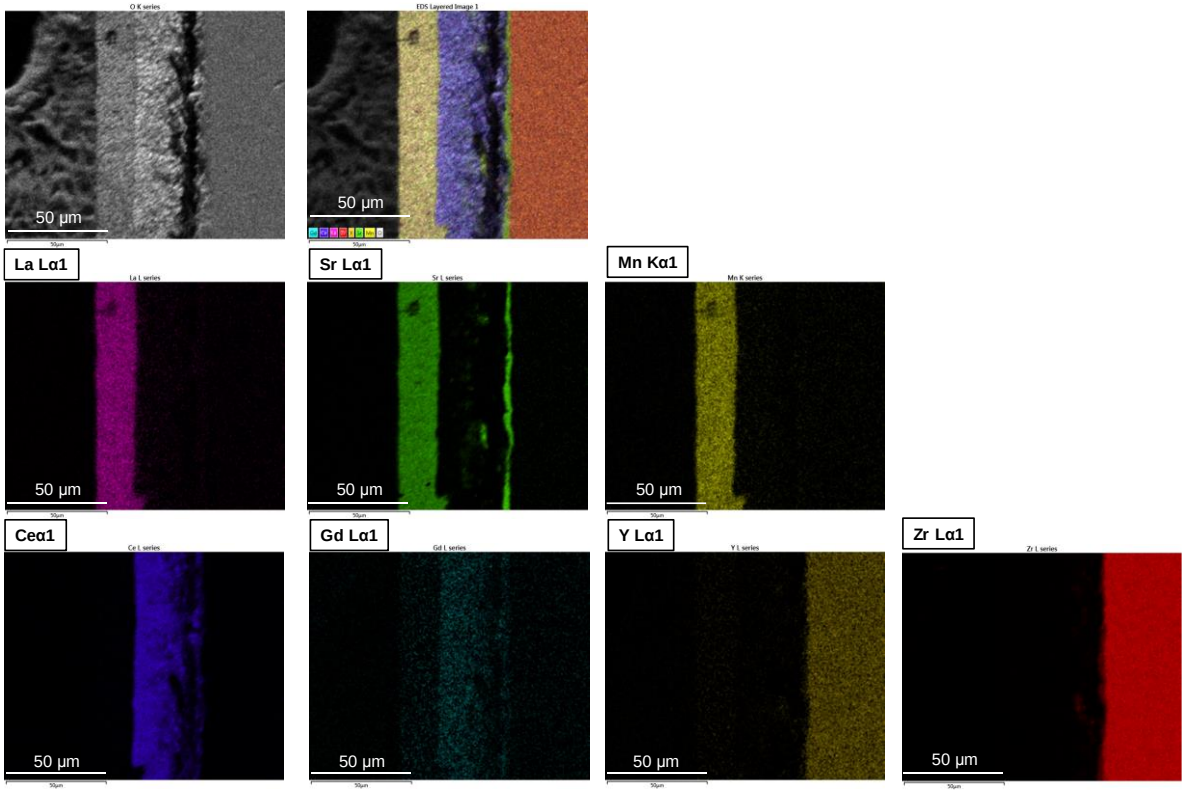

Figure 77 shows the SEM images with the corresponding atomic concentration mapping for La (Lα, 4.65 keV), Sr (Lα, 1.81 keV), Mn(Kα, 5.89 keV), Ce (Lα, 4.84 keV), Gd (Lα, 6.06 keV), Y (Lα, 1.92 keV) and Zr (Lα, 2.04 keV). As shown in SEM micrograph, a gap due to partial delamination at the GDC/YSZ interface is observed in the cell. This delamination is probably caused by the Sr diffusion from L5S15M cathode through the GDC interlayer, since high Sr accumulation (green) is observed at the GDC/YSZ interface. Strontium can subsequently reacts with zirconium forming $SrZrO_3$ in the vicinity of the GDC/YSZ interface and leads to performance degradation [87][88][70].

To confirm the cation diffusion along the L5S15M electrode - GDC interlayer - YSZ electrolyte, a linear EDXS analysis was carried out, that is shown in Figure 78. The intensity of Sr begins to increase within the GDC layer (35 µm) and becomes more intense at the GDC/YSZ interface (around 43 µm), where a strong Zr peak is also visible. In addition, this analysis confirms that Sr is also detected after the gap (56 µm), suggesting that this is the reason for the delamination. Some studies have demonstrated that Sr segregation is mainly produced during the sintering process, where the formation of insulating phases or cracks increase with increasing the sintering temperature [66].

Figure 78. SEM and EDXS images along the cross-section of Au/L5S15M/GDC/YSZ/GDC/L5S15M/Au cell sintered at 1250 °C.

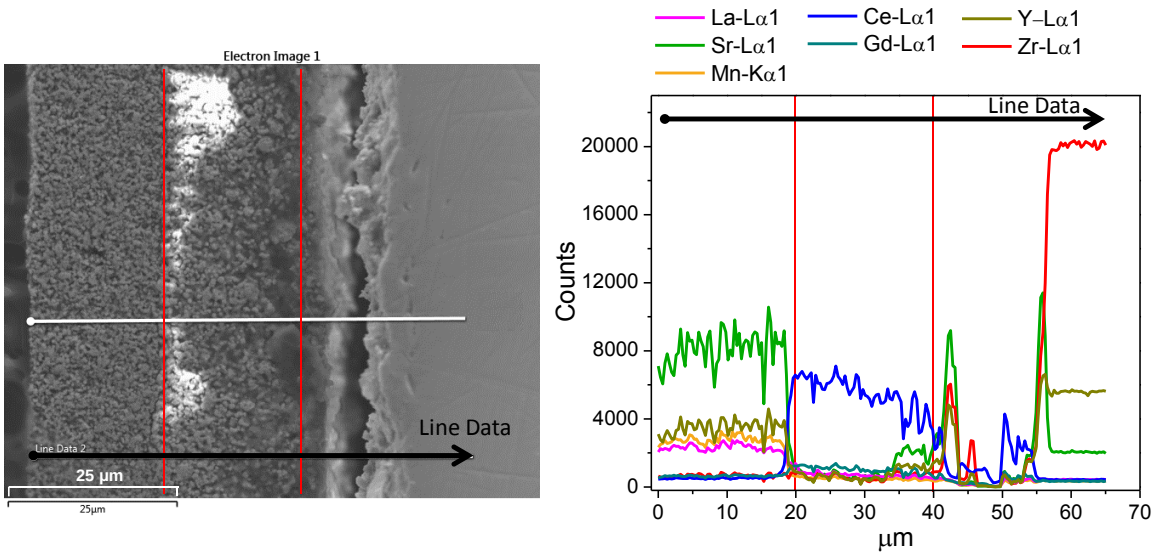

Based on those results, it is clear that the greatest contribution to polarization resistance (LF arc) is related to the formation of a resistive phase rich in strontium at the GDC/YSZ interface. Apparently, at 1250 °C, the formation of such insulating phase during sintering is such that it causes a delamination at the interface, which might also explain the higher resistance values.

The contribution at medium frequency (MF^-) has the same characteristics as that observed in the electrode sintered at 1200 °C; however, the rise of temperature up to 1250 °C results in the increment of the R_{MF-} resistance by almost two orders of magnitude. As observed in the sample sintered at 1200 °C, the high sintering temperature may have caused an excessive grains growth, which is unfavorable for the processes occurring on the surface such as dissociative adsorption of molecular oxygen and/or surface diffusion (O_{ad}), as a first source of explanation. Additionally, and in a similar way as for the cell sintered at 1200 °C, but in a much higher extent, a consequence of Sr diffusion from L5S15M to the GDC/YSZ interface is the strontium depletion of the manganite and in particular of the surface of the L5S15M grains. Such Sr depletion may have modified in an unfavorable way the surface properties of the material creating stronger limitation to the oxygen dissociative adsorption and/or adsorbed oxygen surface diffusion. Indeed, extrapolating the direct reactivity tests between L5S15M and YSZ presented in section 2.5 to the reactivity between both materials throughout the GDC barrier layer, the loss of strontium at the A-site can locally destabilize the RP n=1 structure and induce the formation of secondary phases like $La_{1-x}Sr_xMnO_3$ (LSM) perovskite that can be considered, in comparison to the RP phase, as a poor cathode material. Under this assumption, the poor ionic conductivity of LSM formed in the electrode would be blocking oxygen surface diffusion paths, which is reflected in a drastic increase in polarization resistance [83][89]. Such hypothesis would require the use of high resolution electron microscopy techniques to confirm the existence of such LSM perovskite phase within the electrode material, in particular on the surface of its grains.

According to the literature, the high frequency arc (HF^+) can be related to the grain boundary resistance of the electrolyte. The capacitance values for this contribution are around 10^{-7}-10^{-6} F cm^{-2} for YSZ electrolyte [90] and around 10^{-8}-10^{-7} F cm^{-2} for GDC electrolyte [91]. In the present case, the capacitances obtained are in the order of 10^{-8}-10^{-7} F cm^{-2}, which are similar to those reported for the same phenomenon

observed in cells based on LSCF (or LSM) cathodes on a GDC electrolyte [4][9]. The appearance of such grain boundary resistance is probably due to the presence of Sr within YSZ electrolyte, that segregated at the grain boundaries [45][65].

Finally, many authors have suggested that cell degradation can be related to a simultaneous increase of serial as well as polarization resistance [92][93]. The evolution of the serial resistance can also be examined as a consequence of the reactivity between electrode and electrolyte, particularly high for the sintering temperature of 1250 °C, even if the lack of perfect reproducibility of the GDC/YSZ/GDC assembly can sometimes hinders such phenomena. The formation of additional (insulating) phases between electrolyte and electrode can increase the ohmic resistance of the cell and block the ionic transfer [94][92]. The serial resistance R_S of the symmetrical cells L5S15M/GDC/YSZ/GDC/L5S15M prepared at different temperatures were compared with the serial resistances obtained for GDC/YSZ/GDC sandwich. These sandwiches were measured independently using Pt ink as electrode. The Arrhenius plots of R_S are shown in Figure 79.

Figure 79. Arrhenius plots of the serial resistance (R_S) for the L5S15M/GDC/YSZ/GDC/L5S15M and Pt/GDC/YSZ/GDC/Pt cells measured in air.

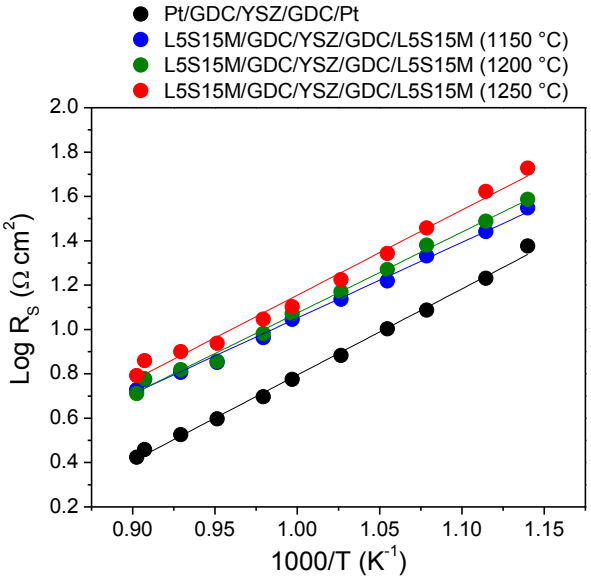

As seen in Figure 79, the addition of the electrode layer generates an increase of serial resistances in comparison with those obtained for the Pt/GDC/YSZ/GDC/Pt sandwich. The R_s resistance is due primarily to the electrolyte resistance; however, the higher values in the complete cells seems to be due to the low conductivity of L5S15M material, especially considering it is porous, and/or to the presence of an insulating phase at the interface GDC/YSZ. We can observe here that R_s values are higher for the cell sintered at 1250 °C than for other temperatures, what is another sign of the already discussed strong diffusion of Sr through the GDC barrier layer and formation of the insulating $SrZrO_3$ phase at the GDC/YSZ interface.

To sum up on the influence of the sintering temperature in the case of an electrode constituted of pure L5S15M, the high sintering temperature of the electrode does not favor the electrochemical performance; in contrast, it not only promotes the grain coarsening but, worst, the Sr diffusion, resulting in the formation of $SrZrO_3$ insulating phase at the GDC/YSZ interface and probable grain boundaries pollution within YSZ electrolyte itself. Moreover, associated Sr depletion within the L5S15M manganite probably modifies the electrode material properties, decreasing its electrocatalytic properties. For those reasons, cell elaboration conditions at a sintering temperature of 1250 °C will not be used in the rest of the study.

3.3.2 USE OF A L5S15M-GDC COMPOSITE

Electrochemical impedance spectroscopy was employed to evaluate the cathode properties of L5S15M-GDC composite electrodes in comparison with L5S15M electrode. It is well know that the addition of a specific amount of an ionic conducting phase, such as YSZ or GDC to the electronically conducting electrode material (LSM) improves the electrocatalytic activity of the electrode [95][15][96]. The improved performance of composite cathode is generally explained as the result of extending the electrochemically active area, such as the triple phase boundary (TPB)

in a pure electronic conductor material. For a mixed ionic-electronic conductor electrode, such as LSCF, which possess a significant ionic conductivity, electrochemical reaction can occur at the whole electrode material [97]. For example, Murray *et al*. reported that the addition of 50 wt% GDC to LSCF produces a significant decrease of the polarization resistance, from 0.114 Ω cm^2 for LSCF to 0.011 Ω cm^2 for LSCF-GDC at 750 °C [56]. On the other hand, some authors explained that the transport properties in a composite are related not only to the composition, but also to the microstructure (such as grain size and porosity) or sintering temperature [9].

The composite was made of 50 wt% of L5S15M and 50 wt% of GDC (thereafter referred to as L5S15M-GDC50), sintered at 1150 or 1200 °C. Figure 80 shows the spectra for L5S15M and L5S15M-GDC50 cathodes sintered at 1150 °C and tested at 800 °C, together with the respective equivalent circuit. Table 23 lists the electrical parameters for each contribution to polarization resistance, derived from model fitting.

Figure 80. Impedance spectra measured in air at 800 °C for L5S15M and L5S15M-GDC50 cathodes sintered at 1150 °C. The numbers indicate the frequency logarithms.

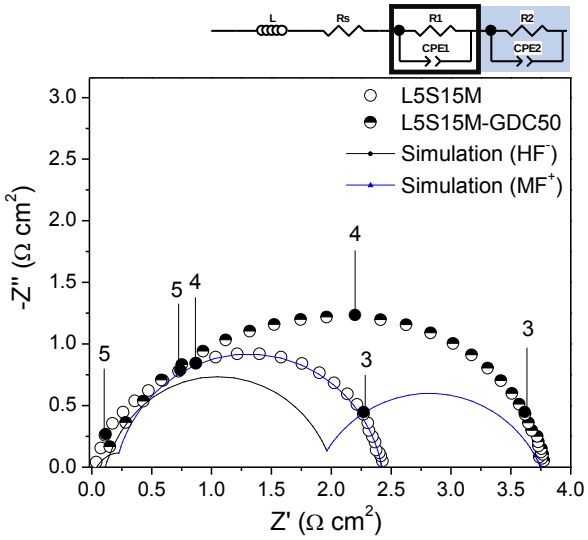

Table 23. Parameters of elementary contributions for L5S15M-GDC50 electrode prepared at 1150 °C and measured in air.

Temp (°C)	R_s (Ωcm²)	HF⁻			MF⁺			R_p (Ω cm²)	ASR (Ω cm²)
		R_1 (Ω cm²)	C_1 (F cm⁻²)	*f* (Hz)	R_2 (Ω cm²)	C_2 (F cm⁻²)	*f* (Hz)		
850	9.96	0.67	8.81E-7	271652	1.43	8.32E-6	13418	2.09	1.05
826	11.04	1.21	8.64E-7	152575	1.49	1.01E-5	10509	2.70	1.35
800	12.75	1.92	9.14E-7	90741	1.86	1.14E-5	7536	3.78	1.89
776	15.06	2.81	9.60E-7	59024	2.38	1.30E-5	5144	5.19	2.59
751	17.70	3.98	1.09E-6	36855	3.10	1.45E-5	3544	7.08	3.54
726	21.37	5.77	1.22E-6	22704	4.15	1.76E-5	2178	9.92	4.96
700	25.96	8.27	1.39E-6	13835	5.49	2.14E-5	1357	13.76	6.88
676	31.62	11.66	1.61E-6	8464	7.48	2.65E-5	802	19.14	9.57
651	40.46	17.15	1.84E-6	5047	10.77	3.32E-5	445	27.92	13.96
625	54.32	28.29	2.20E-6	2553	14.96	4.72E-5	225	43.25	21.63
600	71.07	41.31	2.49E-6	1549	23.28	5.86E-5	117	64.59	32.30

Figure 81. Arrhenius plot of the (a) individual resistances (limiting steps) and (b) area specific resistance (ASR) for L5S15M and L5S15M-GDC50 electrodes (1150 °C) under air.

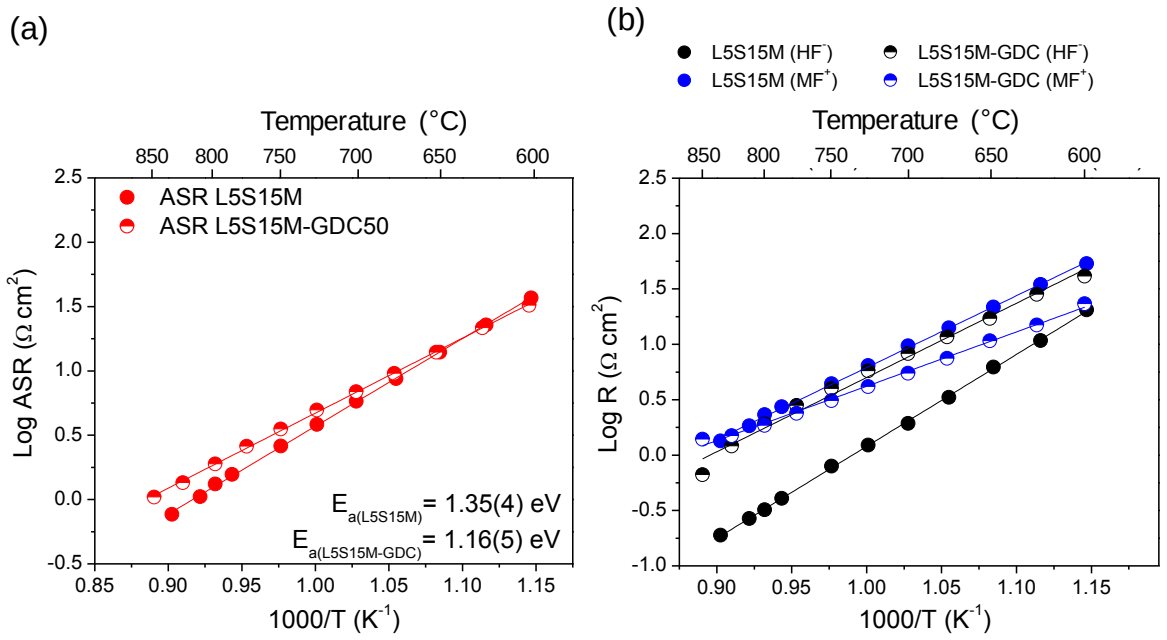

As in the previous case for LSS15M results (section 3.3.1), the spectra for L5S15M-GDC50 composite electrode correspond to at least two overlapping depressed arcs,

a first contribution at high frequency (HF^-) and a second one at medium frequency (MF^+), corresponding to an equivalent circuit consisting of an inductance, a series resistance connected in series with two (R-CPE) subcircuits. For the composite, the two arcs contribute almost equally to the total resistance, while for the L5S15M electrode the main contribution is the medium frequency arc. As seen in Figure 81a, the ASR is not improved by using of L5S15M-GDC50 composite; even below 700 °C both electrodes show very close ASR values. The activation energy values of ASR for both electrodes do not differ significantly, being around 1.2 eV. These activation energies are close to those reported for other composites formed with 50 wt% of GDC, such as LSM-GDC cathode sintered at 1150 °C (1.09 eV) [95] and LSCF-GDC cathode sintered at 1100 °C (1.1 eV) [98]. In addition, from the results of Figure 81b andFigure 82, one can describe the ASR behavior by analyzing the origin of each specific impedance response, which is similar in both electrodes.

Figure 82. Arrhenius plot of the (a) relaxation frequencies and (b) equivalent capacitances for L5S15M and L5S15M-GDC50 composite sintered al 1150 °C.

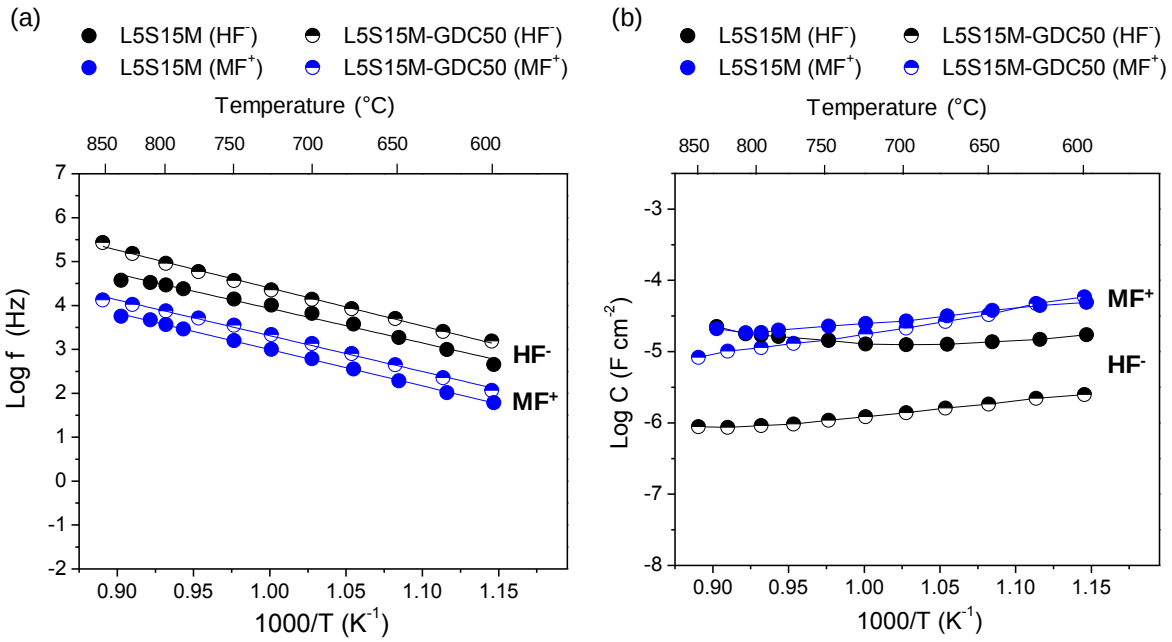

As seen in Figure 82, the frequency range of each arc is the same for both electrodes, what indicates that the same processes are occurring independently of the electrode composition. In the composite, the capacitance values of the high frequency contribution decrease slightly; however, they remain between 10^{-6} and 10^{-5} F cm^{-2}. A detailed analysis of the individual contributions allows to understand the ASR increase observed in the composite. The use of a composite led to a decrease the $R_{(MF+)}$ when the measurement temperature was lower than 750 °C, however, between 850 and 750 °C the $R_{(MF+)}$ for both electrodes was similar. Since this contribution was attributed to the electron transfer with incorporation of oxygen ions into the electrode, one might consider that the ionic conductivity of L5S15M is good at high temperature, while that at low temperature is not high enough and is therefore enhanced by the incorporation of an ionic conductor such as GDC within the electrode. Nevertheless, the $R_{(HF-)}$ contribution, previously attributed to the charge transfer of oxygen ion (O^{2-}) between the electrode and electrolyte, becomes larger for the composite electrode when compared with the L5S15M electrode. Possibly, a sintering temperature of 1150 °C is not enough to achieve a good contact between grains within the composite and/or between the composite and the GDC interlayer. As will be described below, such phenomenon was not detectable when increasing the sintering temperature to 1200 °C.

A similar analysis was carried out for the electrode sintered at 1200 °C. The impedance spectra for L5S15M and L5S15M-GDC50 tested at 800 °C are presented in Figure 83. As in the case of L5S15M (section 3.3.1), the L5S15M-GDC50 composite spectra consist of two overlapped arcs, a main contribution at ultra-medium frequency range MF^+ (10^3-10^4 Hz) and a smaller one at medium frequency MF^- ($10^{1.5}$-10^3 Hz). Table 24 lists the parameters of the circuit elements that are obtained from spectra fitting.

Figure 83. Impedance spectra measured in air at 800 °C for L5S15M and L5S15M-GDC50 electrode sintered at 1200 °C. The numbers indicate the frequency logarithms.

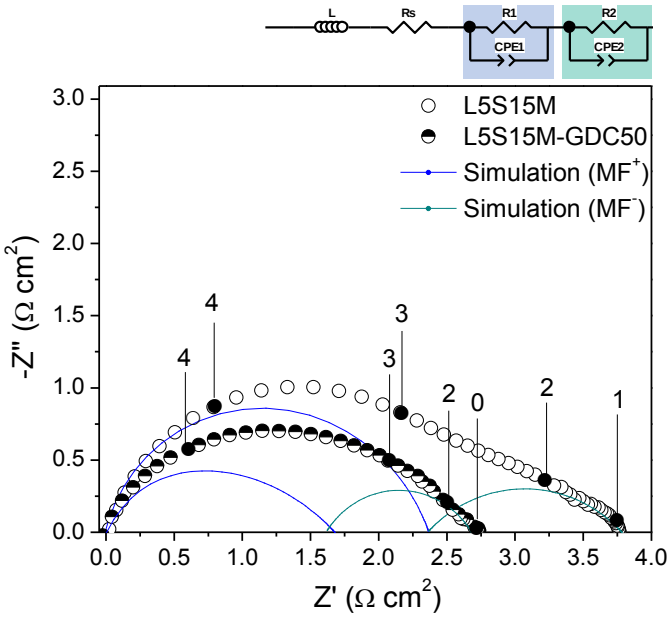

Table 24. Parameters of elementary contributions L5S15M-GDC50 electrode sintered at 1200 °C and measured in air.

Temp. (°C)	R_s (Ω cm²)	MF⁺			MF⁻			R_p (Ω cm²)	ASR (Ωcm²)
		R_1 (Ω cm²)	C_1 (Fcm⁻²)	*f* (Hz)	R_2 (Ω cm²)	C_2 (F cm⁻²)	*f* (Hz)		
850	7.07	0.88	6.98E-6	25945	0.56	1.36E-4	2103	1.43	0.72
826	8.02	1.17	6.16E-6	22065	0.75	1.21E-4	1744	1.93	0.96
800	9.24	1.69	6.87E-6	13738	1.07	1.07E-4	1387	2.75	1.38
776	10.71	2.25	7.31E-6	9684	1.46	1.10E-4	984	3.71	1.86
751	12.66	3.06	6.94E-6	7490	2.16	1.32E-4	561	5.22	2.61
726	15.23	4.25	6.66E-6	5615	3.13	1.89E-4	269	7.39	3.69
700	18.56	6.08	6.90E-6	3798	4.75	2.35E-4	143	10.82	5.41
676	22.82	8.45	7.16E-6	2629	7.44	2.58E-4	83	15.89	7.95
651	28.83	11.94	7.28E-6	1831	12.36	2.72E-4	47	24.30	12.15
625	37.15	17.01	7.00E-6	1337	20.93	2.75E-4	28	37.94	18.97
600	47.28	25.17	6.84E-6	925	35.17	2.80E-4	16	60.34	30.17

Concerning the L5S15M-GDC50 composite electrode, the calculated equivalent capacitance values are in the order of 10^{-5} Fcm^{-2} for the MF^+ arc and in the range 10^{-4} - 10^{-3} Fcm^{-2} for the MF^- arc. The global ASR and the individual resistances

(limiting steps) are displayed in Figure 84. Firstly, the high sintering temperature improved the adhesion between the electrode and the electrolyte, since the HF^- contribution was not identified for any of the electrodes sintered at 1200 °C. The behavior of the MF^+ contribution is similar to that obtained for the electrodes sintered at 1150 °C. This contribution, associated to the electron transfer with incorporation of oxygen ions into the electrode, is improved with the use of a composite. In this case, the high sintering temperature allowed a good connection between the GDC grains, creating a contiguous ionically conducting phase, which apparently improved the ions incorporation. At high measurement temperature, the MF^- resistance values for the pure L5S15M and for the composite electrode are very similar, however, below 725 °C, the MF^- resistance is slightly higher for the composite, *i.e.*, at low temperature, possibly the dissociative adsorption of O_2 molecules from the gas phase is more favorable on the surface L5S15M that on GDC. Despite this, the area specific resistance (ASR) of L5S15M decreased by ~33 % by the addition of 50 wt.% GDC.

Figure 84. Arrhenius plots of the (a) individual resistances (limiting steps) and (b) area specific resistance (ASR) for L5S15M and L5S15M-GDC50 electrodes (1200 °C) in air.

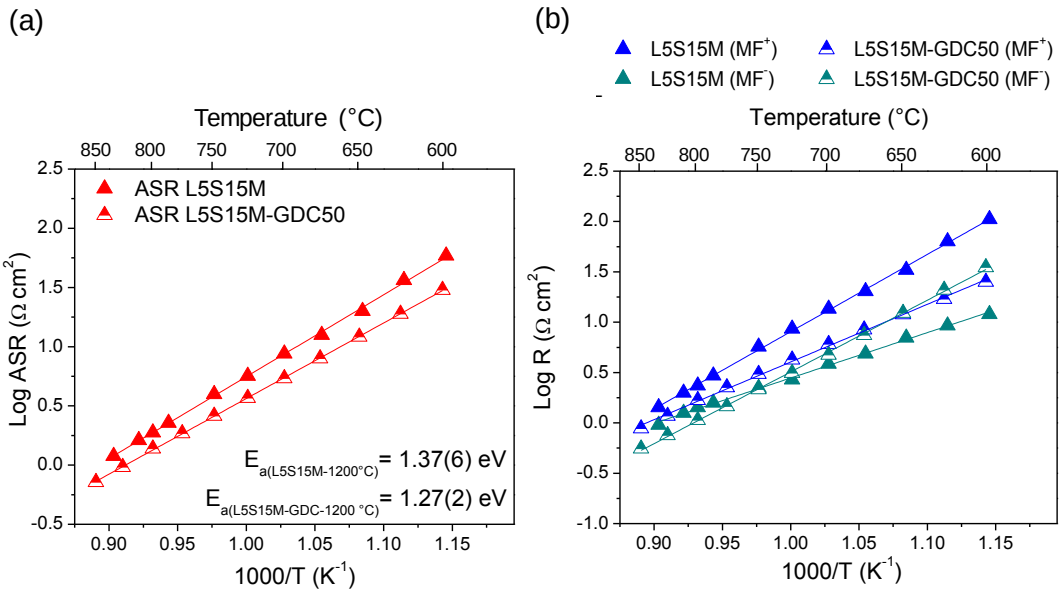

In summary, the electrochemical performance of L5S15M electrode sintered at 1150 °C are not improved by the addition of GDC; however, by increasing the sintering temperature to 1200 °C, the ASR values are slightly lower for L5S15M-GDC50 than for the pure L5S15M electrode. These results suggest that L5S15M certainly behaves as a MIEC, since its own ionic conductivity is sufficiently high to provide superior performance, unlike LSM perovskite (pure electronic conductor), for which the addition of an ionic conducting phase (YSZ) considerably improves the performance compared to a simple porous LSM [99][100].

3.3.3 INFLUENCE OF THE COMPOSITE COMPOSITION (GDC AMOUNT)

At this stage, we observed that the use of a L5S15M-GDC composite can enhance the cathode performance of the Ruddlesden-Popper manganite; in this part, and as a last parameter of study, we describe the effect of varying the relative composition of L5S15M and GDC in the composite electrode. For such study, the electrodes were sintered at 1200 ° C, since a positive effect on the cell performance was observed at such temperature in the case of a 50/50 wt% composite. The composites were prepared using the same methodology as described in section 3.2.1.4, the L5S15M-GDC ratio being modified to produce different composites by mixing L5S15M and GDC in weight ratio of 40:60, 60:40 and 70:30. The abbreviations used to identify the electrodes are given in Table 25.

Table 25. Abbreviations for L5S15M-GDC composites prepared at 1200 °C.

Abbreviation	Composition (%)	
	L5S15M	GDC
L5S15M	100	0
L5S15M-GDC30	70	30
L5S15M-GDC40	60	40
L5S15M-GDC50	50	50
L5S15M-GDC60	40	60

Figure 85 shows the impedance spectra measured in air for the different composite cathodes. In general, the shape of the impedance spectra for the composites does not differ significantly from one to another. In all cases the impedance plots consist of two arcs, a first arc at ultra-medium frequency MF^{+} (10^{3}-10^{4} Hz) and a second one at medium frequency MF^{-} ($10^{1.5}$-10^{3} Hz). Table 26 and Figure 86a summarize the area specific resistance (ASR) values and their respective activation energies obtained for all composite cathodes in comparison to pure L5S15M.

Figure 85. Impedance spectra measured in air at 800 °C for the different L5S15M-based cathodes prepared at 1200 °C. The solid line corresponds to the simulation and the numbers indicate the frequency logarithms.

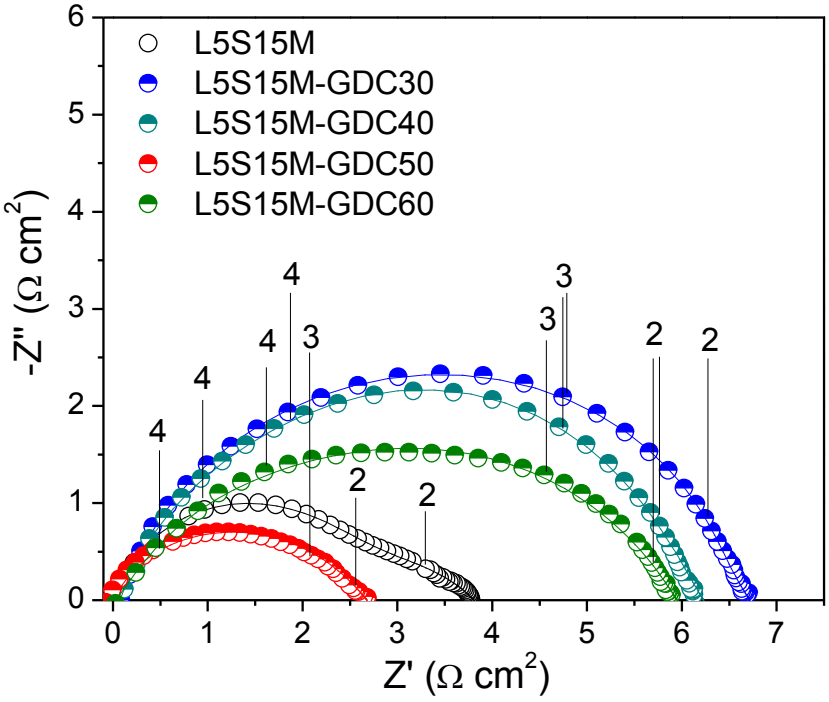

Table 26. Area specific resistance (ASR) values in air for composite cathodes sintered at 1200 °C.

Temp. (°C)	ASR (Ω cm²)				
	L5S15M	**L5S15M-GDC30**	**L5S15M-GDC40**	**L5S15M-GDC50**	**L5S15M-GDC60**
850	1.19	1.71	1.44	0.72	2.18
826	1.63	2.55	2.29	0.96	2.66
800	1.89	3.31	3.00	1.38	2.93
776	2.27	4.06	3.94	1.86	3.33
751	3.97	5.16	5.14	2.61	4.19
726	5.66	7.66	7.65	3.69	5.47
700	8.73	10.90	11.35	5.41	7.61
676	12.58	15.76	16.86	7.95	11.18
651	20.02	24.37	25.85	12.15	16.58
625	36.43	38.59	43.21	18.97	24.60
600	58.71	62.80	65.30	30.17	35.36

Figure 86. Area specific resistance (ASR) for L5S15M and composite electrodes (1200 °C) under air. (a) temperature dependence and (b) GDC amount dependence.

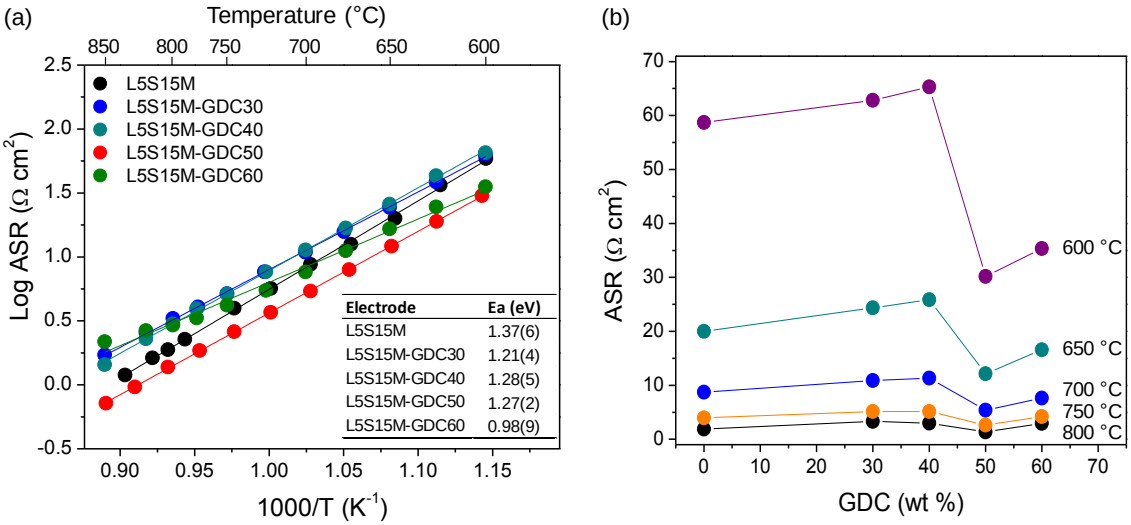

Comparing the ASR of L5S15M with that of the composite electrodes, the only improvement is found in the case of L5S15M-GDC50 electrode; for example, the ASR at 800 °C is 1.89, 3.31, 3.00, 1.38 and 2.93 Ω cm² for 0, 30, 40, 50 and 60 wt% of GDC, respectively. The average activation energy of 1.22(12) eV is in agreement

with that reported for LSCF-GDC50 (1.27 eV) [101] or La_2NiO_4-SDC40 (1.28(4) eV) [61]. The Ea values seems not substantially affected by the GDC amount in the electrode, indicating that the reaction mechanism is similar for the different cathodes. In this way, for the electrodes sintered at 1200 °C, the phenomena that contribute to the polarization (previously described into details) are mainly the electron transfer with incorporation of oxygen ions into the electrode (MF^+) and the dissociative adsorption of molecular oxygen and/or surface diffusion (MF^-).

On the other hand, the variation of the polarization resistances with the GDC content, although complicated to explain, has also been observed in LSCM(GDC-YSZ) and $NdBa_{0.5}Sr_{0.5}Co_{1.5}Fe_{0.5}O_{5+\delta}$(NBSCF)-GDC composites when GDC amount was varied between 0 and 80%. The authors showed that the polarization resistance does not change linearly with the increase of GDC amount. For example, for LSCM(GDC-YSZ) composite, the ASR is minimal using 50 w% GDC, while for (NBSCF)-GDC composite the lowest ASR was obtained using 40 wt % GDC [34][102][103]. In our case (Figure 86b), the ASR shows a slight increase when using up to 40 wt% GDC, then decreases with 50 wt% GDC, and increases again beyond 50 wt% of GDC amount. The latter phenomenon can be explained as an effect of the excessive amount of GDC causing the LSCM particles lose connectivity within the composite, what means a loss of electron conduction [34].

Table 27 summarizes the results of all cell tests in which both the sintering temperature and electrode composition (composite) were varied. The lowest area specific resistance values (ASR) were in the range between 1.32 Ω cm^2 and 1.89 Ω cm^2 at 800 °C, obtained for the pure L5S15M and L5S15M-GDC50 composite electrodes sintered at 1150 y 1200 °C, respectively. It is worth noting that, although the values of ASR and activation energy are very close, the phenomena that contribute to the cathode reaction are strongly dependent on the sintering temperature and only slightly of the electrode composition (composite).

Table 27. Summary of the area specific resistance (ASR) and activation energies for the different electrodes tested in air.

Sintering temperature	**1150 °C**		**1200 °C**					**1250 °C**
Electrode Composition	L5S15M	L5S15M-GDC50	L5S15M	L5S15M-GDC30	L5S15M-GDC40	L5S15M-GDC50	L5S15M-GDC60	L5S15M
ASR (Ω cm^2) 800 °C	1.32	1.89	1.89	3.31	3.00	1.38	2.93	73.44
E_a (eV)	1.35(4)	1.16(5)	1.37(6)	1.21(4)	1.28(5)	1.27(2)	0.98(9)	1.19(6)

As a conclusion concerning this part of the study, since the objective is to use the material as a symmetrical electrode, only L5S15M and L5S15M-GDC50 electrodes sintered at 1150 y 1200 °C were chosen to study the electrochemical hydrogen oxidation mechanism, object of the next section.

3.4 ELECTROCHEMICAL PROPERTIES IN REDUCING ATMOSPHERE

This part of the study is focused on the evaluation of the behavior of $La_{0.5}Sr_{1.5}MnO_{4+\delta}$ (L5S15M) as an SOFC anode. As in the last section, the electrochemical performance in reducing atmosphere was examined as a function of the sintering temperature and the use of a composite. The electrochemical measurements were carried out immediately after the respective electrochemical characterization in air. The cells were evaluated in wet 3% H_2/Ar (3% H_2O), dry 3% H_2/Ar, and wet pure H_2 (3% H_2O) with a flow rate of 150 mL/min between 830 and 600 °C. The impedance spectra were recorded in the frequency range 1 MHz - 10 mHz and normalized with respect to the surface area (1.02 cm^2).

3.4.1 INFLUENCE OF THE SINTERING TEMPERATURE

Figure 87 shows an example of spectrum obtained in wet hydrogen at 700 °C for L5S15M electrodes sintered at 1150 and 1200 °C, as well as the equivalent circuit used to fit each spectrum. Table 28 and 29 list the parameters of the circuit elements which are obtained from the spectrum fitting.

Figure 87. Impedance spectra measured in H_2 (3% H_2O) at 700 °C for L5S15M electrode sintered at (a) 1150 and (b) 1200 °C. The serial resistances have been removed. The numbers indicate the frequency logarithms.

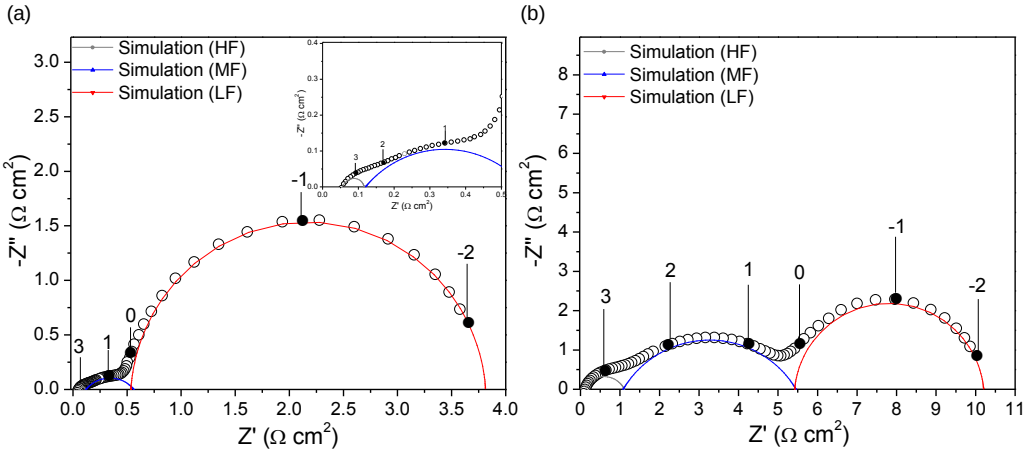

As seen in Figure 87, the change in the shape of impedance spectra with increasing temperature is observed mainly in the arcs at low and middle frequency, which noticeably increase when changing from 1150 to 1200 °C. According to Figure 88, the corresponding area specific resistance (ASR) at 800 °C in wet H_2 of L5S15M electrodes increases approximately three times with increasing sintered temperature, from 0.61 Ω cm^2 to 1.68 Ω cm^2 for the electrodes sintered at 1150 and 1200 °C, respectively. In addition, both electrodes present similar activation energy values for ASR, around 1.2 eV. These values are close that those reported for other anodes measured in reducing atmosphere, such as Ni-YSZ (1.0-1.5 eV wet in different H_2 concentration), LSCM (1.09 eV in wet 5% H_2) [104], LSCM (1.38 eV in wet H_2) [105].and LSTM4646 (1.07(5) eV in wet H_2 [32]).

Table 28. Resistances in H_2-3% H_2O for L5S15M electrodes prepared at 1150 °C and 1200 °C.

Temp. (°C)	L5S15M sintered at 1150 °C						L5S15M sintered at 1200 °C					
	R_s	R_1 (Ω cm^2)	R_2 (Ω cm^2)	R_3 (Ω cm^2)	R_p (Ω cm^2)	ASR (Ω cm^2)	R_s	R_1 (Ω cm^2)	R_2 (Ω cm^2)	R_3 (Ω cm^2)	R_p (Ω cm^2)	ASR (Ω cm^2)
830	3.47	0.01	0.15	0.89	1.04	0.52	4.68	0.13	1.54	1.05	2.72	1.36
800	4.12	0.01	0.18	1.02	1.21	0.61	5.57	0.18	1.89	1.28	3.35	1.68
776	5.16	0.02	0.20	1.28	1.51	0.75	6.95	0.30	2.42	1.82	4.53	2.27
751	5.94	0.03	0.26	1.57	1.85	0.93	8.11	0.44	2.79	2.19	5.41	2.71
726	7.09	0.04	0.33	2.06	2.43	1.22	9.78	0.64	3.35	2.97	6.97	3.48
700	9.18	0.07	0.44	3.28	3.80	1.90	12.67	1.07	4.38	4.79	10.24	5.12
676	11.85	0.12	0.59	5.32	6.02	3.01	16.39	1.79	5.58	7.67	15.03	7.52
651	15.78	0.18	0.84	9.14	10.16	5.08	22.05	2.98	7.65	13.07	23.70	11.85
625	21.16	0.27	1.23	15.20	16.70	8.35	29.58	5.01	9.74	21.68	36.42	18.21
600	29.57	0.40	1.76	26.06	28.22	14.11	41.83	9.71	11.82	36.84	58.37	29.18

Table 29. Relaxation frequencies and equivalent capacitances in H_2-3% H_2O for L5S15M electrodes prepared at 1150 °C and 1200 °C.

Temp. (°C)	L5S15M sintered at 1150 °C						L5S15M sintered at 1200 °C					
	f_1 (Hz)	**f_2 (Hz)**	**f_3 (Hz)**	**C_1 (F cm^{-2})**	**C_2 (F cm^{-2})**	**C_3 (F cm^{-2})**	**f_1 (Hz)**	**f_2 (Hz)**	**f_3 (Hz)**	**C_1 (F cm^{-2})**	**C_2 (F cm^{-2})**	**C_3 (F cm^{-2})**
830	1711	30	0.09	1.03E-2	3.68E-2	2.11	6354	41	0.09	1.96E-4	2.54E-3	1.73
800	2091	26	0.08	5.51E-3	3.36E-2	2.03	5099	32	0.08	1.71E-4	2.66E-3	1.57
776	2198	24	0.06	2.96E-3	3.40E-2	2.00	3687	24	0.06	1.45E-4	2.78E-3	1.40
751	2309	20	0.05	2.17E-3	3.11E-2	1.86	2796	19	0.06	1.31E-4	2.94E-3	1.29
726	2339	17	0.05	1.59E-3	2.88E-2	1.60	2017	16	0.05	1.23E-4	3.03E-3	1.12
700	2358	13	0.04	9.30E-4	2.73E-2	1.13	1265	11	0.04	1.17E-4	3.21E-3	0.77
676	2373	11	0.04	5.82E-4	2.57E-2	0.81	791	8	0.04	1.12E-4	3.50E-3	0.55
651	2392	7	0.03	3.75E-4	2.53E-2	0.56	490	5	0.03	1.09E-4	3.80E-3	0.38
625	2417	6	0.02	2.47E-4	2.20E-2	0.42	306	4	0.03	1.04E-4	4.14E-3	0.28
600	2440	5	0.02	1.63E-4	1.95E-2	0.32	163	3	0.02	1.01E-4	4.84E-3	0.21

Figure 88. Arrhenius plots of ASR for L5S15M electrodes sintered at 1150 and 1200 °C measured in wet H_2 (3% H_2O).

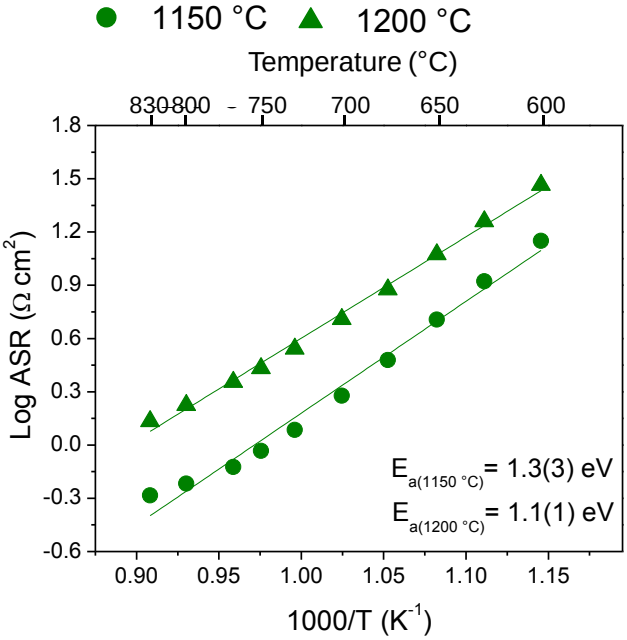

For all spectra measured in wet pure hydrogen, at least two arcs are readily recognized; however, it seems that three arcs are indeed necessary to produce a satisfactory fit. The data were thus fitted using the equivalent circuit $LR_s(R_1CPE_1)(R_2CPE_2)(R_3CPE_3)$, which has also been used to describe the electrochemical behavior of Ni/YSZ cermet or LSTM anodes measured in wet hydrogen (Figure 89) [106][107]. In these materials, three processes were also identified in the spectra, which were attributed to different limiting steps occurring in the anode, depending on the characteristic frequencies, capacitances, and behavior when varying pH_2 and pH_2O.

Figure 89. Impedance spectra of (a) Ni/YSZ anodes measured at 1000 °C and (b) LSTM4646 anode measured at 810 and 760 °C in wet H_2. Taken from [32][106] .

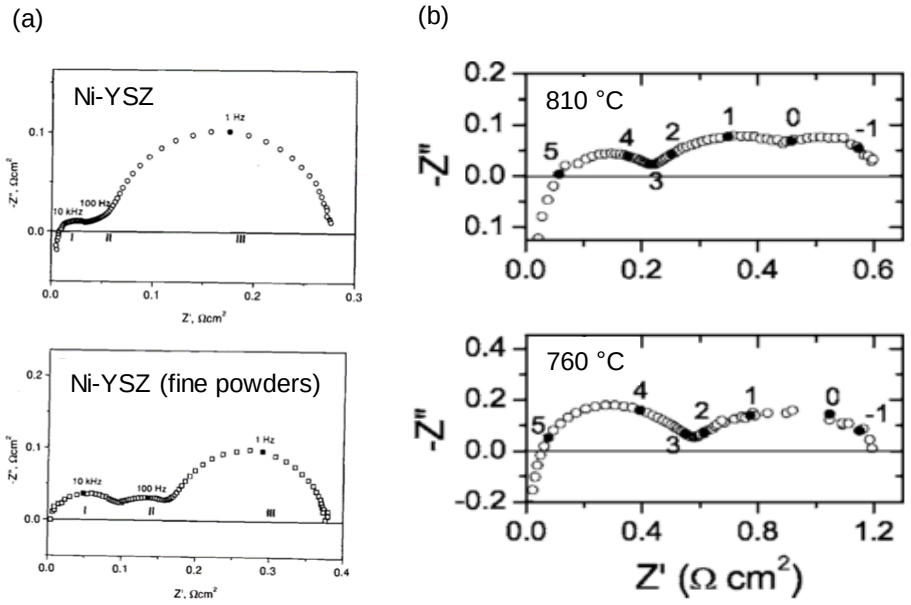

Using the frequency relaxation (Schouler methodology) and equivalent capacitances, the various contributions of the impedance spectra were assigned to different electrochemical processes. As observed in Figure 90, in the whole studied temperature range, three similar processes are identified in electrodes sintered at 1150 or 1200 °C. A first process at high frequency 10^3-10^4 Hz (HF) with equivalent capacitance of 10^{-4}-10^{-3} F cm^{-2}, a second process at medium frequency $10^{0.5}$-10^2 Hz (MF) with equivalent capacitance of 10^{-3}-10^{-2} F cm^{-2} and a third process at low frequency 10^{-2}-10^{-1} Hz (LF) with equivalent capacitance of 10^{-1}-10^0 Fcm^{-2}. Figure 91 shows the variation with temperature of each resistance that contributes to the total polarization resistance.

Figure 90. (a) Relaxation frequencies and (b) equivalent capacitances of the limiting steps for L5S15M electrodes sintered at 1150 and 1200 °C and measured in H_2 (3% H_2O).

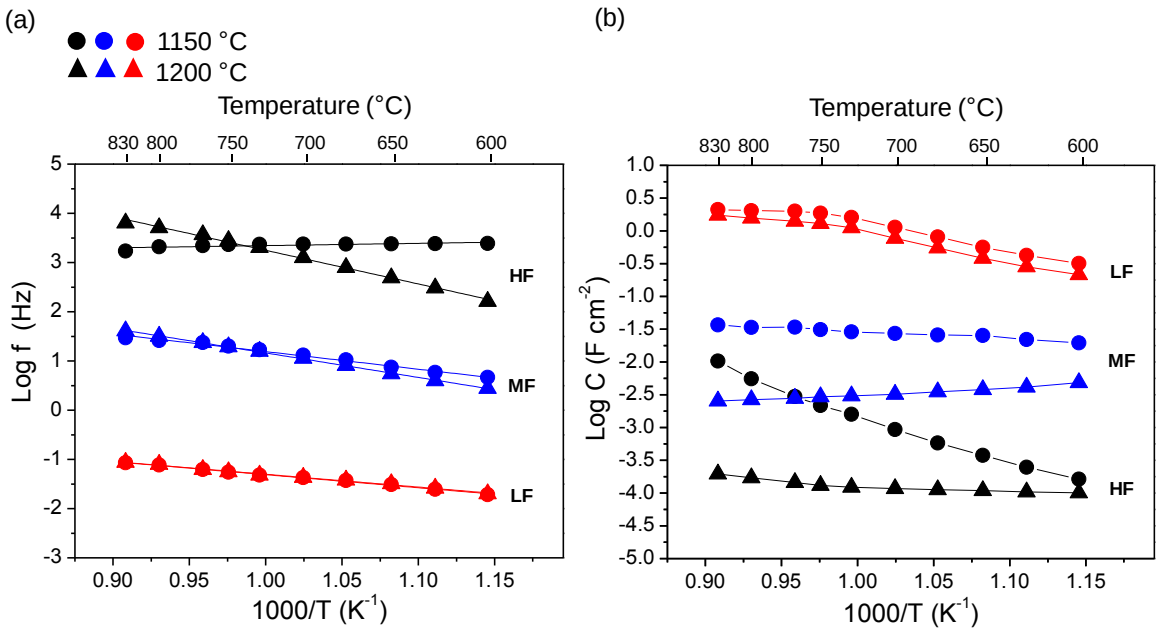

Figure 91. Arrhenius plots of individual resistances (limiting steps) for L5S15M electrode sintered at (a) 1150 °C and (b) 1200 °C and measured in H_2-3% H_2O.

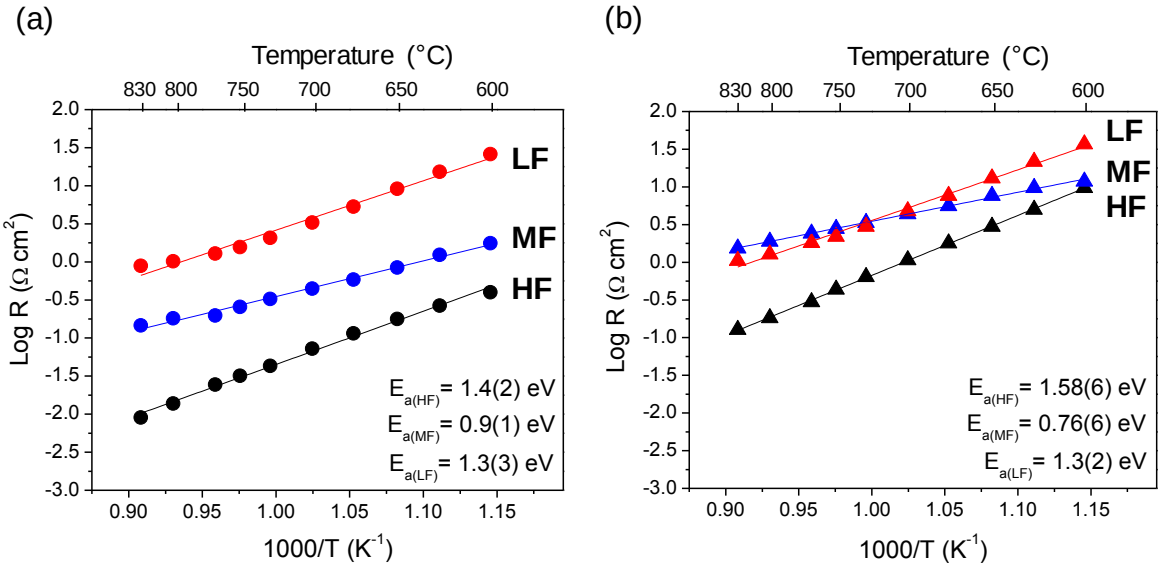

As shown in Figure 91 and Table 38, for the electrode sintered at 1150 °C, the low frequency resistance R_{LF} is the largest contribution to the polarization resistance (~ 90% of R_p), while, for the electrode sintered at 1200 °C, R_{LF} and R_{MF} contribute almost in the same proportions. In both electrodes, the small HF arc represents only 1% (1150 °C) and 5% (1200 °C) of the polarization resistance. The phenomena assigned to each process will be discussed below, considering also the results obtained in wet and dry 3% H_2/Ar, since the temperature, the partial pressure of water (pH_2O) and hydrogen (pH_2) are parameters that can cause individual changes in some of those contributions.

The results obtained in wet H_2 and 3 % H_2/Ar (3% H_2O) were compared with the aim to evaluate the influence of the hydrogen concentration. Figure 92 shows the impedance spectra for L5S15M measured at 800 °C in wet pure and diluted hydrogen. The relaxation frequency was the first considered parameter to identify the similarity of the processes found in both atmospheres (Figure 93).

Figure 92. Impedance spectra measured in H_2 (3% H_2O) and 3 % H_2/Ar (3% H_2O) at 800 °C for L5S15M electrode sintered at (a) 1150 °C and (b) 1200 °C. The numbers indicate the frequency logarithms.

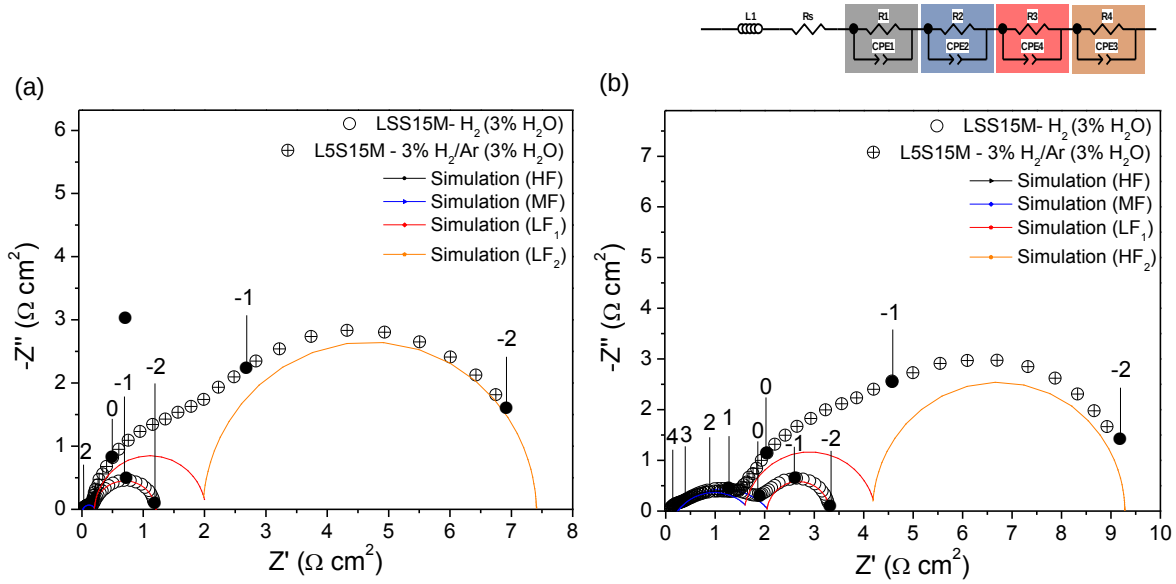

Figure 93. Relaxation frequencies for L5S15M electrodes sintered at (a) 1150 °C and (b) 1200 °C measured in wet H_2 (filled symbols) and 3 % H_2/Ar (empty symbols).

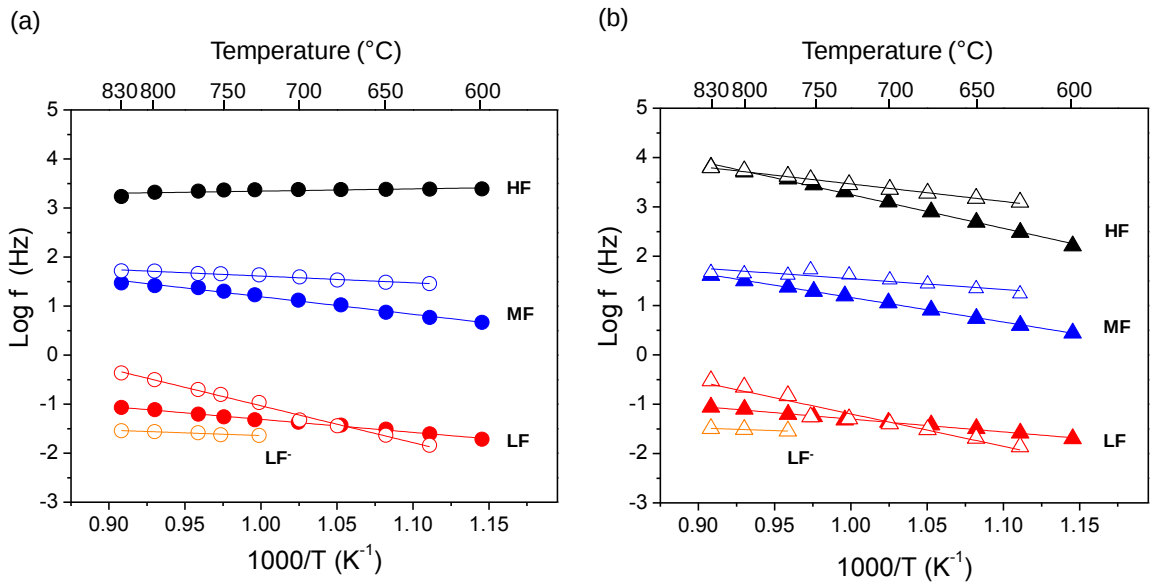

The spectra obtained in diluted hydrogen for L5S15M sintered at 1150 °C were simulated using three (R-CPE) elements connected in series, as follows $LR_s(R_2CPE_2)(R_3CPE_3)(R_4CPE_4)$. It is worth noting that between 830 and 725 °C, an additional contribution is visible at very low frequency LF^- (around $10^{-1.5}$ Hz), which overlaps at lower temperature with the largest low frequency contribution. In addition, for this sample no high frequency (HF) contribution is detected. For the electrode sintered at 1200 °C, the spectra obtained between 830 and 750 °C were analyzed using four (R-CPE) elements with a $LR_s(R_1CPE_1)(R_2CPE_2)(R_3CPE_3)(R_4CPE_4)$ circuit; as in the previous case, an additional arc is identified at very low frequency (LF^-) and high temperature but unlike the electrode sintered at 1150 °C, the spectra measured in diluted hydrogen for the electrode sintered at 1200 °C show a high frequency limiting step, which is in the same range as that obtained in wet pure hydrogen. The electrical parameters for each element derived from spectra fitting are summarized in Annex 10.

3.4.1.1 Electrode process corresponding to the high frequency arc in wet hydrogen

In both cases (electrodes sintered at 1150 and 1200 °C), the capacitances of the HF contribution are about 10^{-4}-10^{-3} F cm^{-2} and do not vary significantly with the measuring temperature. Based on the literature, these values are in the similar order of magnitude (10^{-5}-10^{-4} F cm^{-2}) as an interfacial process identified at high frequency in wet H_2 for $La_{0.4}Sr_{0.6}Ti_{0.4}Mn_{0.6}O_{3-\delta}$ (LSTM4646) [32], $La_{0.75}Ba_{0.25}Cr_{0.5}Mn_{0.5}O_{3-\delta}$ (LBCM) [105] and Ni-YSZ cermet [108] anodes, which was related to charge transfer reactions at the electrode/electrolyte interface. In addition, this process is thermally activated with activation energies of 1.4(2) eV and 1.58(6) eV for the electrodes sintered at 1150 and 1200 °C, respectively. These values are in agreement with those reported for the same process identified in LSTM4646 (0.9-1.5 eV), LBCM (1.58 eV) and Ni-YSZ (1.68 eV) anodes. Based on these characteristics, the HF response can be attributed to the transfer of charged species across LS5S15M/electrolyte interface.

The charge transfer reaction has been primarily studied for Ni-YSZ cermet anode, where is assumed that the oxidation reaction takes place close to the three-phase boundary (TPB); for this case, several controversial mechanisms have been proposed in order to explain the actual pathway or the nature of the elementary steps [109][110]. As discussed by Vogler and Bessler in [30][29], those mechanisms include charge transfer at the TPB through hydrogen spillover, oxygen spillover and hydroxyl spillover (Figure 94).

Figure 94. Elementary kinetic scenarios at a Ni/YSZ TPB. (a) Spillover of hydrogen from the Ni surface onto an oxygen ion or hydroxyl ion on the YSZ surface. (b) Charge-transfer reactions with and without spillover of oxygen ions from the YSZ surface to the Ni surface. (c) Hydroxyl spillover from the YSZ surface to the Ni surface. Taken from [30].

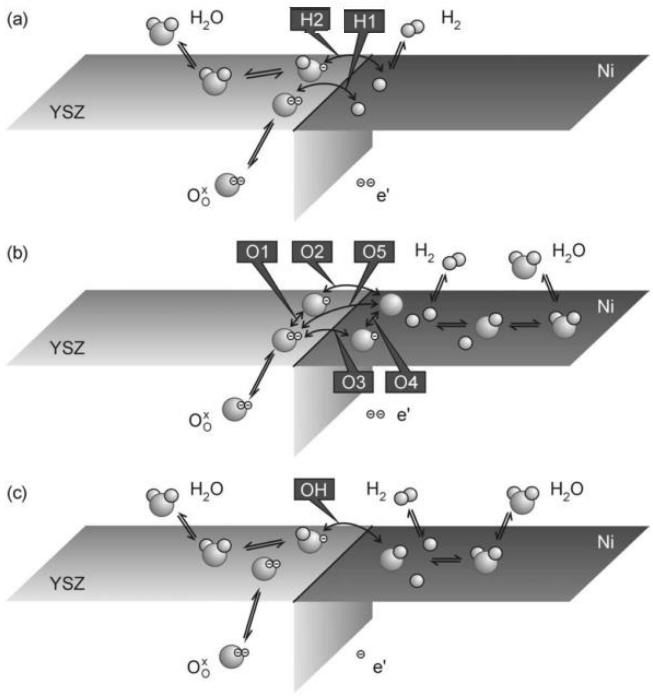

In the hydrogen spillover pathway, Ni-adsorbed H atoms move over the TPB towards the YSZ surface while simultaneously transferring their electrons to the Ni electrode. On the YSZ surface, they can attach either to OH^- or O^{2-} sites, according to the following reactions:

H1 $$H_{Ni} + O_{YSZ}^{2-} \rightleftarrows OH_{YSZ}^{-} + e_{Ni}^{-} + \square_{Ni} \qquad (3\text{-}29)$$

H2 $$H_{Ni} + OH_{YSZ}^{-} \rightleftarrows H_2O_{YSZ} + e_{Ni}^{-} + \square_{Ni} \qquad (3\text{-}30)$$

In the oxygen spillover pathway, the oxygen ions (formally O_{YSZ}^{2-}) may hop from the YSZ surface to the Ni surface, undergoing two charge-transfer reactions that can take place before, after, or during the hop (Equations 3-6 to 3-9):

O1 $$O_{YSZ}^{2-} \rightleftarrows O_{YSZ}^{-} + e_{Ni}^{-}$$ (3-31)

O2 $$O_{YSZ}^{2-} + \square_{Ni} \rightleftarrows O_{Ni}^{-} + e_{Ni}^{-} + \square_{YSZ}$$ (3-32)

O4 $$O_{Ni}^{-} \rightleftarrows O_{Ni} + e_{Ni}^{-}$$ (3-33)

O5 $$O_{YSZ}^{2-} + \square_{Ni} \rightleftarrows O_{Ni} + 2e_{Ni}^{-} + \square_{YSZ}$$ (3-34)

In the hydroxyl spillover, the charge transfer is occurring during hopping of OH^- from YSZ to Ni surface or Ni to YSZ, according to the following reaction:

OH $$OH_{YSZ}^{-} + \square_{Ni} \rightleftarrows OH_{Ni} + e_{Ni}^{-} + \square_{YSZ}$$ (3-35)

The study carried out by Vogler *et al*. demonstrated that only the hydrogen spillover mechanism (Reaction H1 and H2) can reproduce the complete experimental trends, in which the resistance varies slightly with the pH_2 concentration [30]. Despite the fact that these charge-transfer kinetics models have been investigated for the particular case of H_2 oxidation at SOFC Ni/YSZ anodes, these could also be valid for any kind of electrochemical charge transfer reaction, including different SOFC anode materials, obviously considering other parameters within the model [28][31]. However, to confirm the charge transfer processes a deeper study of the electrochemical behavior using different H_2 and H_2O concentrations would be necessary

In our case, the resistance values (R_{HF}) show a very small variation with the change of the H_2 concentration (Figure 95). This behavior was also observed in the Ni-YSZ and LSTM4646 anodes, for which the process observed at high frequency was almost insensitive to atmosphere composition, and in both cases attributed to the charge transfer taking place at the Ni/YSZ or LSTM4646/YSZ interface.

Figure 95. Arrhenius plots of high frequency resistance (R_{HF}) for L5S15M electrode sintered at 1200 °C and measured in wet H_2 (filled symbols) and 3 % H_2/Ar (empty symbols).

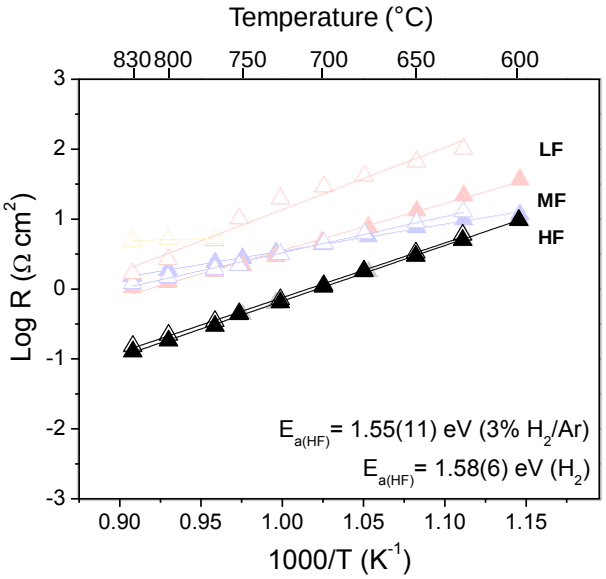

As seen in Figure 91, the HF response increases by one order of magnitude with increasing sintering temperature; for example, at 800 °C, the HF resistance value changes from 0.01 Ω cm^2 to 0.18 Ω cm^2 for the electrodes sintered at 1150 and 1200 °C, respectively. Taking into account the behavior observed in air, the high sintering temperature promotes the Sr diffusion to the electrolyte and therefore the reactivity. If $SrZrO_3$ is assumed to be formed mainly at the GDC/YSZ interface, the presence of such phase probably blocks the charge transfer reaction at the GDC/YSZ interface. Another explanation would be related to the Sr depletion in particular at the interface between L5S15M and GDC, the modification of the boundary chemistry being also responsible for the difficult H-spillover at the GDC/manganite interface, especially if an interfacial LSM perovskite layer has formed, that would be indeed transformed into La_2O_3, SrO and MnO in reducing conditions. The confirmation of such hypotheses is beyond the scope of our study and would require, for example, the use of high resolution microcopy techniques.

3.4.1.2 Electrode process corresponding to the medium frequency arc in wet hydrogen

An MF limiting step ($10^{0.5}$-10^{2} Hz) is clearly identified in both electrodes (sintered at 1150 and 1200 °C) with equivalent capacitances between 10^{-3} and 10^{-2} F cm^{-2}. As observed in Table 28 and Figure 96, the R_{MF} resistances are notably higher for the electrode sintered at 1200 °C; for example, at 800 °C R_{MF} value are 0.18 Ω cm^2 and 1.54 Ω cm^2 for a sintering temperature of 1150 and 1200 °C, respectively. The resistances for this process displays a thermally activated character with activation energies of 0.9(1) eV for the electrode sintered at 1150 °C and 0.76(6) eV for the preparation at 1200 °C. So far, the capacitance values obtained for this MF contribution are compatible with a hydrogen dissociative adsorption process, for which close values have been reported in the electrodes such as: LSTM4646 (30-50 mF cm^{-2}) measured in wet 20 %H_2/Ar between 750 and 850 °C, or LSCM (0.2 mF cm^{-2}), LBCM (0.3-0.6 mF cm^{-2}) and $Ce_{0.5}Sr_{0.5}Cr_{0.5}Mn_{0.5}O_3$ (CeSCM) (0.2-5 mF cm^{-2}) measured in wet H_2 between 800 and 900 °C [32][105][111]. In addition, from the literature, it is known that the process of hydrogen dissociative adsorption generally presents much lower activation energies (0-0.57 eV) than the charge transfer process [112][113]. This is consistent with the results observed in the L5S15M electrodes; for example, for the electrode sintered at 1200 °C, the activation energy for the contribution assigned to the charge transfer process was 1.58(6) eV, while for the MF process attributed to the hydrogen dissociative adsorption, it was 0.76(6) eV.

Figure 96. Arrhenius plots of medium frequency resistance R_{MF} for L5S15M electrode sintered at (a) 1150 °C and (b) 1200 °C and measured in wet H_2 (filled symbols) and wet 3 % H_2/Ar (empty symbols).

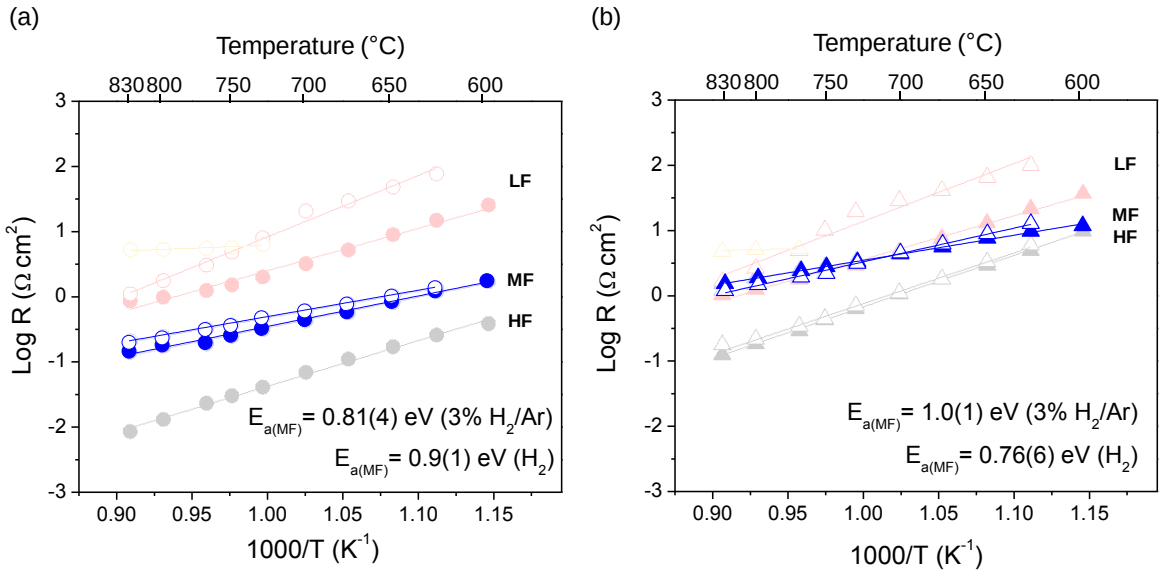

The MF resistance values obtained from the EIS data fits measured in wet diluted (pH$_2$ ≈ 0.03 atm) and pure hydrogen (pH$_2$ ≈ 0.97 atm) are plotted in Figure 96. For the electrode sintered at 1150 °C, the MF resistances slightly increase when decreasing pH$_2$, which would be in agreement with the reports for LSTM4646 anode, for which a contribution with similar characteristics was attributed to the dissociative adsorption of hydrogen on the electrode surface [32]. On the other hand, for the electrode sintered at 1200 °C, no clear trend is observed when changing the H_2 concentration, and we think this is because the medium frequency responses was difficult to isolate from the other responses. In this case, the HF and MF contributions were more strongly overlapped making it difficult to separate them precisely during equivalent circuit fitting.

In summary, the MF contribution is not drastically affected by the hydrogen concentration; however, it undergoes a remarkable increase (by one order of magnitude) with increasing electrode sintering temperature. This phenomenon can

be due to modifications of the electrode microstructure since a high sintering temperature decreases the porosity and increase the grain size, which adversely affect the hydrogen adsorption and dissociation occurring on the electrode surface. Another explanation would be related to the above-mentioned Sr depletion that can have modified the chemistry of the manganite surface, and in particular resulted in the formation of a superficial LSM perovskite layer (the latter being directly reduced into La_2O_3, SrO and MnO in anode conditions).

3.4.1.3 Electrode process corresponding to the low frequency arc in wet hydrogen

From Figure 97, we can observe that the low frequency resistance (LF) for L5S15M electrodes sintered at 1150 and 1200 °C substantially increases with decreasing H_2 concentration. In both cases, the difference is more noticeable at low measurement temperature. Regardless of hydrogen concentration, the process is thermally activated with activation energies of ~1.3 and ~1.8 eV in wet H_2 and 3% H_2/Ar, respectively. From literature, resistances at low frequency have been attributed to gas conversion, gas diffusion or surface diffusion processes. However, the gas conversion process is characterized by having resistances slightly thermally deactivated; for example, E_a= -0.09 eV for Ni/YSZ [106] or E_a= -0.2(1) eV for LSTM4646 electrodes [32][114]. On the other hand, the gas diffusion impedance presents a slight temperature dependency, with activation energies close to zero, as was demonstrated for nickel-ceria infiltrated Nb-doped $SrTiO_3$ anode and Ni-YSZ cermet [115][116][117]. Therefore, this would be in contradiction with the high activation energies obtained for the LF contribution in L5S15M electrode. Hence, gas conversion or gas diffusion processes do not seem to be the best explanation for the LF resistance, suggesting that the surface diffusion is the process that mainly contributes to the polarization resistance. Moreover, the gas diffusion process is

generally observed when the hydrogen concentration is low, which could explain the LF^{-} contribution observed when using diluted hydrogen [116][118].

Figure 97. Arrhenius plots of low frequency resistance (R_{LF}) for L5S15M electrode sintered at (a) 1150 °C and (b) 1200 °C and measured in wet H_2 (filled symbols) and wet 3 % H_2/Ar (empty symbols).

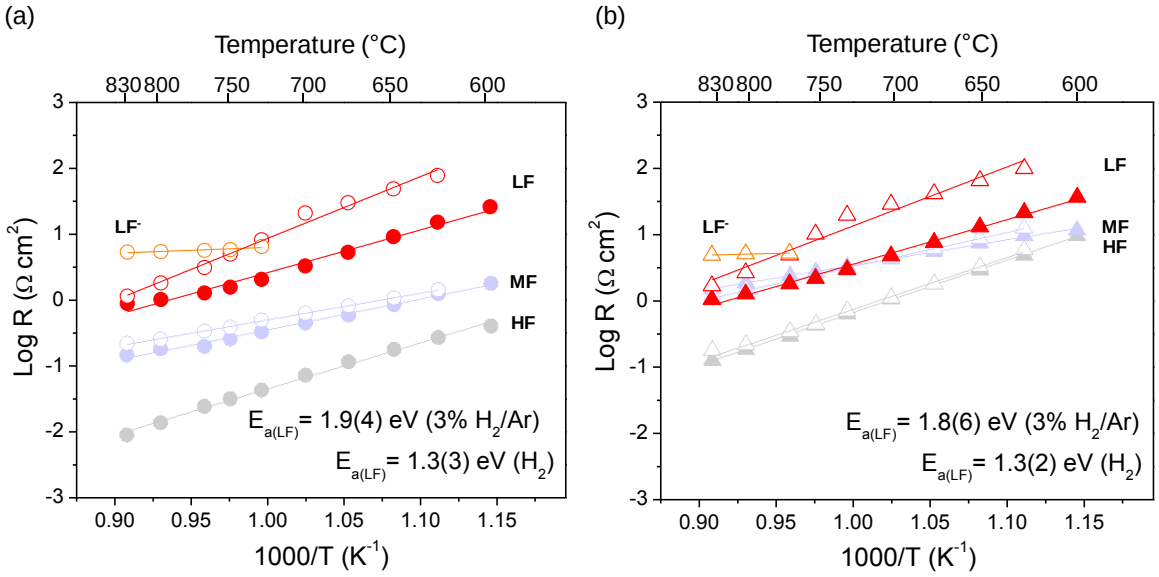

The assignment of the LF process would be also in agreement with what has been reported by Jiang and Badwal, who proposed that the low frequency contribution could be attributed to the surface diffusion. In the experiments carried out for Ni-YSZ cermets, they observed a decrease of low frequency resistance with the addition of 2% H_2O to H_2 in comparison with the results obtained in dry H_2. Besides, the resistance decreased with increasing H_2 concentration; for example, for 70% Ni-30% YSZ cermet the R_p changed from ~0.25 Ω cm^2 in 10% H_2 (2% H_2O) to ~0.12 Ω cm^2 in 100 %H_2 (2% H_2O) at 1000 °C [115]. In our case, the results are similar, because irrespective of the electrode sintering temperature (i) the addition of 3% H_2O has a drastic effect on the electrochemical performance, especially on the low frequency arc, which presents a high resistance when the electrode is measured in dry hydrogen (Figure 98) and (ii) the LF resistances increases with decreasing H_2

concentration; for example, for the electrode sintered at 1150 °C, the resistance increases from 1.02 Ω cm^2 in H_2/Ar (3% H_2O) to 1.82 Ω cm^2 in 3% H_2/Ar (3% H_2O), measured at 800 °C.

Figure 98. Impedance spectra measured in wet and dry 3 % H_2/Ar at 800 °C for L5S15M electrode sintered at (a) 1150 °C and (b) 1200 °C. The numbers indicate the frequency logarithms.

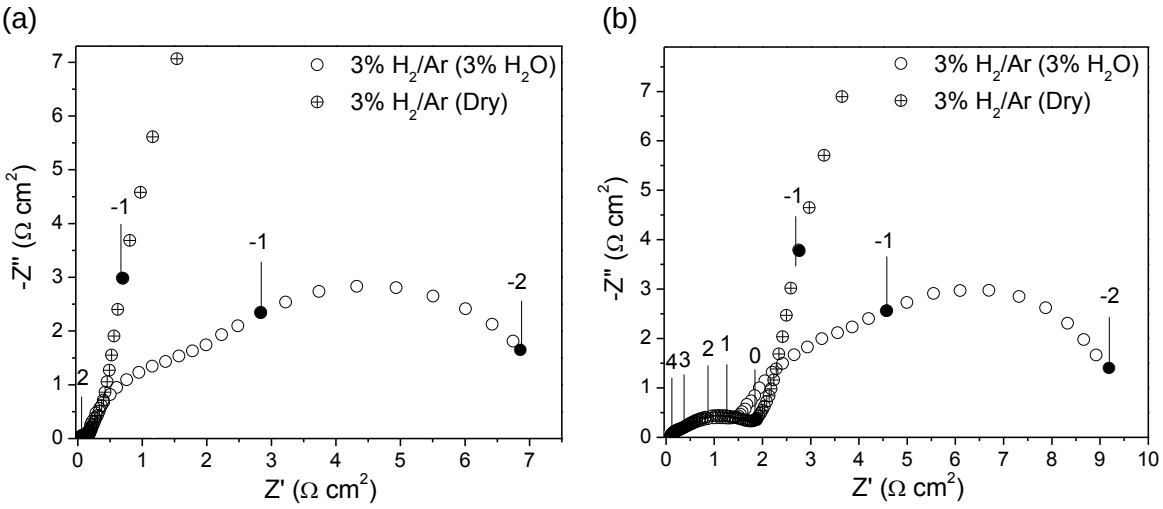

On the other hand, the equivalent capacitance is another parameter that can help to corroborate the process. The capacitances reported by Jiang and Badwal were in the range of 0.1-1 F cm^{-2}, the values increasing with increasing H_2 concentration, with values of 0.08 and 0.5 F cm^{-2} using 10% H_2 (2% H_2O) and 100% H_2 (2% H_2O), respectively [115]. In our case, the capacitance values (C_{LF}) also increase with increasing the H_2 concentration (see Figure 90 and Table S4); for example, for the electrode sintered at 1150 °C, the capacitance at 800 °C increases from 0.28 F cm^{-1} using 3 % H_2/Ar (3% H_2O) to 2.03 F cm^{-1} using 100% H_2 (3% H_2O). Based on all those results, we propose that the thermally activated LF resistance in L5S15M electrode is related to the surface diffusion of H_{ad}, considering that the hydrogen spillover mechanism describes the charge transfer reactions [30][119]. On the other hand, as observed in Figure 97, R_{LF} is not affected by the increase of the sintering

temperature, possibly because this process is more influenced by the availability of H_{ad} species than by the microstructural characteristics of the surface.

3.4.2 USE OF A L5S15M-GDC50 COMPOSITE

Based on the previously obtained results concerning the electrochemical behavior of L5S15M in air (Section 3.3), we selected the L5S15M-GDC50 electrodes sintered at 1150 and 1200 °C to study the influence of using a composite on the electrochemical properties of the material in reducing atmosphere.

3.4.2.1 L5S15M-GDC50 electrode sintered at 1150 °C

As seen in Figure 99a, for the composite L5S15M-GDC50, the ASR values are higher compared to L5S15M electrode, although the activation energies remain almost constant around 1 eV (considering the standard deviation). These activation energy values are in agreement with those reported by different anodes such as: $La_{0.75}Sr_{0.25}Cr_{0.5}Mn_{0.5}O_{3-\delta}$-YSZ (50-50 wt.%) (1.09 eV) [104], $(La_{0.75}Sr_{0.25})_{0.95}Cr_{0.5}Mn_{0.5}O_{3-\delta}$ modified with $CeO_{2-\delta}$ (0.9 eV) [120] and $Sr_2MgMoO_{6-\delta}$-GDC (50-50 wt.%) (0.8 eV) [121].

Figure 100 shows the spectra for L5S15M and L5S15M-GDC50 electrodes sintered at 1150 °C and tested at 800 °C in wet H_2. The spectra consist of three arcs at high frequency HF (10^3 Hz), medium frequency MF ($10^{1.5}$ Hz) and low frequency LF (10^{-1}). As for L5S15M electrode, the spectra for L5S15M-GDC50 composite were fitted using the equivalent circuit $LR_s(R_1CPE_1)(R_2CPE_2)(R_3CPE_3)$. Table 30 lists the electrical parameters for each element derived from spectra fitting.

Figure 99. Arrhenius plots of (a) ASR and (b) individual resistances (limiting steps) for L5S15M (filled symbols) and L5S15M-GDC50 (half-filled symbols) electrodes sintered at 1150 °C measured in wet H_2 (3% H_2O).

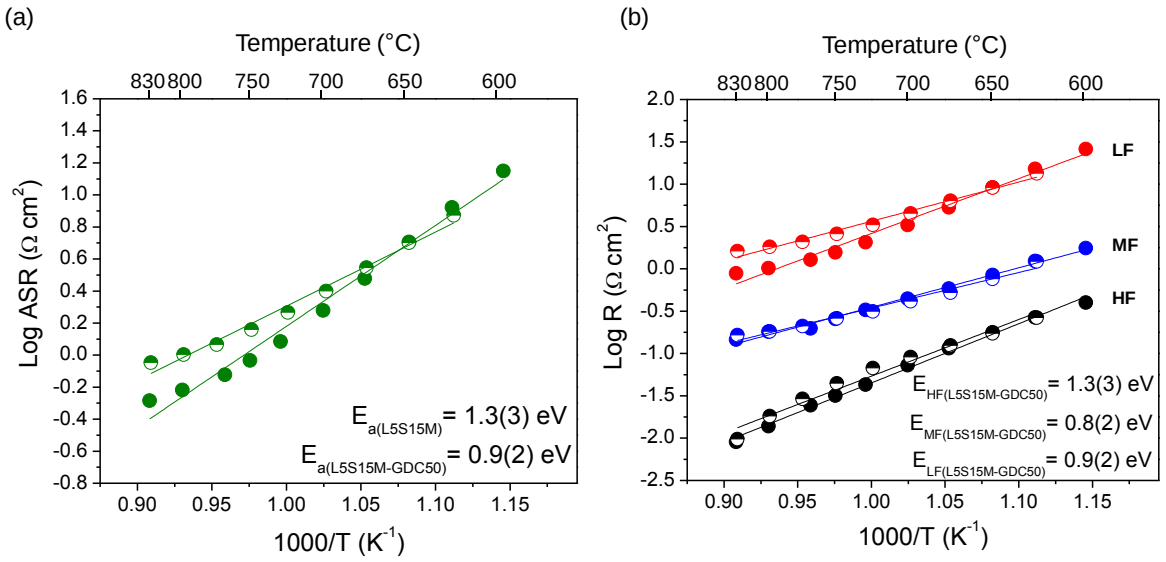

Figure 100. Impedance spectra measured in H_2 (3% H_2O) at 800 °C for L5S15M and L5S15M-GDC50 electrodes sintered at 1150 °C. The serial resistances have been removed. The numbers indicate the frequency logarithms.

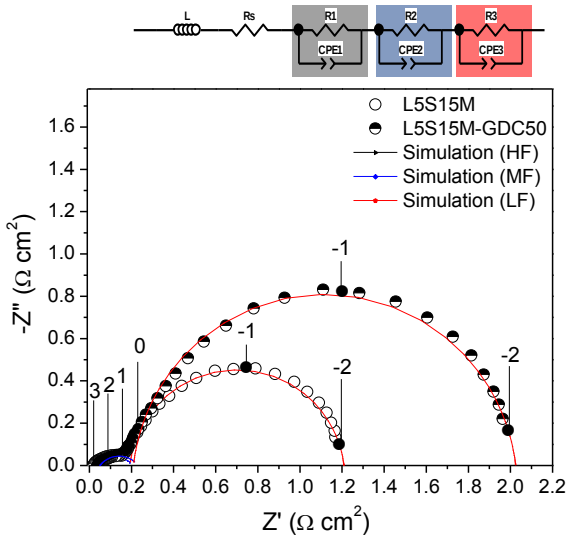

Table 30. Parameters of elementary contributions for L5S15M-GDC50 electrode sintered at 1150 °C and measured in wet H_2 (3% H_2O).

Temp. (°C)	R_s (Ωcm^2)	HF			MF			LF				
		R1 (Ωcm^2)	C1 (Fcm^{-2})	*f* (Hz)	R2 (Ωcm^2)	C2 (Fcm^{-2})	*f* (Hz)	R3 (Ωcm^2)	C3 (Fcm^{-2})	*f* (Hz)	R_p (Ωcm^2)	ASR (Ωcm^2)
827	6.94	0.01	1.03E-2	1597	0.17	4.02E-2	24	1.62	1.09	0.09	1.80	0.90
801	8.03	0.02	5.43E-3	1606	0.18	3.37E-2	26	1.82	1.12	0.08	2.02	1.01
776	9.83	0.03	2.95E-3	1857	0.21	3.04E-2	25	2.09	1.15	0.07	2.33	1.16
751	11.97	0.04	2.11E-3	1697	0.26	1.98E-2	31	2.58	1.22	0.05	2.88	1.44
751	14.88	0.07	1.57E-3	1515	0.31	1.56E-2	32	3.32	1.10	0.04	3.70	1.85
701	19.02	0.09	1.29E-3	1366	0.41	1.11E-2	35	4.52	1.00	0.04	5.02	2.51
676	24.68	0.12	9.85E-4	1300	0.52	8.68E-3	35	6.37	0.58	0.04	7.02	3.51
651	32.55	0.17	7.27E-4	1270	0.76	5.68E-3	37	9.14	0.44	0.04	10.07	5.04
626	44.18	0.26	4.53E-4	1328	1.22	2.99E-3	44	13.42	0.33	0.04	14.91	7.45

Figure 101. (a) Relaxation frequencies and (b) equivalent capacitances for L5S15M (filled symbols) and L5S15M-GDC50 (half-filled symbols) electrodes sintered at 1150 °C and measured in wet H_2 (3% H_2O).

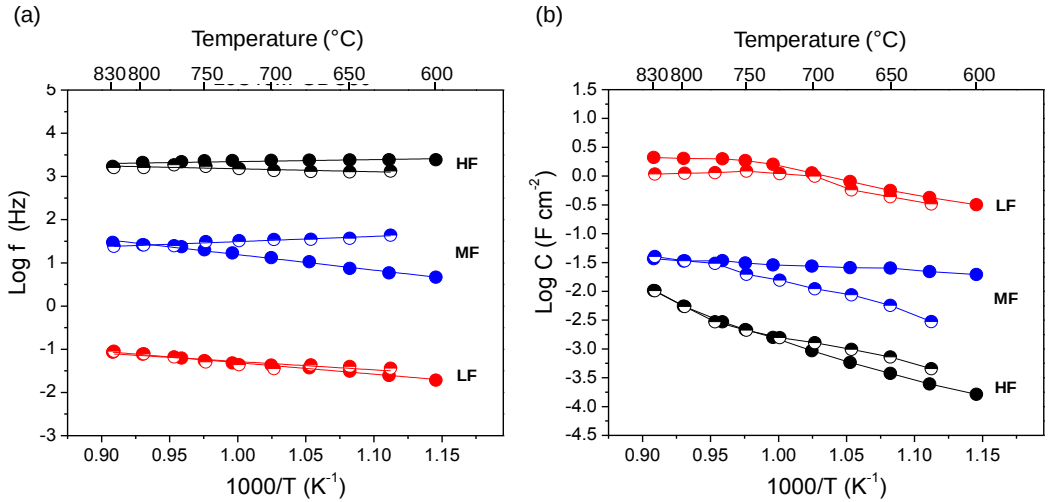

Based on the Schouler-type representation [59], one can infer that the origin of each specific impedance response is similar in both pure and composite electrodes (Figure 101). For both the pure and the composite electrodes, the arc at low frequency (LF) represents the highest contribution to the polarization resistance, and is affected by the GDC addition to the L5S15M electrode. As clearly shown in Figure 99, the R_{HF} and R_{MF} values do not change with the use of the composite, while the R_{LF} resistance slightly increases with the addition of GDC to L5S15M, especially at high temperature; for example, at 800 °C the R_{LF} values were 1.02 and 1.82 Ω cm^2 for L5S15M and L5S15M-GDC50, respectively. The similarity between the resistance values obtained for the two electrodes may be due to the fact that 1150°C is not a sufficient sintering temperature to achieve a good connection either between GDC particles or between GDC and L5S15M phase. Instead, the presence of GDC phase with “low connectivity” can affect the electrode microstructure by blocking the available surface for the transport of charged species along the manganite grains, generating an increase in the corresponding contribution. A similar phenomenon has been observed for the LSCM/YSZ anode sintered at 1100 °C; the poor contact between the LSCM and YSZ particles resulted in a situation where the relatively large LSCM grains being covered by fine YSZ particles (0.2 μm) impeding the diffusion reactions [113].

3.4.2.2 L5S15M-GDC50 electrode sintered at 1200 °C

In the case of L5S15M-GDC50 electrode sintered at 1200 °C, the ASR (Figure 102a) decreases when the L5S15M-GDC50 composite is used as electrode. This behavior is opposite to that observed for the electrodes sintered at 1150 °C, for which the use of a composite does not improve the electrochemical performance. However, for all electrodes, the activation energies of ASR in hydrogen is around 1 eV, suggesting that the nature of the main limiting process is the same in all electrodes investigated, independently of the electrode composition and sintering temperature.

Figure 102. Arrhenius plots of (a) ASR and (b) individual resistances (limiting steps) for L5S15M (filled symbols) and L5S15M-GDC50 (half-filled symbols) electrodes sintered at 1200 °C and measured in wet H_2 (3% H_2O).

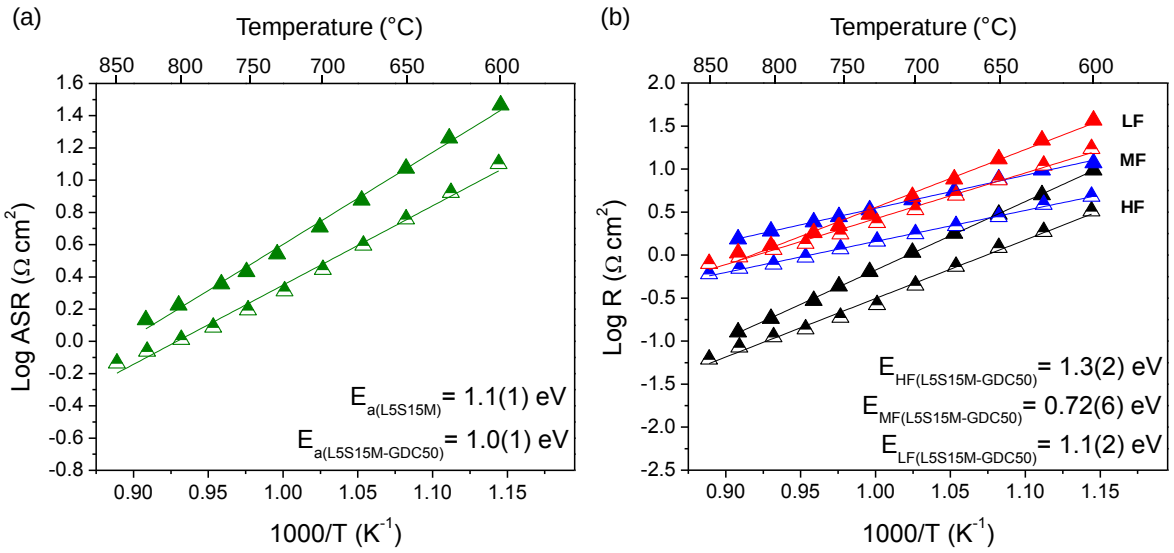

The impedance spectra obtained under wet H_2 atmosphere show three depressed arcs at high frequency HF ($10^{2.5}$-10^4 Hz), medium frequency MF (10^1-10^2 Hz) and low frequency LF ($10^{-1.5}$-$10^{-0.8}$). All the spectra were fitted using the equivalent circuit $LR_s(R_1CPE_1)(R_2CPE_2)(R_3CPE_3)$. However, at high temperature (700 - 800 °C), the distinction between HF and MF arcs is extremely difficult because the HF arc is small and is overlapping the MF arc (Figure 103). Table 31 lists the parameters of the circuit elements, which are obtained from spectra fitting.

The variation of the individual resistances (Figure 102b) and equivalent capacitances allows to understand the effect of the composite on each limiting step (Figure 104). As seen in Figure 104, the values of equivalent capacitances and relaxation frequencies for L5S15M-GDC50 composite are very close to those reported for L5S15M electrode, confirming that the same limiting processes are present in both electrodes, regardless of the electrode composition.

Figure 103. Impedance spectra measured in wet H_2 (3% H_2O) at 800 °C for L5S15M and L5S15M-GDC50 electrodes sintered at 1200 °C. The serial resistances have been removed. The numbers indicate the frequency logarithms.

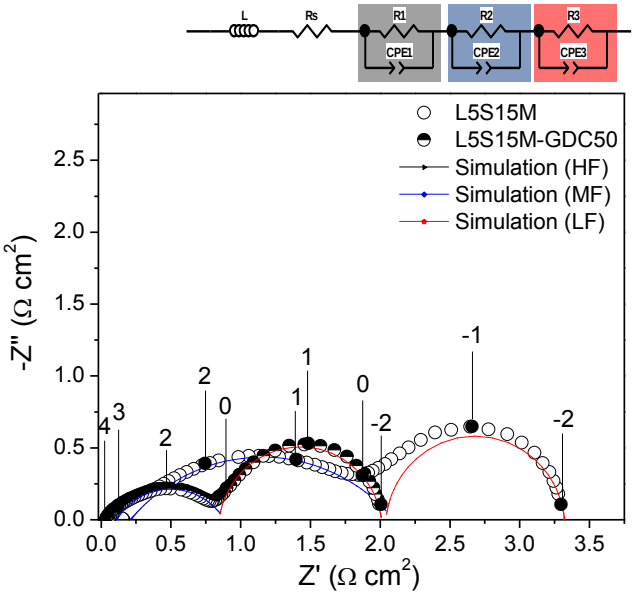

From Figure 102b, the high frequency response R_{HF} is found lower for the composite than for L5S15M electrode, both sintered at 1200 °C. In this case, the decrease in R_{HF} resistance is noticeable; for example, at 800 °C are 0.18 Ω cm^2 for L5S15M and 0.11 Ω cm^2 for L5S15M-GDC50. The activation energies (Ea_{HF}) are similar for L5S15M (1.58(6) eV) and L5S15M-GDC50 (1.3(2) eV) electrodes sintered at 1200 °C, which are in the range of the values reported for the same contribution in other anodes such as LSTM4646 (0.9-1.5 eV [34]) or Ni-YSZ (1.68 eV) [115]. According to the results, the increase in sintering temperature up to 1200 °C seems to favor the establishment of a correct GDC network, which improves the contribution attributed to the transfer of charged species across the electrode/electrolyte interface, if we assume that such mechanism occurs at the LS5S15M/GDC interface, what seems finally more reasonable than the GDC/YSZ interface for which no real effect of the composite would have been observed for R_{HF} component. The addition of a good ionic conductor such as GDC allows an improvement of the ionic

conduction properties of the material, facilitating the diffusion of oxygen ions from the electrolyte to the LS5S15M/GDC interface, and therefore the rate of the hydrogen spillover reactions (H1 and H2). Additionally, it is worth noting that GDC oxide presents an appreciable electronic conductivity under reducing conditions [43], what may favorably influence the charge transfer reactions.

The MF and LF processes are also improved with the addition of 50 wt% GDC; although the resistance decrease is more remarkable for the process assigned to the hydrogen dissociative adsorption (MF), the process attributed to the surface diffusion is also slightly affected. It is reasonable to think that GDC prevents excessive growth of L5S15M grains, by providing a porous composite anode with well-interconnected particles that increases the area for the reactions occurring on the surface.

Figure 104. a) Relaxation frequencies and (b) equivalent capacitances for L5S15M (filled symbols) and L5S15M-GDC50 (half-filled symbols) electrodes sintered at 1200 °C and measured in wet H_2 (3% H_2O).

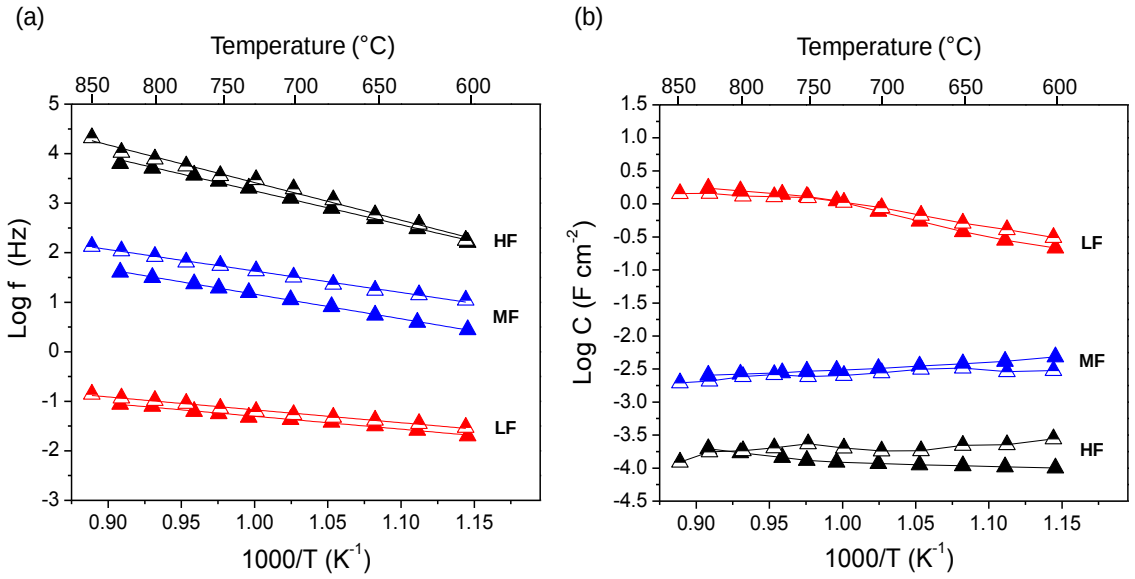

Table 31. Parameters of elementary contributions for L5S15M-GDC50 electrode sintered at 1200 °C and measured in wet H_2 (3% H_2O).

Temp. (°C)		HF			MF			LF				
	R_s (Ωcm^2)	**R1 (Ωcm^2)**	**C1 (Fcm^{-2})**	***f* (Hz)**	**R2 (Ωcm^2)**	**C2 (Fcm^{-2})**	***f* (Hz)**	**R3 (Ωcm^2)**	**C3 (Fcm^{-2})**	***f* (Hz)**	**R_p (Ωcm^2)**	**ASR (Ωcm^2)**
852	4.10	0.06	1.23E-4	21049	0.60	1.95E-3	135	0.80	1.43	0.14	1.46	0.73
827	4.77	0.09	1.77E-4	10603	0.70	2.08E-3	109	0.95	1.44	0.12	1.73	0.87
800	5.65	0.11	1.83E-4	7796	0.78	2.43E-3	84	1.16	1.32	0.10	2.05	1.03
776	6.77	0.14	2.04E-4	5659	0.95	2.60E-3	65	1.37	1.29	0.09	2.45	1.22
751	8.23	0.19	2.34E-4	3605	1.18	2.43E-3	55	1.76	1.25	0.07	3.13	1.56
726	10.20	0.27	2.01E-4	2987	1.45	2.53E-3	43	2.39	1.06	0.06	4.11	2.05
701	12.91	0.45	1.82E-4	1958	1.77	2.78E-3	32	3.36	0.88	0.05	5.58	2.79
676	16.50	0.74	1.84E-4	1173	2.20	3.14E-3	23	4.96	0.67	0.05	7.89	3.95
651	21.63	1.23	2.22E-4	586	2.79	3.28E-3	17	7.45	0.51	0.04	11.47	5.73
626	28.94	1.87	2.26E-4	376	3.87	2.89E-3	14	11.03	0.41	0.04	16.77	8.38
601	39.62	3.25	2.77E-4	177	4.82	3.00E-3	11	17.27	0.31	0.03	25.34	12.67

The summary of the area specific resistances and activation energies for all the electrodes investigated in reducing conditions are displayed in Table 32.

Table 32. Summary of the area specific resistance (ASR) and activation energies for the different electrodes tested in wet H_2 (3% H_2O).

Sintering temperature (°C)	**1150**		**1200**	
Electrode Composition	L5S15M	L5S15M-GDC50	L5S15M	L5S15M-GDC50
ASR (Ω cm^2) 800 °C	0.61	1.01	1.36	1.03
E_a (eV)	1.3(3)	0.9(2)	1.1(1)	1.0(1)

The lowest area specific resistance (ASR) values have been obtained for the pure L5S15M electrode sintered at 1150 °C. The ASR value at 800 °C in wet H_2 for L5S15M (ASR= 0.61 Ω cm^2) is lower than that obtained for $La_{0.6}Sr_{1.4}MnO_4$ at 800 °C (ASR=1 Ω cm^2, using LSGM electrolyte [38]) and close to the values reported for LSCM anode at 925 °C (0.47 Ω cm^2 using YSZ electrolyte [22]). The sintering temperature has a different effect on the electrochemical performance of L5S15M and L5S15M-GDC electrode. For both composite electrodes, the ASR values are very close, while for the pure electrodes, the ASR increases by 2-3 times when the sintering temperature is increased.

3.5 CONCLUSIONS

The Ruddlesden-Popper manganite $La_{0.5}Sr_{1.5}MnO_{4\pm\delta}$ (L5S15M) has been studied as possible electrode material for symmetrical solid oxide fuel cells (SOFC). The electrochemical impedance spectroscopy (EIS) technique was used to study the electrode behavior of Au/L5S15M(GDC)/GDC//YSZ//GDC/L5S15M(GDC)/Au symmetrical cell. The influence of electrode composition (pure L5S15M or L5S15M:GDC composites) as well as sintering temperature were studied in oxidizing

(cathode) and reducing atmosphere (anode). In air, the electron transfer between the electrode and oxygen, and incorporation of oxygen ions into the electrode process is the dominant contribution to the overall polarization when the electrodes are sintered at 1150 and 1200 °C. However, sintering the electrode at 1200 °C generated microstructural modifications affecting the oxygen dissociative adsorption/desorption or surface diffusion processes occurring on the electrode surface. In addition, the results obtained by scanning electron microscopy (SEM) and energy dispersive X-ray spectroscopy (EDXS) showed that the increasing temperature promotes the chemical reactivity between the electrode and electrolyte, which was reflected in an increase of polarization resistance. Increasing the sintering temperature up to 1250 °C increases the Sr diffusion through GDC interlayer, which leads to Sr accumulation at the GDC/YSZ interface with $SrZrO_3$ formation and subsequent cell performance degradation. The increase of sintering temperature not only affected the electrode microstructure but also increased the Sr diffusion to the GDC/YSZ interface, which possibly generated a depletion of strontium from manganite. The combined effect of these phenomena generated strong limitations mainly to the oxygen dissociative adsorption and/or adsorbed oxygen surface diffusion and grain boundary.

The addition of oxygen-ion conducting GDC into L5S15M enhances the electron transfer with incorporation of oxygen ions into the electrode process, whereas it is unfavorable to the charge transfer of oxygen ions at the electrode/electrolyte interface and dissociative adsorption of molecular oxygen processes. Since the improvement of one process is counterbalanced by the worsening of another, the addition of GDC phase does not greatly improve the electrode polarization resistance, regardless of the electrode sintering temperature.

The impedance behavior for the hydrogen oxidation reaction on L5S15M and L5S15M-GDC50 electrodes is characterized by three rate limiting processes, which behave very differently with respect to the H_2 or H_2O concentration, as well as with

the sintering temperature or electrode composition (composite). The good stability and limited volume changes of L5S15M under reducing atmospheres allows to maintain the mechanical integrity of the cell layers after heating and cooling in air and hydrogen, yielding promising ASR values, specifically, for the electrode sintered at 1150 °C. For all L5S15M electrodes, the increase in the sintering temperature from 1150 to 1200 °C, that implied Sr depletion, formation of $SrZrO_3$ and possible formation/reduction of a LSM perovskite, has a negative impact on the contributions attributed to the charge transfer at the electrode/electrolyte interface and the dissociative adsorption of hydrogen processes. In all cases, the low frequency response assigned to the surface diffusion represents the highest contribution to the total polarization resistance. The addition of oxygen-ionic conducting GDC into L5S15M has different effects on rate-limiting steps depending on the sintering temperature, the contribution attributed to the charge transfer at the electrode/electrolyte interface and the dissociative adsorption processes are only improved when the electrode composite is sintered at 1200 °C, while the surface diffusion process does not improve significantly in any of the cases.

In summary, the $La_{0.5}Sr_{1.5}MnO_{4\pm\delta}$ (L5S15M) manganite presents an acceptable electrochemical behavior in both oxidizing and reducing atmosphere. Combining the results obtained for electrode optimization in both atmospheres, the best electrochemical performance is reached for the pure L5S15M electrode sintered at 1150 °C. In this case, the ASR values obtained at 800 °C are 1.32 and 0.61 Ω cm^2 in air and wet H_2, respectively. Taking into account that the main rate-limiting steps are due to processes occurring on the surface, these results can presumably be improved using advanced electrode preparation methods as the formation of an ionic conducting scaffold impregnated by a precursor solution of the electron conducting oxide or the addition of a catalytically active phase (*e.g.* Ni for anodes) [36][122][123][124].

3.6 REFERENCES

[1] F. Ramadhani, M. A. Hussain, H. Mokhlis, and S. Hajimolana, "Optimization strategies for Solid Oxide Fuel Cell (SOFC) application: a literature survey," *Renew. Sustain. Energy Rev.*, vol. 76, pp. 460–484, 2017.

[2] R. J. Kee, H. Zhu, and D. G. Goodwin, "Solid-oxide fuel cells with hydrocarbon fuels," *Proc. Combust. Inst.*, vol. 30, no. 2, pp. 2379–2404, Jan. 2005.

[3] N. Q. Minh, "Solid oxide fuel cell technology - Features and applications," *Solid State Ionics*, vol. 174, no. 1–4, pp. 271–277, 2004.

[4] J. Nielsen and J. Hjelm, "Impedance of SOFC electrodes: A review and a comprehensive case study on the impedance of LSM:YSZ cathodes," *Electrochim. Acta*, vol. 115, pp. 31–45, 2014.

[5] Q.-A. Huang, R. Hui, B. Wang, and J. Zhang, "A review of AC impedance modeling and validation in SOFC diagnosis," *Electrochim. Acta*, vol. 52, no. 28, pp. 8144–8164, 2007.

[6] Q. A. Huang, R. Hui, B. Wang, and J. Zhang, "A review of AC impedance modeling and validation in SOFC diagnosis," *Electrochim. Acta*, vol. 52, no. 28, pp. 8144–8164, 2007.

[7] J. Hanna, W. Y. Lee, Y. Shi, and A. F. Ghoniem, "Fundamentals of electro- and thermochemistry in the anode of solid-oxide fuel cells with hydrocarbon and syngas fuels," *Prog. Energy Combust. Sci.*, vol. 40, no. 1, pp. 74–111, 2014.

[8] M. P. Carpanese, D. Clematis, A. Bertei, A. Giuliano, A. Sanson, E. Mercadelli, C. Nicolella, and A. Barbucci, "Understanding the electrochemical behaviour of LSM-based SOFC cathodes. Part I — Experimental and electrochemical," *Solid State Ionics*, vol. 301, pp. 106–115, 2017.

[9] V. Dusastre and J. a Kilner, "Optimisation of composite cathodes for intermediate temperature soild oxide fuel cell applications," *Solid State Ionics*, vol. 126, no. 1–2, pp. 163–174, 1999.

[10] R. Sayers, M. Rieu, P. Lenormand, F. Ansart, J. A. Kilner, and S. J. Skinner, "Development of lanthanum nickelate as a cathode for use in intermediate temperature solid oxide fuel cells," *Solid State Ionics*, vol. 192, no. 1, pp. 531–534, 2011.

[11] E. C. Thomsen, G. W. Coffey, L. R. Pederson, and O. A. Marina, "Performance of lanthanum strontium manganite electrodes at high pressure," *J. Power Sources*, vol. 191, no. 2, pp. 217–224, 2009.

[12] A. C. Co and V. I. Birss, "Mechanistic analysis of the oxygen reduction reaction at (La,Sr)MnO_3 cathodes in solid oxide fuel cells," *J. Phys. Chem. B*, vol. 110, no. 23, pp. 11299–11309, 2006.

[13] G. E. Youngblood, A. S. Rupaak, L. R. Pederson, and J. L. Bates, "Solid Oxide Fuel Cells, S. C. Singhal and H. Iwahara, Editors, PV 93-4, p. 585," *Electrochem. Soc. Proc. Ser. Pennington, NJ*, 1993.

[14] M. J. L. Ostergard and M. B. Mogensen, "ac Impedance study of the oxygen reduction mechanism on LSM in SOFC," *Electrochim. Acta*, vol. 38, no. 14,

pp. 2015–2020, 1993.

[15] E. P. Murray, T. Tsai, and S. A. Barnett, “Oxygen transfer processes in (La,Sr)MnO_3/Y_2O_3-stabilized ZrO_2 cathodes: an impedance spectroscopy study,” *Solid State Ionics*, vol. 110, no. 3–4, pp. 235–243, 1998.

[16] S. B. Adler, J. A. Lane, and B. C. H. Steele, “Electrode kinetics of porous mixed-conducting oxygen electrodes,” *J. Electrochem. Soc*, vol. 143, no. 11, p. 3554, 1996.

[17] M. J. Jørgensen and M. Mogensen, “Impedance of solid oxide fuel cell LSM/YSZ composite cathodes,” *J. Electrochem. Soc.*, vol. 148, no. 5, p. A433, 2001.

[18] C. Sun, R. Hui, and J. Roller, “Cathode materials for solid oxide fuel cells: a review,” *J. Solid State Electrochem.*, vol. 14, no. 7, pp. 1125–1144, Oct. 2010.

[19] A. Mai, M. Becker, W. Assenmacher, F. Tietz, D. Hathiramani, E. Ivers-Tiffée, D. Stöver, and W. Mader, “Time-dependent performance of mixed-conducting SOFC cathodes,” *Solid State Ionics*, vol. 177, no. 19–25 SPEC. ISS., pp. 1965–1968, 2006.

[20] S. P. Jiang, “A comparison of O_2 reduction reactions on porous (La,Sr)MnO_3 and (La,Sr)(Co,Fe)O_3 electrodes,” *Solid State Ionics*, vol. 146, pp. 1–22, 2002.

[21] S. Liping, H. Lihua, Z. Hui, L. Qiang, and C. Pijolat, “La substituted Sr_2MnO_4 as a possible cathode material in SOFC,” *J. Power Sources*, vol. 179, pp. 96–100, 2008.

[22] S. LiPing, L. Qiang, H. Li-Hua, Z. Hui, Z. Guo-Ying, L. Nan, J.-P. Viricelle, and C. Pijolat, “Synthesis and performance of $Sr_{1.5}La_xMnO_4$ as cathode materials for intermediate temperature solid oxide fuel cell,” *J. Power Sources*, vol. 196, no. 14, pp. 5835–5839, 2011.

[23] C. Munnings, S. Skinner, G. Amow, P. Whitfield, and I. Davidson, “Structure, stability and electrical properties of the $La_{(2-x)}Sr_xMnO_{4\pm\delta}$ solid solution series,” *Solid State Ionics*, vol. 177, no. 19–25, pp. 1849–1853, 2006.

[24] K. Mizusaki, J. Tawaga, H. Saito, T. Kamitami, K. Yamamura, T. Hirano, K. Ehara, S. Takagi, T. Hikita, T. Ippommatsu, M. Nakagava, S. Hashimoto, “Preparation of nickel pattern electrodes on YSZ and electrochemical propertis in H_2-H_2O atmospheres,” *Electrochem. Soc.*, vol. 141, no. 8, pp. 533–541, 1994.

[25] J. Mizusaki, H. Tagawa, T. Saito, T. Yamamura, K. Kamitani, K. Hirano, S. Ehara, T. Takagi, T. Hikita, M. Ippommatsu, S. Nakagawa, and K. Hashimoto, “Kinetic studies of the reaction at the nickel pattern electrode on YSZ in H_2-H_2O atmospheres,” *Solid State Ionics*, vol. 70–71, no. PART 1, pp. 52–58, 1994.

[26] W. G. Bessler, S. Gewies, and M. Vogler, “A new framework for physically based modeling of solid oxide fuel cells,” *Electrochim. Acta*, vol. 53, no. 4, pp. 1782–1800, 2007.

[27] A. Bieberle, L. P. Meier, and L. J. Gauckler, “The electrochemistry of Ni pattern anodes used as solid oxide fuel cell model electrodes,” *J. Electrochem. Soc.*, vol. 148, no. 6, pp. A646–A656, 2001.

[28] W. G. Bessler, J. Warnatz, and D. G. Goodwin, “The influence of equilibrium

potential on the hydrogen oxidation kinetics of SOFC anodes," *Solid State Ionics*, vol. 177, no. 39–40, pp. 3371–3383, 2007.

[29] W. G. Bessler, M. Vogler, H. Störmer, D. Gerthsen, A. Utz, A. Weber, and E. Ivers-Tiffée, "Model anodes and anode models for understanding the mechanism of hydrogen oxidation in solid oxide fuel cells," *Phys. Chem. Chem. Phys.*, vol. 12, no. 42, p. 13888, 2010.

[30] M. Vogler, A. Bieberle-Hütter, L. Gauckler, J. Warnatz, and W. G. Bessler, "Modelling study of surface reactions, diffusion, and spillover at a Ni/YSZ patterned anode," *J. Electrochem. Soc.*, vol. 156, no. 5, p. B663, 2009.

[31] T. Zhu, D. E. Fowler, K. R. Poeppelmeier, M. Han, and S. A. Barnett, "Hydrogen oxidation mechanisms on perovskite solid oxide fuel cell anodes," *J. Electrochem. Soc.*, vol. 163, no. 8, pp. F952–F961, 2016.

[32] Q. X. Fu, F. Tietz, and D. Stöver, "$La_{0.4}Sr_{0.6}Ti_{1-x}MnxO_{3-\delta}$ perovskites as anode materials for solid oxide fuel cells," *J. Electrochem. Soc.*, vol. 153, no. 4, pp. D74–D83, 2006.

[33] J. C. Ruiz-Morales, J. Canales-Vázquez, J. Peña-Martínez, D. M. López, and P. Núñez, "On the simultaneous use of $La_{0.75}Sr_{0.25}Cr_{0.5}Mn_{0.5}O_{3-\delta}$ as both anode and cathode material with improved microstructure in solid oxide fuel cells," *Electrochim. Acta*, vol. 52, no. 1, pp. 278–284, 2006.

[34] J. C. Ruiz-Morales, J. Canales-Vázquez, B. Ballesteros-Pérez, J. Peña-Martínez, D. Marrero-López, J. T. S. Irvine, and P. Núñez, "LSCM-(YSZ-CGO) composites as improved symmetrical electrodes for solid oxide fuel cells," *J. Eur. Ceram. Soc.*, vol. 27, no. 13–15, pp. 4223–4227, Jan. 2007.

[35] C. Jin, Z. Yang, H. Zheng, C. Yang, and F. Chen, "$La_{0.6}Sr_{1.4}MnO_4$ layered perovskite anode material for intermediate temperature solid oxide fuel cells," *Electrochem. commun.*, vol. 14, no. 1, pp. 75–77, 2012.

[36] J. Shen, G. Yang, Z. Zhang, W. Zhou, W. Wang, and Z. Shao, "Tuning layer-structured $La_{0.6}Sr_{1.4}MnO_{4+\delta}$ into a promising electrode for intermediate-temperature symmetrical solid oxide fuel cells through surface modification," *J. Mater. Chem. A*, vol. 4, pp. 10641–10649, 2016.

[37] D. Marinha, L. Dessemond, and E. Djurado, "Comprehensive review of current developments in IT-SOFCs," *Curr. Inorg. Chem.*, vol. 3, no. 1, pp. 2–22, 2013.

[38] E. V. Tsipis and V. V. Kharton, "Electrode materials and reaction mechanisms in solid oxide fuel cells: a brief review," *J. Solid State Electrochem.*, vol. 12, no. 11, pp. 1367–1391, 2008.

[39] S. P. Jiang, "Development of lanthanum strontium manganite perovskite cathode materials of solid oxide fuel cells: a review", *J. Mater. Sci.,* vol. 43, no. 21. 2008.

[40] M. J. Jørgensen, S. Primdahl, C. Bagger, and M. Mogensen, "Effect of sintering temperature on microstructure and performance of LSM-YSZ composite cathodes," *Solid State Ionics*, vol. 139, no. 1–2, pp. 1–11, 2001.

[41] P. Hjalmarsson and M. Mogensen, "$La_{0.99}Co_{0.4}Ni_{0.6}O_{3-\delta}$–$Ce_{0.8}Gd_{0.2}O_{1.95}$ as composite cathode for solid oxide fuel cells," *J. Power Sources*, vol. 196, no. 17, pp. 7237–7244, 2011.

[42] Hyun Jun Ko, J.-J. Lee, and S.-H. Hyun, "Structural stability of the GDC

electrolyte for low temperature SOFCs depending on fuels," *ECS Trans.*, vol. 25, no. 2, pp. 1611–1616, 2009.

[43] B. C. H. Steele, "Appraisal of $Ce_{1-y}Gd_yO_{2-y}$ electrolytes for IT-SOFC operation at 500 °C," *Solid State Ionics*, vol. 129, pp. 95–110, 2000.

[44] M. Li, Y. T. Li, D. W. Li, and Y. T. Long, "Recent developments and applications of screen-printed electrodes in environmental assays-A review," *Anal. Chim. Acta*, vol. 734, pp. 31–44, 2012.

[45] M. Mogensen, N. M. Sammes, and G. A. Tompsett, "Physical, chemical and electrochemical properties of pure and doped ceria," *Solid State Ionics*, vol. 129, pp. 63–94, 2000.

[46] V. Kharton, F. Marques, and a Atkinson, "Transport properties of solid oxide electrolyte ceramics: a brief review," *Solid State Ionics*, vol. 174, no. 1–4, pp. 135–149, 2004.

[47] A. Atkinson, "Chemically-induced stresses in gadolinium-doped ceria solid oxide fuel cell electrolytes," *Solid State Ionics*, vol. 95, pp. 249–258, 1997.

[48] C. Ding, H. Lin, K. Sato, Y. Tsutai, H. Ohtaki, M. Iguchi, C. Wada, and T. Hashida, "Preparation of Doped Ceria Electrolyte Films for SOFCs by Spray Coating Method," *J. Dispers. Sci. Technol.*, vol. 30, no. 2, pp. 241–245, 2009.

[49] Z. Duan, M. Yang, A. Yan, Z. Hou, Y. Dong, Y. Chong, M. Cheng, and W. Yang, "$Ba_{0.5}Sr_{0.5}Co_{0.8}Fe_{0.2}O_{3-\delta}$ as a cathode for IT-SOFCs with a GDC interlayer," *J. Power Sources*, vol. 160, no. 1, pp. 57–64, 2006.

[50] D. Tian, B. Lin, Y. Yang, Y. Chen, X. Lu, Z. Wang, W. Liu, and E. Traversa, "Enhanced performance of symmetrical solid oxide fuel cells using a doped ceria buffer layer," *Electrochim. Acta*, vol. 208, pp. 318–324, 2016.

[51] D. Wang, J. Wang, C. He, Y. Tao, C. Xu, and W. G. Wang, "Preparation of a $Gd_{0.1}Ce_{0.9}O_{2-\delta}$ interlayer for intermediate-temperature solid oxide fuel cells by spray coating," *J. Alloys Compd.*, vol. 505, no. 1, pp. 118–124, 2010.

[52] A. Rolle, V. Thoréton, P. Rozier, E. Capoen, O. Mentré, B. Boukamp, and S. Daviero-Minaud, "Evidence of the current collector effect: Study of the SOFC cathode material $Ca_3Co_4O_{9+\delta}$," *Fuel Cells*, 2012.

[53] D. Johnson, "ZView: a Software Program for IES Analysis, Version 3.4c." Scribner Associates, Inc., Southern Pines, NC, p. 8886, 2004.

[54] N. Hildenbrand, P. Nammensma, D. H. a Blank, H. J. M. Bouwmeester, and B. a. Boukamp, "Influence of configuration and microstructure on performance of $La_2NiO_{4+\delta}$ intermediate-temperature solid oxide fuel cells cathodes," *J. Power Sources*, vol. 238, pp. 442–453, 2013.

[55] E. Chinarro, J. R. Jurado, F. M. Figueiredo, and J. R. Frade, "Bulk and grain boundary conductivity of $Ca_{0.97}Ti_{1-x}Fe_xO_{3-\delta}$ materials," *Solid State Ionics*, vol. 160, pp. 161–168, 2003.

[56] E. Perry Murray, M. J. Sever, and S. A. Barnett, "Electrochemical performance of (La,Sr)(Co,Fe)O_3-(Ce,Gd)O_3 composite cathodes," *Solid State Ionics*, vol. 148, no. 1–2, pp. 27–34, 2002.

[57] A. Esquirol, N. P. Brandon, J. A. Kilner, and M. Mogensen, "Electrochemical characterization of $La_{0.6}Sr_{0.4}Co_{0.2}Fe_{0.8}O_3$ cathodes for intermediate-temperature SOFCs," *J. Electrochem. Soc.*, vol. 151, no. 11, pp. A1847–

A1855, 2004.

[58] K. Zhao, Y.-P. Wang, M. Chen, Q. Xu, B.-H. Kim, and D.-P. Huang, "Electrochemical evaluation of $La_2NiO_{4+\delta}$ as a cathode material for intermediate temperature solid oxide fuel cells," *Int. J. Hydrogen Energy*, vol. 39, no. 13, pp. 7120–7130, 2014.

[59] E. Schouler, "Study of oxide solid electrolyte based cells by the complex impedance technique-application to the accurate measurement of conductivity and to the study of the oxygen electrode reaction," Institut National Polytechnique de Grenoble (INPG)-France, 1979.

[60] M. Liu, M. Liu, D. Ding, K. Blinn, X. Li, and L. Nie, "Enhanced performance of LSCF cathode through surface modification," *Int. J. Hydrogen Energy*, vol. 37, no. 10, pp. 8613–8620, 2012.

[61] K. Zhao, Q. Xu, D. P. Huang, M. Chen, and B. H. Kim, "Electrochemical evaluation of $La_2NiO_{4+\delta}$-based composite electrodes screen-printed on $Ce_{0.8}Sm_{0.2}O_{1.9}$ electrolyte," *J. Solid State Electrochem.*, vol. 16, no. 8, pp. 2797–2804, 2012.

[62] S. Sunde, "Calculations of impedance of composite anodes for solid oxide fuel cells," *Electrochim. Acta*, vol. 42, no. 17, pp. 2637–2648, 1997.

[63] M. J. Escudero, A. Aguadero, J. A. Alonso, and L. Daza, "A kinetic study of oxygen reduction reaction on La_2NiO_4 cathodes by means of impedance spectroscopy," *J. Electroanal. Chem.*, vol. 611, no. 1–2, pp. 107–116, 2007.

[64] Y. P. Wang, Q. Xu, D.-P. Huang, K. Zhao, M. Chen, and B.-H. Kim, "Evaluation of $La_{1.8}Sr_{0.2}NiO_{4+\delta}$ as cathode for intermediate temperature solid oxide fuel cells," *Int. J. Hydrogen Energy*, vol. 41, no. 15, pp. 6476–6485, 2016.

[65] R. Kiebach, W. Zhang, M. Chen, K. Norrman, H. J. Wang, J. R. Bowen, R. Barfod, P. V. Hendriksen, and W. Zhang, "Stability of $La_{0.6}Sr_{0.4}Co_{0.2}Fe_{0.8}O_3/Ce_{0.9}Gd_{0.1}O_2$ cathodes during sintering and solid oxide fuel cell operation," *J. Power Sources*, vol. 283, pp. 151–161, 2015.

[66] F. Wang, M. Nishi, M. E. Brito, H. Kishimoto, K. Yamaji, H. Yokokawa, and T. Horita, "Sr and Zr diffusion in LSCF/10GDC/8YSZ triplets for solid oxide fuel cells (SOFCs)," *J. Power Sources*, vol. 258, pp. 281–289, 2014.

[67] M. Z. Khan, R. H. Song, S. B. Lee, J. W. Lee, T. H. Lim, and S. J. Park, "Effect of GDC interlayer on the degradation of solid oxide fuel cell cathode during accelerated current load cycling," *Int. J. Hydrogen Energy*, vol. 39, no. 35, pp. 20799–20805, 2014.

[68] D. Szymczewska, J. Karczewski, A. Chrzan, and P. Jasinski, "CGO as a barrier layer between LSCF electrodes and YSZ electrolyte fabricated by spray pyrolysis for solid oxide fuel cells," *Solid State Ionics*, vol. Article in, 2016.

[69] J. C. De Vero, K. Develos-Bagarinao, H. Kishimoto, T. Ishiyama, K. Yamaji, T. Horita, and H. Yokokawa, "Influence of $La_{0.6}Sr_{0.4}Co_{0.2}Fe_{0.8}O_{3-\delta}$ microstructure on GDC Interlayer stability and cation diffusion across the LSCF/GDC/YSZ Interfaces," *J. Electrochem. Soc.*, vol. 163, pp. F1463–F1470, 2016.

[70] F. Wang, M. E. Brito, K. Yamaji, D. H. Cho, M. Nishi, H. Kishimoto, T. Horita, and H. Yokokawa, "Effect of polarization on Sr and Zr diffusion behavior in LSCF/GDC/YSZ system," *Solid State Ionics*, vol. 262, pp. 454–459, 2014.

[71] M. Morales, V. Miguel-Pérez, A. Tarancón, A. Slodczyk, M. Torrell, B. Ballesteros, J. P. Ouweltjes, J. M. Bassat, D. Montinaro, and A. Morata, "Multi-scale analysis of the diffusion barrier layer of gadolinia-doped ceria in a solid oxide fuel cell operated in a stack for 3000 h," *J. Power Sources*, vol. 344, pp. 141–151, 2017.

[72] F. Mauvy, C. Lalanne, J.-M. Bassat, J. C. Grenier, H. Zhao, L. Huo, and P. Stevens, "Electrode properties of $Ln_2NiO_{4+\delta}$ (Ln=La, Nd, Pr). AC impedance and DC polarization studies," *J. Electrochem. Soc.*, vol. 153, no. 8, p. A1547, 2006.

[73] L. Mogni, N. Grunbaum, F. Prado, and A. Caneiro, "Oxygen reduction reaction on Ruddlesden–Popper phases studied by Impedance Spectroscopy," *J. Electrochem. Soc.*, vol. 158, no. 2, pp. B202-207, 2011.

[74] K. V. G. Kutty, C. K. Mathews, T. N. Rao, and U. V. Varadaraju, "Oxide ion conductivity in some substituted rare earth pyrozirconates," *Solid State Ionics*, vol. 80, no. 1–2, pp. 99–110, 1995.

[75] A. Mai, V. A. C. Haanappel, S. Uhlenbruck, F. Tietz, and D. Stöver, "Ferrite-based perovskites as cathode materials for anode-supported solid oxide fuel cells: Part I. Variation of composition," *Solid State Ionics*, vol. 176, no. 15–16, pp. 1341–1350, 2005.

[76] H. Yokokawa, H. Tu, B. Iwanschitz, and A. Mai, "Fundamental mechanisms limiting solid oxide fuel cell durability," *J. Power Sources*, vol. 182, no. 2, pp. 400–412, 2008.

[77] C. Endler-Schuck, J. Joos, C. Niedrig, A. Weber, and E. Ivers-Tiffée, "The chemical oxygen surface exchange and bulk diffusion coefficient determined by impedance spectroscopy of porous $La_{0.58}Sr_{0.4}Co_{0.2}Fe_{0.8}O_{3-\delta}$ (LSCF) cathodes," *Solid State Ionics*, vol. 269, pp. 67–79, 2015.

[78] J. D. Kim, G. D. Kim, J. W. Moon, Y. il Park, W. H. Lee, K. Kobayashi, M. Nagai, and C. E. Kim, "Characterization of LSM-YSZ composite electrode by ac impedance spectroscopy," *Solid State Ionics*, vol. 143, no. 3–4, pp. 379–389, 2001.

[79] S. P. Yoon, S. W. Nam, S. G. Kim, S. A. Hong, and S. H. Hyun, "Characteristics of cathodic polarization at Pt/YSZ interface without the effect of electrode microstructure," *J. Power Sources*, vol. 115, no. 1, pp. 27–34, 2003.

[80] D. Chen, R. Ran, K. Zhang, J. Wang, and Z. Shao, "Intermediate-temperature electrochemical performance of a polycrystalline $PrBaCo_2O_{5+\delta}$ cathode on samarium-doped ceria electrolyte," *J. Power Sources*, vol. 188, no. 1, pp. 96–105, 2009.

[81] T. Kenjo and M. Nishiya, "$LaMnO_3$ air cathodes containing ZrO_2 electrolyte for high temperature solid oxide fuel cells," *Solid State Ionics*, vol. 57, no. 3–4, pp. 295–302, 1992.

[82] G. C. Kostogloudis, G. Tsiniarakis, and C. Ftikos, "Chemical reactivity of perovskite oxide SOFC cathodes and yttria stabilized zirconia," *Solid State Ionics*, vol. 135, no. 1–4, pp. 529–535, 2000.

[83] A. Mitterdorfer and L. J. Gauckler, "$La_2Zr_2O_7$ formation and oxygen reduction kinetics of the $La_{0.85}Sr_{0.15}Mn_yO_3$, O_2(g)|YSZ system," *Solid State Ionics*, vol.

111, no. 3–4, pp. 185–218, 1998.

[84] M. C. Brant and L. Dessemond, “Electrical degradation of LSM-YSZ interfaces,” *Solid State Ionics*, vol. 138, pp. 1–17, 2000.

[85] A. Mai, V. A. C. Haanappel, F. Tietz, and D. Stöver, “Ferrite-based perovskites as cathode materials for anode-supported solid oxide fuel cells. Part II. Influence of the CGO interlayer,” *Solid State Ionics*, vol. 177, no. 19–25 SPEC. ISS., pp. 2103–2107, 2006.

[86] G. Constantin, C. Rossignol, P. Briois, A. Billard, L. Dessemond, and E. Djurado, “Efficiency of a dense thin CGO buffer layer for solid oxide fuel cell operating at intermediate temperature,” *Solid State Ionics*, vol. 249–250, pp. 98–104, 2013.

[87] H. G. Jung, Y. K. Sun, H. Y. Jung, J. S. Park, H. R. Kim, G. H. Kim, H. W. Lee, and J. H. Lee, “Investigation of anode-supported SOFC with cobalt-containing cathode and GDC interlayer,” *Solid State Ionics*, vol. 179, no. 27–32, pp. 1535–1539, 2008.

[88] M. Z. Khan, M. T. Mehran, R. H. Song, J. W. Lee, S. B. Lee, T. H. Lim, and S. J. Park, “Effect of GDC interlayer thickness on durability of solid oxide fuel cell cathode,” *Ceram. Int.*, vol. 42, no. 6, pp. 6978–6984, 2015.

[89] A. Endo, H. Fukunaga, C. Wen, and K. Yamada, “Cathodic reaction mechanism of dense $La_{0.6}Sr_{0.4}CoO_3$ and $La_{0.81}Sr_{0.09}MnO_3$ electrodes for solid oxide fuel cells,” *Solid State Ionics*, vol. 135, no. 1–4, pp. 353–358, 2000.

[90] M. J. Verkerk, B. J. Middelhuis, and A. J. Burggraaf, “Effect of grain boundaries on the conductivity of high-purity ZrO_2-Y_2O_3 ceramics,” *Solid State Ionics*, vol. 6, no. 2, pp. 159–170, 1982.

[91] G. Christie and F. P. Van Berkel, “Microstructure-ionic conductivity relationships in ceria-gadolinia electrolytes,” *Solid State Ionics*, vol. 83, no. 1–2, pp. 17–27, 1996.

[92] A. Hagen, Y. L. Liu, R. Barfod, and P. V. Hendriksen, “Assessment of the cathode contribution to the degradation of anode-supported solid oxide fuel fells,” *J. Electrochem. Soc.*, vol. 155, no. 10, p. B1047, 2008.

[93] L. Barelli, E. Barluzzi, and G. Bidini, “Diagnosis methodology and technique for solid oxide fuel cells: A review,” *Int. J. Hydrogen Energy*, vol. 38, no. 12, pp. 5060–5074, 2013.

[94] J. Nielsen and M. Mogensen, “SOFC LSM:YSZ cathode degradation induced by moisture: An impedance spectroscopy study,” *Solid State Ionics*, vol. 189, no. 1, pp. 74–81, 2011.

[95] E. Perry Murray and S. A. Barnett, “$(La,Sr)MnO_3$-$(Ce,Gd)O_{2-x}$ composite cathodes for solid oxide fuel cells,” *Solid State Ionics*, vol. 143, no. 3–4, pp. 265–273, 2001.

[96] C. Xia, Y. Zhang, and M. Liu, “LSM-GDC composite cathodes derived from a sol-gel process,” *Electrochem. Solid-State Lett.*, vol. 6, no. 12, p. A290, 2003.

[97] B. Fan, J. Yan, and X. Yan, “The ionic conductivity, thermal expansion behavior, and chemical compatibility of $La_{0.54}Sr_{0.44}Co_{0.2}Fe_{0.8}O_{3-\delta}$ as SOFC cathode material,” *Solid State Sci.*, vol. 13, no. 10, pp. 1835–1839, 2011.

[98] W. G. Wang and M. Mogensen, “High-performance lanthanum-ferrite-based

cathode for SOFC," *Solid State Ionics*, vol. 176, no. 5–6, pp. 457–462, 2005.

[99] M. J. L. Østergard, C. Clausen, C. Bagger, and M. Mogensen, "Manganite-zirconia composite cathodes for SOFC: Influence of structure and composition," *Electrochim. Acta*, vol. 40, no. 12, pp. 1971–1981, 1995.

[100] S. Wang, Y. Jiang, Y. Zhang, J. Yan, and W. Li, "Promoting effect of YSZ on the electrochemical performance of YSZ+LSM composite electrodes," *Solid State Ionics*, vol. 113–115, pp. 291–303, 1998.

[101] D. Beckel, U. P. Muecke, T. Gyger, G. Florey, A. Infortuna, and L. J. Gauckler, "Electrochemical performance of LSCF based thin film cathodes prepared by spray pyrolysis," *Solid State Ionics*, vol. 178, no. 5–6, pp. 407–415, 2007.

[102] J. Kim, W. Seo, J. Shin, M. Liu, and G. Kim, "Composite cathodes composed of $NdBa_{0.5}Sr_{0.5}Co_2O_{5+\delta}$ and $Ce_{0.9}Gd_{0.1}O_{1.95}$ for intermediate-temperature solid oxidefuel cells," *J. Mater. Chem. A*, vol. 1, no. 3, pp. 515–519, 2013.

[103] C. Kim, J. Kim, J. Shin, and G. Kim, "Effects of composite cathode on electrochemical and redox properties for intermediate-temperature solid oxide fuel cells," *Int. J. Hydrogen Energy*, vol. 39, no. 35, pp. 20812–20818, 2014.

[104] J. C. Ruiz-Morales, J. Canales-Vázquez, D. Marrero-López, J. T. S. Irvine, and P. Núñez, "Improvement of the electrochemical properties of novel solid oxide fuel cell anodes, $La_{0.75}Sr_{0.25}Cr_{0.5}Mn_{0.5}O_{3-\delta}$ and $La_4Sr_8Ti_{11}Mn_{0.5}Ga_{0.5}O_{37.5-\delta}$, using Cu–YSZ-based cermets," *Electrochim. Acta*, vol. 52, pp. 7217–7225, 2007.

[105] E. Lay, L. Dessemond, and G. Gauthier, "Ba-substituted LSCM anodes for solid oxide fuel cells," *J. Power Sources*, vol. 221, pp. 149–156, 2013.

[106] S. Primdahl and M. Mogensen, "Oxidation of hydrogen on Ni/Yttria-stabilized zirconia cermet anodes," *J. Electrochem. Soc.*, vol. 144, no. 10, pp. 3409–3419, 1997.

[107] J. Divisek, L. G. J. De Haart, P. Holtappels, T. Lennartz, W. Malléner, U. Stimming, and K. Wippermann, "The kinetics of electrochemical reactions on high temperature fuel cell electrodes," *J. Power Sources*, vol. 49, pp. 257–270, 1994.

[108] P. Holtappels, "Reaction of hydrogen/water mixtures on nickel-zirconia Cermet electrodes: I. DC polarization characteristics," *J. Electrochem. Soc.*, vol. 146, no. 5, pp. 1626–1625, 1999.

[109] W. C. Conner and J. L. Falconer, "Spillover in heterogeneous catalysis," *Chem. Rev.*, vol. 95, no. 3, pp. 759–788, 1995.

[110] K. V. Hansen, K. Norrman, and M. Mogensen, "H_2-H_2O-Ni-YSZ electrode performance," *J. Electrochem. Soc.*, vol. 151, no. 9, pp. A1436–A1444, 2004.

[111] E. Lay, L. Dessemond, and G. Gauthier, "Synthesis and characterization of $Ce_xSr_{1-x}Cr_{0.5}Mn_{0.5}O_{3-\delta}$ perovskites as anode materials for solid oxide fuel cells (SOFC)," *Electrochimica Acta*, vol. 216. pp. 420–428, 2016.

[112] S. P. Jiang, W. Wang, and Y. D. Zhen, "Performance and electrode behaviour of nano-YSZ impregnated nickel anodes used in solid oxide fuel cells," *J. Power Sources*, vol. 147, no. 1–2, pp. 1–7, 2005.

[113] S. P. Jiang, X. J. Chen, S. H. Chan, J. T. Kwok, and K. A. Khor, "$(La_{0.75}Sr_{0.25})(Cr_{0.5}Mn_{0.5})O_3$/YSZ composite anodes for methane oxidation

reaction in solid oxide fuel cells," *Solid State Ionics*, vol. 177, no. 1–2, pp. 149–157, 2006.

[114] S. Primdahl, "Gas Conversion Impedance: A test geometry effect in characterization of solid oxide fuel cell anodes," *J. Electrochem. Soc.*, vol. 145, no. 7, p. 2431, 1998.

[115] S. Jiang and S. P. S. Badwal, "An electrode kinetics study of H_2 oxidation on Ni/$Y2O_3$-ZrO_2 cermet electrode of the solid oxide fuel cell," *Solid State Ionics*, vol. 123, no. 1–4, pp. 209–224, 1999.

[116] A. Mohammed Hussain, J. V. T. Høgh, T. Jacobsen, and N. Bonanos, "Nickel-ceria infiltrated Nb-doped $SrTiO_3$ for low temperature SOFC anodes and analysis on gas diffusion impedance," *Int. J. Hydrogen Energy*, vol. 37, no. 5, pp. 4309–4318, 2012.

[117] S. Primdahl and M. Mogensen, "Gas diffusion impedance in characterization of solid oxide fuel cell anodes," *J. Electrochem. Soc.*, vol. 146, no. 8, p. 2827, 1999.

[118] P. V. Aravind, J. P. Ouweltjes, and J. Schoonman, "Diffusion impedance on nickel/gadolinia-doped ceria anodes for solid oxide fuel cells," *J. Electrochem. Soc.*, vol. 156, no. 12, p. B1417, 2009.

[119] R. Kramer and M. Andre, "Adsorption of atomic hydrogen on alumina by hydrogen spillover," *J. Catal.*, vol. 58, no. 2, pp. 287–295, 1979.

[120] V. Kharton, E. Tsipis, I. Marozau, a Viskup, J. Frade, and J. Irvine, "Mixed conductivity and electrochemical behavior of $(La_{0.75}Sr_{0.25})_{0.95}Cr_{0.5}Mn_{0.5}O_{3-\delta}$," *Solid State Ionics*, vol. 178, no. 1–2, pp. 101–113, 2007.

[121] D. Marrero-López, J. Peña-Martínez, J. C. Ruiz-Morales, M. Gabás, P. Núñez, M. A. G. Aranda, and J. R. Ramos-Barrado, "Redox behaviour, chemical compatibility and electrochemical performance of $Sr_2MgMoO_{6-\delta}$ as SOFC anode," *Solid State Ionics*, vol. 180, no. 40, pp. 1672–1682, 2010.

[122] J. Shen, G. Yang, Z. Zhang, M. O. Tadé, W. Zhou, and Z. Shao, "Improved performance of a symmetrical solid oxide fuel cell by swapping the roles of doped ceria and $La_{0.6}Sr_{1.4}MnO_{4+\delta}$ in the electrode," *J. Power Sources*, vol. 342, pp. 644–651, 2017.

[123] G. Yang, C. Su, R. Ran, M. O. Tade, and Z. Shao, "Advanced symmetric solid oxide fuel cell with an infiltrated K_2NiF_4-type La_2NiO_4 electrode," *Energy & Fuels*, vol. 28, no. 1, pp. 356–362, 2014.

[124] L. Thommy, O. Joubert, J. Hamon, and M. T. Caldes, "Impregnation versus exsolution: Using metal catalysts to improve electrocatalytic properties of LSCM-based anodes operating at 600 °C," *Int. J. Hydrogen Energy*, vol. 41, no. 32, pp. 14207–14216, 2016.

GENERAL CONCLUSION

This work was dedicated to the synthesis, structural, electrical and electrochemical characterization of the Ruddlesden Popper (RP) manganites $RE_xA_{2-x}MnO_{4\pm\delta}$ (RE: La, Nd and A: Sr, Ca), in order to determine their potential as electrode materials for symmetrical Solid Oxide Fuel Cells (S-SOFC).

In a first step, the materials were synthesized both by sol gel method and solid-state reaction. Their basic structural characterizations were carried out by Rietveld refinement using X-ray Powder Diffraction data (XRPD). Single phase compounds were obtained for the following compositions: $La_xSr_{2-x}MnO_{4\pm\delta}$ (x= 0.25, 0.4, 0.5 and 0.6), $Nd_xSr_{2-x}MnO_{4\pm\delta}$ (x=0.4 and 0.5) and $Nd_xCa_{2-x}MnO_{4\pm\delta}$, (x=0.25, 0.4 and 0.5). The strontium-based compounds present a tetragonal structure with space group *I*4/*mmm,* whereas the calcium-based compounds exhibit an orthorhombic distortion (space group *Fmmm*).

The chemical stability in reducing atmosphere was the first criterion for selecting the materials that can be used as potential symmetrical electrodes. The $La_xSr_{2-x}MnO_{4\pm\delta}$ (x= 0.25, 0.4, 0.5 and 0.6) and $Nd_xSr_{2-x}MnO_{4\pm\delta}$ (x=0.4, 0.5 and 0.6) compounds are stable under reducing atmosphere, maintaining their K_2NiF_4-type structure with *I*4/*mmm* symmetry, while, in contrast, $Nd_xCa_{2-x}MnO_{4\pm\delta}$, (x=0.25, 0.4 and 0.5) compounds decompose whatever the degree of neodymium substitution.

Thermogravimetric reduction carried out on the $RE_xSr_{2-x}MnO_{4\pm\delta}$ (RE: La, Nd) compounds showed that the manganese oxidation state changes from Mn^{4+} to Mn^{2+} within the Ruddlesden-Popper structure, always providing a mixed valence that favors the redox stability. In these materials, the variation of lattice parameters, the decrease of the equatorial Mn-O1 bond lengths and the increase of the axial Mn-O2 bond lengths during reduction was attributed to Jahn-Teller distortion induced by the increasing amount of Mn^{3+} in the structure. The reoxidation process allowed the parameters change back to the initial values, demonstrating that the reduction process was completely reversible.

For $La_{0.5}Sr_{1.5}MnO_{4\pm\delta}$ (L5S15M) material, information about the oxygen vacancies formation during reduction was obtained from Neutron Powder Diffraction (NPD) experiments, carried out in the nuclear reactor of the Léon Brillouin Laboratory (CEA/Saclay-France). Sequential Rietveld refinements of the NPD patterns revealed that oxide-ion vacancies are confined at the equatorial sites (O1) in the "MnO_2" layers. This oxygen loss generates variations in the mean oxidation state of Mn, showing that the compound has a mixed valence Mn^{4+}/Mn^{3+} below 550°C and changes to Mn^{3+}/Mn^{2+} when the temperature reaches 850°C. In addition, this study confirms that Jahn-Teller distortion of the [MnO_6] octahedron causes a strong variation of the Mn-O2 axial bond and decrease of Mn-O1/Mn-O2 ratio during heating under hydrogen.

$La_{0.5}Sr_{1.5}MnO_{4\pm\delta}$ (L5S15M) and $Nd_{0.5}Sr_{1.5}MnO_{4\pm\delta}$ (N5S15M) materials react with YSZ electrolyte to form $(La,Nd)_{1-x}Sr_xMnO_3$ and $SrZrO_3$ phases. In contrast, the materials are chemically compatible with GDC electrolyte both in oxidizing and reducing atmosphere. After structural and electrical characterization and since the substitution with Nd did not diminish the reactivity with YSZ, the $La_{0.5}Sr_{1.5}MnO_{4\pm\delta}$ (L5S15M) compound was selected to be evaluated as air and hydrogen electrode. In addition, L5S15M material presented thermal expansion coefficients that match rightly with the common electrolyte materials.

The electrical properties of $La_xSr_{2-x}MnO_{4\pm\delta}$ (x= 0.25, 0.4, 0.5 and 0.6) series were studied in air and reducing atmosphere. In air, the materials present a semiconductor behavior that involves that the charge transport occurs via thermally activated hopping of small polarons. The variation of the electrical conductivity for the different compounds was attributed to the enlargement of the equatorial Mn-O1 distance that affects the charge carrier mobility (n-type). In reducing atmosphere, the conductivity notably drops possibly because the presence of oxygen vacancies can block the carrier hopping through the Mn-O1-Mn path. However, the electrical conductivity

values obtained both in oxidizing and reducing atmosphere are estimated to be sufficient for an active layer of symmetrical SOFC.

In a second part of this work, the electrochemical performances of L5S15M were studied using Electrochemical Impedance Spectroscopy (EIS) measurements. The cells consisting of a YSZ electrolyte, a GDC barrier layer and an L5S15M active layer were evaluated in a single atmosphere, either air or hydrogen. The impedance study was focused on the evaluation of the influence of electrode composition (pure L5S15M or L5S15M:GDC composites) as well as sintering temperature on the electrochemical performance.

The electrochemical behavior of L5S15M electrode for oxygen reduction reaction revealed that area specific resistance (ASR) increases with increasing sintering temperature. The use of equivalent circuits to estimate the contributions to the resistance is a key tool for analyzing the rate-limiting step(s) occurring at the SOFC electrode. Thus, the electrode sintered at 1150 °C presents two limiting steps: i) at high frequency, the charge transfer of oxygen ions (O^{2-}) at the electrode/electrolyte interface and ii) at medium frequency, the electron transfer between the electrode and oxygen (and subsequent incorporation of oxygen ion into the electrode). For the electrode sintered at 1200 °C, a better adhesion between electrode and electrolyte is achieved leading to the high frequency contribution disappearance. However, at medium frequency, the contribution observed in the electrode sintered at 1150 °C is accompanied by a new one that corresponds to the dissociative adsorption/desorption and/or surface diffusion of adsorbed oxygen. The increase of the electrode sintering temperature up to 1250 °C does not favor the electrochemical performance. In contrast, this promotes the Sr diffusion from the electrode to the GDC/YSZ interface. The Sr accumulation (and $SrZrO_3$ formation) at the GDC/YSZ interface leads to the partial delamination of the electrode and Sr depletion within the manganite, resulting in cell performance degradation. Besides, mixing GDC with

L5S15M to form a composite electrode does not significantly improve the electrochemical performance.

The hydrogen oxidation reaction has been also studied on L5S15M and L5S15M-GDC50 electrodes sintered at 1150 and 1200 °C. The electrochemical behavior in wet H_2 obtained for the electrode sintered at 1150 °C ($ASR_{800\ °C}$ = 0.61 Ω cm^2) is significantly better than those obtained for the electrode sintered at 1200 °C ($ASR_{800\ °C}$ = 1.68 Ω m^2). Three rate limiting processes are identified in both the pure and the composite electrodes. The process at high frequency (transfer of charged species across electrode/electrolyte interface), and the process at medium frequency (hydrogen dissociative adsorption) are affected by the electrode sintering temperature, while the highest contribution to resistance, at low frequency, is related to the surface diffusion process of H_{ad} species. The formation of a composite electrode enhanced the anode performance when it was sintered at 1200 °C, but the better performance is indeed obtained for an anode made of pure L5S15M and sintered at 1150 °C.

In summary, the redox stability, the chemical and thermomechanical matching with other cell components, the sufficient electrical conductivity in both oxidizing and reducing atmosphere and acceptable electrochemical behavior of L5S15M as cathode and anode, demonstrates that this material is a good candidate to work as electrode in a symmetrical SOFC.

DIVULGATION

Congresses

Mónica V. Sandoval, Carolina Cardenas, Caroline Pirovano, E. Capoen, P. Roussel and G. Gauthier. "Performance of $La_{0.5}Sr_{1.5}MnO_{4\pm\delta}$ as electrode material for symmetrical Solid Oxide Fuel Cell". 21st International Conference on Solid State Ionics (SSI 2017), Padova, Italy, June 18-23, 2017.

Silvia Durán, Mónica V. Sandoval, Caroline Pirovano, Konrad Swierczek, P. Roussel and G. Gauthier. "Synthesis and study of $Nd_xM_{2-x}MnO_{4\pm\delta}$ (M: Ca, Sr) as symmetric SOFC electrode materials". 21st International Conference on Solid State Ionics (SSI 2017), Padova, Italy, June 18-23, 2017.

Mónica V. Sandoval, C. Pirovano, E. Capoen, P. Roussel and G. Gauthier. "Synthesis, characterization and electrical properties of $Sr_{2-x}La_xMnO_{4\pm\delta}$ ($0.25\leq x\leq 0.6$) series for SOFC electrode" European Material Research Society Spring Meeting (E-MRS Spring 2016), Lille, France, May 2-6, 2016.

Mónica V. Sandoval, Caroline Pirovano, Edouard Capoen, Pascal Roussel and Gilles H. Gauthier. "Synthesis and preliminary characterization of $Sr_{2-x}La_xMnO_{4\pm\delta}$ ($0.25\leq x\leq 0.6$) series as symmetric SOFC electrode". 20th International Conference on Solid State Ionics (SSI2015), June 14-19, Keystone, Colorado, USA, 2015.

Mónica V. Sandoval, N.G. Martinez, S. Vázquez-Cuadriello, M.A. Macias, L. Suescun, P. Roussel and G.H. Gauthier "Thermal stability and compatibility with SOFC/PCFC electrolyte of $La_4BaCu_5O_{13+\delta}$ and $La_{6.4}Sr_{1.6}Cu_8O_{20\pm\delta}$ perovskites" 20th International Conference on Solid State Ionics (SSI2015), June 14-19, Keystone, Colorado, USA, 2015.

Publications

Mónica V. Sandoval, Caroline Pirovano, Edouard Capoen, Romain Jooris, Florence Porcher, Pascal Roussel and Gilles H. Gauthier. In-depth study of the Ruddlesden-Popper $La_xSr_{2-x}MnO_{4\pm\delta}$ family as possible electrode materials for symmetrical SOFC. International Journal oh Hydrogen Energy, vol. 42 (34), pp. 21930-21943, 2017

Mónica V. Sandoval, Silvia Durán, Andrea Prada, Caroline Pirovano, Konrad Swierczek, P. Roussel and G. Gauthier. Synthesis and study of $Nd_xAE_{2-x}MnO_{4\pm\delta}$ (AE: Ca, Sr) as symmetric SOFC electrode materials. Submitted to Solid State Ionics, 2017.

Other works

Mario A. Macias, Mónica V. Sandoval, Nelson G. Martinez, Santiago Vázquez-Cuadriello, L. Suescun, P. Roussel, Konrad Swierczek and G.H. Gauthier. Synthesis

and preliminary study of $La_4BaCu_5O_{13+\delta}$ and $La_{6.4}Sr_{1.6}Cu_8O_{20\pm\delta}$ ordered perovskites as SOFC/PCFC electrode materials. Solid State Ionics, vol. 288, pp. 68-75, 2016

Mónica V. Sandoval, Aracely Matta, Tulio Matencio, Rosana Zacarias Domingues, Gustavo A. Ludwig, Matias De Angelis Korb, Célia de Fraga Malfatti, Paola Gauthier-Maradei and Gilles H. Gauthier. Barium-modified NiO–YSZ/NiO–GDC cermet as new anode material for solid oxide fuel cells (SOFC). Solid State Ionics, 261,36-44, 2014.

ANNEXES

Annex 1

Graphical result of Rietveld refinement of $RE_xA_{2-x}MnO_{4\pm\delta}$ (RE: La, Nd and A: Sr, Ca) as-synthesized materials.

Figure S1. Graphical result of Rietveld refinement of $La_xSr_{2-x}MnO_{4\pm\delta}$ (x=0.25) as-synthesized material.

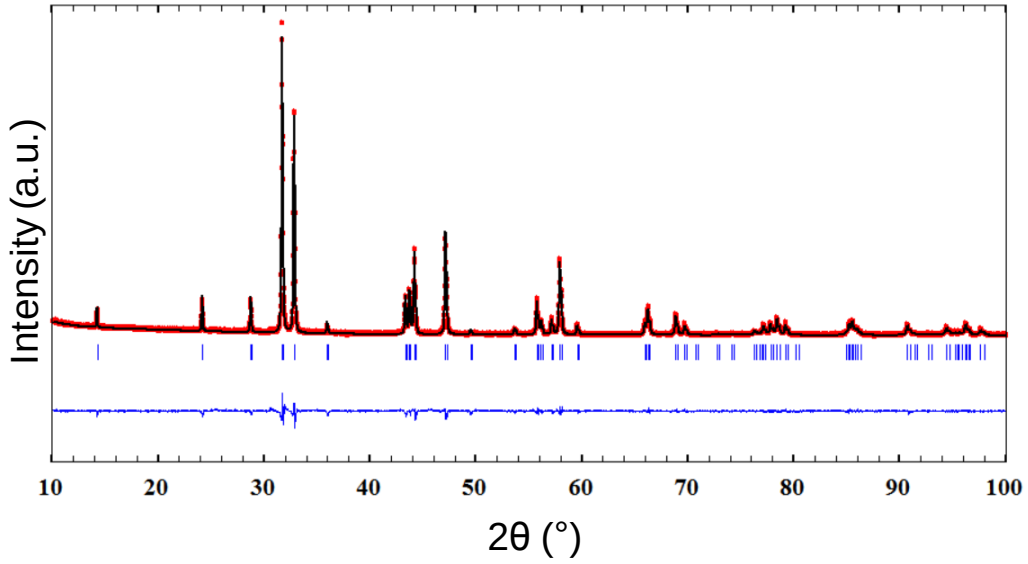

Figure S2. Graphical result of Rietveld refinement of $La_xSr_{2-x}MnO_{4\pm\delta}$ (x=0.4) as-synthesized material.

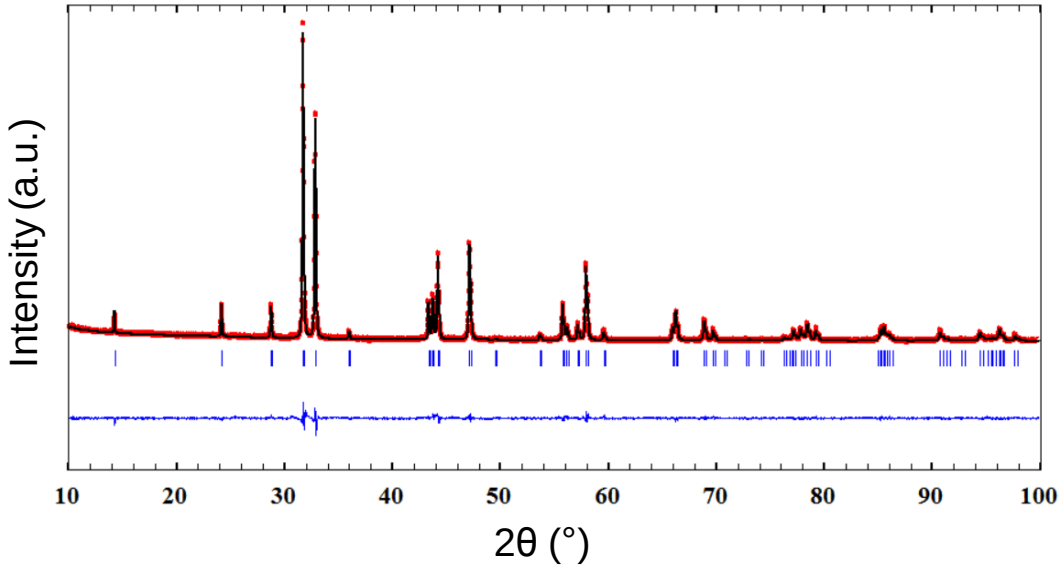

Figure S3. Graphical result of Rietveld refinement of $La_xSr_{2-x}MnO_{4\pm\delta}$ (x=0.5) as-synthesized material.

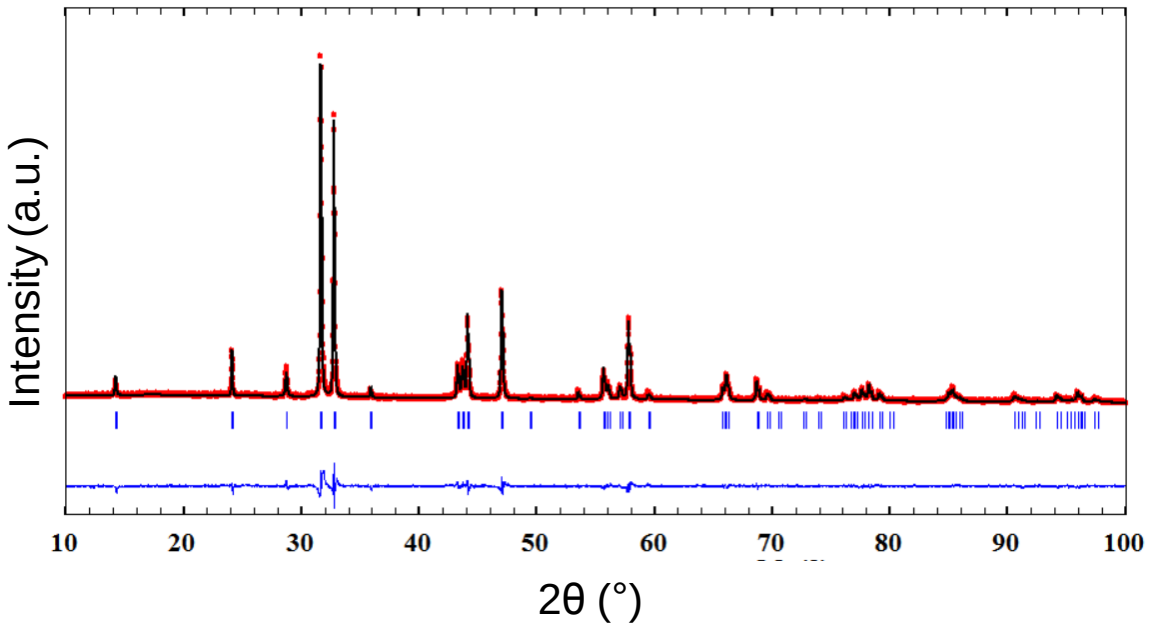

Figure S4. Graphical result of Rietveld refinement of $La_xSr_{2-x}MnO_{4\pm\delta}$ (x=0.6) as-synthesized material.

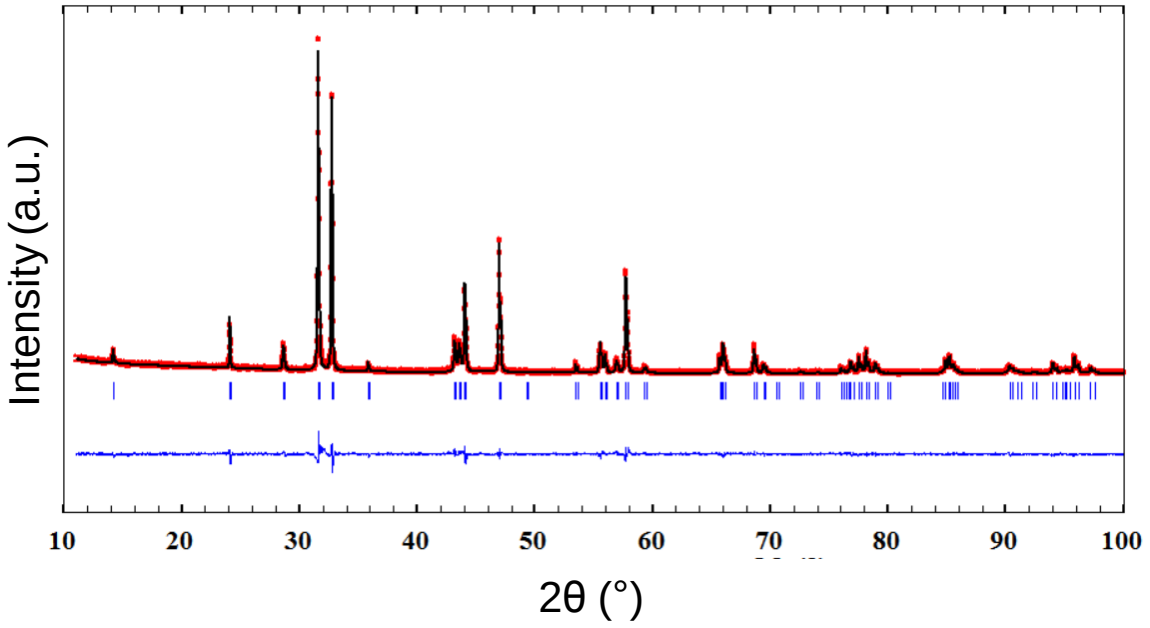

Figure S5. Graphical result of Rietveld refinement of $Nd_xSr_{2-x}MnO_{4\pm\delta}$ (x=0.25) as-synthesized material.

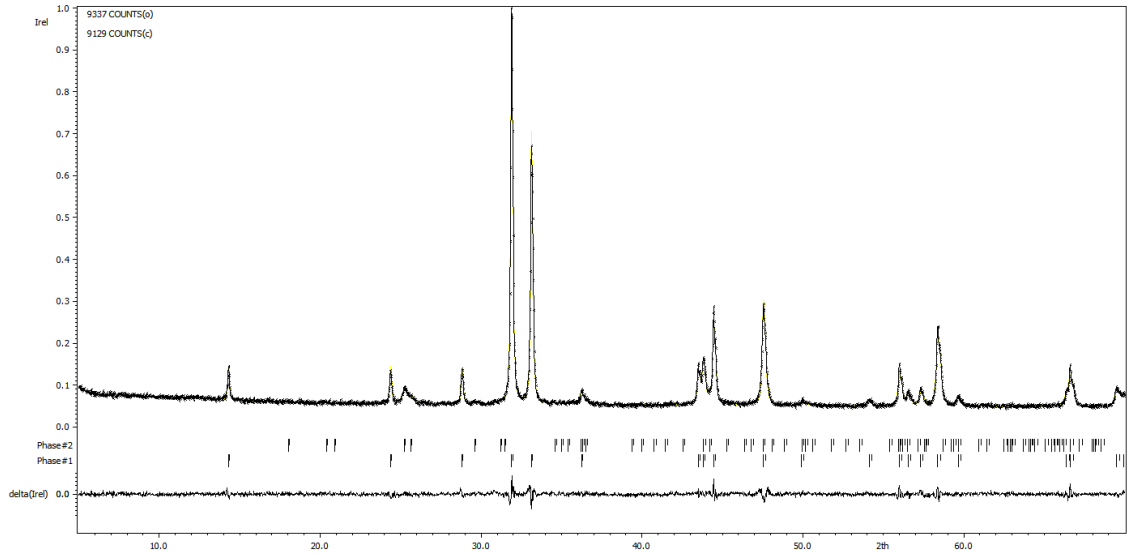

Figure S6. Graphical result of Rietveld refinement of $Nd_xSr_{2-x}MnO_{4\pm\delta}$ (x=0.4) as-synthesized material.

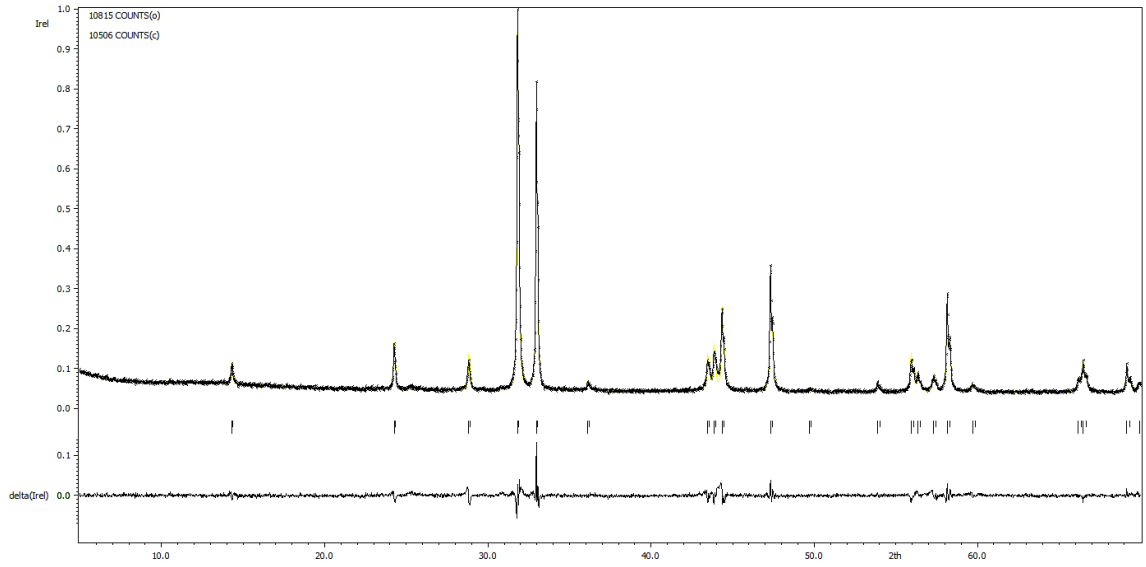

Figure S7. Graphical result of Rietveld refinement of $Nd_xSr_{2-x}MnO_{4\pm\delta}$ (x=0.6) as-synthesized material.

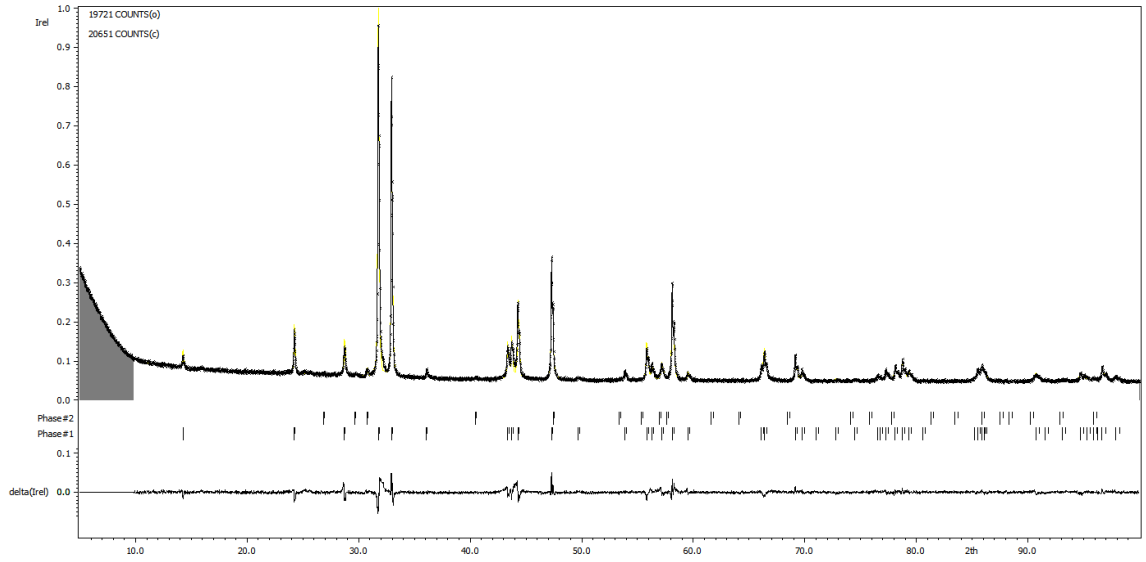

Figure S8. Graphical result of Rietveld refinement of $La_xCa_{2-x}MnO_{4\pm\delta}$ (x=0.15) as-synthesized material.

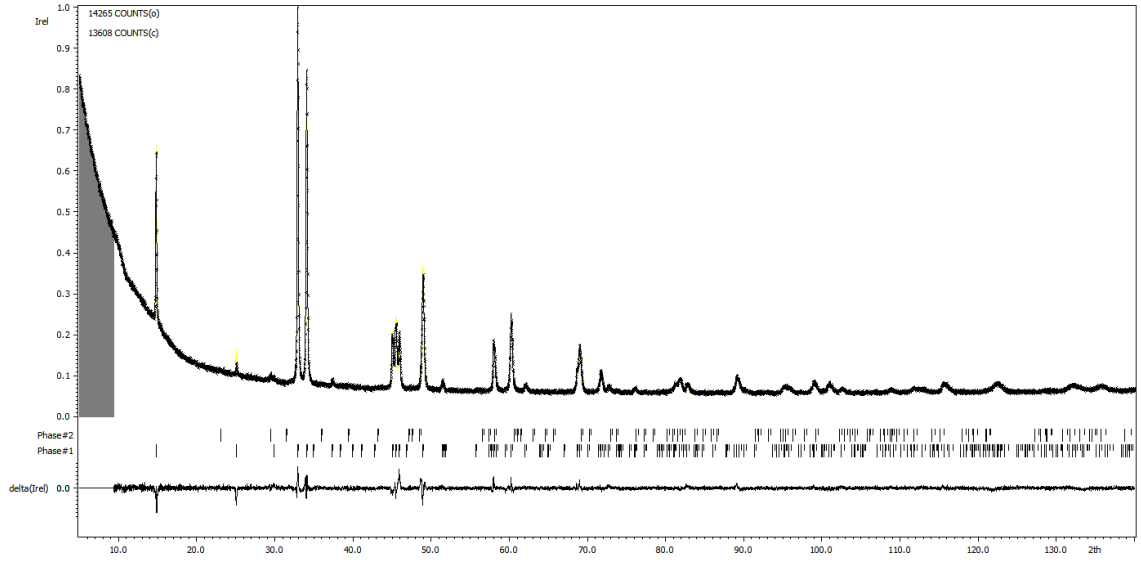

Figure S9. Graphical result of Rietveld refinement of $La_xCa_{2-x}MnO_{4\pm\delta}$ (x=0.25) as-synthesized material.

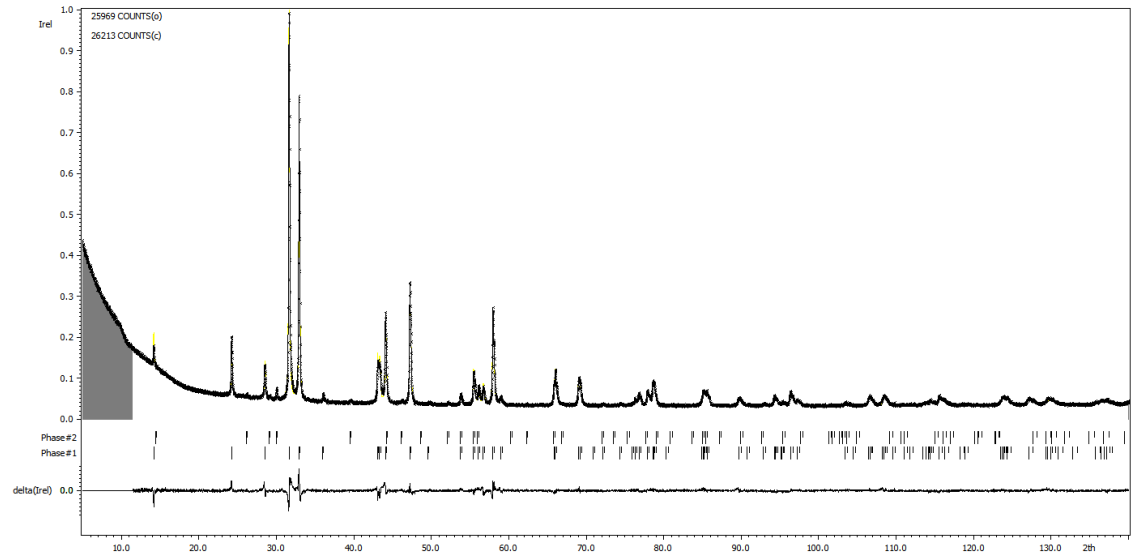

Figure S10. Graphical result of Rietveld refinement of $Nd_xCa_{2-x}MnO_{4\pm\delta}$ (x=0.25) as-synthesized material

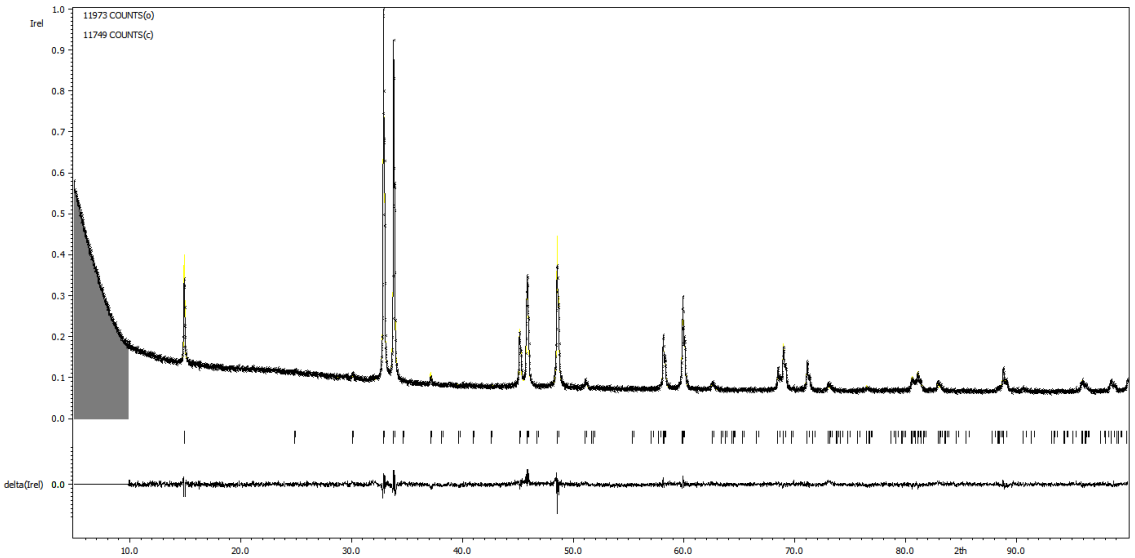

Figure S11. Graphical result of Rietveld refinement of $Nd_xCa_{2-x}MnO_{4\pm\delta}$ (x=0.4) as-synthesized material

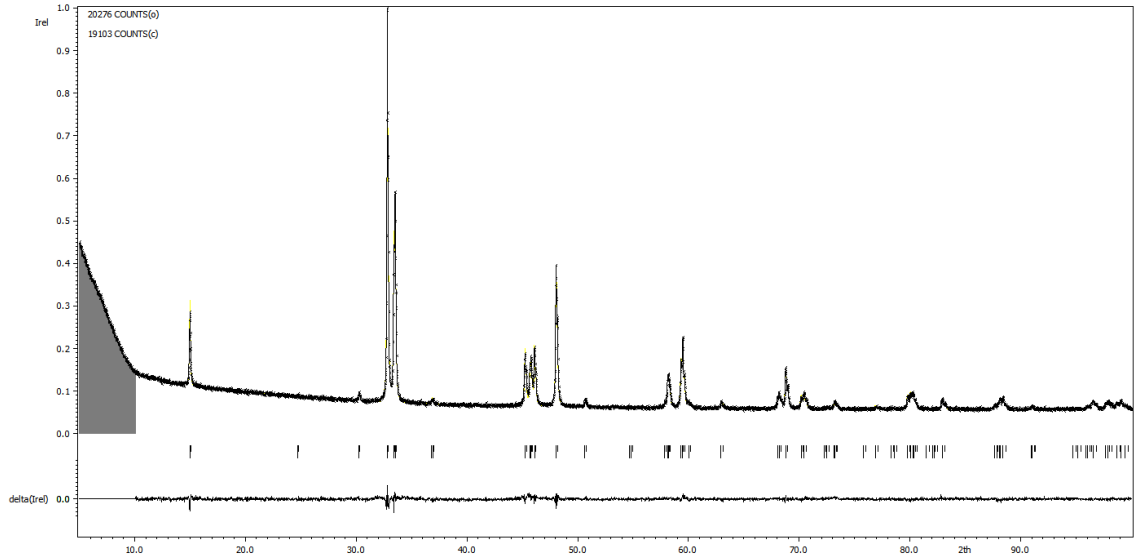

Figure S12. Graphical result of Rietveld refinement of $Nd_xCa_{2-x}MnO_{4\pm\delta}$ (x=0.5) as-synthesized material

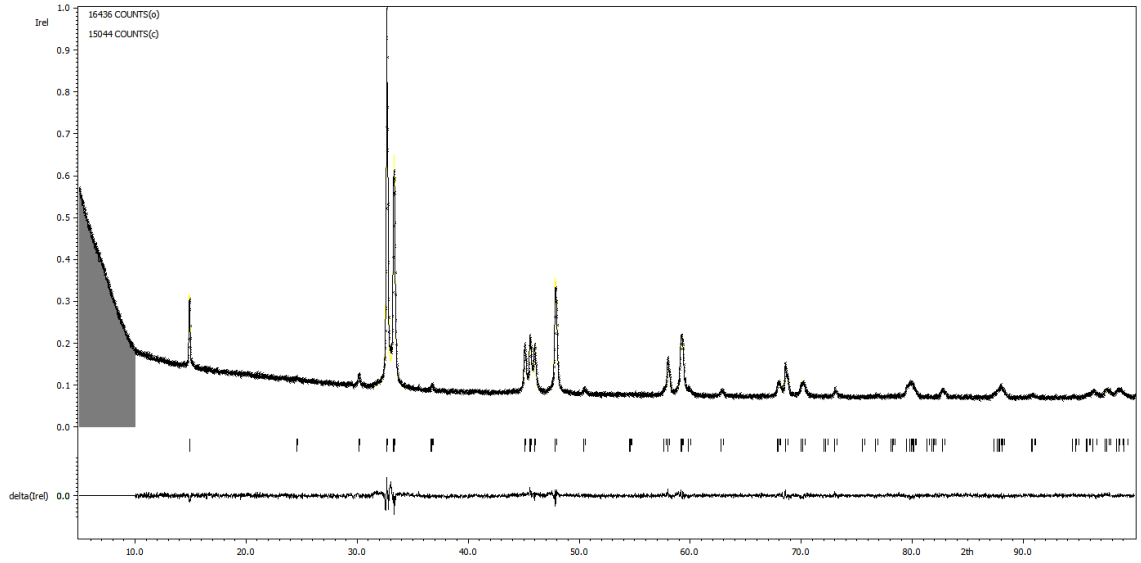

Annex 2

Comparison of the refinement of $Nd_{0.5}Ca_{1.5}MnO_{4\pm\delta}$ using $I4_1/acd$ and *Fmmm* space group.

Figure S13. Comparison of the refinement of $Nd_{0.5}Ca_{1.5}MnO_{4\pm\delta}$ using the (a) $I4_1/acd$ and (b) *Fmmm* space group.

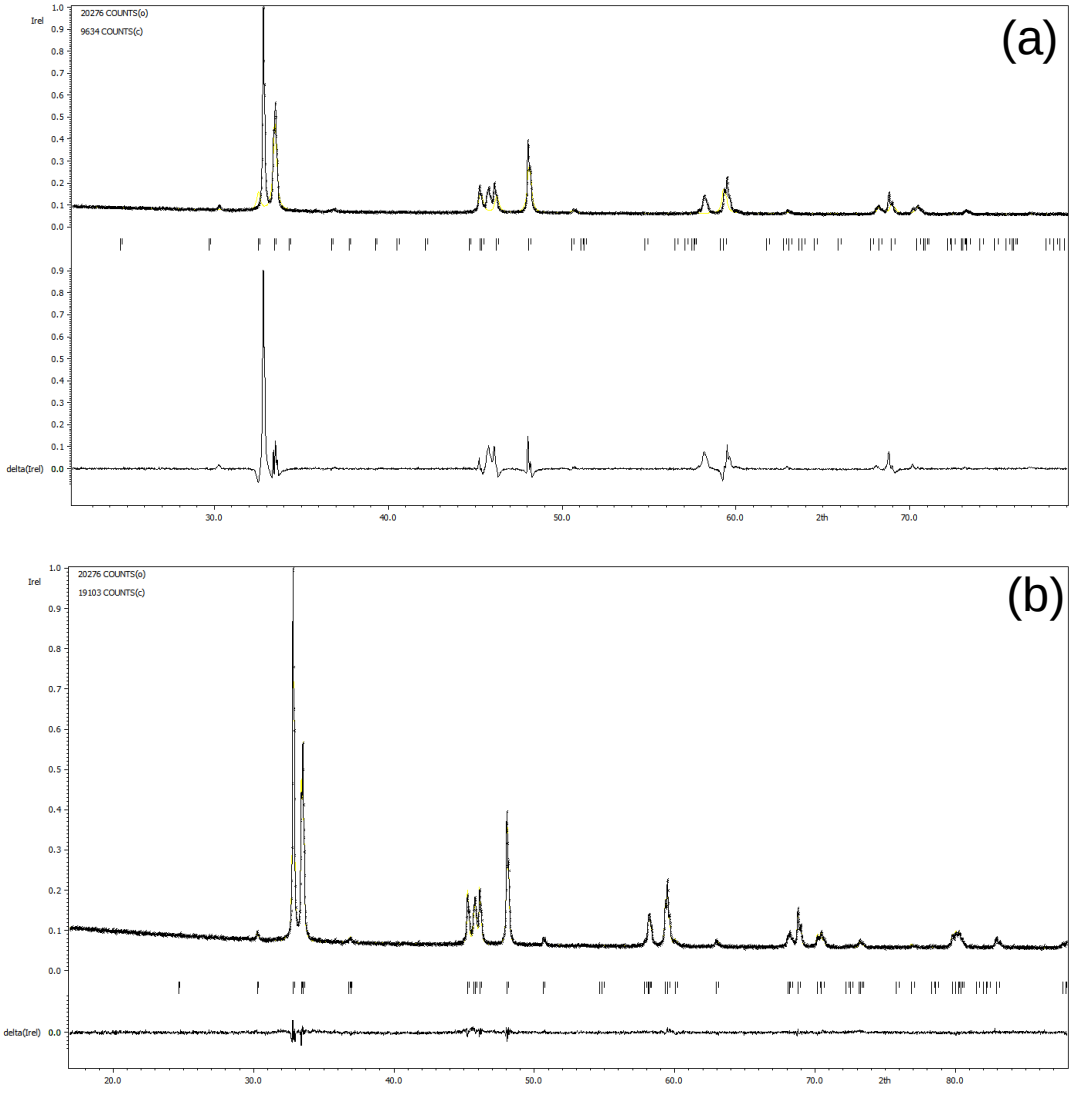

Annex 3

Graphical result of Rietveld refinement of $La_xSr_{2-x}MnO_{4\pm\delta}$ series after reduction in 3% H_2/Ar at 850 °C for 16 h.

Figure S14. Graphical result of Rietveld refinement of $La_xSr_{2-x}MnO_{4\pm\delta}$ (x=0.25) after reduction in 3% H_2/Ar at 850 °C for 16 h.

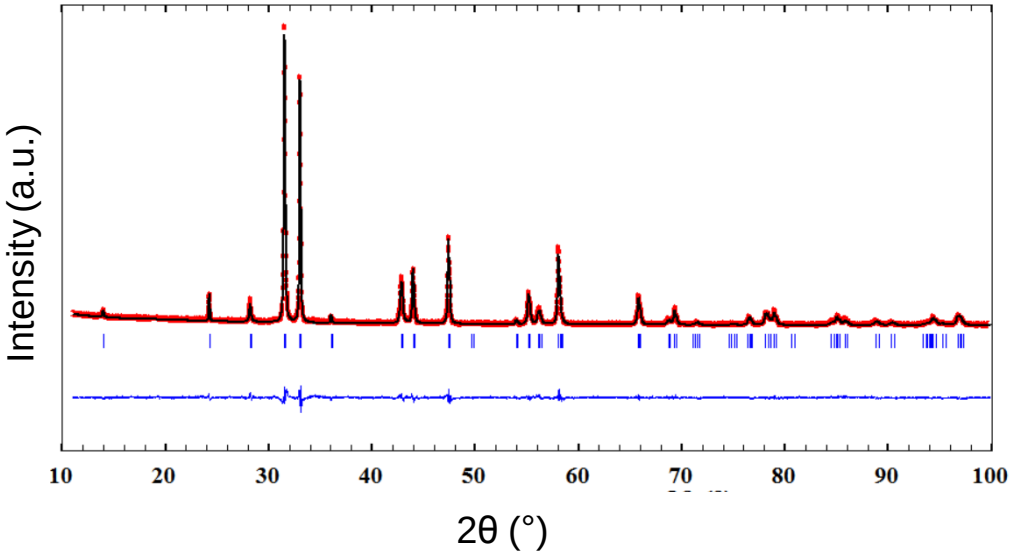

Figure S15. Graphical result of Rietveld refinement of $La_xSr_{2-x}MnO_{4\pm\delta}$ (x=0.4) after reduction in 3% H_2/Ar at 850 °C for 16 h.

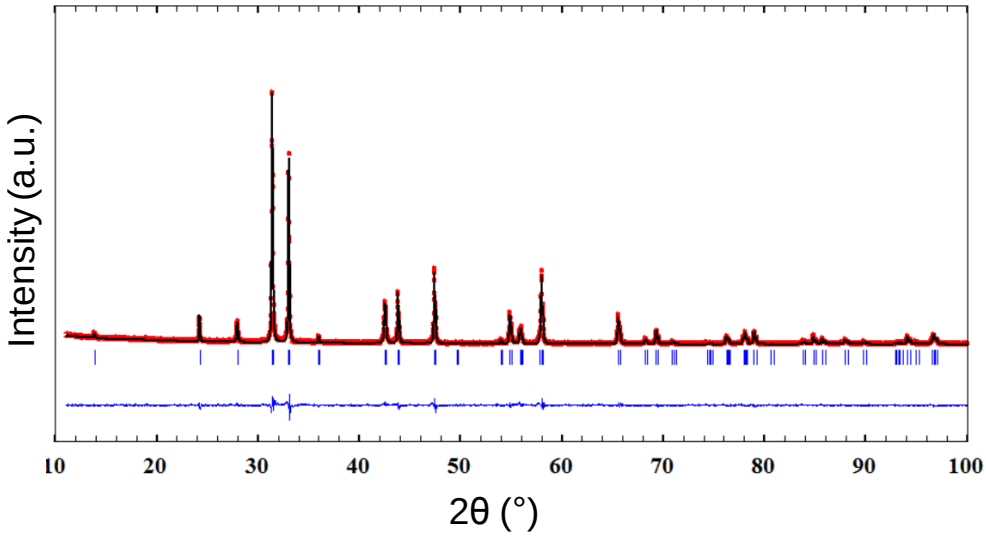

Figure S16. Graphical result of Rietveld refinement of $La_xSr_{2-x}MnO_{4\pm\delta}$ (x=0.6) after reduction in 3% H_2/Ar at 850 °C for 16 h.

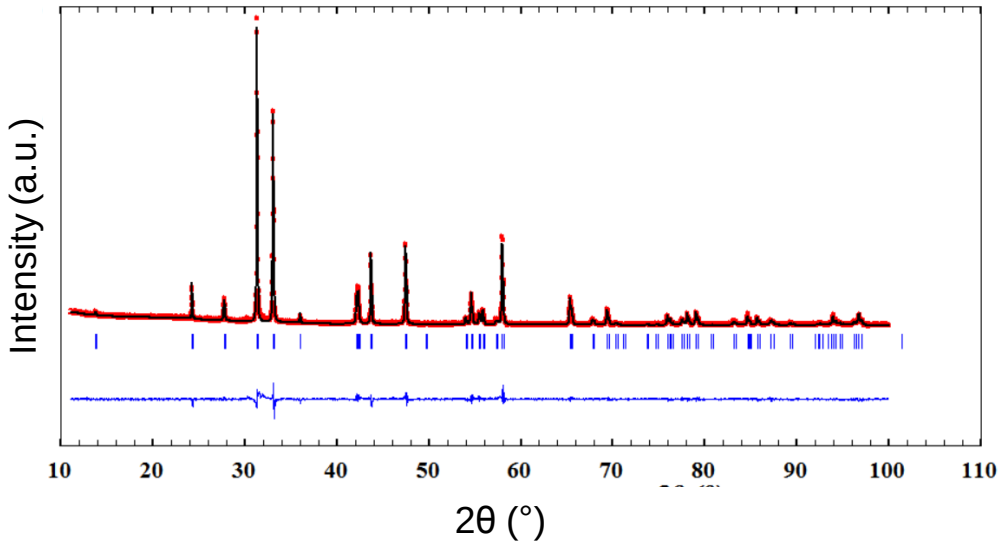

Annex 4

Graphical results of Rietveld refinement of $Nd_xSr_{2-x}MnO_{4\pm\delta}$ series after reduction in 3% H_2/Ar at 850 °C for 16 h.

Figure S17. Graphical result of Rietveld refinement of $Nd_xSr_{2-x}MnO_{4\pm\delta}$ (x=0.25) after reduction in 3% H_2/Ar at 850 °C for 16 h.

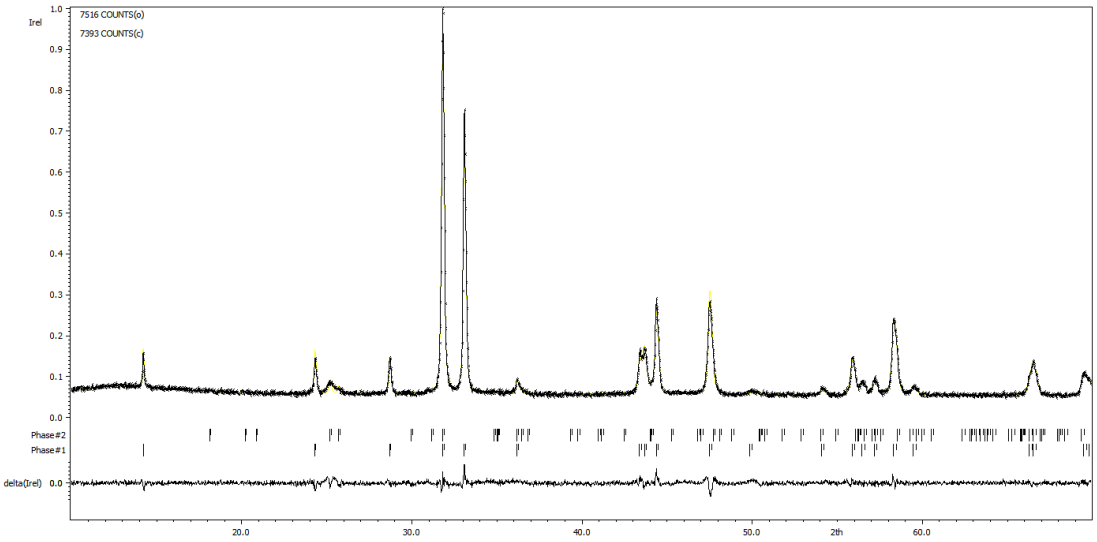

Figure S18. Graphical result of Rietveld refinement of $Nd_xSr_{2-x}MnO_{4\pm\delta}$ (x=0.4) after reduction in 3% H_2/Ar at 850 °C for 16 h.

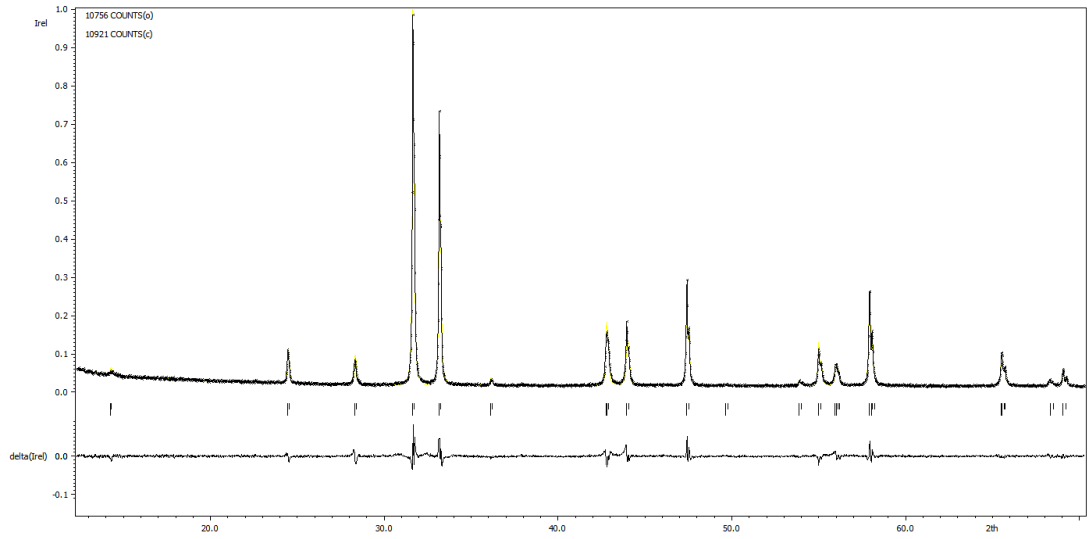

Figure S19. Graphical result of Rietveld refinement of $Nd_xSr_{2-x}MnO_{4\pm\delta}$ (x=0.5) after reduction in 3% H_2/Ar at 850 °C for 16 h.

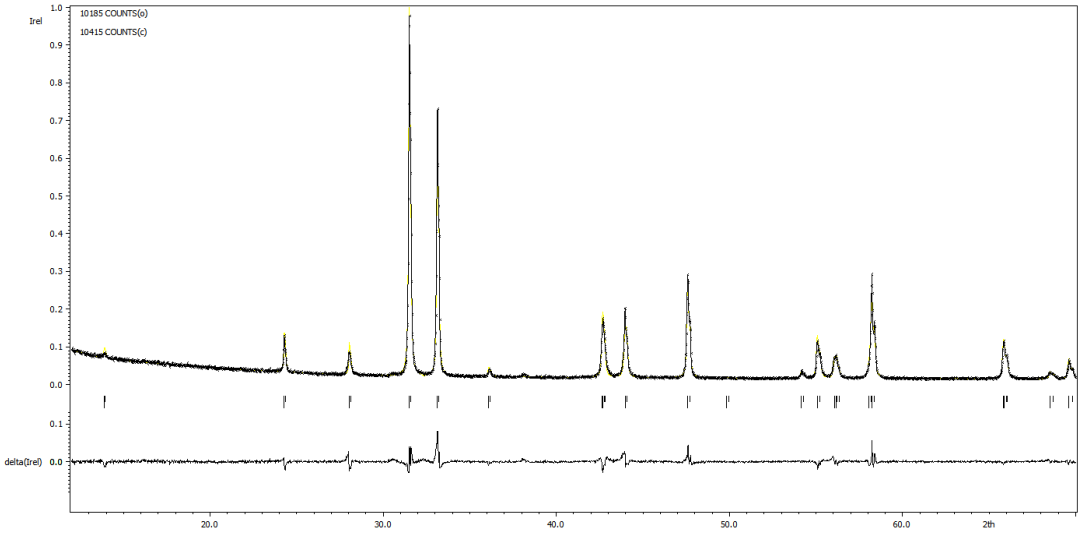

Figure S20. Graphical result of Rietveld refinement of $Nd_xSr_{2-x}MnO_{4\pm\delta}$ (x=0.5) after reduction in 3% H_2/Ar at 850 °C for 16 h.

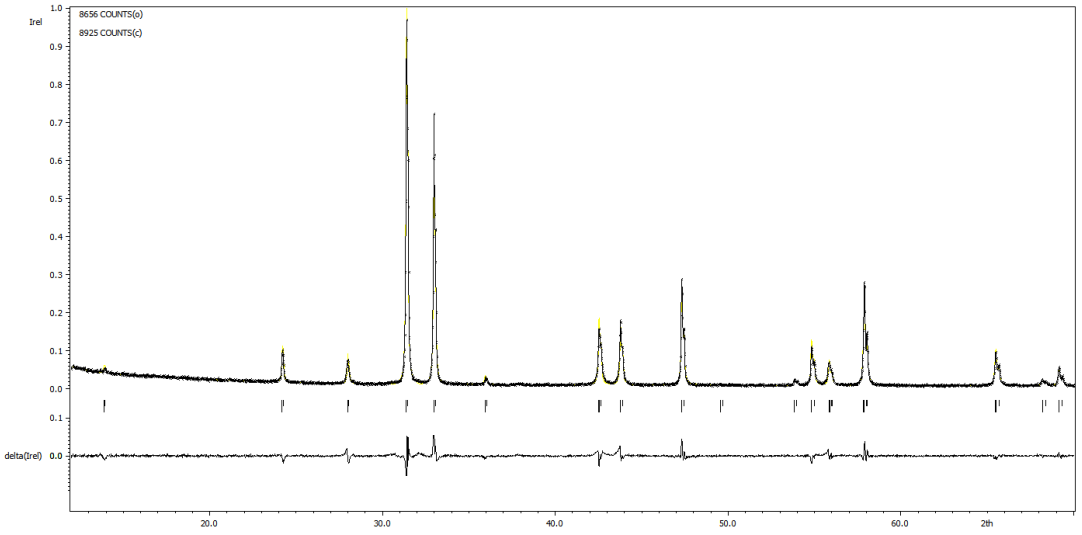

Annex 5

Thermogravimetric profiles for $La_xSr_{2-x}MnO_{4\pm\delta}$ (x=0.4 and 0.6) in air

Figure S21. Thermogravimetric profiles for $La_xSr_{2-x}MnO_{4\pm\delta}$ (x=0.4 and 0.6) in air

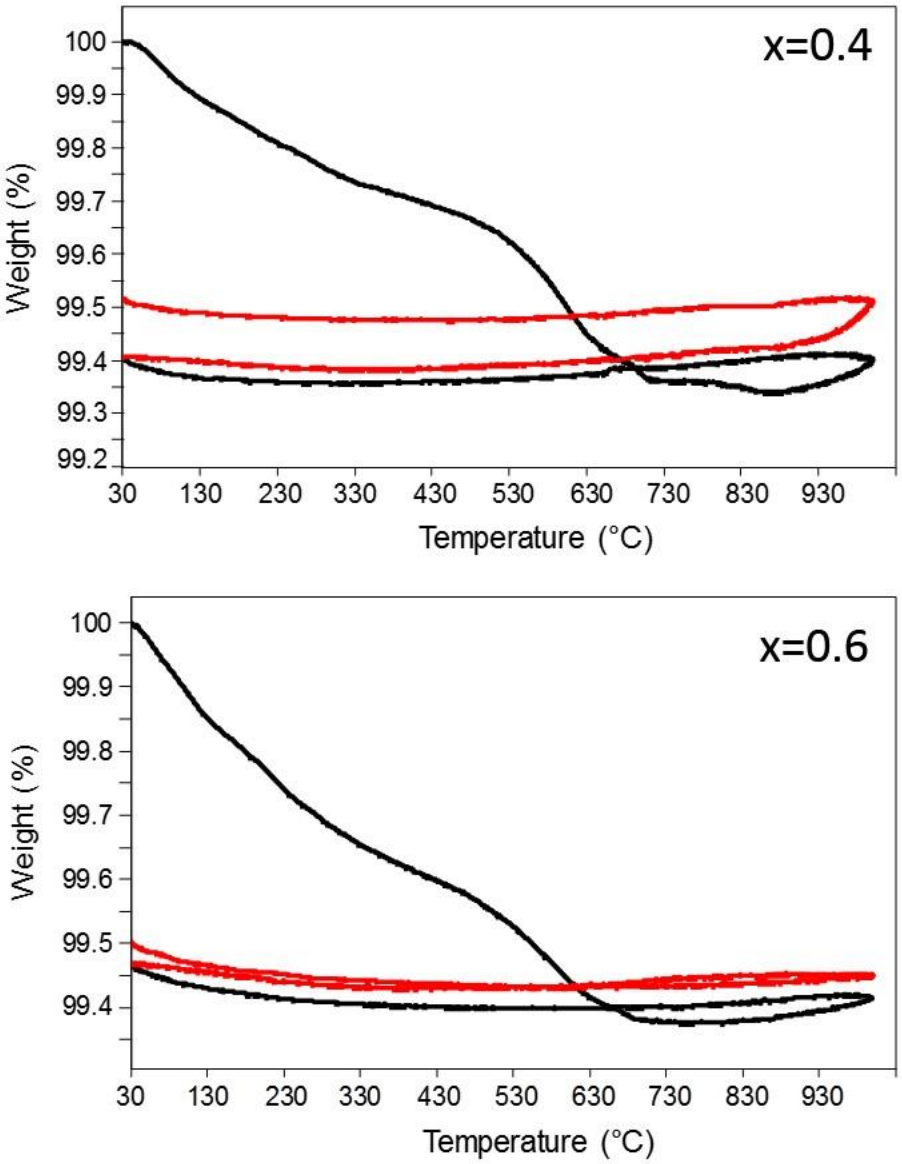

Annex 6

Structural parameters of $La_{0.5}Sr_{1.5}MnO_{4\pm\delta}$ derived from in situ neutron diffraction data

Table S1. Structural parameters of $La_{0.5}Sr_{1.5}MnO_{4\pm\delta}$ derived from in situ neutron diffraction data collected upon heating in 3% H_2/Ar.

Temperature (°C)	*a*(Å)	*c*(Å)	V(Å^3)	*z*	*z*	**O2**		**La/Sr**		**Mn**	
				La/Sr	O2	U_{11}	U_{33}	U_{11}	U_{33}	U_{11}	U_{33}
200	3.8670(3)	12.455(1)	186.25(3)	0.3576(4)	0.1604(5)	0.010(2)	0.015(4)	0.007(2)	0.007(3)	0.004(3)	0.001(5)
250	3.8696(4)	12.470(2)	186.72(4)	0.3581(5)	0.1608(7)	0.014(3)	0.018(5)	0.007(2)	0.011(3)	0.004(4)	0.014(8)
300	3.8704(3)	12.515(1)	187.47(3)	0.3563(5)	0.1611(6)	0.019(3)	0.016(4)	0.009(2)	0.015(3)	0.015(4)	0.007(7)
350	3.8719(3)	12.563(2)	188.33(3)	0.3548(6)	0.1616(6)	0.031(4)	0.010(4)	0.009(2)	0.018(3)	0.016(5)	0.009(8)
400	3.8727(5)	12.622(2)	189.31(4)	0.3561(6)	0.1620(7)	0.035(4)	0.014(4)	0.012(2)	0.019(3)	0.010(5)	0.026(10)
410	3.8720(4)	12.639(2)	189.49(4)	0.3554(6)	0.1619(8)	0.035(5)	0.024(5)	0.012(2)	0.018(4)	0.019(5)	0.015(9)
430	3.8711(5)	12.673(2)	189.89(5)	0.3560(6)	0.1618(7)	0.034(4)	0.022(5)	0.011(2)	0.020(4)	0.011(5)	0.020(9)
450	3.8721(5)	12.689(2)	190.24(5)	0.3561(5)	0.1615(7)	0.033(4)	0.023(5)	0.010(2)	0.016(3)	0.015(5)	0.029(10)
470	3.8718(6)	12.701(2)	190.38(5)	0.3561(6)	0.1621(8)	0.041(5)	0.021(5)	0.011(2)	0.017(4)	0.015(5)	0.032(11)
490	3.8725(6)	12.718(3)	190.73(6)	0.3576(6)	0.1623(8)	0.032(5)	0.016(5)	0.011(2)	0.021(4)	0.012(5)	0.038(13)
510	3.8720(6)	12.736(2)	190.94(5)	0.3567(5)	0.1626(7)	0.039(5)	0.016(4)	0.012(2)	0.019(4)	0.013(5)	0.031(10)
530	3.8732(6)	12.741(3)	191.14(6)	0.3576(6)	0.1626(8)	0.035(5)	0.015(5)	0.011(2)	0.022(4)	0.010(5)	0.039(13)
550	3.8731(6)	12.748(2)	191.24(5)	0.3557(5)	0.1625(7)	0.041(5)	0.024(5)	0.013(2)	0.013(3)	0.015(5)	0.022(9)
570	3.8740(6)	12.753(2)	191.39(5)	0.3539(8)	0.1622(12)	0.046(7)	0.041(8)	0.018(3)	0.014(4)	0.017(6)	0.024(11)
590	3.8751(5)	12.765(2)	191.68(5)	0.3542(7)	0.1621(9)	0.048(5)	0.029(6)	0.016(2)	0.020(4)	0.016(5)	0.015(9)
610	3.8756(5)	12.763(2)	191.71(5)	0.3544(6)	0.1632(8)	0.047(6)	0.036(6)	0.018(2)	0.025(4)	0.023(6)	0.016(9)
630	3.8766(5)	12.779(2)	191.72(6)	0.3547(6)	0.1629(9)	0.038(6)	0.039(6)	0.021(2)	0.017(4)	0.020(6)	0.023(10)
650	3.8778(7)	12.793(3)	192.38(6)	0.3561(6)	0.1636(8)	0.045(6)	0.026(6)	0.013(2)	0.020(4)	0.013(6)	0.024(11)
670	3.8784(5)	12.806(2)	192.62(5)	0.3538(7)	0.1611(9)	0.049(6)	0.026(6)	0.019(2)	0.025(5)	0.016(6)	0.024(11)
690	3.8787(5)	12.807(3)	192.66(5)	0.3527(8)	0.1621(12)	0.058(7)	0.040(9)	0.015(2)	0.022(5)	0.022(6)	0.027(13)
710	3.8792(6)	12.825(2)	193.00(5)	0.3546(7)	0.1623(9)	0.049(6)	0.024(6)	0.017(2)	0.026(5)	0.017(6)	0.026(12)
730	3.8797(6)	12.828(2)	193.09(6)	0.3564(8)	0.1630(10)	0.037(7)	0.027(7)	0.023(3)	0.018(6)	0.004(7)	0.028(2)
750	3.8801(7)	12.846(3)	193.40(6)	0.3552(7)	0.1616(9)	0.044(6)	0.031(6)	0.024(3)	0.026(5)	0.008(6)	0.054(14)
770	3.8809(5)	12.856(2)	193.62(5)	0.3530(8)	0.1624(10)	0.053(6)	0.037(8)	0.020(2)	0.028(5)	0.019(6)	0.030(13)
790	3.8812(5)	12.864(2)	193.78(5)	0.3532(9)	0.1611(13)	0.057(6)	0.046(10)	0.017(2)	0.028(5)	0.012(6)	0.049(16)
810	3.8819(6)	12.875(2)	194.01(5)	0.3560(9)	0.1643(18)	0.054(7)	0.102(15)	0.018(2)	0.019(5)	0.010(6)	0.080(12)
830	3.8830(5)	12.885(2)	194.27(5)	0.3548(8)	0.1637(9)	0.051(6)	0.034(7)	0.024(3)	0.028(5)	0.027(7)	0.022(12)
850	3.8846(8)	12.899(4)	194.65(8)	0.3555(1)	0.1622(13)	0.046(6)	0.029(10)	0.020(3)	0.030(6)	0.014(6)	0.054(18)

Annex 7

Principles of Electrochemical Impedance Spectroscopy (EIS)

Electrochemical Impedance Spectroscopy (EIS) or AC impedance plays an important role in fundamental and applied electrochemistry and materials science [1]. The EIS is a powerful technique for fuel cell diagnosis which can give information on individual losses, including oxygen reduction or hydrogen oxidation reaction kinetics, mass-transfer, and electrolyte membrane resistance losses. Application areas include electrode/electrolyte assembly optimization and fabrication, component down-selection, electrolyte-related conductivity, fuel cell stack impedance, and fuel cell localized impedance. In the optimization of fuel cell performance, the major focuses of the EIS have been the temperature, microstructure, pressure and flow rate effects [2].

The data are usually provided by measurement equipment as real Z' and imaginary Z'' parts of the impedance and represented as a Nyquist plot (Figure S22). The results are analyzed using equivalent circuits. Equivalent circuits (EC) should always be selected on the basis of an intuitive understanding of the electrochemical system, as long as they are based on the chemical and physical properties of the system. Most of the circuit elements in the model are common electrical elements such are resistor, capacitors and inductors. Some knowledge of the impedance of the standard circuit components is therefore quite useful. The impedance of a resistor is independent of frequency and has only a real impedance component. Because there is no imaginary impedance, the current through a resistor is always in phase with the voltage. The impedance of an inductor increases as frequency increases. Inductors have only an imaginary impedance component [3].

[1] E. Barsoukov and J. R. Macdonald, *Impedance Spectroscopy*. 2005.
[2] Q. A. Huang, R. Hui, B. Wang, and J. Zhang, "A review of AC impedance modeling and validation in SOFC diagnosis," *Electrochim. Acta*, vol. 52, no. 28, pp. 8144–8164, 2007.
[3] R. Cottis and S. Turgoose, *Electrochemical Impedance and Noise*. Unites State of America: NACE International, 1999.

Figure S22. Ideal Nyquist plot of impedance and its equivalent circuit.

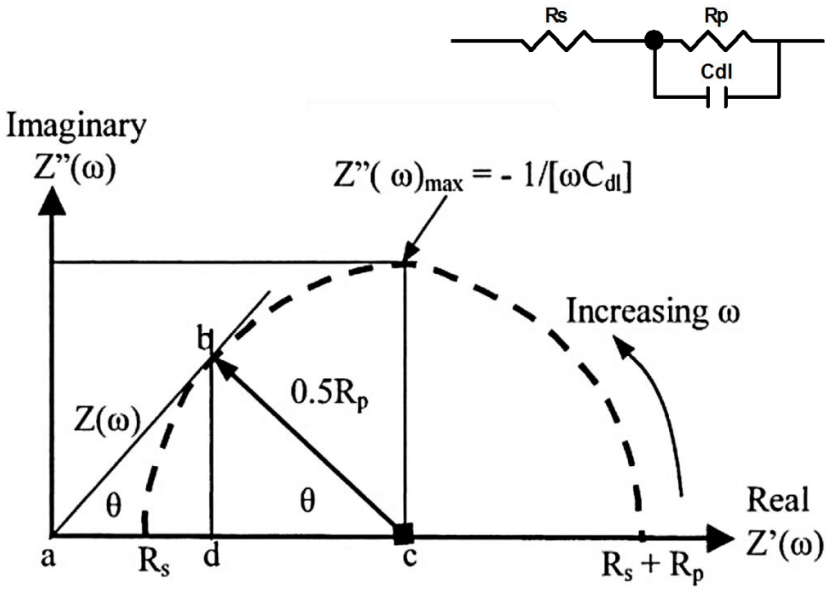

Consider a simple equivalent circuit with the double-layer capacitance in parallel with the polarization resistance, the expression for the real and the imaginary parts of the impedance is:

$$Z = \frac{R}{1+\omega^2 C^2 R^2} - \frac{j\omega R^2}{1+\omega^2 C^2 R^2} \qquad \text{(S36)}$$

$$Z = Z' + jZ'' \qquad \text{(S37)}$$

For the analysis of SOFC cells, usually a resistor (R_s) is connected in series to give the circuits shown in Figure S22. R_s is the sum of the electrolyte resistance and the electrode material resistance of both the anode and cathode and the contact resistances between the electrodes and current collectors [4].

With such a system, a semi-circle is traced out with center at Z'= R_s +R_p/2 and diameter R_p. R_s can be obtained from the high frequency intercept with the real axis,

[4] N. Perez, *Electrochemistry and Corrosion Science*. Boston, United states of America: Kluwer Academic Publishers, 2004.

and the total resistance $R_s + R_p$ from the low frequency intercept. One point to note is that the frequency at the top of arc, when - Z'' is at a maximum, is given by:

$$\omega_{max} = 2\pi\, f_{max} = \frac{1}{RC} \qquad \text{(S38)}$$

In all real systems, some deviation from ideal behavior can be observed. If the electrode surfaces are rough or if one or more of the dielectric materials in the system is inhomogeneous, many of these microscopic current filaments would be different. In a response, to a small-amplitude excitation signal, this would lead to frequency-dependent effects, which can often be modeled with simple distributed circuit elements. For example, many capacitors in EIS experiments, most prominently the double-layer capacitor C_{dl}, often do not behave ideally due to the distribution of currents and electroactive species. Instead, these capacitors often act like a constant phase element (CPE), which is an element widely used in impedance data modeling.

The impedance of a CPE has the form of dependency on an effective CPE coefficient *Q* [$ohm^{-1}s^n$] as:

$$Z_{CPE} = \frac{1}{Q(j\omega)^p} \qquad \text{(S39)}$$

In the Nyquist plot, a circuit composed of a single CPE element produces a straight line, which makes an angle of -p*90° with the x-axis (Figure S23). A circuit composed of a resistor R in parallel with a CPE produces a plot with a depressed semicircular arc with an angle of (p-1)*90°. For double-layer analysis, the parameter *Q* is essentially a constant representing an interfacial charging by both surface and electroactive species. CPE element with $0 \leq p \leq 1$ can be further separated into a frequency-dependent "pure" capacitor element with p=1 and "pure" resistor with p=0 that can be in parallel or in series [5].

[5] V. F. Lvovich, Impedance Spectroscopy: Applications to electrochemical and dielectric phenomena, Unites State of America: Wiley, 2012.

Figure S23. The Nyquist plot of the single CPE(*Q*) and a parallel resistor and CPE circuits.

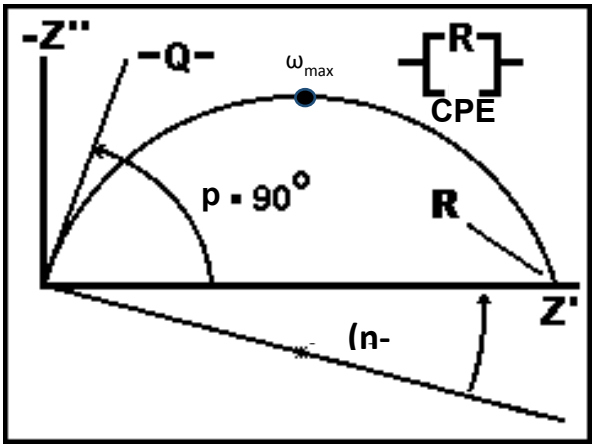

The true capacitance can be estimated from CPE (*Q*) using the following relationship [6][7]:

$$C = R^{\frac{(1-p)}{p}} Q^{\frac{1}{p}} \qquad \text{(S40)}$$

Despite CPE parameter is widely used to describe the electrode processes, one of its main problem is that it is only valid over a limited frequency range. CPE may be distorted at extremely low and high frequencies. In any physically valid model, there should be a shortest and a largest possible relaxation time. This is, however, not true for CPE. Therefore, CPE usually needs to be modified at both ends of the frequency spectrum. In many cases, this does not pose a problem, since impedance measurements are not carried out at extreme frequencies and/or the phenomenon represented by the CPE element is prominent only in a narrow range of frequencies, typically 1-3 orders of magnitude.

[6] E. Chinarro, J. R. Jurado, F. M. Figueiredo, and J. R. Frade, "Bulk and grain boundary conductivity of $Ca_{0.97}Ti_{1-x}Fe_xO_{3-\delta}$ materials," *Solid State Ionics*, vol. 160, pp. 161–168, 2003.

[7] P. Hjalmarsson, M. Søgaard, and M. Mogensen, "Electrochemical behaviour of $(La_{1-x}Sr_x)Co_{1-y}Ni_yO_{3-\delta}$ as porous SOFC cathodes," *Solid State Ionics*, vol. 180, pp. 1395–1405, 2009.

A more significant practical interpretation problem is related to CPE element flexibility. A CPE element can be very often used to fit into any type of experimental impedance data simply by varying the p-parameter. The choice of CPE representation should always be based on an understanding of the nature of studied distributed process. For the charge-transfer-related low frequency impedance data, several realistic possibilities grounded in the actual physic of the process exist for a CPE and not for a pure capacitance. In the process of heterogeneous electron transfer, the non-uniformity of rough electrode surfaces (inhomogeneity, roughness, edge orientation and porosity) is frequently responsible for non-ideality and observed frequency dispersions and their resulting CPE behavior. The following process may be responsible for the deviations from ideal resistor and capacitor response: (i) electrode inhomogeneity and surface roughness, (ii) electrode porosity, (iii) variability in thickness and conductivity of surface coating, (iv) slow, uneven adsorption process, (v) nonuniform potential and current distribution at the surface and (vi) grain boundaries and crystal phases on polycrystalline electrode [5].

Finally, in order to evaluate the global performance of the material assembly, it is possible to deduce the area specific resistance (ASR) from the polarization resistance (R_p), which is the sum of the individual resistances with the formula:

$$ASR = \frac{R_p S}{2} \qquad \text{(S41)}$$

where *S* is the electrode surface area (cm^2) and the factor 2 accounting for the fact that the cell is symmetrical.

Annex 8

Reactions at the cathode (Oxygen reduction)

The electrode reaction mechanism is a fundamental issue for electrochemistry study. The researchers began to try to build up SOFC cathode models over the past 20 years, including the detailed cathode reaction steps and its possible relationship with the improvement of cell performance.

The overall reaction for the oxygen reduction at an SOFC cathode can be written globally as:

$$\frac{1}{2}O_2^{gas} + 2e'^{,electrode} + V_O^{\bullet\bullet,electrolyte} \underset{\leftarrow}{\rightarrow} O_O^{x,electrolyte} \qquad \text{(S42)}$$

This reaction is made up of a series of bulk and surface processes that can include several rate-determining steps. There is no general model to describe the mechanism of oxygen reduction; however, experimental results show that the reaction depends on the temperature, the gas partial pressure (pO_2), the nature of the electrolyte and the nature of the electrode (electronic conductor, MIEC). In the case of porous electrode, the reaction at gas/solid interface and transport into the bulk are also affected by structural parameters, such as net surface area, content of porosity, and surface tortuosity [8].

According to the literature, the oxygen reduction reaction involves the following steps (Figure S24) [9][10][11]:

[8] Y. Li, R. Gemmen, and X. Liu, "Oxygen reduction and transportation mechanisms in solid oxide fuel cell cathodes," *J. Power Sources*, vol. 195, no. 11, pp. 3345–3358, 2010.
[9] R. N. Singh, "High-Temperature Seals for Solid Oxide Fuel Cells (SOFC)," *J. Mater. Eng. Perform.*, vol. 15, no. 4, pp. 422–426, 2006.
[10] D. Marinha, L. Dessemond, and E. Djurado, "Comprehensive review of current developments in IT-SOFCs," *Curr. Inorg. Chem.*, vol. 3, no. 1, pp. 2–22, 2013.
[11] L. Mogni, "Estudio de nuevos conductores mixtos para aplicaciones electroquímicas de alta temperatura," Universidad Nacional de Cuyo y C.N.E.A, 2007.

Figure S24. Steps for the oxygen reduction reaction reported or theorized in the literature (taken from [12]).

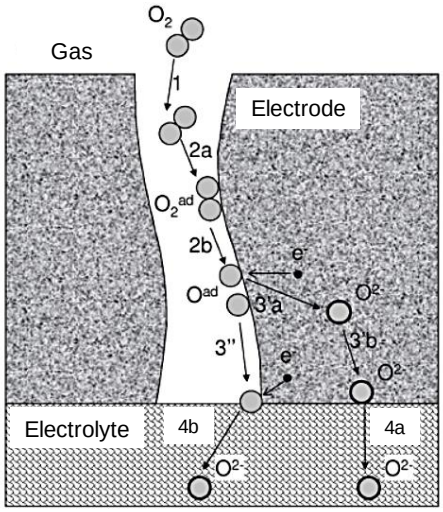

1. Gas diffusion.

   The diffusion of oxygen can occur both in the free gas phase or/and in the porosity of the electrode:

$$O_2^{gas} \underset{\leftarrow}{\rightarrow} O_2^{gas/electrode} \qquad \text{(S43)}$$

   The gas diffusion in porous electrodes is the main source of concentration polarization (concentration difference between bulk gas and functional layers) in Solid Oxide Fuel Cells. However, the diffusion process has not been well understood yet, due to the fact that 1) gas phase is a multicomponent gas mixture, including reactants, carrier gas and possibly products; 2) the porous electrode, through which gas phase has to travel could have a very complicated microstructure. In addition, the observed dependence of limiting currents on oxygen partial pressure (proportional to oxygen partial pressure) and gas flow rate supports the diffusion of oxygen as the slow step [13].

[12] L. Baqué, "Preparación y caracterización de cátodos de alto rendimiento para celdas de combustible de óxido sólido de temperatura intermedia," Universidad Nacional de Cuyo, 2011.
[13] Y. Fu, Y. Jiang, S. Poizeau, A. Dutta, A. Mohanram, J. D. Pietras, and M. Z. Bazant, "Multicomponent gas diffusion in porous electrodes," *J. Electrochem. Soc.*, vol. 162, no. 6, pp. F613–F621, 2015.

2. Adsorption and dissociation.

   The adsorption process may involve two successive stages, non-dissociative adsorption followed by dissociation, or a single dissociative adsorption stage. If *s* is an adsorption site available on the surface, the reactions can be described as:

   - Non-dissociative adsorption (molecular oxygen is absorbed on the electrode surface). The oxygen activity in the adsorbed layer determines the electrode potential, and surface concentration variation is responsible for large capacitive effects.

   $$O_2^{gas/cathode} + s \rightleftarrows O_{2,ad} \qquad \text{(S44)}$$

   - Dissociative adsorption.

   $$O_2^{gas/cathode} + 2s \rightleftarrows 2O_{ad} \qquad \text{(S45)}$$

3. Transport of the oxygen and/or electroactive species to the electrode/electrolyte interface.

   With mixed conductors, it is possible for species adsorbed on the surface to be transported through the bulk of the material to the electrode/ electrolyte interface. If bulk transport is facile, this path may dominate, extending both the accessible surface for O_2 reduction as well as broadening the active charge-transfer area. This stage involves the following steps:

   3a. Ionic incorporation into the electrode (with charge-transfer).

   $$O_{ad} + ne^- \rightleftarrows O_{ad}^{-n} \qquad \text{(S46)}$$

   $$O_{ad}^{2-} + V_O^{\bullet\bullet} \rightleftarrows O^{2-,cathode} \qquad \text{(S47)}$$

3b. Diffusion of oxygen (O^{2-}) inside the electrode (bulk diffusion).

$$O^{2-,cathode} \rightleftarrows O^{2-,cathode/electrolyte} \qquad \text{(S48)}$$

3''. Surface diffusion of adsorbed oxygen atoms to a three-phase boundary (TPB).

$$O_{ad}^{-n} \rightleftarrows O_{TPB}^{-n} \qquad \text{(S49)}$$

4. Incorporation of the oxygen into the electrolyte (ionic transfer).
   In the case of a MIEC, only the ionic transfer in the DPB (*double phase boundary*) occurs (4a), since the charge transfer already occurred at the electrode/gas interface.

$$O^{2-,cathode/electrolyte} + V_{O,electrolyte} \rightleftarrows O^{2-,electrolyte} \quad \text{(S50)}$$

   If the electrode material is an electronic conductor, this stage occurs at the TPB involving a charge transfer process (4b), as follows:

$$O^{-n,TPB} + V_{O,electrolyte} + (1+n)e^- \rightleftarrows O^{2-,electrolyte} \quad \text{(S51)}$$

According to the simplified and well-known reaction mechanism at the cathode, the oxygen gas is reduced at the interface between the gas phase and the mixed-conductor, producing oxygen ions and consuming electrons. The oxygen ions are then transported through the mixed conductor to the electrolyte, while the electrons are supplied from the current-collector. In this mechanism, the reaction to occur over a finite region of the mixed-conducting surface, beyond the confines of the three-phase boundary (TPB). However, the reaction mechanism proposed for a mixed-conductor involves multiple steps occurring at different locations in a macroscopically defined three-dimensional space. In this way, it is not possible to embody this mechanism mathematically without addressing the three-dimensionality of these physical phenomena.

In order to answer this, Adler *et al*. developed a model in which each element of this mechanism was treated as a macroscopically defined process (interfacial charge-transfer, exchange of O_2 at the mixed-conductor surface, transport of charged species in the mixed conductor, diffusion of O_2 in the gas). In principle, the authors proposed that all these processes could be described and measured independently, either as a bulk material property or as an interfacial property between two phases. For materials for which this approach is successful, it provides a quantitative formalism for connecting the overall electrode kinetics to the bulk and interfacial

properties of the materials [14]. The electrochemical cell modeled is illustrated in Figure S25.

Figure S25. Cell geometry considered in the Adler's model [14].

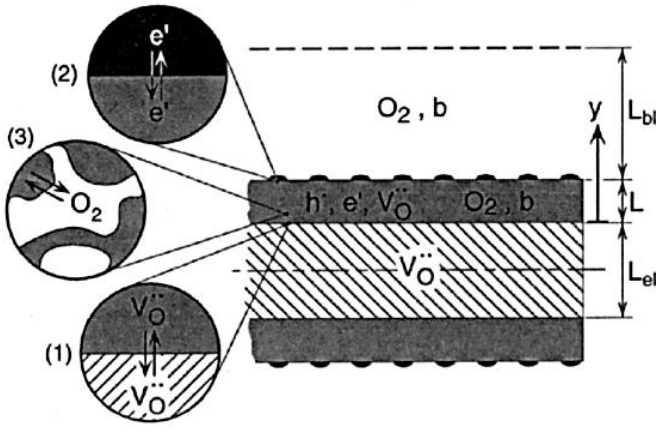

Adler proposed a symmetric cell configuration consisting of an electrolyte pellet (thickness L_{el}) with two identical oxygen electrodes (thickness L). Both electrodes are exposed to the same gas atmosphere, but each is separated from the well-mixed gas by a boundary layer (thickness L_{bl}). We specify that the overall reaction occurs via three physically separated interfacial reactions: (1) charge-transfer of oxygen ion vacancies across the mixed conductor/electrolyte interface, (2) charge-transfer of electrons across the current-collector/mixed conductor interface, and (3) the chemical exchange of oxygen at the gas/mixed-conductor interface. For this third reaction, the gas/MIEC interface includes the entire internal surface area of the porous mixed conductor as well as the boundary between the porous region and the gas-phase boundary layer. These interfacial reactions are linked indirectly by transport of oxygen ions and electrons (or holes) in the mixed conductor and diffusion of molecular oxygen inside the pores of the catalyst and in the gas-phase boundary layer [14]. The measured impedance (Figure S26) is expressed as the

[14] S. B. Adler, J. A. Lane, and B. C. H. Steele, "Electrode kinetics of porous mixed-conducting oxygen electrodes," *J. Electrochem. Soc*, vol. 143, no. 11, p. 3554, 1996.

sum of $R_{electrolyte}$ (electrolyte resistance) + $Z_{interface}$ (electrochemical kinetic impedance at electrolyte-electrode interface) + $Z_{chemical}$ (chemical impedance arising from oxygen absorption, and diffusion in solid and gas phase both inside and outside the electrode),

$$\boldsymbol{Z} = R_{electrolyte} + Z_{interface} + Z_{chem} \qquad \text{(S52)}$$

Figure S26. Schematic of the total impedance as predicted by Eq. (3-20) and (b) Plot of the 'chemical' impedance in the limit of Eq. (3-21).

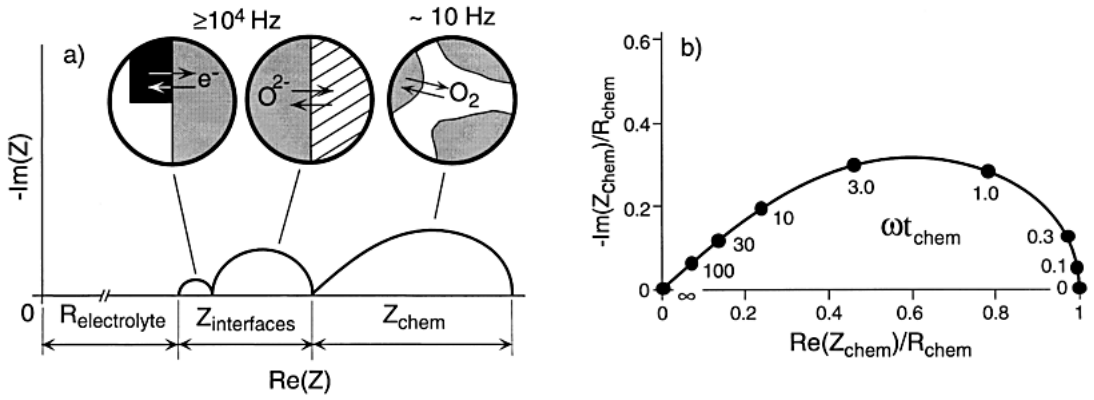

In the case of semi-infinite thick porous cathode with no limitations from gas phase diffusion, the chemical impedance (Z_{chem}) is co-limited by absorption and transport of oxygen [15]. This can be expressed as follows:

$$Z_{chem} = R_{chem}\sqrt{\frac{1}{1+j\omega t}} = R_{chem}\sqrt{\frac{1}{1+j\omega(R_{chem}C_{l_\delta})}} \qquad \text{(S53)}$$

Where R_{chem} is the characteristic resistance, t is the time constant and C_{l_δ} is the capacitance, reflecting co-limitation by surface kinetic and transport properties of the mixed conductor:

$$R_{chem} = \frac{RT}{4F^2}\sqrt{\frac{fV_m}{\tilde{D}_{eff}\, ar_o}} = \sqrt{\frac{4R_{surf}}{\sigma_{i.eff}a}} \qquad \text{(S54)}$$

$$C_{l_\delta} = \frac{4F^2}{RT}\,\frac{(1-\epsilon)l_\delta}{fV_m} \qquad \text{(S55)}$$

[15] S. B. Adler, "Mechanism and kinetics of oxygen reduction on porous $La_{1-x}Sr_xCoO_{3-\delta}$ electrodes," *Solid State Ionics*, vol. 111, pp. 125–134, 1998.

where V_m is the molar volume, $\widetilde{D}_{eff} = (1-\epsilon)\widetilde{D}/\tau$ is the effective oxygen-ion chemical diffusion coefficient in the solid (corrected for porosity and path tortuosity), $\sigma_{i.eff}$ is the effective ionic conductivity, and r_o and *f* are the linearized rate of oxygen absorption/desorption and a thermodynamic factor, respectively. R_{chem} can be also expressed in terms of surface and bulk resistances defined for a thin film as:

$$R_{surf} = \frac{RT}{4F^2}\,\frac{1}{2r_0} \qquad \text{(S56)}$$

$$R_{bulk} = \frac{RT}{4F^2}\,\frac{fV_mL}{2\widetilde{D}} = \frac{L}{\sigma_i} \qquad \text{(S57)}$$

where R_{surf} denotes area of specific resistance related to the oxygen reduction at the gas-film interface, and R_{bulk} represents area-specific resistance related to the oxide ion conductivity of the film [16][17]. Over the years, contributions of various researchers, and primarily Adler's model, have enriched the understanding of the cathode mechanisms and how these mechanisms relate to material properties and microstructure [14][18][19][20][21]. Consequently, this model has been especially used to explain the impedance data for $La_{0.6}Sr_{0.4}Co_{0.2}Fe_{0.8}O_{3-\delta}$ (LSCF) [14], $La_{0.8}Sr_{0.2}CoO_{3-\delta}$ (LSC) [22], $Sm_{0.5}Sr_{0.5}CoO_{3-\delta}$ [23], among others.

[16] S. B. Adler, "Factors governing oxygen reduction in solid oxide fuel cell cathodes," *Chem. Rev.*, vol. 104, no. 10, pp. 4791–4843, 2004.

[17] N. Mahato, A. Banerjee, A. Gupta, S. Omar, and K. Balani, "Progress in material selection for Solid Oxide Fuel Cell technology: A Review," *Prog. Mater. Sci.*, vol. 72, pp. 141-337, Feb. 2015.

[18] A. M. Svensson, S. Sunde, and K. Nisancioglu, "A mathematical model of the porous SOFC cathode," *Solid State Ionics*, vol. 86–88, pp. 1211–1216, 1996.

[19] A. M. Svensson and S. Sunde, "Mathematical Modeling of Oxygen Exchange and Transport in Air-Perovskite-Yttria-Stabilized Zirconia Interface Regions," *J. Electrochem. Soc.*, vol. 144, no. 8, pp. 2719–2731, 1997.

[20] A. Endo, H. Fukunaga, C. Wen, and K. Yamada, "Cathodic reaction mechanism of dense $La_{0.6}Sr_{0.4}CoO_3$ and $La_{0.81}Sr_{0.09}MnO_3$ electrodes for solid oxide fuel cells," *Solid State Ionics*, vol. 135, no. 1–4, pp. 353–358, 2000.

[21] M. Gong, R. S. Gemmen, and X. Liu, "Modeling of oxygen reduction mechanism for 3PB and 2PB pathways at solid oxide fuel cell cathode from multi-step charge transfer," *J. Power Sources*, vol. 201, pp. 204–218, 2012.

[22] S. B. Adler, "Limitations of charge-transfer models for mixed-conducting oxygen electrodes," *Solid State Ionics*, vol. 135, no. 1–4, pp. 603–612, 2000.

[23] M. Koyama, C. Wen, T. Masuyama, J. Otomo, H. Fukunaga, K. Yamada, K. Eguchi, and H. Takahashi, "The mechanism of porous $Sm_{0.5}Sr_{0.5}CoO_3$ cathodes used in Solid Oxide Fuel Cells," *J. Electrochem. Soc.*, vol. 148, no. 7, pp. A795–A801, 2001.

Annex 9

Reactions at the anode (Hydrogen oxidation)

The reaction mechanism describing chemistry and electrochemistry within an SOFC anode is extremely complex. The elementary reaction steps may include homogeneous gas-phase chemistry, heterogeneous surface reactions of ad/desorbing species, homogeneous surface dissociation and reactions between adsorbed species, and heterogeneous charge-transfer reactions. Understanding the reaction mechanism and kinetics that occur at the anode and elucidating structure-property-performance relationships are paramount to optimize the anode and operating conditions. However, extensive experimental investigation, as well as the modeling, are required [24].

The successful identification of the rate limiting step (which likely depends on temperature, current density, and/or other variables), would allow electrode performance improvement by minimizing its limiting effects. In the last decade, numerous mechanistic theories have been proposed debating the different rate determining steps. That particular step might include: adsorption [25][26], surface diffusion [27][28], charge transfer [29][30], catalytic effects of water [25], among others.

[24] B. Shri Prakash, et al., “Properties and development of Ni/YSZ as an anode material in solid oxide fuel cell: A revie,” *Renew. Sustain. Energy Rev.*, vol. 36, pp. 149-179, 2014.

[25] A. Bieberle, L. P. Meier, and L. J. Gauckler, “The electrochemistry of Ni pattern anodes used as solid oxide fuel cell model electrodes,” *J. Electrochem. Soc.*, vol. 148, no. 6, pp. A646-A656, 2001.

[26] S. Jiang and S. P. S. Badwal, “An electrode kinetics study of H2 oxidation on Ni/Y_2O_3-“ZrO_2 cermet electrode of the solid oxide fuel cell,” *Solid State Ionics*, vol. 123, no. 1–4, pp. 209-224, 1999.

[27] M. Mogensen and S. Skaarup, “Kinetic and geometric aspects of solid oxide fuel cell electrodes,” *Solid State Ionics*, vol. 86–88, no. PART 2, pp. 1151-1160, 1996.

[28] K. Mizusaki, et al., “Preparation of nickel pattern electrodes on YSZ and electrochemical propertis in H_2-H_2O atmospheres,” *Electrochem. Soc.*, vol. 141, no. 8, pp. 533-541, 1994.

[29] M. Brown, S. Primdahl, and M. Mogensen, “Structure/Performance Relations for Ni/Yttria-Stabilized Zirconia Anodes for Solid Oxide Fuel Cells,” *J. Electrochem. Soc.*, vol. 147, no. 2, p. 475, 2000.

[30] P. Holtappels, “Reaction of hydrogen/water mixtures on nickel-zirconia cermet electrodes: I. DC polarization characteristics,” *J. Electrochem. Soc.*, vol. 146, no. 5, pp. 1626-1625, 1999.

Several authors have tried to understand the precise anodic reaction mechanism at the state-of-the-art Ni-YSZ cermet by the conventional electrochemical methods. Using DC polarization curves, current interruption analysis, and AC impedance spectra analysis, the anode properties have been measured as functions of the partial pressure of reactant/product (pH_2 or pH_2O) and temperature. The dependences of pH_2 and pH_2O for the reaction rates are somewhat different depending on the authors and samples. The reason for this difference can stem from the microstructure of the Ni-cermet anodes and experimental conditions (such as temperature and total pressure of fuel), which may affect the sensitivity of reaction rates to the reaction species. However, relatively strong pH_2O dependence was observed in the reported data, suggesting the importance of H_2O in the anodic reaction. In view of the observed dependence of reaction rates on pH_2 and pH_2O, some reaction models were proposed for Ni-YSZ anodes. For considering the reaction mechanism, several kinds of reaction paths must be considered at the anode/electrolyte interface. The movements of reaction gases and ions are composed of several elemental steps, as shown Figure S27, in which any of the following steps could be rate determining: (i) diffusion of reaction species (H_2 and H_2O) in gas phase, (ii) dissociative adsorption of reaction gases at the solid surfaces (formation of H_{ad}, O_{ad}, OH_{ad}^-,… on metal or oxide surfaces), (iii) surface diffusion of H_{ad}, O_{ad}, OH_{ad}^- on anode surface or diffusion of H in the metal to the reaction sites, and (iv) charge transfer of reaction species and formation of H_2O at reaction sites [31].

[31] T. Horita, H. Kishimoto, K. Yamaji, Y. Xiong, N. Sakai, M. E. Brito, and H. Yokokawa, “Materials and reaction mechanisms at anode/electrolyte”, *Solid State Ionics,* vol. 177, pp.1941-1948, 2006

Figure S27. Schematic diagram of possible reaction process for H_2 oxidation around the H_2-H_2O/anode/electrolyte interfaces. (a): proposed by Holtappels *et al*. [32], (b): proposed by Jiang and Badwal [33].

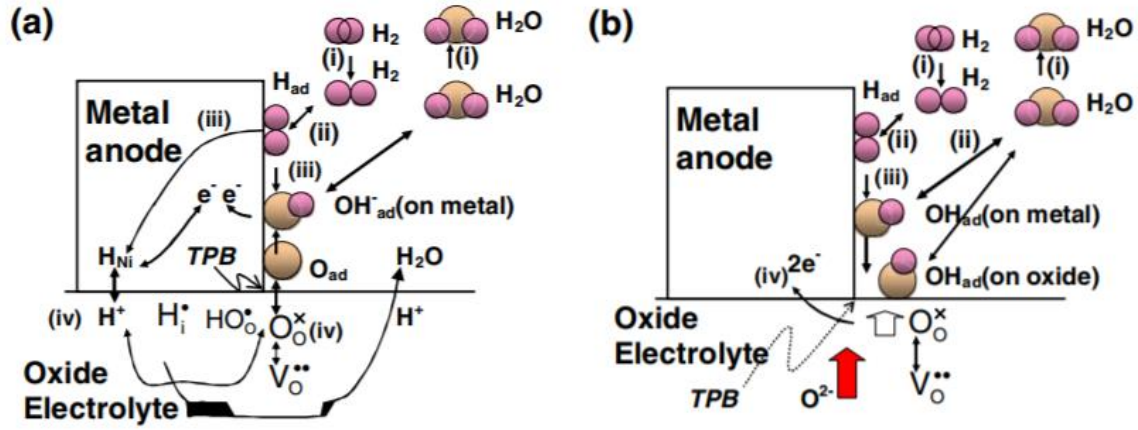

The well know reaction mechanisms are hydrogen spillover and oxygen spillover. The term spillover is used to describe the process by which a molecule adsorbs or reacts on one of the phases (Ni or YSZ) before diffusing over onto the second phase, where it is free to react with other adsorbed species.

The hydrogen spillover mechanism first proposed by Mogensen and Lindegaard [34] has had numerous variations over the years. Globally, gas-phase molecular hydrogen H_2(g) is adsorbed and subsequently dissociates on the Ni surface (Ni). The adsorbed hydrogen atoms H(Ni) are then transported as protons H^+ (Ni) - which requires the release of an electron to the anode e^- (Ni) - to the TPB region. Oxygen

[32] P. Holtappels, L. G. J. de Haart, and U. Stimming, "Reaction of hydrogen water mixtures on nickel-zirconia cermet electrodes II. AC polarization characteristics," *J. Electrochem. Soc.*, vol. 146, no. 8, pp. 2976-2982, 1999.

[33] S. P. Jiang, "Hydrogen oxidation at the nickel and platinum electrodes on yttria-tetragonal zirconia electrolyte," *J. Electrochem. Soc.*, vol. 144, no. 11, p. 3777, 1997.

[34] M. Mogensen and T, Lindegaard "The kinetics of hydrogen oxidation on a Ni/YSZ SOFC electrode at 1000 °C," *Singhal SC, Iwahara H, Ed. Solid oxide fuel cells III. Pennington, NJ Electrochem. Soc. 3rd Int. Symp. Solid Oxide Fuel Cells (SOFC-III),* Honolulu, HI, USA., pp. 484-493, 1993.

ions on the electrolyte O^{2-} (YSZ) react with the protons and form adsorbed hydroxyl ions OH^- (YSZ). Two hydroxyl ions then react on the YSZ surface to form water and O^{2-} (YSZ). Others authors such as Boer [35] and Lee [36] included intermediate steps in order to provide better agreement with experimental results, but in all cases the hydrogen spillover process is characterized by adsorption of molecular hydrogen on the Ni surface, and desorption of water from the YSZ surface.

Oxygen spillover suggests that oxygen ions are transported by surface spillover from the electrolyte (*i.e.* YSZ) to the nickel at (or very near) the TPB, where they react with adsorbed hydrogen to generate water and electrons. Unlike hydrogen spillover, the adsorption of molecular hydrogen and desorption of water both take place on the Ni surface. For this model, Bieberle and Gauckler compared experimental EIS to simulation results of nickel-patterned anodes exposed to gaseous H_2-H_2O mixtures, detailing the kinetics of an electrochemical model for SOFC anodes [37].

Bessler *et al*. [38] address the general misunderstanding in most SOFC reaction-kinetic studies that electrochemical reaction rates depend only on reactant concentrations. The reaction rates and electrochemical equilibrium depend on reactant and product concentrations, because it is a dynamic equilibrium between forward and backward reactions. The authors develop a thermodynamic model of the TPB that describes the coupling of electroactive intermediates with global gas-phase species. The model is used to study the behavior of the reaction pathways discussed above, and results are compared to published experimental data. The five charge-transfer reactions are summarized in Table S2.

[35] B. de Boer, “SOFC Anode: hydrogen oxidation at porous nickel and nickel/ yttria-stabilised zirconia cermet electrodes,” Netherlands: University of Twente, 1998.
[36] W. Y. Lee, D. Wee, and A. F. Ghoniem, “An improved one-dimensional membrane-electrode assembly model to predict the performance of solid oxide fuel cell including the limiting current density,” *J. Power Sources*, vol. 186, no. 2, pp. 417–427, Jan. 2009.
[37] A. Bieberle and L. J. Gauckler, “State-space modeling of the anodic SOFC system Ni, H_2-H_2O|YSZ,” *Solid State Ionics*, vol. 146, no. 1-2, pp. 23-41, 2002.
[38] W. G. Bessler, J. Warnatz, and D. G. Goodwin, “The influence of equilibrium potential on the hydrogen oxidation kinetics of SOFC anodes,” *Solid State Ionics*, vol. 177, no. 39-40, pp. 3371.

Table S2. Elementary charge-transfer reactions analyzed by Bessler *et al*. in [38].

No.	Label	Reaction
1	O spillover[a]	$O^{2-}(YSZ) + (Ni) \rightleftharpoons O(Ni) + (YSZ) + 2e^{-}(Ni)$
2	OH spillover	$OH^{-}(YSZ) + (Ni) \rightleftharpoons OH(Ni) + (YSZ) + e^{-}(Ni)$
3	H spillover to O[b]	$H(Ni) + O^{2-}(YSZ) \rightleftharpoons (Ni) + OH^{-}(YSZ) + e^{-}(Ni)$
4	H spillover to OH	$H(Ni) + OH^{-}(YSZ) \rightleftharpoons (Ni) + H_2O(YSZ) + e^{-}(Ni)$
5	H interstitial[c]	$H_i^{\times}(Ni) \rightleftharpoons H_i^{\cdot}(YSZ) + e^{-}(Ni)$

According to Bessler *et al*., the well-established activating effects of water on the anode kinetics can be explained by Nernst-potential (equilibrium-potential) effects alone, without the need to assume any additional kinetic or catalytic effect. The results indicate that all charge-transfer reactions have a strong and highly nonlinear kinetic dependence on gas-phase hydrogen and water partial pressures due to equilibrium-potential effects, and this behavior is distinctly different for the various mechanisms. All mechanisms given in Table S2 show an increase in exchange current density with increasing pH_2O. However, with increasing pH_2, the O and OH spillover reactions show decreasing kinetics, while the H spillover and H interstitial reaction kinetics are increasing. This finding supports a conclusion that the dominating reaction mechanism and kinetics of charge-transfer may change with operating conditions. In addition, although the model is unable to consistently interpret all published experimental results simultaneously, they agree mostly that the rate-limiting step in pattern anodes is charge-transfer, and the observations are most consistent with a surface hydrogen spillover reaction (Table S2, No. 4) as rate-determining [39].

[39] J. Hanna, W. Y. Lee, Y. Shi, and A. F. Ghoniem, “Fundamentals of electro- and thermochemistry in the anode of solid-oxide fuel cells with hydrocarbon and syngas fuels,” *Prog. Energy Combust. Sci.*, vol. 40, no. 1, pp. 74-111, 2014.

Annex 10

Table S3. Resistances for L5S15M electrodes prepared at 1150 °C and 1200 °C measured in wet 3% H_2/Ar (3% H_2O).

	L5S15M sintered at 1150 °C						**L5S15M sintered at 1200 °C**						
Temp. (°C)	**R_s**	**R1 (Ω cm²)**	**R2 (Ω cm²)**	**R3 (Ω cm²)**	**R_p (Ω cm²)**	**ASR (Ω cm²)**	**R_s**	**R1 (Ω cm²)**	**R2 (Ω cm²)**	**R3 (Ω cm²)**	**R4 (Ω cm²)**	**R_p (Ω cm²)**	**ASR (Ω cm²)**
828	5.24	0.22	1.15	5.35	6.71	3.36	4.70	0.15	1.21	1.69	4.94	7.99	4.00
802	6.00	0.25	1.82	5.44	7.51	3.76	5.41	0.22	1.48	2.67	5.10	9.47	4.73
770	7.29	0.33	3.13	5.69	9.15	4.57	6.66	0.35	1.94	4.95	5.31	12.54	6.27
754	8.61	0.38	4.97	5.83	11.18	5.59	7.93	0.45	2.20	10.20		12.85	6.42
728	10.58	0.49	8.18	6.50	15.17	7.58	9.89	0.71	3.14	19.62		23.47	11.73
702	13.21	0.62	20.93		21.55	10.78	12.55	1.13	4.54	28.93		34.60	17.30
679	16.32	0.81	29.99		30.80	15.40	15.62	1.83	6.18	41.49		49.50	24.75
651	21.33	1.06	48.84		49.90	24.95	20.89	3.32	8.93	65.69		77.94	38.97
627	27.86	1.42	77.53		78.95	39.47	27.75	5.98	12.78	100.20		118.96	59.48

Table S4. Relaxation frequencies and equivalent capacitances for L5S15M electrodes prepared at 1150 °C and 1200 °C measured in wet 3% H_2/Ar (3% H_2O).

	L5S15M sintered at 1150 °C						**L5S15M sintered at 1200 °C**							
Temp. (°C)	**f_1 (Hz)**	**f_2 (Hz)**	**f_3 (Hz)**	**C_1 (F cm^{-2})**	**C_2 (F cm^{-2})**	**C_3 (F cm^{-2})**	**f_1 (Hz)**	**f_2 (Hz)**	**f_3 (Hz)**	**f_4 (Hz)**	**C_1 (F cm^{-2})**	**C_2 (F cm^{-2})**	**C_3 (F cm^{-2})**	**C_4 (F cm^{-2})**
828	27	0.43	0.03	2.74E-2	3.21E-1	1.04	6225	47	0.30	0.03	1.7E-4	2.83E-3	0.31	1.00
802	29	0.32	0.03	2.19E-2	2.77E-1	1.07	4876	44	0.22	0.03	1.5E-4	2.43E-3	0.27	1.01
770	25	0.20	0.03	1.92E-2	2.58E-1	1.07	3433	41	0.15	0.03	1.3E-4	2.00E-3	0.22	1.05
754	25	0.16	0.02	1.65E-2	2.04E-1	1.15	2915	53	0.08		1.2E-4	1.36E-3	0.19	
728	24	0.11	0.02	1.36E-2	1.82E-1	1.06	2121	42	0.05		1.1E-4	1.21E-3	0.16	
702	20	0.05		1.26E-2	1.60E-1		1636	33	0.04		8.6E-5	1.06E-3	0.14	
679	14	0.04		1.36E-2	1.47E-1		1396	27	0.03		6.2E-5	9.38E-4	0.13	
651	13	0.02		1.17E-2	1.41E-1		1342	22	0.02		3.6E-5	8.13E-4	0.12	
627	10	0.01		1.18E-2	1.42E-1		1117	17	0.01		2.4E-5	7.21E-4	0.12	